EROSION, CORROSION AND EROSION-CORROSION OF OIL AND GAS PIPELINE STEELS

by

Md. Aminul Islam

Submitted in partial fulfilment of the requirements
for the degree of Doctor of Philosophy

at

Dalhousie University
Halifax, Nova Scotia
November 2015

To my wonderful wife and family – those who suffered

And to the memory of my late grandfather Hafez Mukhbul Ahmed
I know you would have been happy

Table of Contents

List of Tables

List of Figures

Abstract

Oil and gas industry spends millions of dollars every year dealing with problems caused by erosion-corrosion. During the transportation of oil and gas, pipes are exposed to flowing corrosive environment which causes erosion-corrosion. The high degradation rates attributed to this mechanism can create increased challenges to project economy and operation where material integrity, accurate erosion-corrosion rate prediction and long term performance are key concerns. Although the problem caused by the interaction of erosion and corrosion is severe, the mechanism of synergy is still not thoroughly understood because of its complexity. This research focuses on understanding the degradation processes of pipeline steels in CO_2 containing salt water. The application of cyclic erosion-corrosion allowed the individual contribution of erosion and corrosion components of mass loss to be quantified and mechanisms by which erosion affects corrosion and vice-versa to be identified. The present research also correlates erosion and corrosion response of steel to its microstructure.

List of Abbreviations and Symbols Used

Abbreviations

AcC	Accelerated Cooling
AISI	American Iron and Steel Institute
API	American Petroleum Institute
ASTM	American Society for Testing and Materials
BCC	Body Centered Cubic
BE	Binding Energy
BS	British Standards
CFD	Computational Fluid Dynamics
CST	Cooling Stop Temperature
DH	Dislocation Hardening
DIN	Germany Steel Grades
EDS	Energy Dispersive Spectroscopy
EOR	Enhanced Oil Recovery
FBC	Fluidized Bed Combustion
FRT	Finish Rolling Temperature
GB	China Steel Grades
GR	Grain Refinement
HSLA	High-strength Low Alloy Steel
HSS	High-strength Steel

ICP	Inductively Coupled Plasma Mass Spectrometry
ISO	International Organization for Standardization
JIS	Japanese Steel Grades
JISC	Japanese Industrial Standards Committee
KE	Kinetic Energy
M	Molar
NBS	National Standards Body
OCP	Open Circuit Potential
PDF	Powder Diffraction File
PH	Precipitation Hardening
PR	Pearlite Reduction
R_a	Average Roughness
RMS	Root Mean Square
SAE	Society of Automotive Engineers
SPE	Solid Particle Erosion
SRT	Slab Reheating Temperature
TMT	Thermo-Mechanical Treatment
UNS	Unified Numbering System
XPS	X-ray Photoelectron Spectroscopy
XRD	X-ray Diffraction

Symbols

a	Thermal diffusivity of the erodent, ($m^2\ s^{-1}$)
A	Surface area (mm^2)
A_1	Entire surface of the specimen exposed to corrosion (mm^2)
A_2	Surface area exposed to corrosion only (mm^2)
A_3	Surface of the specimen exposed to erosion and corrosion (mm^2)
C_0	Corrosion rate in absence of erosion ($\mu m\ s^{-1}$)

C_e	Total corrosion component (μm s^{-1})
ΔC_e	Change in corrosion rate due to erosion (μm s^{-1})
Cp	Specific heat
d	Density (g cm^{-3})
D_t	Density of target material
D_p	Density of abrasive particle
E	Normalized erosion rate
E_1	Erosion rate
E_0	Erosion rate in the absence of corrosion (μm s^{-1})
E_c	Total erosion component (μm s^{-1})
E_{corr}	Corrosion potential (mV)
ΔE_c	Change in erosion rate due to corrosion (μm s^{-1})
EW	Equivalent weight
f_c	Proportion of particles impacting the surface
H_s	Static hardness of target material
H_d	Dynamic hardness of target material
I_{corr}	Corrosion current density (μA cm^{-2})
I^*_{corr}	Corrosion current density during erosion-corrosion (μA cm^{-2})
k	Constant
k_4	Ratio of vertical to horizontal force components on the particle
K_1	Constant (1×10^6 μm cm^{-1})
K_2	Constant (277.78 μm hr cm^{-1} s^{-1})
K_3	Constant (1.03×10^{-7} μm g μA^{-1} cm^{-1} yr^{-1})
n	Velocity exponent
r_0	Radius of the erodent (m)
S	Synergistic component
t	Test duration (s)
T	Total mass loss rate of the material (μm s^{-1})
T_m	Melting temperature

V	Normalized particle velocity
V_1	Velocity (m s^{-1})
V_m	Volume of material removed
ΔW	Weight loss of the specimen (g)
α	Particle impact angle (°)
a_r/ε_c^2	Constant (0.7)
β_a	Anodic beta (mV $decade^{-1}$)
β_c	Cathodic beta (mV $decade^{-1}$)
v	Particle velocity (m s^{-1})

Acknowledgements

The last few years were the toughest and eventful period of my life. But now that I look back from the end of the road, I see a very rewarding and educational experience. And I want to take a moment to acknowledge the people who had contributed to making this so.

I will never forget the fall 2008, I walked into Professor Zoheir Farhat's office for the first time. Unbeknownst to me, it was only the beginning of a long eventful journey together of scientific discoveries and endeavors. I am truly grateful to have him not only as my M.A.Sc. and Ph.D. supervisor, but also as my mentor, philosopher and guardian for more than the last seven years of my life. There is so much to learn from him, the most valuable of which I found was to approach research with a direct and positive attitude, passion and enthusiasm. I also found this to be true for life outside academia. I consider myself honored and fortunate to receive the mentorship of this great person. He is a true source of inspiration for me. Nevertheless, because of you, I believe my writing is now almost readable!

I would like to express my sincerest and heartfelt gratitude towards Dr. George Jarjoura. I am very thankful to have the opportunity to share some of his wealth of wisdom and knowledge in corrosion. I am very grateful to Professor Akram Alfantazi, Professor Andrew Warkentin and Dr. Richard Chromik. I certainly could not have made it this far without their knowledge, expertise and invaluable suggestions.

I would like to gratefully acknowledge Qatar National Research Fund (a member of Qatar Foundation) for their financial support (NPRP grant no. 6-027-2-010 and 08-159-2-046) and the student scholarship I have received from Department of Process Engineering and Applied Science and Faculty of Graduate Studies, Dalhousie University.

Over the course of the last few years I had the opportunity to work with some very bright and enthusiastic minds. I thankfully acknowledge the contributions of Tahrim Alam, Syed Zakaria, Tousif Ahmed and William Judge. I appreciate the help, assistance and support I received from my colleagues and friends Avijit Sinha, Rabin Neupane, Chenxin Jin, Momotaj Aghdasi, Chukwuma Onuoha, Abdullah Almotairi, Dr. Abdulwahab Ibrahim and all my present and past Advance Tribology Laboratory (ATL) group members. I would like to thank Dean Grijm of the machine and instrument shops, Patricia Scallion of the Institute for Research in Materials, Gerald Fraser of the Minerals Engineering Centre and Allison Fulford of Sexton Library for their valuable expertise, resources and support throughout the entire length of this project.

I will never forget the care and affection I received from my friends and neighbors from the Bangladeshi Community in Halifax during my studentship. I would like to particularly acknowledge Shamsuzzaman bhai, Mehdi bhai, Sharif bhai, Rupok bhai and Rinku apu, Mushfiq bhai and Tithi bhabi, Kakon bhai and Toma bhabi, Rizwana apu and Rifat bhai , Fatmi and Nitol, Aminul Islam Bappy, Shakil, Robin, Towfiq and Jahed -I thank you all for the good times.

I do not have words to express my gratitude towards my family-my parents, who has been a source of encouragement and inspiration to me throughout my life, my Grandma, my sisters-Shanu, Shrity and Nidhi, my aunt-Shilpy

and Milky and my uncle Mahfuz. It would not have been possible without your endless love and support.

This thesis is a legacy of the sacrifice of my wife Fahria, who had placated the anxieties and stresses of a graduate student with her endless love, care, affection and constant support. I never quite understood how you managed to do that, but I do know that I always had you by my side.

Finally, I am grateful to you Almighty, because you gave me the strength and determination to carry on throughout this very difficult but rewarding phase of my life.

Md. Aminul Islam
Halifax, November, 2015

Chapter 1

Introduction

Pipelines move over two thirds of the oil and gas transported annually worldwide. Pipelines are the most convenient means of transporting enormous quantities of natural gas and crude oil from production sites to the consumer and can last for several decades with minimal maintenance. Compared to other modes of transportation, in the US and Canada, pipelines carry 60% of all petroleum products. Figure 1-1 shows the relative contribution by each mode of transportation [1]. In North America alone, there are almost 500,000 miles of transmission pipeline networks carrying crude oil and natural gas, and over 2 million miles of inter-city natural gas distribution pipelines carrying natural gas to businesses and consumers [2].

In addition to their efficiency, pipelines have unmatched environmental and safety benefits. In contrast to other inland transport modes, pipelines do not crowd our highways and rivers and they produce negligible air pollution. Pipelines also have a lower spill rate per barrel of oil transported than competing modes of transportation, namely trucks and barges.

Table 1-1 compares incident rates for road, rail and pipeline transportation modes [2]. The majority of incidents occur on road and rail, as shown by Transportation Department data. Road transport has the highest rate of incidents, with 19.95 per billion ton-miles. This is followed by rail, with 2.08 per billion ton-miles. Natural-gas pipelines came next, with 0.89 per billion

ton-miles. Oil pipelines were the safest, with 0.58 incidents per billion ton-miles.

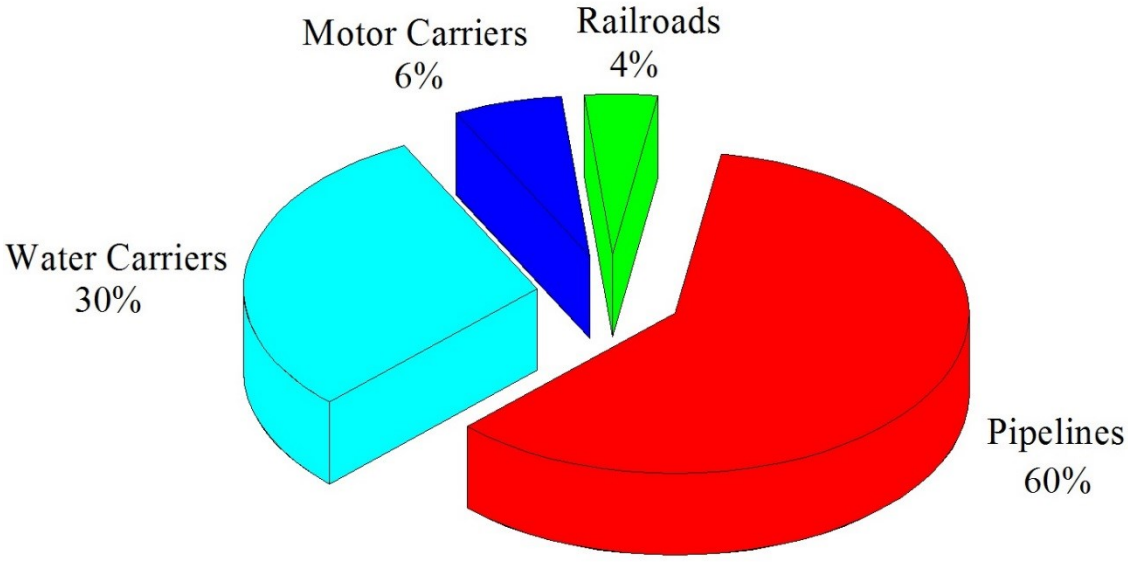

Figure 1-1 **Transportation of petroleum products by mode [1].**

Table 1-1 **Petroleum and natural-gas incident rates: pipelines vs road and railway (2005-2009) [2].**

Mode	Avg. billion ton-miles per year	Avg. incidents per year	Incidents per billion ton-miles
Road	34.8	695.2	19.95
Railway	23.9	49.6	2.08
Petroleum pipeline	584.1	339.6	0.58
Natural gas pipeline	338.5	299.2	0.89

High Strength Low Alloy (HSLA) steels, such as API X-series [3], are extensively utilized in oil and gas transportation pipelines. API steels have a low price-to-strength ratio with minimum yield strength of 480 MPa. In addition to material strength, API steels provide good weldability because of their low carbon contents.

The development of high strength API pipeline steels began in the seventies, when hot rolling and normalizing were replaced by thermo-mechanical rolling. The latter process enables materials up to API X70 (480 MPa) to be produced from steels that are micro-alloyed with niobium and vanadium and have reduced carbon content. An improved processing method, consisting of thermo-mechanical rolling plus subsequent accelerated cooling, emerged in the eighties. By this method, it has become possible to produce higher strength materials like API X80 (550 MPa), having a further reduced carbon content and thereby excellent field weldability. Additions of molybdenum, copper and nickel enable the strength level to be raised to that of grades API X100 (690 MPa) and API X120 (820 MPa) when the steel is processed by thermo-mechanical rolling plus modified accelerated cooling. The historical development of API X-series pipeline steels is illustrated in Figure 1-2.

Today, much of the existing global infrastructure uses pipe grades API X70 and API X80 steels [4]. However, the industry has recently witnessed an increased interest in the possibility of using higher strength pipeline steels such as API X100 [5]–[7]. More recently, for the first time, TransCanada installed and welded the highest grade pipeline steel available in the world today, *i.e.*, API X120, and steps are under way to address many of the characteristics of this steel [8]. The use of a high strength grade offers potential benefits with respect to using a higher operating pressure without increasing the pipe wall thickness. This in turn offers economic benefits arising from lower material, transportation and fabrication costs.

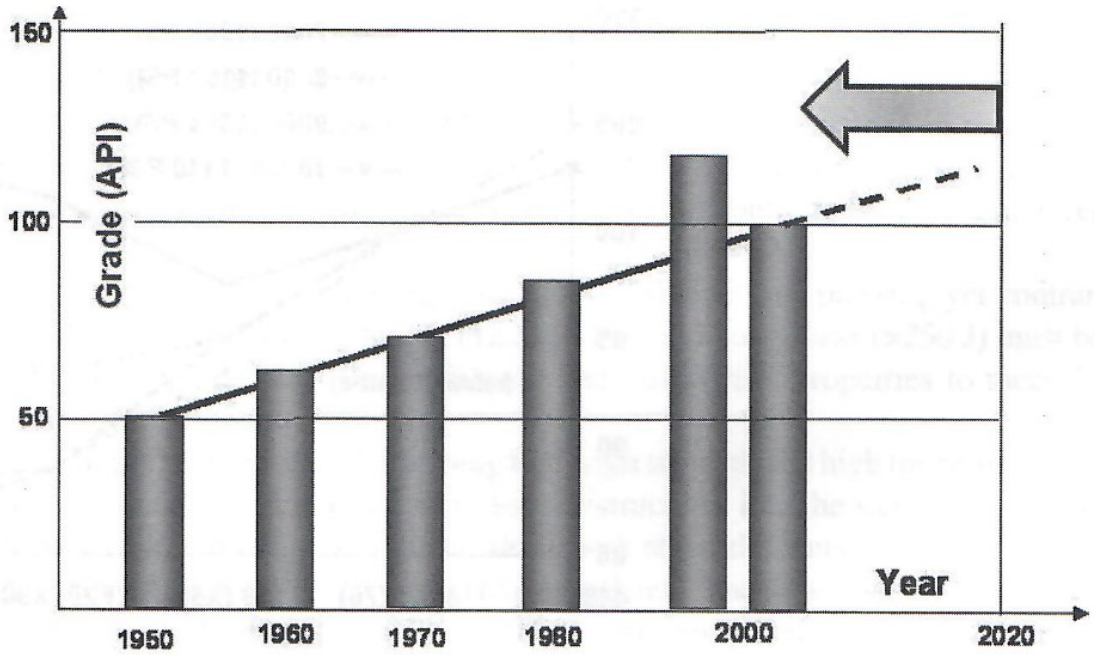

Figure 1-2 Historical development of API X-series pipeline steels [9].

However, one major drawback of API X-series pipeline steels is their susceptibility to erosion-corrosion attack. Oil and gas transmission pipelines are subjected to severe erosive and corrosive conditions during their operation. Despite pipelines good safety record, the erosion-corrosion damage-related cost to the global transmission pipeline industry is approximately $50 billion annually, in addition to the irreversible damage to life and the environment [10], [11]. The cost of erosion-corrosion attack to the global oil and gas industry has drawn significant attention among researchers in recent years.

Corrosion is a material degradation process, which occurs due to chemical or electrochemical action, while erosion is a mechanical wear process due to both fluid flow and particulate matter abrasion (such as sand particles and corrosion by-products). In enhanced oil recovery (EOR), CO_2 gas injection, is the most-commonly used approach as it reduces the oil viscosity and assists

in the recovery effort [5]–[8]. The presence of CO_2 gas in pipeline systems induces CO_2 corrosion, or 'sweet corrosion'. This type of attack is the most prevalent form of attack encountered in oil and gas pipelines. Corrosion of carbon steel in CO_2 containing environment is very complex and requires extensive attention. Various mechanisms have been proposed to explain the phenomenon. However, these mechanisms either apply to very specific conditions or have not received widespread recognition or acceptance. On the other hand, solid particle erosion of steel is a function of abrasive particle properties, target material, erodent velocity, abrasive feed rate and impact angle. From these conditions, the impact angle and particle velocity have been identified as two parameters that significantly influence erosion rate and surface degradation in tribo-systems. In addition, steel microstructure, which directly influences its hardness and ductility, plays an important role in determining erosion rate. The combined effect of erosion and corrosion, known as synergism effect, is significantly higher than the sum of the individual contributions acting separately. In oil and gas transportation pipelines erosion-corrosion synergism is a significant problem. Synergism is not well quantified due to the complexities of the phenomena and because of the lack of detailed knowledge of the separate kinetics of pure erosion and pure corrosion.

1.1 Objectives

The need to understand the occurrence of erosion-corrosion phenomenon is one prerequisite in preventing such failure by developing strategies for combating degradation and prolonging the life of the steel pipe. Unfortunately, the erosion-corrosion attack is not well understood and it's unclear how corrosion affects erosion and vice-versa. The present work, examines erosion-corrosion effects on API X42, API X70 and API X100 steels under different environmental conditions. The research provides a comprehensive and a systematic investigation on the individual contributions of corrosion and erosion acting separately and on their synergistic effect when the two processes act together. The main obstacle tackled in this study is separating the individual contributions of erosion and corrosion to the overall metal loss and evaluating the synergistic effects of one mechanism over the other. The study also correlates erosion response and corrosion layers formation to the steel microstructure. In addition, erosion mechanism maps are developed for the various API steels. These maps provide engineers and designers with the necessary data to make appropriate material selection decisions under different operating conditions.

Erosion-corrosion is one of the most important metal degradation mode that affects many industries including pipelines, pumps, turbines, offshore structures, etc. The present research generates new knowledge and establishes the fundamental principles governing materials behavior under erosion-corrosion conditions. The work is expected to create interest from oil and gas and steel manufacturing industries. The specific objectives of the research are summarized as follows:

1. Investigate the effect of impact angle and particle velocity on erosion of carbon and API steels and identify possible erosion mechanisms during the process.

2. Investigate the effect of microstructure on erosion behavior of carbon steel.

3. Develop erosion mechanism maps for carbon and API pipeline steels.

4. Study the formation of corrosion layer in sweet environment and identify its role in the degradation of oil and gas pipeline steel.

5. Investigate the effect of the steel microstructure on passive film formation and characteristics.

6. Quantify the synergistic effect and develop enhanced understanding of erosion-corrosion mechanisms.

1.2 Thesis Outline

The contents of this thesis are arranged in the following sequence:

A review of pertinent background information on classification of steel and the development of high-strength low alloy steel (HSLA) are provided in Chapter 2. This is followed by an up-to-date review of erosion behavior, corrosion mechanisms and erosion-corrosion of pipeline steels. Materials characterization (based on their physical and chemical properties) and experimental methods employed in erosion, corrosion, erosion-corrosion tests and their corresponding operating conditions are outlined in details in Chapter 3. Experimental results and relevant discussions are given in Chapter 4. Conclusions of this research, contributions and recommendations for future work are summarized in Chapter 5.

Chapter 2

Literature Review

Extensive literature review on high-strength low alloy steel, erosion, corrosion and erosion-corrosion of steel is included in this chapter.

2.1 Classification of Steel

Steel standards vary from country to country and can be classified based on manufacturing method (Bessemer steel, open-hearth steel, electric-furnace steel, crucible steel, etc.), according to their final use (machine steel, spring steel, boiler steel, structural steel or tool steel), mechanical properties and hardenability. However, a majority of standards are defined in terms of the chemical composition and indicate (by means of a numbering system) the approximate content of the important elements in the steel.

Based on their chemical composition and physical properties, steel grades have been developed by a number of standards organizations. The following is a list of different steel grades used around the world:

i. American Iron and Steel Institute (AISI) and Society of Automotive Engineers (SAE) steel grades
ii. International Organization for Standardization (ISO standard)
iii. Unified Numbering System (UNS)
    (a) ASTM International
    (b) Society of Automotive Engineers (SAE)

iv. British Standards (BS standard)
v. Japanese Steel Grades (JIS standard)
vi. German Steel Grades (DIN standard)
vii. Chinese Steel Grades (GB standard)

AISI and SAE steel grade specifications represent the results of the cooperative effort of the American Iron and Steel Institute (AISI) and Society of Automotive Engineers (SAE) in a simplification program aimed at greater efficiency in meeting the steel needs of American industry. The first digit of the four or five numerical designation indicates the type of steel. For example, 1 indicates carbon steel, 2 for nickel steel, 3 for nickel-chromium steel, etc. In the case of simple alloy steels, the second digit indicates the approximate percentage of the predominant alloying element. The last two or three digits usually indicate the mean carbon content divided by 100. Thus, the symbol 2520 indicates a nickel steel of approximately 5 percent nickel and 0.20 percent carbon. In addition to the numerals, AISI specifications may include a letter prefix to indicate the manufacturing process employed in producing the steel. The prefix 'C' denotes open-hearth furnace, or basic oxygen furnace, while 'E' denotes electric arc furnace steel. SAE specifications also employ the same four-digit numerical designations as the AISI specifications, with the elimination of all letter prefixes. An 'H' suffix can be added to any designation to denote hardenability. SAE and AISI specification for carbon, alloy and stainless steel are given in Table 2-1, Table 2-2 and Table 2-3.

International Organization for Standardization (ISO) is an international standard-setting body composed of representatives from various national standard organizations. ISO standards for steel are usually based on the final application. For example, ISO 65 is for carbon steel tubes suitable for screwing application and ISO 7-1, ISO 657 are used for hot-rolled steel sections [12]–[14]. ISO 898 is used for fasteners made from carbon and alloy steel, and ISO 2852 is for stainless steel clamp pipe couplings used in the

food-industry [15]–[17]. ISO 8501 is used for preparation of steel substrates before application of paints and related products, and ISO 3506 is used for corrosion-resistant stainless steel fasteners [18]–[20].

Table 2-1 SAE designation for carbon and alloy steel [21]–[23].

SAE Designation	Type
1xxx	Carbon steels
2xxx	Nickel steels
3xxx	Nickel-chromium steels
4xxx	Molybdenum steels
5xxx	Chromium steels
6xxx	Chromium-vanadium steels
7xxx	Tungsten steels
8xxx	Nickel-chromium-vanadium steels
9xxx	Silicon-manganese steels

Table 2-2 SAE designation for stainless steel [24]–[27].

SAE Designation	Type
100 Series	Austenitic chromium-nickel-manganese alloys
200 Series	Austenitic chromium-nickel-manganese alloys
300 Series	Austenitic chromium-nickel alloys
400 Series	Ferritic and martensitic chromium alloys
500 Series	Heat-resisting chromium alloys
600 Series	Martensitic precipitation hardening alloys

Table 2-3 AISI designation of steel [28].

AISI Designation	Type
10xx	Basic open-hearth and acid Bessemer carbon steel
11xx	Basic open-hearth and acid Bessemer carbon steel, high S, low P
12xx	Basic open-hearth carbon steels, high S, high P
13xx	Manganese (1.75%)
23xx	Nickel (3.50%)
31xx	Nickel (1.25%), Chromium (0.60%)
40xx	Molybdenum (0.20 or 0.25%)
41xx	Chromium 0.50, 0.80, Molybdenum (0.20 or 0.35%)
44xx	Molybdenum (0.53%)
48xx	Nickel (3.50%), Molybdenum (0.25%)
50xx	Chromium (0.40%)
61xx	Chromium (0.60%), Vanadium (0.13%)
86xx	Nickel (0.55%), Chromium (0.50%), Molybdenum (0.20%)
92xx	Silicon (2.00%)
93xx	Nickel (3.25%), Chromium (1.20%), Molybdenum (0.12%)
98xx	Nickel (1.00%), Chromium (0.80%), Molybdenum (0.25%)

Table 2-4 UNS designation for steel [29]–[33].

UNS Series	Type
D00001 to D99999	Specified mechanical property steels
G00001 to G99999	AISI and SAE carbon and alloy steels (except tool steels)
H00001 to H99999	AISI and SAE H-steels
J00001 to J99999	Cast steels (except tool steels)
K00001 to K99999	Miscellaneous steels and ferrous alloys
S00001 to S99999	Heat and corrosion resistant (stainless) steels
T00001 to T99999	Tool steels, wrought and cast

The Unified Numbering System (UNS) is an alloy designation system widely accepted in North America. It consists of a prefix letter and five digits designating the material composition. For example, a prefix of 'S' indicates stainless steel alloys, 'C' for copper, brass or bronze alloys, and 'T' for tool steels. The UNS is managed jointly by the ASTM International and SAE International. A UNS number alone does not constitute a full material specification because it establishes no requirements for material properties, heat treatment, form, or quality. UNS designation for steel is given in Table 2-4.

British Standards (BS) are the standards produced by BSI Group, which is incorporated under a Royal Charter (and which is formally designated as the National Standards Body (NSB) for the UK). The standards produced are titled British Standard XXXX[-P]:YYYY where XXXX is the number of the standard, P is the number of the part of the standard (where the standard is split into multiple parts), and YYYY is the year in which the standard came into effect. The standard simply provides a shorthand way of claiming that certain specifications are met, while encouraging manufacturers to adhere to a common method for such a specification. As for example, BS 5400-5:2005 steel is the code of practice for design of composite bridges [28]. On the other hand, JIS standards are developed by the Japanese Industrial Standards Committee (JISC) in Tokyo. The specifications begin with the prefix JIS, followed by a letter 'G' for carbon and low-alloy steels. Examples: JIS G3445 STKM11A is a low-carbon tube steel containing 0.12% C, 0.35% Si, 0.60% Mn, 0.04% P, 0.04% S; JIS G4403 SKH2 (AISI T1Grade) is a tungsten high speed tool steel containing 0.73-0.83% C, 3.8-4.5% Cr, 0.4% Mn, 0.4% Si, 0.8-1.2% V and 17-19% W [28]. German steel specifications often start with the letters DIN and followed by an alphanumeric or a numeric code. For examples, DIN 40NiCrMo66 is a Ni-Cr-Mo steel that contains 0.35-0.45% C, 0.9-1.4% Cr, 0.5-0.7% Mn, 0.2-0.3% Mo, 1.4-1.7% Ni, 0.035% S; DIN 17200 is

a non-resulfurized carbon steel containing 0.17-0.245% C, 0.3-0.6% Mn, 0.02-0.035% S and 0.4% max Si [28].

Steels are sometimes classified by the broad range of carbon content, such as, low, medium, high and ultrahigh carbon steel. Low-carbon steels contain up to 0.30 wt% C. The largest category of this class of steel is flat-rolled products (sheet or strip, usually in the cold-rolled and annealed condition). The carbon content for these high formability steels is very low (less than 0.10 wt% C), with up to 0.4 wt% Mn. Automobile body panels, thin plate and wire products are usually made of these steels. For structural plates and sections, the carbon content may be increased to approximately 0.30 wt%, with higher manganese content (up to 1.5 wt%). Medium carbon steels are similar to low carbon steels except that the carbon ranges from 0.30 to 0.60 wt% and the manganese from 0.60 to 1.65 wt%. Increasing the carbon content to approximately 0.5 wt% with an accompanying increase in manganese allows medium carbon steels to be used in the quenched and tempered condition. The uses of medium carbon-manganese steels include shafts, axles, gears, crankshafts, couplings and forgings. Steels in the 0.40 to 0.60 wt% C range are also used for rails, railway wheels and rail axles. High carbon steels contain from 0.60 to 1.00 wt% C with manganese contents ranging from 0.30 to 0.90 wt%. High carbon steels are used for spring materials and high-strength wires. Ultrahigh carbon steels are experimental alloys containing 1.25 to 2.0 wt% C. These steels are thermo-mechanically processed to produce microstructures that consist of ultra-fine, equiaxed grains of spherical, discontinuous pro-eutectoid carbide particles.

2.1.1 High-Strength Low Alloy Steel (HSLA)

In order to allow exploitation in aggressive environments, the steel pipe industry has conducted extensive efforts to develop line pipe steel grades with superior mechanical (ductility, strength and toughness) and metallurgical properties to improve both performance and transportation efficiency. The need to achieve higher strength accompanied with sufficient toughness and ductility pushed the development of HSLA aiming at performance and durability to operate in harsh environments. Unlike other steels, HSLA steels are not made to meet a specific chemical composition but rather specific mechanical properties. HSLA steels typically contain very low carbon content (between 0.05–0.25 wt%) to retain formability and weldability and small amounts of alloying elements (micro alloyed), such as Nb, V, Ti and Mo [34]–[39]. High-strength steels possess highly refined grain and high cleanliness. They are characterized by low sulphur content and reduced amount of detrimental second phases such as oxides, inclusions and pearlite [40]–[42].

The American Petroleum Institute (API) is a leader in the development of petroleum and petrochemical equipment and operating standards. Many of these standards are adopted by ISO for worldwide acceptance. API 5L series are used for the specification of pipeline steel. The purpose of this specification is to provide standards for pipe suitable for conveying gas, water and oil. This specification covers seamless and welded steel line pipe. For example, API 5L X70 refers to pipeline steel having a yield strength of 70 ksi produced from steels that are micro-alloyed with niobium and vanadium and have reduced carbon content. An improved processing method, consisting of thermo-mechanical rolling plus subsequent accelerated cooling produces higher strength materials like API 5L X80 (80 ksi), having a further reduced carbon content and thereby excellent field weldability. Additions of molybdenum, copper and nickel enable the strength level to be raised to that

of grade API 5L X100 (100 ksi), when the steel is processed by thermo-mechanical rolling plus modified accelerated cooling. Steel microstructure, alloying element and thermo-mechanical treatment are the three important factors that govern the property of HSLA steel [43].

2.1.1.1 Effect of Microstructure

The final steel microstructure is a key variable in determining material properties and ensuring safe and optimal performance; it has to be specifically designed for specific conditions [44]–[46]. The most modern line pipe steels have different and complex microstructural arrangements depending on their chemical compositions and processing routes. Microstructural features such as dislocations, grain boundaries and precipitates, govern the mechanical properties of steels and in HSLA; they develop in the course of transformation from austenite during cooling. Grain refinement is the only method by which both strength and toughness can simultaneously be improved. Figure 2-1 shows the combination of various types of microstructures and their contributions to mechanical strength and toughness of steels [47]. The loss of strength resulting from reduced pearlite contents can be offset by precipitation and dislocation hardening. Reduction of pearlite content, grain refining, dislocation hardening and precipitation hardening contribute individually and in combination to the development of X70 steel from X60, with improved weldability and favorable ductile-brittle transition temperature. Further increase in strength and toughness, which led to the development of X80 steel, can only be attained by changing the microstructure of the steel matrix from ferrite/pearlite to ferrite/ bainite.

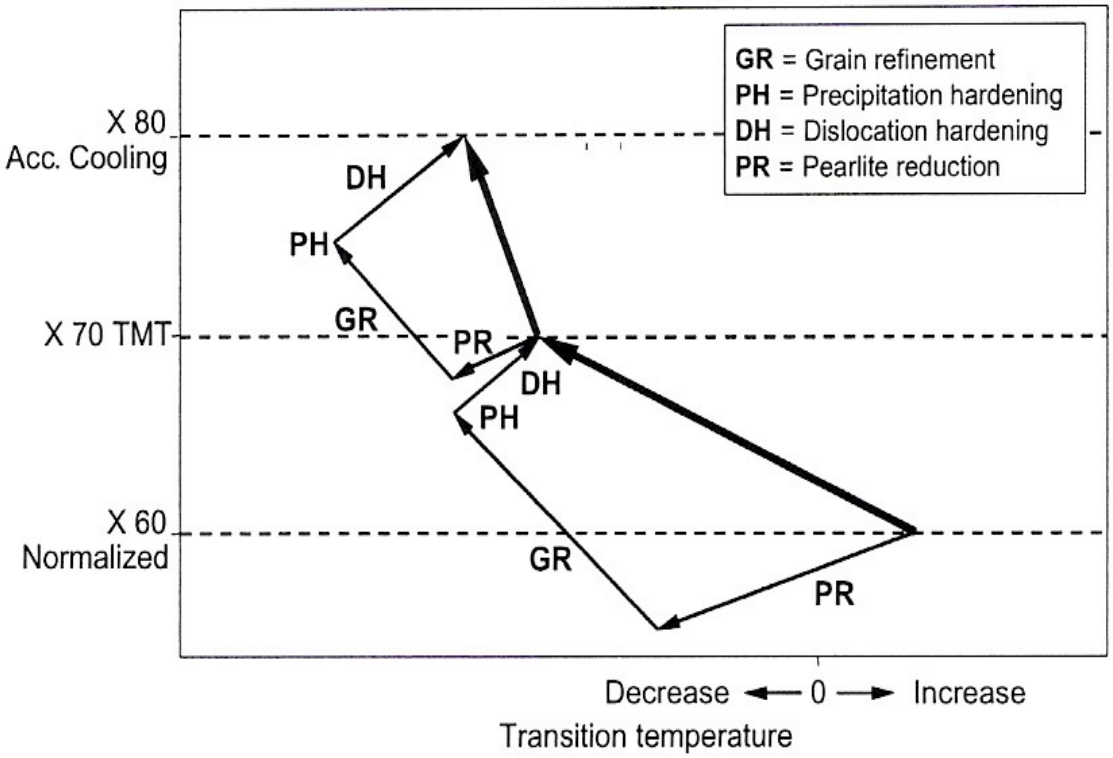

Figure 2-1 **Effect of microstructure on strength and toughness of HSLA steel [47].**

2.1.1.2 Effect of Alloying Element

Micro-alloying of steels with small amounts of strong carbo-nitride forming elements have achieved a great improvement in their mechanical properties. The alloying elements improve the mechanical properties through the refinement of the ferrite grain size by the formation of a fine sub-grain structure; strain induced precipitation of the carbides and nitrides and precipitation strengthening of ferrite [48], [49]. Table 2-5 presents an overview of the relevant alloying elements for HSLA line pipe steels and their respective effect and reason of adding [50]–[52].

Table 2-5 **Major effects of alloying elements in high-strength low alloy steel [50]–[52].**

Element (wt%)	Effect and reason of adding
C (0.03-0.10)	Matrix strengthening (by precipitation)
Mn (1.6-2.0)	Delays austenite decomposition during Accelerated cooling (AcC) Substitutional strengthening effect Decreases ductile to brittle transition temperature Indispensable to obtain a fine-grained lower bainite microstructure
Si (up to 0.6)	Improvement in strength (solid solution)
Nb (0.03-0.06)	Reduces temperature range in which recrystallization is possible between rolling passes Retards recrystallization and inhibit austenite grain growth (improves strength and toughness by grain refinement)
Ti (0.005-0.03)	Grain refinement by suppressing the coarsening of austenite grains (TiN formation) Strong ferrite strengthener Fixes the free Ni (prevent detrimental effect of Ni on hardenability)
Ni (0.2-1.0)	Improves the properties of low carbon steels without impairing field weldability and low temperature toughness In contrast to Mg and Mo, Ni tends to form less hardened microstructural constituents detrimental to low temperature toughness in the plate (increases fracture toughness)
V (0.03-0.08)	Leads to precipitation strengthening during the tempering treatment Strong ferrite strengthener
Mo (0.2-0.6)	Improves hardenability and thereby promotes the formation of the desired lower bainite microstructure

2.1.1.3 Thermo-Mechanical Rolling and Accelerated Cooling

Thermo-mechanical rolling results in a significant reduction to the ferrite grain size. During the production of HSLA steel, accelerated cooling process is adopted in order to achieve a homogeneous fine grained microstructure and hence improved strength, toughness and cracking resistance, compared to steels produced by conventional thermo-mechanical rolling. Figure 2-2 shows the metallurgical processes occurring during thermo-mechanical rolling in conjunction with accelerated cooling [53].

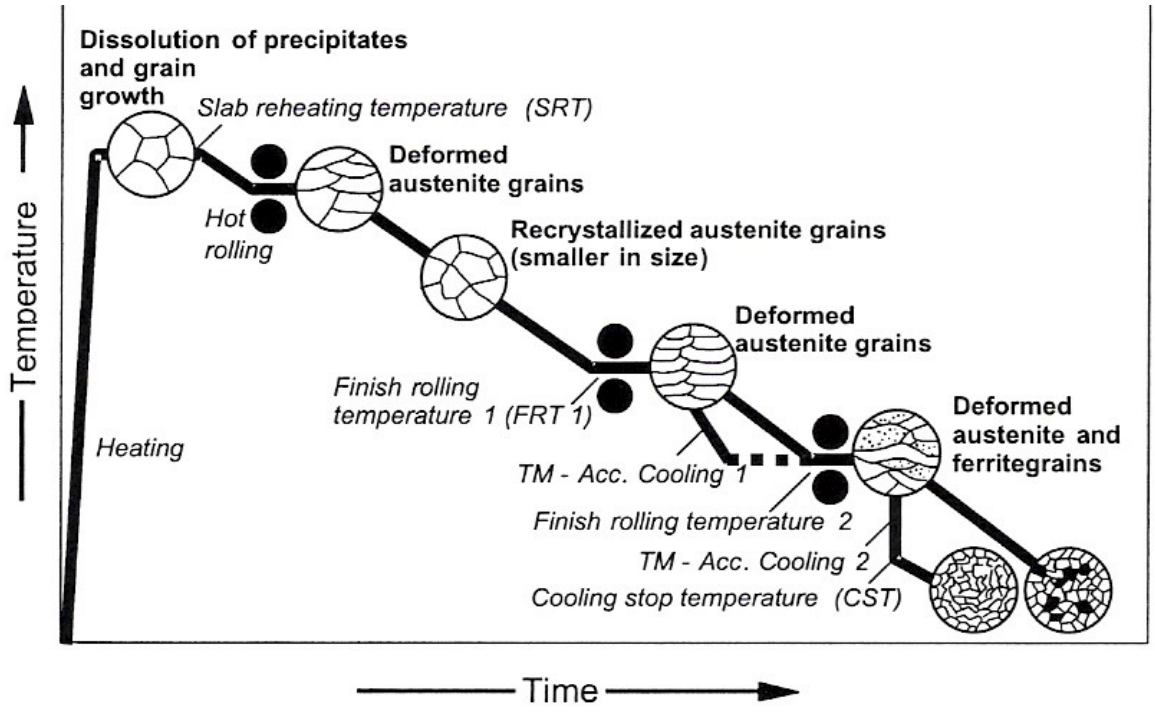

Figure 2-2 Schematic illustration of thermo-mechanical rolling with and without accelerated cooling during the 2nd and 3rd rolling stage [53].

2.2 Erosion of Steel

Erosion is a mechanical wear process that gradually removes material by repeated deformation and cutting actions caused by solid particle impingement [54]–[56]. It is a material loss process that results from repeated impact of small, solid particles. In some cases solid particle erosion (SPE) is a useful phenomenon, as in sandblasting and high-speed abrasive water jet cutting. However, in many engineering systems, including steam and jet turbines, pipelines and valves carrying particulate matter and fluidized bed combustion (FBC) systems, erosion causes significant damage to the equipment in service [26], [57]–[62]. Solid particle erosion is to be expected whenever hard particles are entrained in a gas or liquid medium impinging on a solid surface at any significant velocity (greater than 1 m s^{-1}) [63]. Erosion has received significant attention among researchers in recent years [64]–[73]. Much work has been directed towards providing a fundamental understanding of this complex mode of failure and proposing models and mechanisms that would account for the observed erosion rates [74]–[77].

Carbon steels are common in the construction of oil and gas pipelines. Despite their excellent mechanical, metallurgical and structural properties, limited erosion resistance depresses their performance under field operating conditions [78]–[84]. During transportation, oil and gas are accompanied by sand particles, which erode the steel pipe. Several investigations have been reported explaining this complex failure mode under specific experimental conditions [65], [74]–[76]. A comprehensive view of erosion modes and mechanisms under a wide range of operating conditions is lacking.

Erosion is a complex time dependent phenomenon. Several factors have been identified by researchers that influence erosion rate, such as, impacting particle properties (density, hardness, size and shape), target material

properties (hardness, ductility and microstructure) and particle flux [85]–[91]. Impact angle and erodent velocity have been highlighted by many researchers as key parameters affecting erosion rate [85]–[98]. Although the hardness of steels can be dramatically increased by heat treatment, there is no evidence that this improves erosion resistance. Contrary to Finnie's theory [99]–[101], several authors have demonstrated that the erosion rate at a fixed impact angle (α) is nearly independent of hardness for individual steels [70]. Salik and Buckley [102] found almost no effect of hardness on erosion for 1045 steel eroded by fine (~100 μm) crushed glass at 90° incidence. Other authors have also demonstrated that hardness has little effect on erosion resistance and, for a given steel, erosion resistance sometimes increases slightly with increasing hardness [103]. For example, Levy and Jahanmir [104] found a small increase in erosion resistance for heat treated 1075 steel with increasing material hardness. Extensive research work has been carried out to determine the effect of these factors on erosion mechanisms [70], [99], [101], [105]–[114].

2.2.1 Effect of Impact Angle on Erosion

The effect of impact angle on erosion has been investigated extensively in the open literature [115]–[117]. Materials can be broadly classified as ductile or brittle depending upon their erosion rate on the impact angle (α). Ductile materials, such as pure metals, have a maximum erosion rate at low angles of incidence (typically 15° to 30°), while for brittle materials, such as ceramics, the maximum erosion is at or near 90°. Typical dependence of erosion on the impact angle is shown in Figure 2-3. According to the literature, brittle materials fracture at high-impact angles whereas ductile materials experience heavy plastic deformation. Oka [92] found that erosion rate depends strongly on impact angle and suggested that, at low angle, cutting mechanism dominates, which takes place as a result of abrasive

particles sliding on the surface. Finnie [99] and Bitter [118], [119] also reported that, at low impact angle, erosion occurs from the cutting action of erosive particles irrespective of their shape and size. Others found that erosion by oblique impact of spherical particles proceeds by ploughing action [120], [121]. Hutchings [110] proposed that erosion of ductile metals at normal incidence usually occurs by delamination. Extending Hutchings's theory further, Levy [122] reported that delamination mechanism of ductile metals prevails not only at normal impact erosion but at oblique impact as well.

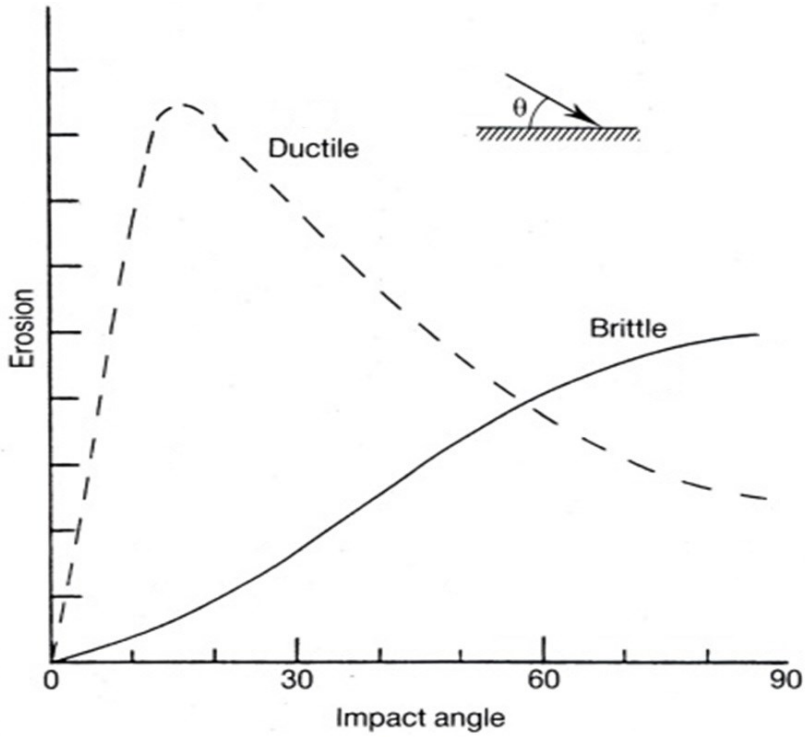

Figure 2-3 Typical dependence of erosion on impact angle [120].

2.2.2 Effect of Particle Velocity on Erosion

Abrasive particle velocity exhibits a complex relationship with erosion rate. Lopez [123] studied the effect of velocity and concluded that surface damage increases with increasing impact velocity of the abrasive particles. In early

1960, Finnie demonstrated that a strong correlation exists between the volume of material removal by erosion and the square of the velocity of abrasive particles [100]. More recently, it has been shown that erosion rate follows an empirical power law relationship with velocity [117], [124]–[129],

$$E_1 = kV_1^n \qquad \text{Equation 2-1}$$

where, E_1 is the erosion rate, V_1 is velocity, k is a constant and n is the velocity exponent. The velocity exponent has values between 2 to 3.5 for metallic materials [130]. The increase in erosion rate with velocity is associated with the increase in kinetic energy of the erodent causing more effective damage on the metal surface. Furthermore, the friction force acting on the surface during impact and its effective path of action plays a significant role during erosion. The normal component of impact velocity (indenting component) is mostly responsible for the depth, while the horizontal component of impact velocity is responsible for the shape of the erosion scar [119].

2.2.3 Effect of Particle Distribution on Erosion

In this section, the effect of particle distribution is discussed based on particle size, shape, hardness and flux.

2.2.3.1 Particle Size

The size of erodent particles has little or no effect on the erosion rate for ductile materials as long as the particle size is above 100 μm [88]. However, erosion rate decreases rapidly with decreasing particle size below 100 μm. This is known as the size effect and is also common in abrasive wear. Misra and Finnie [88] discussed many theories that have explained this effect and

concluded that it is probably due to an increase in the flow stress with decreasing indentation size (particle size).

2.2.3.2 Particle Shape

It is well established that sharp abrasive particles cause more material removal than spherical particles [99], [109], [110], [131]–[136]. In ductile materials, round particles deform the surface by ploughing and displacing material to the sides and front. For angular shaped particles, cutting action is observed to occur by different processes depending on the orientation of the erodent particle as it strikes the target surface, as well as, whether the particle rolls forwards or backwards during contact [120]. For round shaped abrasive particles, erosion resistance increases with increasing hardness of the steel. However, for sharp abrasive particles, erosion resistance is independent of the hardness and depends on the microstructure and the operating erosion mechanisms during the process [90], [102], [137], [138].

2.2.3.3 Particle Hardness

The hardness of the erodent particles relative to the material being eroded is an important factor in erosion. In order for erosion to occur, abrasive particles must be harder than the target material [108]. Wellinger and Uetz [139] found that erosion rate drops dramatically when the abrasive particle hardness is lower than the material being eroded. On the other hand, when the abrasive particle hardness is at least an order of magnitude higher than the base material, erosion rate becomes significant [88]. This also explains why the heat treatment of steels appears to have almost no effect on their erosion resistance [140]. This is because if the abrasive particle hardness is considerably higher than the base material, a relatively small increase in material hardness, due to heat treatment, would have insignificant effect on erosion.

2.2.3.4 Particle Flux

Particle feed rate plays an important role during erosion and has been investigated in the open literature [115], [141]–[146]. Levy and co-workers [95] have conducted a comprehensive study on the sensitivity of erosion rate to variations in abrasive particle feed rate. They found that, for spherical particles, an order of a magnitude increase in abrasive feed rate decreased metal loss by 50%. They related this to particle interference at the higher feed rate that reduced the effectiveness of the particles to erode the surface. They suggested that the primary mode of this interference was particles rebounding up from the surface deflecting incoming particles in the downward-moving stream. However, for sharp abrasive particles, they reported only 14% decrease in material loss for a similar increase in abrasive feed rate. They speculated that sharp particles are more effective in material removal as compared to spherical particles and tend to reduce the particle interference effect. They also found that as the abrasive particle size increases, the sensitivity of erosion rate to particle feed rate significantly drops.

2.2.4 Erosion Mechanisms

Different erosion mechanisms often coexist, interact and compete. When examining erosion scars it is typical to find evidence of different mechanisms. There could be different erosion mechanisms acting independently or there could be features indicating different stages of a complex erosion process. Erosion mechanisms can be broadly divided into two main categories: ductile and brittle. The major difference between the two main erosion categories becomes clear when comparing the erosion rate at different angles of impact [93], [147], [148]. In the case of ductile materials, such as steel, the maximum

erosion rate is usually found to occur at an impact angle between 15° and 30°, while in brittle materials this occurs at approximately 90° [80].

During erosion, single impacts of abrasive particles can't remove material except above a specific critical velocity [131] and for specific particle orientations [149], [150]. In the majority of cases, direct material removal does not occur, but a crater forms as a result of particle impact and the displaced material forms a lip at the edges of the crater. As noted by Hutchings [151] and many other authors, including Finnie et al., [152], such lip becomes vulnerable to direct removal upon subsequent particle impact. Abrasive particles impact may also create extruded platelets that are eventually removed by fracture [152], [153]. Finnie [99], [100] proposed that in order to account for the fact that the actual erosion rate is much lower than the predicted one, it is necessary to assume that only a small fraction of the particles remove material in an idealized manner. Additional impacts are often required to remove the displaced material from the edge of a crater [152].

Bellman and Levy [78], extensively studied erosion at oblique angles of incidence. They provided convincing experimental evidence that one mechanism of material removal during erosion involves the deformation of surface material into thin platelets through repeated impacts. These platelets eventually become detached and form thin plate-like debris. Bellman and Levy believed that platelet formation is the primary, and probably the only, mechanism of material removal. However, erosion debris particle studies indicate that micro-cutting mechanism is also operative during erosion at low impact angles [154], [155]. Others [154]–[160] have shown that ploughing and different cutting modes dominate erosion mechanisms at a given impact angle and particle velocity.

For the erosion of ductile metals, Finnie [99] and Bitter [119] reported that, at low impact angle, erosion occurs from the cutting action of the erosive particle irrespective of its shape and size. Others [120] have reported that there are three different types of cutting depending on the shape and orientation of the erodent particles. For erosion by oblique impact of spherical particles, the material is removed by ploughing action (Figure 2-4). For angular shaped particles, cutting action is identified to be the dominant process by which erosion takes place. Cutting may occur by different modes depending on the orientation of the erodent particle as it strikes the target surface, as well as whether the particle rolls forward or backward during contact. Figure 2-4 shows cutting type I and type II as proposed by Hutchings [120] for particles rolling forward and backward, respectively. Cutting type II is reported to occur over only a narrow range of particle geometries and impact conditions [120]. In normal impact erosion of ductile materials, plastic deformation and fracture is observed to be the mechanism of material removal. Hutchings [110] proposed that erosion of ductile metals at normal incidence occurs by delamination and suggested that a critical plastic strain is required for an extruded lip to become detached from the target surface. Table 2-6 summarizes different types of erosion mechanisms reported in the literature [99], [119], [120].

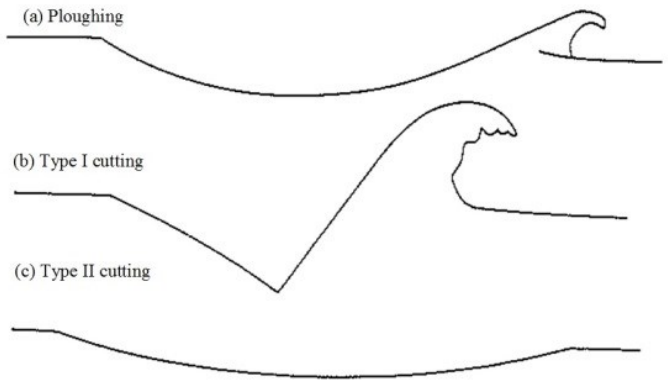

Figure 2-4 Cutting mechanisms during oblique impact erosion [120].

Table 2-6 Common types of erosion mechanisms [99], [119], [120].

Types of erosion		
Ploughing	Impingement angle < 90°	Displacing materials to the front and sides of the particle. Repeated impacts on the neighboring site cause removal of highly strained materials from the terminal lip of the crater.
Cutting	Type I, impingement angle < 90°	Material is removed by repeated impacts on a prominent lip formed by the indenting angular particle.
	Type II, impingement angle < 90°	A true cutting action where material is removed as a chip from the target surface by the impact of a sharp tip of the erodent particle.
Plastic deformation and fracture	Impingement angle = 90°	Repeated impacts of erodent particles at normal incidence cause fracture of a material from the impact site.
Delamination	Impingement angle = 90°	Formation of sub-surface cracks parallel to the eroded surface, extension of these cracks to the surface and formation of plate-like debris.

2.2.5 Mathematical Erosion Models

Erosion resistance is not an intrinsic material property. It depends on the operating parameters and conditions. Finnie [99] derived a mathematical correlation between erosion rate, and particle velocity, impact angle, density and hardness of the target material. He suggested that the mechanisms involved in oblique and normal impact of erodent particles are entirely different and must be modeled separately. Mathematical erosion models developed by various researchers [110], [161]–[163] for oblique and normal impact of erodent particles are discussed next.

2.2.5.1 Oblique Impact Erosion Model by Finnie

At oblique impact angles, Finnie [99], [140] defines the volume of material removed (V_m) as the volume swept out by the tip of the particle, purely as a result of plastic deformation. The cutting action of the particle stops when either the horizontal motion of the particle ceases or when the particle tip leaves the surface. Finnie proposed the following relationships for erosion at oblique impact [99], [140],

$$V_m = \left(\frac{f_c}{2k_4}\right)\frac{D_t V_1^2}{0.9272 H_s}\left(sin2\alpha - \frac{8}{k_4}sin^2\alpha\right); \qquad tan\alpha \leq \frac{k_4}{8}$$

Equation 2-2

$$V_m = \left(\frac{f_c}{16}\right)\frac{D_t V_1^2}{0.9272 H_s}(cos^2\alpha); \qquad tan\alpha \geq \frac{k_4}{8}$$

where, f_c is the proportion of particles impacting the surface and cutting in an idealized manner. V_1 is the erodent particle impact velocity, D_t and H_s are the density and static hardness of target material, respectively, and α is the particle impact angle. In Equation 2-2, k_4 is the ratio of vertical to horizontal force components on the particle and is assumed to be constant.

2.2.5.2 Normal Impact Erosion Model by Hutchings

The erosion for ductile materials at normal impact by spherical particles occurs by the formation and subsequent detachment of platelets of metal lying parallel to the eroded surface [120]. The model developed by Hutchings [110] assumes that detachment of platelets is only possible when the accumulated plastic strain within the fragments, after many cycles of plastic deformation, reaches a critical value. The final expression for dimensionless erosion rate (E) was expressed as,

$$E = 0.033 \frac{\alpha_r D_t D_p^{\frac{1}{2}} V_1^3}{\varepsilon_c^2 H_d^{\frac{3}{2}}}$$ Equation 2-3

where, H_d and D_t are the dynamic hardness and density of the target material respectively, D_p is the density of erodent particles, and V_1 is the erodent particle velocity. The term α_r/ε_c^2 cannot be measured independently. Hutchings assumed the value of α_r/ε_c^2 to be equal to 0.7.

2.2.5.3 Normal Impact Erosion Model by Sundararajan and Shewmon

For normal impact, Sundararajan and Shewmon [162] derived an equation for erosion on the basis of the critical stain criteria. They assumed that at normal impact, erosion occurs mainly through the removal of localized extruded lips along the rim of the crater after a certain number of particle impacts on the material surface. The criteria for the removal of such lips are assumed to be based on a critical strain which the lips attain after a number of particle impacts. This model takes into account the thermo-physical properties of the material undergoing erosion. The final expression for the dimensionless erosion (E) was given as,

$$E \approx \frac{6.5 \times 10^{-3} V_1^{2.5} D_p^{0.25}}{C_p T_m^{0.75} H_s^{0.25}}$$ Equation 2-4

where, V_1 is the velocity of impacting particles and D_p, C_p, T_m, H_s are the density, specific heat, melting temperature, and static hardness of the target material, respectively.

2.3 Corrosion of Steel

Corrosion is the result of a chemical reaction between a metal and its surroundings during which the metal is oxidized. By definition, corrosion is "*an irreversible interfacial reaction of a material (metal, ceramic, and polymer) with its environment, which results in consumption of the material or in dissolution into the material of a component of the environment.*" [28]. In general, corrosion can be defined as the destruction of a material by chemical, electrochemical or metallurgical interaction between the environment and the material. Substantial advances in the field of corrosion science have resulted in defining many forms of corrosion. However, the most familiar and often used categorization of corrosion is the eight forms presented by Fontana. These are uniform attack, galvanic or two-metal corrosion, crevice corrosion, pitting, intergranular corrosion, selective leaching, stress corrosion and erosion-corrosion [164], [165].

2.3.1 Classification of Corrosion

The classification of corrosion is based on visual characteristics of the morphology of attack. Fontana and Greene's introductory remarks in their chapter on forms of corrosion indicate that this classification is arbitrary and many of the forms are interrelated, making exact distinction impossible [166]. Other prominent corrosion authors such as Uhlig [167] and Evans [168] have avoided a classification format and have simply discussed the classical types of corrosion (for example, pitting and crevice corrosion) as they relate to specific metals and alloys. A brief description of the eight forms of corrosion are given below [164], [165]:

(a) Uniform Attack

Uniform attack is the most common form of corrosion. It is normally characterized by a chemical or electrochemical reaction which proceeds uniformly over the entire exposed surface or over a large area. The metal becomes thinner and eventually fails. For example, a piece of steel or zinc immersed in diluted sulfuric acid will normally dissolve at a uniform rate over its entire surface [169]. An iron roof will show essentially the same degree of rusting over its entire outside surface. Uniform attack, or general overall corrosion, represents the greatest destruction of metal on a tonnage basis. This form of corrosion, however, is not of too great concern from a technical standpoint, because the life of equipment can be accurately estimated on the basis of comparatively simple tests. Uniform attack can be prevented or reduced by proper materials, including coatings, inhibitors or cathodic protection [170]–[172].

(b) Galvanic Corrosion

A potential difference usually exists between two dissimilar metals when they are immersed in a corrosive or conductive solution. If these metals are placed in contact (or otherwise electrically connected), this potential difference produces electron flow between the metals [173]–[175]. Corrosion of the less corrosion-resistant metal is usually increased and attack of the more resistant material is decreased, as compared to the behavior of these metals when they are not in contact [176]. The less resistant metal becomes anodic, and the more resistant metal becomes cathodic. Usually, the cathode or cathodic metal corrodes very little or not at all in this type of couple. Due to the electric currents and dissimilar metals involved, this form of corrosion is called galvanic, or two-metal corrosion [177].

(c) Crevice Corrosion

Intense localized corrosion frequently occurs within crevices and other shielded areas on metal surfaces exposed to corrosive solution. This type of attack is usually associated with small volumes of stagnant solution caused by holes, gasket surfaces, lap joints, surface deposits and crevices under bolt and rivet heads [178]–[180]. As a result, this form of corrosion is called crevice corrosion or sometimes, deposit or gasket corrosion.

(d) Pitting

Pitting is a form of extremely localized attack that results in holes through the metal. Pits are sometimes isolated or so close together that they look like a rough surface. Generally, a pit may be described as a cavity or hole with the surface diameter about the same as or less than the depth. Pitting is one of the most destructive and insidious forms of corrosion causing equipment to fail because of perforation with only a small percent weight loss of the entire structure. Pits are often difficult to detect because of their small size and they are usually covered with corrosion products [181]. In addition, pitting is difficult to measure quantitatively because of the varying depths and numbers of pits that may occur under identical conditions [182]–[184]. Pitting is also difficult to predict using laboratory tests. Pitting is particularly vicious because it is localized and failure due to pitting often occur with extreme suddenness.

(e) Intergranular Corrosion

In most applications, grain boundaries have little effect. However, under certain conditions, grain interfaces become reactive and intergranular corrosion results. Localized attack at and adjacent to grain boundaries, with relatively little corrosion of the grains, is known as intergranular corrosion

[185]. The alloy disintegrates (grains fall out) and/or loses its strength [186]–[188]. Intergranular corrosion may be caused by impurities at the grain boundaries, enrichment of one of the alloying elements, or depletion of one of these elements adjacent to grain-boundaries [189]. For example, small amounts of iron in aluminum, wherein the solubility of iron is low, have been shown to segregate in the grain boundaries and cause intergranular corrosion. Also, depletion of chromium in the grain-boundary regions results in intergranular corrosion of stainless steels [190]–[192].

(f) Selective Leaching

Selective leaching is the removal of one element from a solid alloy by corrosion processes. The most common example is the selective removal of zinc in brass alloys (dezincification). Similar processes occur in other alloy systems in which aluminum, iron, cobalt, chromium and other elements are removed [193]. Selective leaching is the general term that describes these processes, and its use precludes the creation of terms such as de-aluminumification, and de-cobaltification [194]–[196].

(g) Erosion-Corrosion

Erosion-corrosion is the acceleration or increase in the rate of deterioration or attack on a metal because of relative movement between a corrosive fluid and the metal surface [197]–[199]. Metal is removed from the surface as dissolved ions, or it forms solid corrosion products, which are mechanically swept from the metal surface [200]. Erosion-corrosion is characterized in appearance by grooves, gullies, waves, rounded holes and valleys, and usually exhibits a directional pattern [201]–[204]. Metal loss due to erosion-corrosion is underestimated when corrosion tests are run under static conditions.

(h) Stress-Corrosion Cracking

Stress-corrosion cracking refers to cracks caused by the simultaneous presence of tensile stress and a specific corrosive medium. During stress-corrosion cracking, the metal or alloy is virtually unattacked over most of its surface, while fine cracks progress through it. This cracking phenomenon has serious consequences since it can occur at stresses within the range of typical design stress [205]–[207]. Many investigators have classified all cracking failures occurring in corrosive mediums as stress corrosion cracking, including failures due to hydrogen embrittlement [208]. However, these two types of cracking failures respond differently to environmental variables. For example, cathodic protection is an effective method for preventing stress corrosion cracking whereas it rapidly accelerates hydrogen-embrittlement [209]–[212]. Hence, the importance of considering stress-corrosion cracking and hydrogen embrittlement as separate phenomena is obvious.

2.3.2 Corrosion Mechanisms of Pipeline Steel

Sweet corrosion (CO_2 corrosion) of carbon steel is one of the most common problems in oil and gas industry. As the oil and gas emerge from geological formations, they are often accompanied by water and varying amount of 'acid gases', carbon dioxide (CO_2). In addition, CO_2 is sometimes dissolved deliberately in water and pumped into wells to reduce the viscosity of oil to enhance recovery [10], [11], [213]. Many researchers [214]–[224] have studied this type of corrosion behavior.

During corrosion, the presence of CO_2 in solution leads to the formation of a weak carbonic acid (H_2CO_3). The presence of carbonic acid drives the carbonate and bicarbonate (CO_3^{2-} and HCO_3^-) reduction reactions. This initiating step is represented by the reaction,

$$CO_2 + H_2O \leftrightarrow H_2CO_3$$ Equation 2-5 (a)

The subsequent corrosion process is controlled by three cathodic reactions and one anodic reaction [225], [226]. Cathodic reactions include the reduction of carbonic acid into bicarbonate ions, reduction of bicarbonate ions into carbonate ions and the reduction of hydrogen ions to hydrogen gas. However, the reduction of hydrogen ions to hydrogen gas is less likely to occur at high pH (in weak acids environment (*i.e.* carbonic acid)).

$$2H_2CO_3 + 2e^- \rightarrow 2H^+ + 2HCO_3^-$$ Equation 2-5 (b)

$$2HCO_3^- + 2e^- \rightarrow 2H^+ + 2CO_3^{2-}$$ Equation 2-5 (c)

$$2H^+ + 2e^- \rightarrow H_2$$ Equation 2-5 (d)

In carbonate/bicarbonate media, the anodic reaction involves the oxidation of iron to ferrous (Fe^{2+}) ion,

$$Fe \rightarrow Fe^{2+} + 2e^-$$ Equation 2-5 (e)

These corrosion reactions provide a chemical environment which promotes the formation of iron carbonate ($FeCO_3$), where ferrous ions react directly with carbonate ions. It can also be formed by a two-step process when ferrous ions react with bicarbonate ions, iron bicarbonate forms, which subsequently dissociates into iron carbonate along with carbon dioxide and water [227].

$$Fe^{2+} + CO_3^{2-} \rightarrow FeCO_3$$ Equation 2-5 (f)

$$Fe^{2+} + 2HCO_3^- \rightarrow Fe(HCO_3)_2$$ Equation 2-5 (g)

$$Fe(HCO_3)_2 \rightarrow FeCO_3 + CO_2 + H_2O$$ Equation 2-5 (h)

CO_2 corrosion is influenced by several factors, such as pH, CO_2 partial pressure, dissolved oxygen in the solution, temperature, solution composition, flow and iron content in the solution. The pH of the solution plays an important role in determining the corrosion rate of carbon steel in CO_2

environment. Increasing the pH of the solution leads, in general, to a reduction in corrosion rate by influencing the electrochemical mechanisms and the formation of protective iron carbonate film [228]–[230]. When the pH of solution rises, the cathodic reduction of carbonic acid and bicarbonate ions (Equation 2-5 (b) and Equation 2-5 (c)) slow down which, in turn, decreases the anodic dissolution rate of iron (Equation 2-5 (e)). Furthermore, at high pH values, a protective carbonate scale forms on the surface which reduces corrosion rate significantly [229], [231], [232]. This reduction in corrosion rate is due to the low solubility of iron carbonate in the solution [228], [229], [233]–[236]. Moreover, increasing CO_2 partial pressure decreases the pH of the solution which, subsequently increases the rate of reduction of carbonic acid leading to higher corrosion rates [200], [235]–[241].

Dissolved oxygen in the corrosive solution plays a significant role during corrosion. Iron carbonate ($FeCO_3$) is unstable in the presence of oxygen [242] and higher oxygen concentrations contribute to an increase in the rate of the cathodic reaction (oxygen reduction) [240]. In some cases, dissolved oxygen dominates the oxidation process, which affects the composition and formation of passive film [242], [243].

Steels may have various phases (ferrite, pearlite, bainite, martensite) depending upon the chemical composition, fabrication process, and heat treatment. The presence and amount of these phases influence the corrosion resistance of the steel [244]. However, both laboratory experiments and field experience have shown that depending upon the environment (pH, solution composition, temperature) the protective properties and the adherence of passive films may vary significantly for carbon steels with the same composition and microstructure. As a consequence, extensive research work has been carried out to identify the role of the various environmental and metallurgical factors that influence the corrosion process in aqueous solutions containing CO_2 [200], [228], [245]–[249]. Crolet et al., [246] suggested that

corrosion layers containing the same solid components can be extremely protective or even corrosive depending upon the location of these components.

The adherence of the corrosion product film has often been related to the presence of iron carbide. It is believed that the carbide phase strengthens the film and anchors it to the steel substrate. Hence, the size and distribution of carbides (depends on the heat treatment) is very important. However, there is no agreement on the mechanism and on how the microstructure and the heat treatment actually affect the growth and stability of the iron carbonate film. It has been reported that normalized plain steel with a pearlitic microstructure (lamellar cementite) is far superior than the quenched and tempered alloy steel with a tempered martensitic microstructure (globular structure) [228], [240], [245], [247], [250]. Ueda [228] proposed that lamellar cementite acts as a cathodic site and accelerates the dissolution of iron. Thus, the local concentration of Fe^{2+} ions increases in the cavities between cementite platelets leading to $FeCO_3$ formation. As a consequence, lamellar cementites anchor the corrosion product. However, in case of homogeneously dispersed cementite (tempered microstructure), the corrosion product peels off partially because of the lack of anchoring.

Zhao et al., [214] studied the formation and characteristics of the CO_2 corrosion product layer on the surface of P110 steel in a simulated corrosion medium (Cl^- 110.0 g/l, SO_4^{2-} 1.2 g/l, HCO_3^- 0.15 g/l, Mg^{2+} 1.0 g/l, Ca^{2+} 6.0 g/l, Na^++ K^+ 100.0 g/l, Fe^{2+} 0.1 g/l, Fe^{3+} 0.03 g/l). They found that the uniform corrosion rate gradually decreases with increasing exposure time and after 240 hours of immersion, the corrosion film consists of two layers; the inner layer adjacent to the substrate is thin and compact, whereas the external layer is thick and loose. Considerable defects such as pores, gaps and breakdown exist in the external layer. Lopez et al., [251] studied the influence of inhibitors and steel microstructure on corrosion layers in CO_2 environment and reported the presence of $FeCO_3$ in all samples. However,

they suggested that the proportion of iron carbonate and various iron oxides depends on the microstructure of the base material. Wu et al., [252] characterized the surface film formed under CO_2 corrosion on N80 steel and concluded that the formation of complex carbonate contributes to the enhanced stability of the surface film. They noted that it was not the thickness of the film but the structure and its morphology that lead to low corrosion and protectiveness. They also proposed that the corrosion layer containing the same solid components can be either protective or corrosive. In general, the protective characteristic of a corrosion film depends on both the steel characteristics (microstructure, heat treatment, alloying element) and environmental variables (pH, temperature, flow rate, solution composition).

2.4 Erosion-Corrosion of Steel

Erosion–corrosion is common in oil and gas processing plants and pipelines where there is interaction between solid particles, corrosive fluid and target material [253]–[258]. Here, the observed mass loss is higher than the summation of mass loss due to pure erosion and pure corrosion. The interaction between these two processes has been referred to by different researchers as a 'synergistic' effect [82], [198], [204], [257]–[263]. Erosion-corrosion synergism normally takes place in pipe bends (elbows), tube constrictions, and other structures that alter flow direction or velocity. During erosion-corrosion, corrosion products are first deposited on the internal pipeline surface in the form of scale. The main product, which is $FeCO_3$, initially, acts as a protective barrier to prevent the corrosion of the steel surface. Once the scale has grown to a certain thickness, it becomes considerably brittle and is easily removed by the mechanical forces of the flow [264]–[266]. Thus, the newly exposed areas become highly susceptible to the corrosion process. Several investigations [26], [214], [219], [221], [267]–[275] have been reported to study the erosion-corrosion phenomena involved. It is believed that erosion affects corrosion by removal of surface deposits, increase in local turbulence and surface roughness. The action of mechanical wear results in damage of the passive film, leading to exposure of fresh, bare surfaces to the corrosive medium. This accelerates the corrosion process which, in turn, leads to the development of a new passive film which will eventually be damaged by further mechanical action. These two sub-processes - wear and passivation - repeat alternately. If the ability of the self-passivation of materials is weak, then materials will undergo significant corrosion damage. In addition, high speed abrasive particles deform the metal significantly, and hence, become inhomogeneous in its residual stress distribution (formation of work hardened layer) and electrochemical properties. The work hardened layer, has high chemical activities and can

form primary micro-cells because of strain differences with adjacent low-strain domains, thus accelerating the metal dissolution process [276]–[278]. It has also been reported in previous investigation [279] that corrosion removes the work hardened layer and exposes fresh unhardened surfaces for further erosion.

To quantify the synergistic effect, it is important to clarify whether erosion affects corrosion, corrosion affects erosion, or both. It is worthwhile to separate the erosion-caused metal loss from the corrosion-caused metal loss to clarify the transition between the erosion-corrosion regimes. This would indicate whether erosion or corrosion is the dominant degradation process and provides useful information on the selection of materials and prevention of erosion-corrosion. To analyze the synergistic effect and understand the mechanism of interaction between erosion and corrosion, it is important to provide accurate erosion and corrosion baselines and to separate the contributions of erosion and corrosion from the total synergism.

2.4.1 The Synergy between Erosion and Corrosion

In order to identify the effect of corrosion on erosion and vice-versa, it is important to separate the metal loss contributions due to erosion, corrosion and their interactions. The synergism can be determined by an experimental program which includes three types of tests, pure erosion, pure corrosion and combined tests. Various techniques [280], [281] have been used by different researchers to quantify these components which facilitate the analysis of material loss mechanisms and the development of predictive models [106], [282]–[286]. The total material loss during erosion-corrosion process can be defined as [287], [288],

$$T = E_0 + C_0 + S \qquad \text{Equation 2-6}$$

where, T is the total mass loss rate of the material, E_0 is the erosion rate in absence of corrosion, C_0 is the corrosion rate in absence of erosion and S is the synergistic component and is defined as,

$$S = \Delta C_e + \Delta E_c \qquad \text{Equation 2-7}$$

where,

$$\Delta C_e = C_e - C_0 \qquad \text{Equation 2-8}$$

$$\Delta E_c = E_c - E_0 \qquad \text{Equation 2-9}$$

ΔC_e is the change in corrosion rate due to erosion and ΔE_c is the change in erosion rate due to corrosion, E_c is the total erosion component in the presence of corrosion and C_e is the total corrosion component in the presence of erosion. It is important to note that erosion-corrosion mass loss can sometimes be lower than the summation of mass loss due to pure erosion and pure corrosion. In that case, the effect is called 'antagonistic' effect or negative synergism [289]. Figure 2-5 shows the contribution to the total weight loss of each component, erosion, corrosion and erosion + corrosion as a representative example. The synergistic effect is pronounced for the carbon alloy steels, but it is relatively small for the stainless steels.

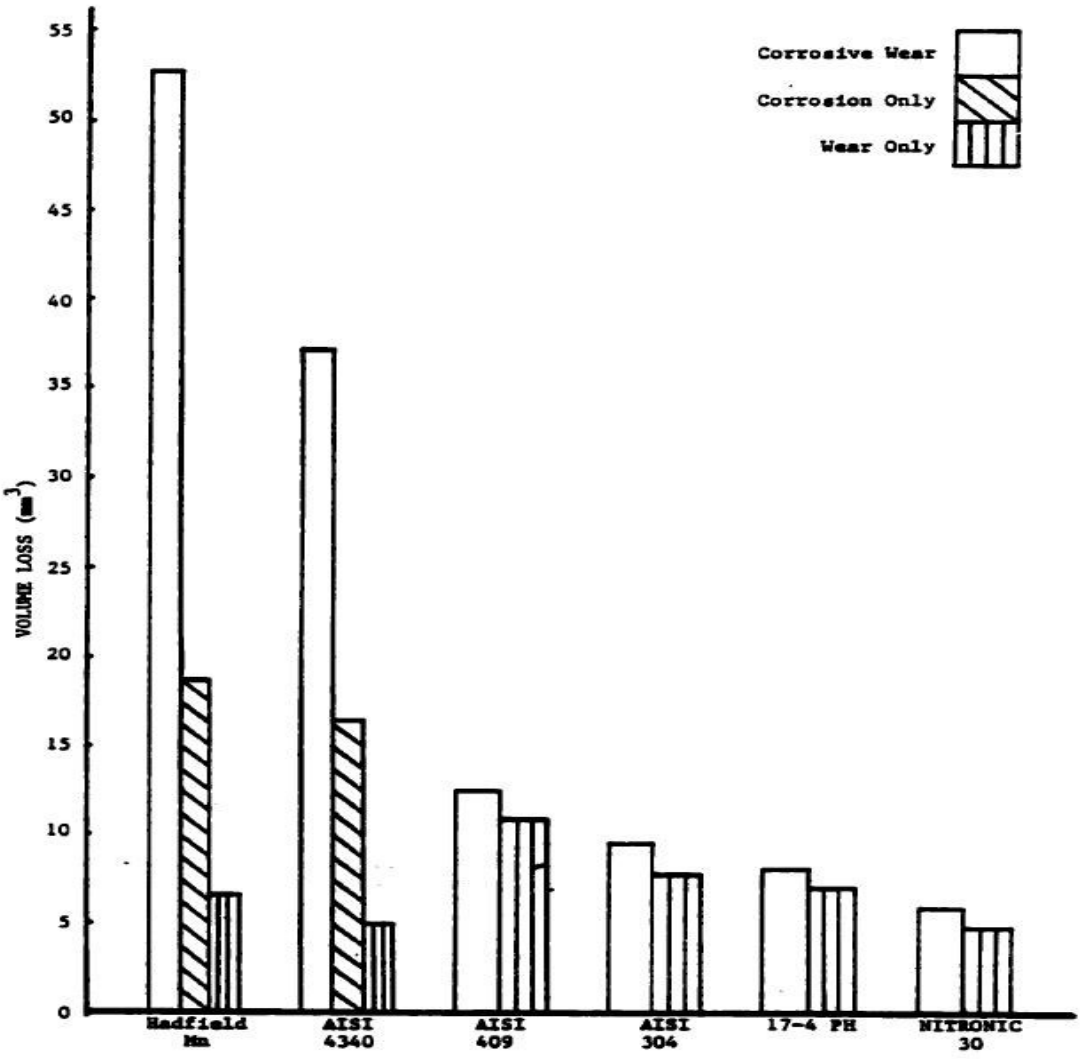

Figure 2-5 Erosion-corrosion synergism for carbon and stainless steels [290].

2.4.2 Erosion-Corrosion Mechanisms Maps

To the designers and engineers who have to make optimal decisions in situations where tribological considerations are significant, it is important for them to have access to information relating to the erosion-corrosion process of interest. This specific set of data should be able to provide the appropriate information for material selection and choice of suitable operating conditions for a particular set of materials. There are many ways of presenting erosion-

corrosion data. Tabulation of erosion-corrosion rates and identification of the dominant mechanisms of erosion-corrosion, under the operating conditions of interest using worn surface examination techniques, are the most common modes of presentation. However, 'mechanism maps', as defined in the early work of Lim and Ashby [291], demonstrate the change in material loss mechanisms as a function of the main process parameters. Contours of material loss rates are superimposed on these diagrams enabling the mechanistic description to be linked to a material loss rate. Such an approach makes an improvement in material selection and process parameter optimization. An erosion-corrosion mechanism map will not only provide a graphical representation of erosion-corrosion data; it also provides an overall framework for the erosion-corrosion behavior of a particular system into which individual erosion-corrosion mechanisms observed under various operating conditions may be fitted. Hutchings et al., [110], [161], [292] provided examples of erosion maps, which display the regimes of particle size and impact velocity over which different mechanisms of erosion dominate. Stack et al., [280], [289], [293]–[298] proposed an aqueous erosion-corrosion map showing the transitions between various regimes of aqueous erosion-corrosion in terms of erodent velocity and potential. It is interesting to note that, there is a regime in the erosion-corrosion map within which neither corrosion, nor erosion is expected to occur. The ability to locate such safety zones where degradation of materials would be at a minimum is one of the major strengths of erosion-corrosion mechanism maps.

An erosion-corrosion map in aqueous environments was constructed schematically by Stack [299], for Fe in $NaHCO_3/Na_2CO_3$ buffer solutions and is shown in Figure 2-6. As shown in the map, an increase in the erosion parameter (particle velocity) and the corrosion parameter (potential) has changed the degradation behavior of the material. They have considered the

corrosion processes in terms of dissolution or passivation and divided the regimes as,

i. Erosion dominated
ii. Erosion-corrosion dominated
    (a) Erosion-dissolution dominated
    (b) Erosion-passivation dominated
iii. Corrosion-dominated
    (a) Dissolution dominated
    (b) Passivation dominated

The exact locations of the regimes on such maps as a function of the aqueous erosion- corrosion variables need to be established. Clearly if the potential is fixed at high values, the erosion process effects a transition from 'passivation' to 'erosion-dominated' behavior as a function of velocity. However, at lower potentials, active dissolution is the predominant degradation process and therefore, transitions from 'dissolution' to 'erosion-dominated' behavior occur as a function of increasing particle velocity, flux and angularity.

Figure 2-6 indicates that at low potentials and low velocities in cathodic conditions, neither erosion nor corrosion occurs. At high velocities, plastic deformation takes place and therefore, a transition to 'pure' erosion occurs. As the applied potential is increased, and dissolution of metal is initiated, the transitions between the erosion-dissolution regimes are achieved. An increase in velocity shifts the 'erosion-dominated' regime to higher potentials because the corrosion rate (*i.e.* the dissolution rate), as a function of increasing potential, increases in this region. It can be seen that a similar phenomenon applies in the passive region, although the boundaries are less dependent on potential because the passive film thickness does not increase significantly with increasing potential in this case.

The map shows that in the passive region, the transition to 'erosion-dominated' behavior shifts to lower velocities than in the dissolution region. This is justified on the basis of the fact that the relative contribution of corrosion to the overall erosion rate decreases as a function of potential in the conditions studied. Hence, the metal loss due to corrosion decreases with increasing applied potential, as the transition from active to passive behavior occurs.

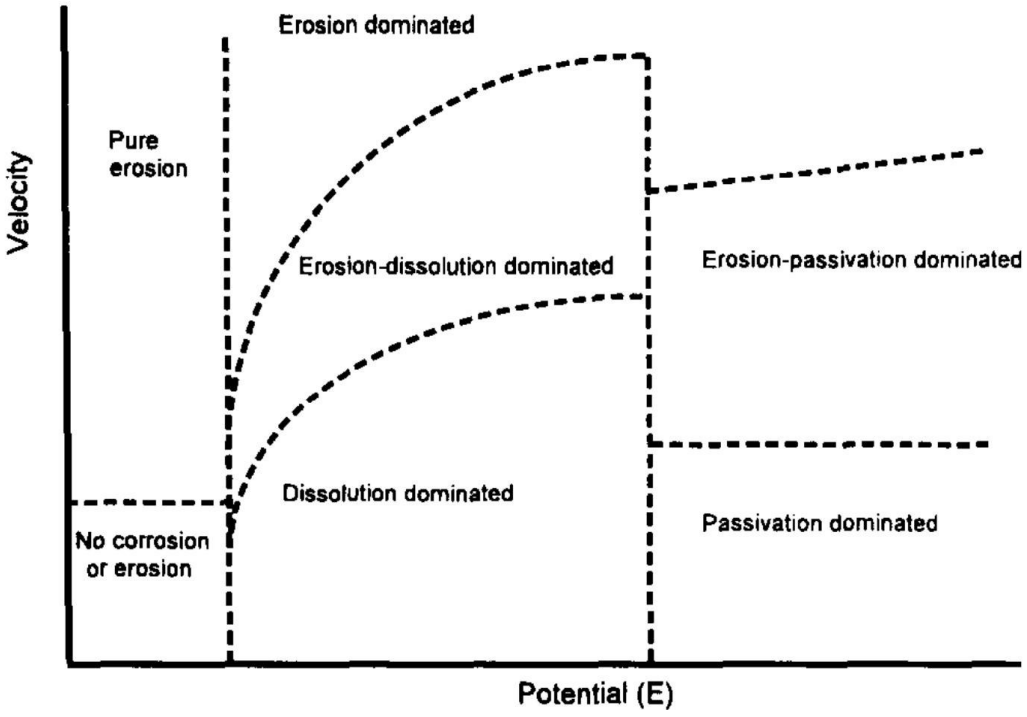

Figure 2-6 Schematic diagram of an aqueous erosion-corrosion map for Fe in $NaHCO_3/Na_2CO_3$ where the transitions between the erosion-corrosion regimes are given as functions of velocity and potential [299].

Chapter 3

Experimental Details

This chapter contains materials characterization and experimental methodology employed in this research.

3.1 Materials Characterization

Specimens were characterized for their physical and chemical properties. ICP, XRD, SEM and optical microscopy examination were employed to characterize the materials and are discussed in this section.

3.1.1 Physical and Chemical Properties

In this study AISI 1018, AISI 1080, API X42, API X70 and API X100 steel coupons (15.8 ± 0.03 mm diameter and 6.1 ± 0.02 mm thick) were used as test specimens and alpha aluminum oxide (Al_2O_3) powder was used as abrasive medium. Mechanical properties of these steels are given in Table 3-1. The compositions were determined using inductively coupled plasma mass spectrometry (ICP) and are summarized in Table 3-2. X-ray diffraction (XRD) experiments were carried out using a high-speed Bruker D8 Advance system employing Cu-Kα1 radiation having a wave length (λ) of 1.54 Å, tube voltage of 40 kV and tube current of 40 mA. Figure 3-1 shows the XRD pattern of API X42 steel as a representative example. XRD peaks were matched to those in

the Powder Diffraction Files (PDF) and identified as carbon steel peaks having a BCC crystal structure.

The hardness and Young's modulus of the specimens were measured using a nano-indentation system with a Berkovich diamond indenter (pyramid shape) having an angle of 65.3° between the tip axis and the faces of the triangular pyramid. Thirty six indentations (at random locations) were performed on each specimen using a constant load of 400 mN. Representative load vs depth profiles for AISI 1018 and AISI 1080 steels are shown in Figure 3-2. The total penetration depth consists of a plastic component and an elastic recovery component which occurs during unloading. Hardness and Young's modulus of the specimens were then calculated from maximum load, indentation depth and the slope of the load vs depth profile using Oliver and Pharr method [300]. The average hardness and Young's modulus values for AISI 1018 and AISI 1080 steels are summarized in Table 3-3. It is important to note that hardness and Young's modulus generated from nano-indentation tests are expected to be different from those obtained from conventional uniaxial tensile experiments. The differences are due to the fact that the state of stress underneath a sharp indenter is complex and quite different from that in a tensile test and there is no direct correlation between the two tests. As expected, the hardness of AISI 1080 is higher (81%) compared to AISI 1018 steel due to the higher amount of carbon and higher pearlite content in the microstructure. Young's modulus of AISI 1080 steel is around 6% less than AISI 1018 steel. As the elastic modulus is structure-insensitive property, its variation with the microstructure is minimal and its value mainly determined from the atomic bond strength of the steel. Hence, similar Young's modulus for AISI 1018 and AISI 1080 is to be expected. It is also observed from Figure 3-2 that the depth of penetration of AISI 1018 steel is higher than that of AISI 1080, which reflects its higher ductility.

Physical properties and chemical composition of alumina abrasive is given in Table 3-4. Malvern Mastersizer 3000 laser diffraction particle size analyzer was used to measure the particle size distribution of the aluminum oxide erodent following ISO standard [301]. The abrasive particle size distribution is shown in Figure 3-3. These results give a mode of about 63 ± 3 μm and an average abrasive particle size of about 57 ± 3 μm. SEM image of the alumina erodent reveals irregular angular shaped particles as shown in Figure 3-4 (a). Figure 3-4 (b) is a magnified image of Figure 3-4 (a) illustrating the sharp edge of the abrasive particle which is primarily responsible for material removal during the erosion process.

Table 3-1 Mechanical properties of carbon and pipeline steels [302]–[305].

Properties	AISI 1018	AISI 1080	API X42	API X70	API X100
Yield strength (MPa)	310	585	290	482	690
Elongation (%)	20	12	23	17	15.2
Elastic modulus (GPa)	205	200	210	203	210
Density (g cm^{-3})	7.87	7.87	7.87	7.87	7.87
Vickers hardness (GPa)	1.29	3.03	1.34	1.81	2.50

Table 3-2 Chemical composition of carbon and pipeline steels.

Elements	AISI 1018	AISI 1080	API X42	API X70	API X100
C	0.182	0.814	0.169	0.061	0.103
Si	0.095	0.120	0.067	0.150	0.151
Mn	0.754	0.598	0.372	1.223	1.221
Cr	0.181	0.122	0.027	0.018	0.070
P	0.040	0.040	0.040	0.010	0.010
Cu	0.186	0.230	0.008	0.008	0.009
Ti	0.008	0.001	0.002	0.015	0.018
S	0.021	0.014	0.004	0.002	0.001
Fe	balance	balance	balance	balance	balance

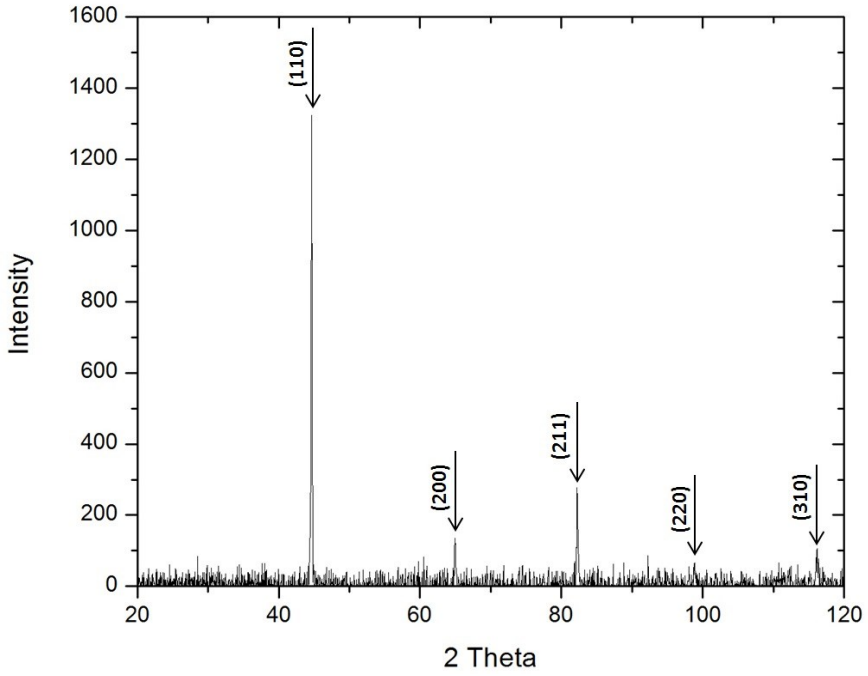

Figure 3-1 XRD pattern of API X42 steel identified as carbon steel peaks having a BCC crystal structure.

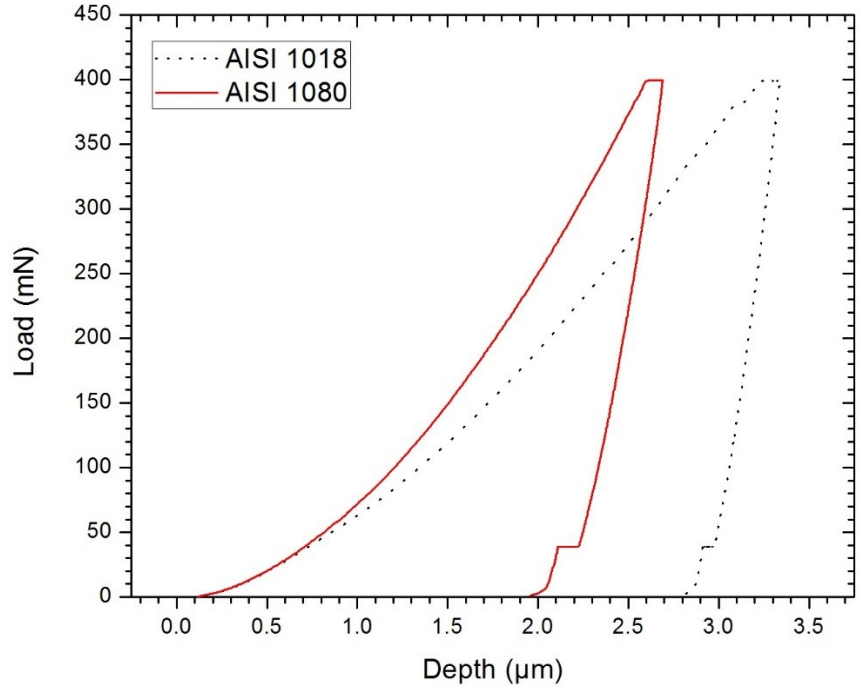

Figure 3-2 Load vs indentation depth profile for AISI 1018 and AISI 1080 steels.

Table 3-3 Average hardness and Young's modulus of AISI 1018 and AISI 1080 steels.

Steel	Hardness (GPa)	Young's modulus (GPa)
AISI 1018	1.81 ± 0.1	124.48 ± 0.5
AISI 1080	3.27 ± 0.1	117.95 ± 0.5

Table 3-4 Physical properties and chemical composition of aluminum oxide [306].

Physical properties	
Crystal phase	Alpha
Specific gravity	3.95 g cm^{-3}
Particle shape	Sharp, angular
Vickers hardness	27.13 GPa
Average particle size	57 ± 2 μm

Chemical Composition					
AlO_2	TiO_2	SiO_2	Fe	MgO	Alkali
99.5	0.099	0.05	0.08	0.02	0.30

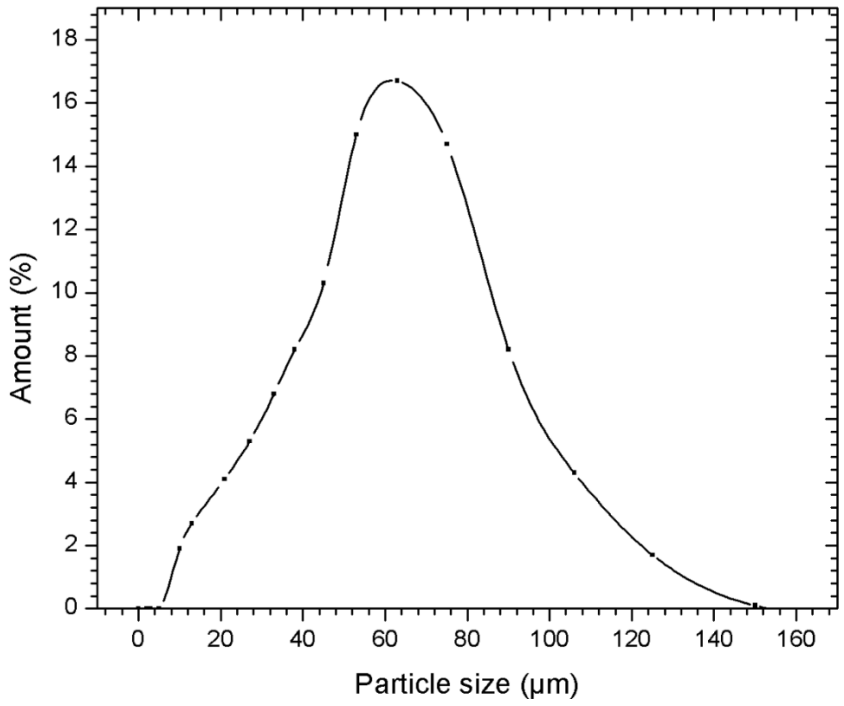

Figure 3-3 Particle size distribution of alumina abrasive having an average particle size of 57 ± 3 μm.

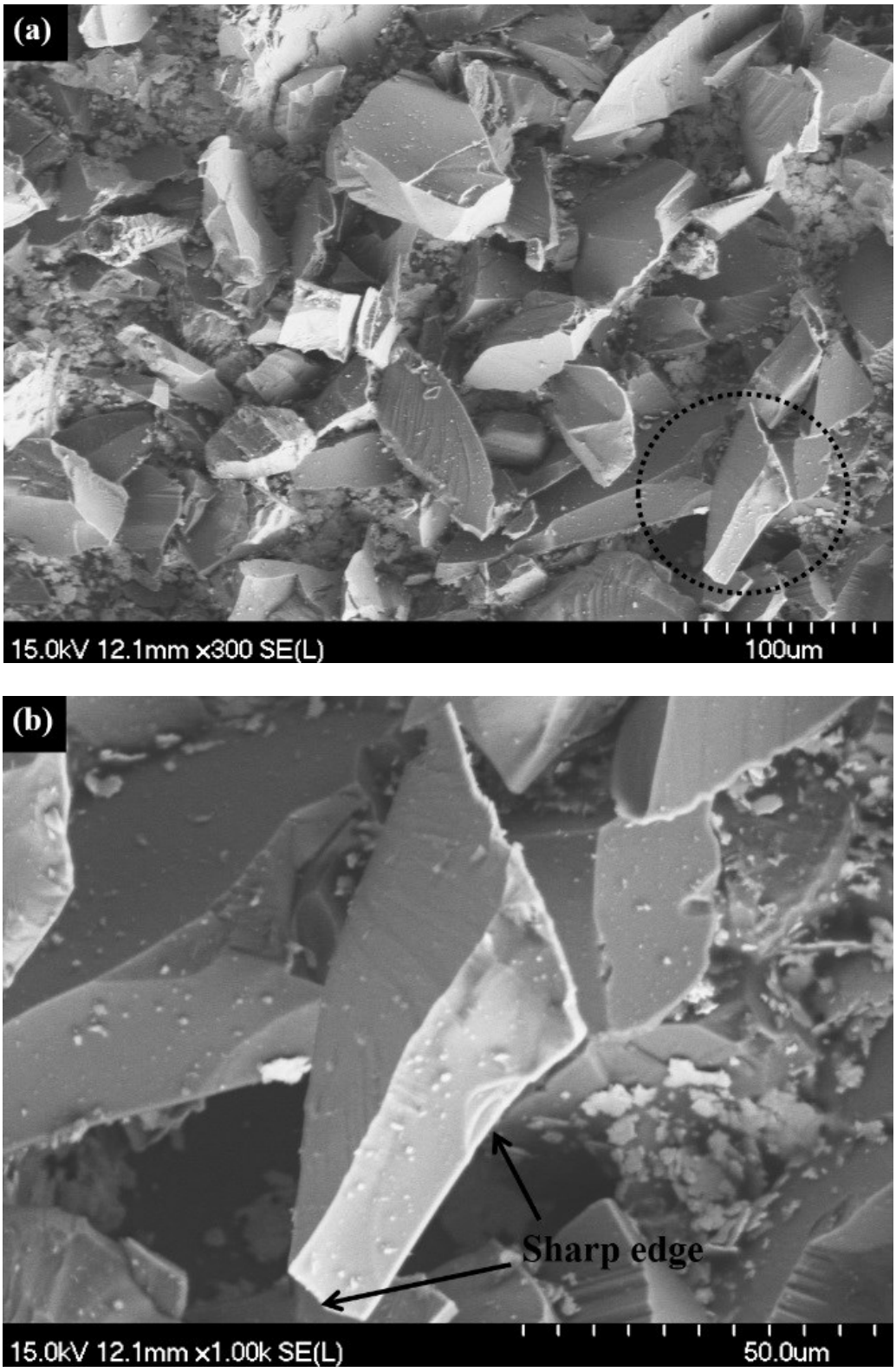

Figure 3-4 SEM micrograph of the alumina abrasive showing irregular shaped particles.

3.1.2 Optical Microscopy

Steel specimens were ground using 240, 320, 400 and 600 grit SiC abrasive papers followed by polishing with 1 µm, 0.3 µm and 0.05 µm gamma alumina suspension for microscopic observation. Specimens were then cleaned in an ultrasonic bath and etched using a 5% Nital solution to reveal the microstructure. Optical micrographs of AISI 1018, AISI 1080, API X42, API X70 and API X100 are shown in Figure 3-5 (a), (b), (c), (d) and (e), respectively. The microstructure of AISI 1018, AISI 1080, API X42 and API X70 steel consisted of a mixture of ferrite and pearlite (Figure 3-5 (a)-(d)). However, the microstructure of API X100 steel comprised of very fine bainite and ferrite having lath-like and granular type morphology (Figure 3-5 (e)). The addition of molybdenum, copper and nickel in API X100 increases the temperature of the maximum rate of pearlite transformation and decreases the temperature of the maximum rate of bainite transformation and thus promotes the formation of the desired lower bainite microstructure [48], [49]. A similar type of microstructure for API X100 was previously observed by others [307]. Microstructural constituents and average grain size for these steels are shown in Table 3-5.

Table 3-5 Average grain size and microstructure for carbon and API steels.

Steels	Microstructural constituents	Average grain size
AISI 1018	Ferrite + Pearlite	10 ± 2 µm
AISI 1080	Ferrite + Pearlite	12 ± 2 µm
API X42	Ferrite + Pearlite	10 ± 2 µm
API X70	Ferrite + Pearlite	5 ± 1 µm
API X100	Ferrite + Bainite	2 ± 1 µm

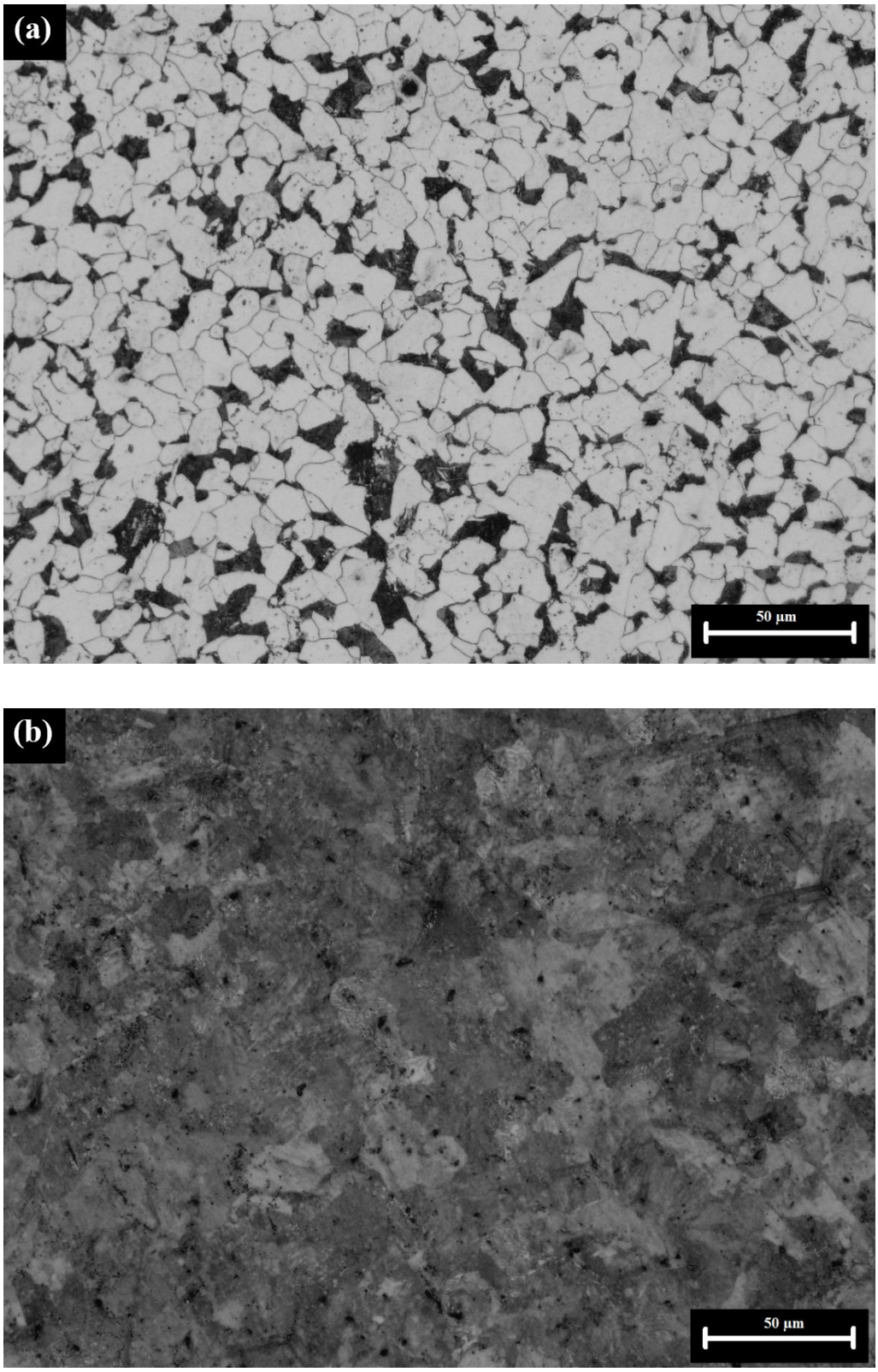

Figure 3-5 Optical micrograph of (a) AISI 1018 and (b) AISI 1080 steels.

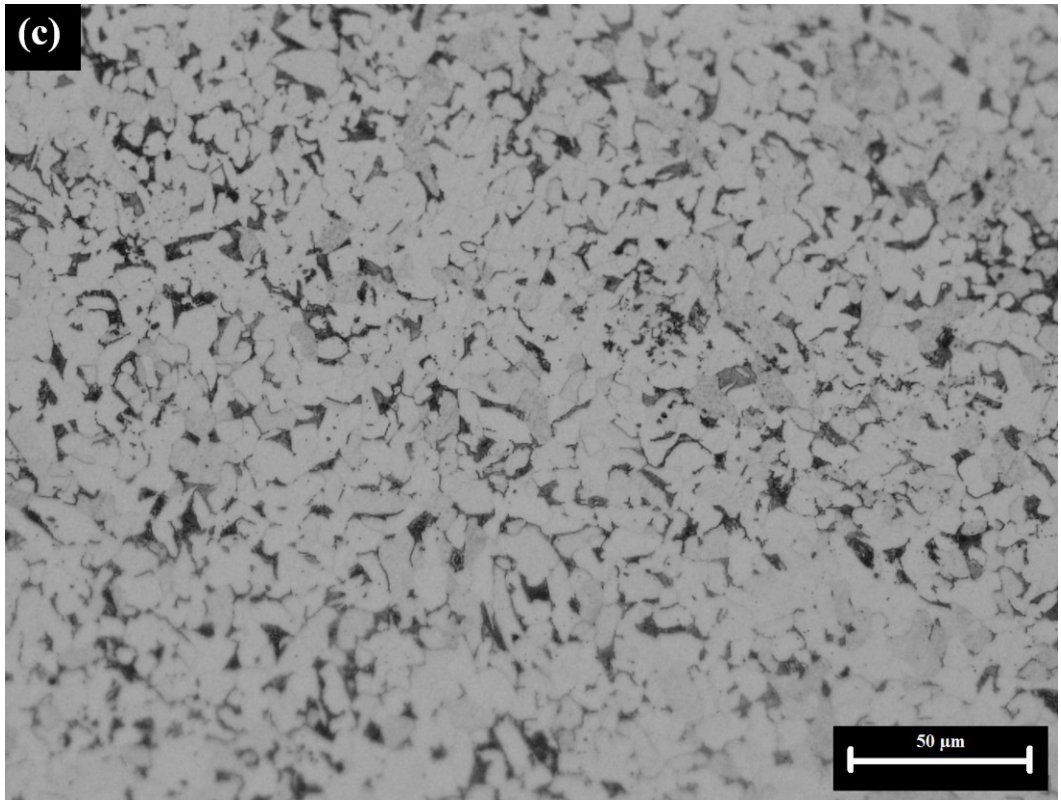

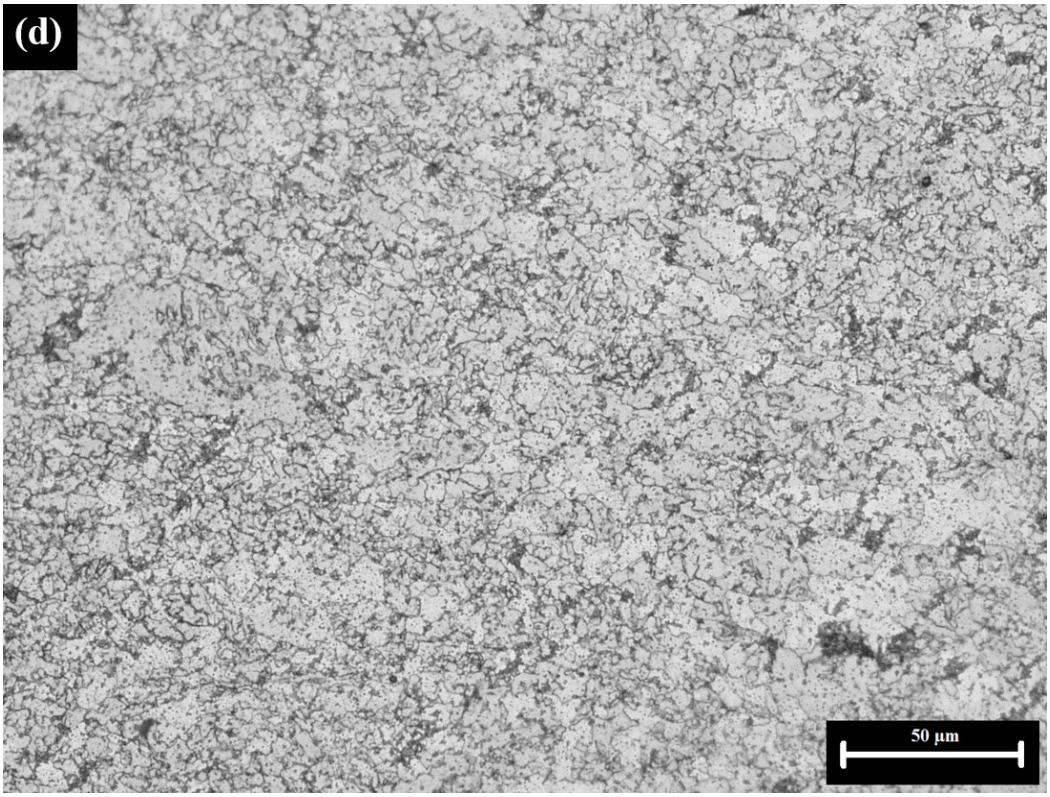

Figure 3-5 Optical micrograph of (c) API X42 and (d) API X70 steels.

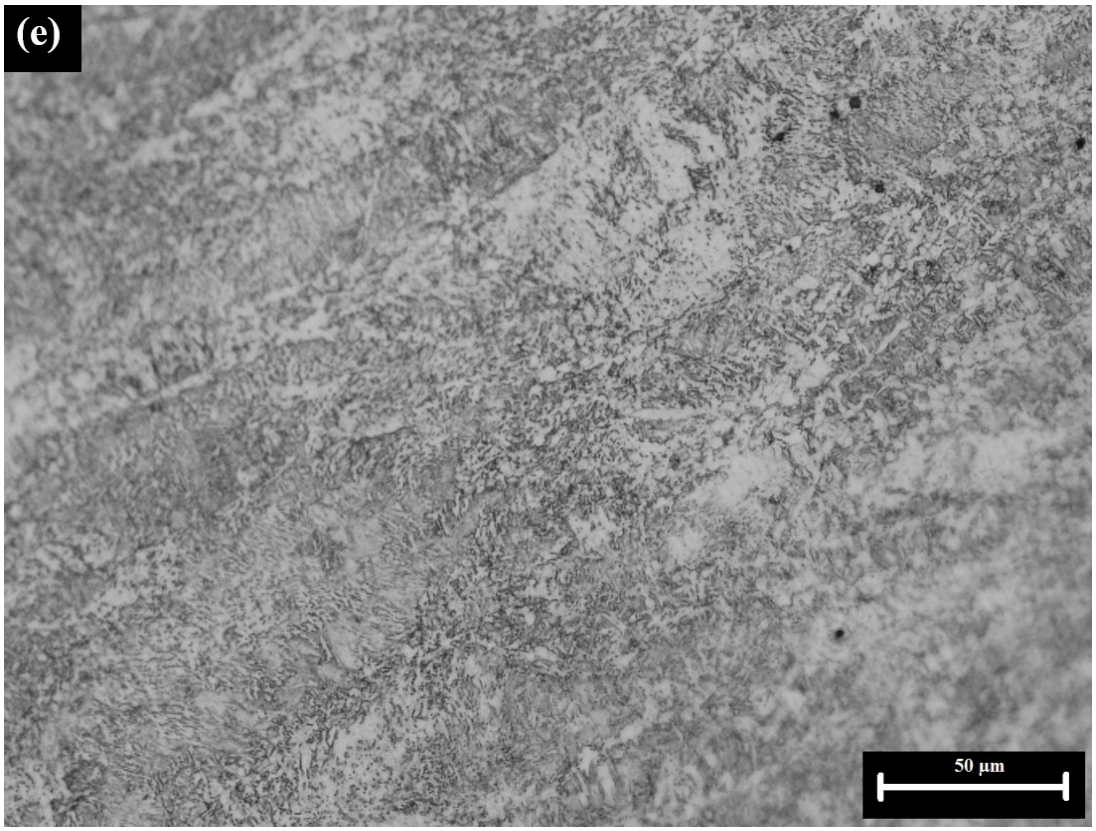

Figure 3-5 Optical micrograph of (e) API X100 steels.

3.2 Experimental Setup and Operating Conditions

This section provides relevant information about the experimental setup and operating conditions used in this study for erosion, corrosion and erosion-corrosion.

3.2.1 Erosion

A sand blaster type erosion tester, capable of eroding material from a test specimen under well controlled exposure conditions was used for this study (Figure 3-6). The erosion tester was designed to control and adjust particle impact velocity, particle flux, specimen location and orientation relative to the impinging stream. A schematic diagram of the erosion tester is shown in Figure 3-7. The erosion tester is composed of an abrasive feed meter (acts as a reservoir tank and controls the abrasive feed rate), air flow meter, pressure gauge and a specimen chamber. In order to achieve a uniform particle distribution in the stream a nozzle (inner diameter: 2.3 mm, length: 33 mm) having a length to diameter ratio of 14:1 was used. Figure 3-8 and Figure 3-9 show the isometric view and inside chamber of the erosion tester, respectively.

Different researchers have used various methods to measure particle velocity, which include Laser Doppler Velocimetry (LDV) [308], slotted double cylinders [309] and others [147], [310]. In this study, gas pressure was measured and particle velocity was determined as a function of pressure using a double-disc method [310]. Figure 3-10 (a) shows the correlation between particle velocity and air jet pressure for the gas blast erosion apparatus in which particles are accelerated by air flow along a straight cylindrical nozzle. Actual abrasive feed rate is accurately determined by measuring the weight of the abrasive coming through the nozzle per unit

time and is constant for a given velocity. However, higher feed rate accompanies higher particle velocity due to higher pressure (suction force). The calibration curve for abrasive feed rate and particle velocity is shown in Figure 3-10 (b). It should be noted that error bars in plots in the present work represent standard deviations of several measurements made per data point. Operating conditions for erosion tests are given in Table 3-6. The abrasive particle velocity range used in this study was 36 to 81 m s^{-1} (Table 3-6). The ASTM standard [68] recommends a particle velocity of 30 m s^{-1}. However, different researchers have used diverse particle velocities in their studies. For example, Ruff and Ives [310] used 71-88 m s^{-1} particle velocity range. Other researchers [161], [311] also used higher particle velocities than stated in the ASTM standard. In this study, a wide range of particle velocity was used in order to assess the effect of particle velocity on erosion and erosion-corrosion. Specimens were weighed using a digital balance (with an accuracy of 1×10^{-5} g) before and after each erosion test. The eroded specimens were cross-sectioned in a longitudinal direction in order to investigate the sub-surface of the erosion scars. Specimens were cut using a Buehler® isomet 1000 slow precision saw using a diamond wafering blade (15.2 cm dia. × 0.5 cm thick). Isomet 1000 precision saw has an automatic cut-off switch; a counter balanced sliding load weight system, a built-in metric digital micrometer cross-feed for sample location and a removable coolant tray with built-in dressing device, in order to avoid excessive heating. Erosion rate in the absence of corrosion (E_0) (μm s^{-1}) was calculated using the following equation [288],

$$E_0 = \left[\frac{\Delta W}{A\ d\ t}\right] K_1 \qquad \text{Equation 3-1}$$

where, ΔW is the weight loss (g) of the specimen, A is the surface area (mm^2), d is the density ($g\ cm^{-3}$), t is test duration (s) and K_1 is a constant (1×10^6 µm cm^{-1}).

To be able to compare erosion rates performed using different particle velocities, the erosion rate needs to be normalized with respect to the particle flow rate for a given particle velocity. That is, the normalized erosion (E) rate is calculated by dividing erosion rate (mg s^{-1}) by the abrasive particle flow rate (mg s^{-1}) using the following equation [312]:

$$\text{Normalized erosion rate, } E = \frac{\text{Erosion rate (mg s}^{-1})}{\text{Particle flow rate (mg s}^{-1})} \qquad \text{Equation 3-2}$$

Table 3-6 Operating conditions for solid particle erosion tests.

Parameter	Operating condition
Nozzle diameter	2.3 mm
Standoff distance	3 mm
Test gas	Dry compressed air
Test duration	10, 180, 420 and 600 s
Test temperature	Room temperature ± 3°C
Angle of incidence	30°, 45°, 60° and 90°
Particle velocity	36, 47, 63 and 81 m s^{-1}

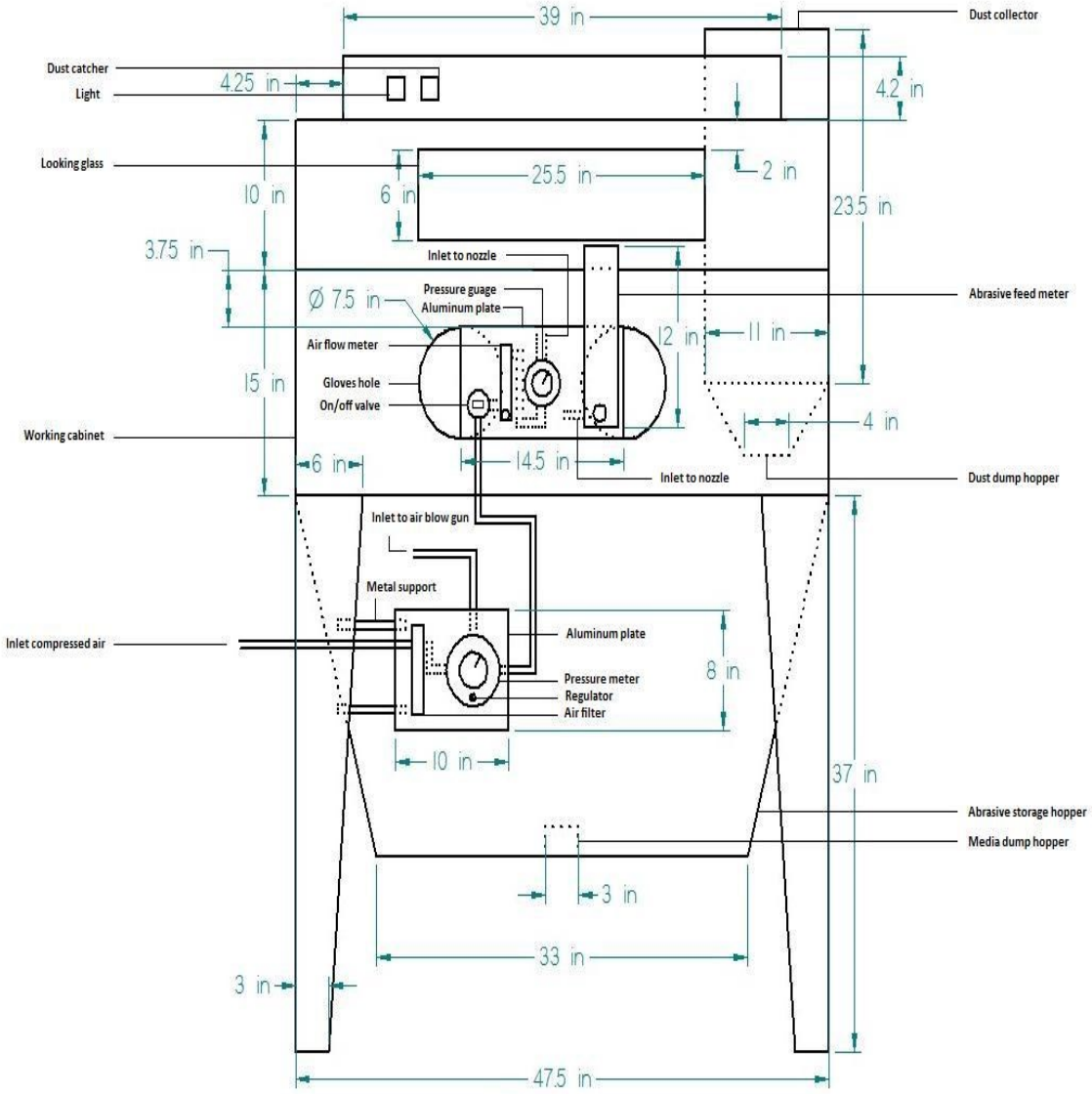

Figure 3-6 Experimental setup for solid particle erosion tester.

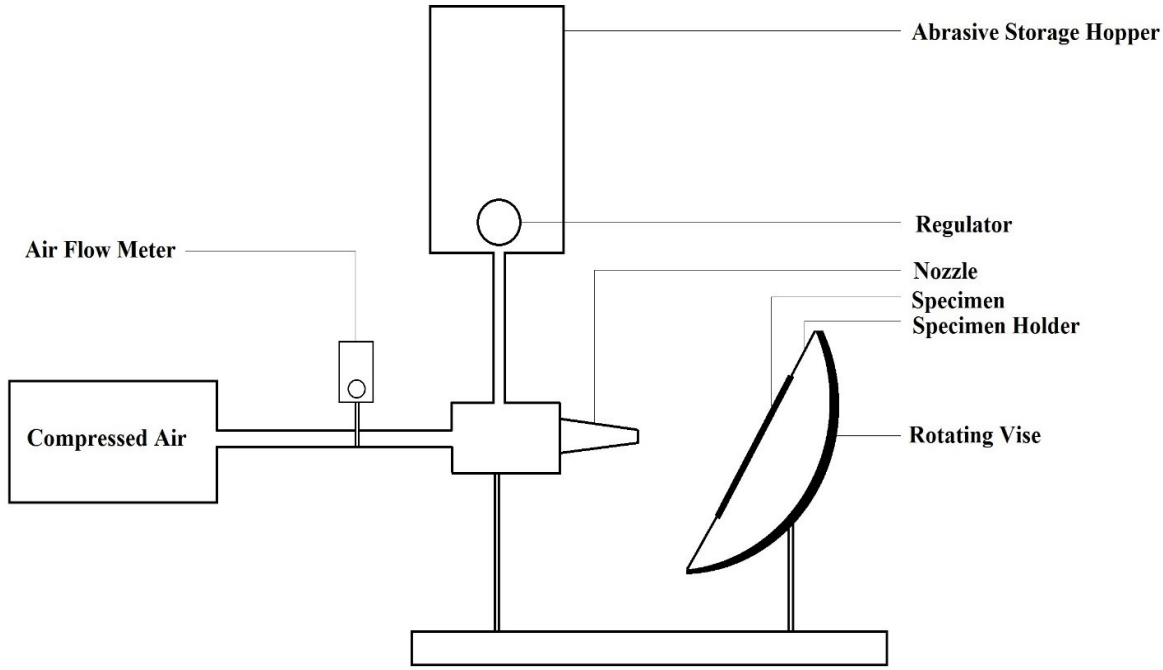

Figure 3-7 Schematic diagram of solid particle erosion tester.

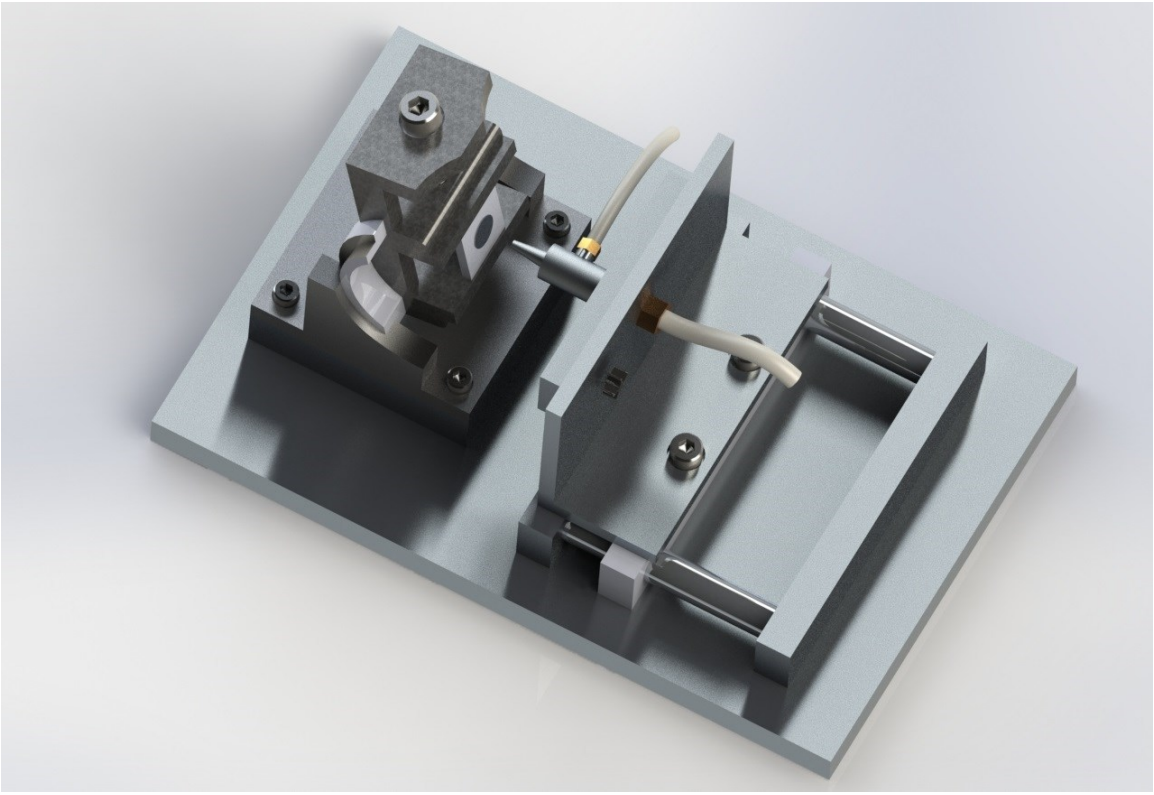

Figure 3-8 Isometric view of erosion sample holder (SolidWorks).

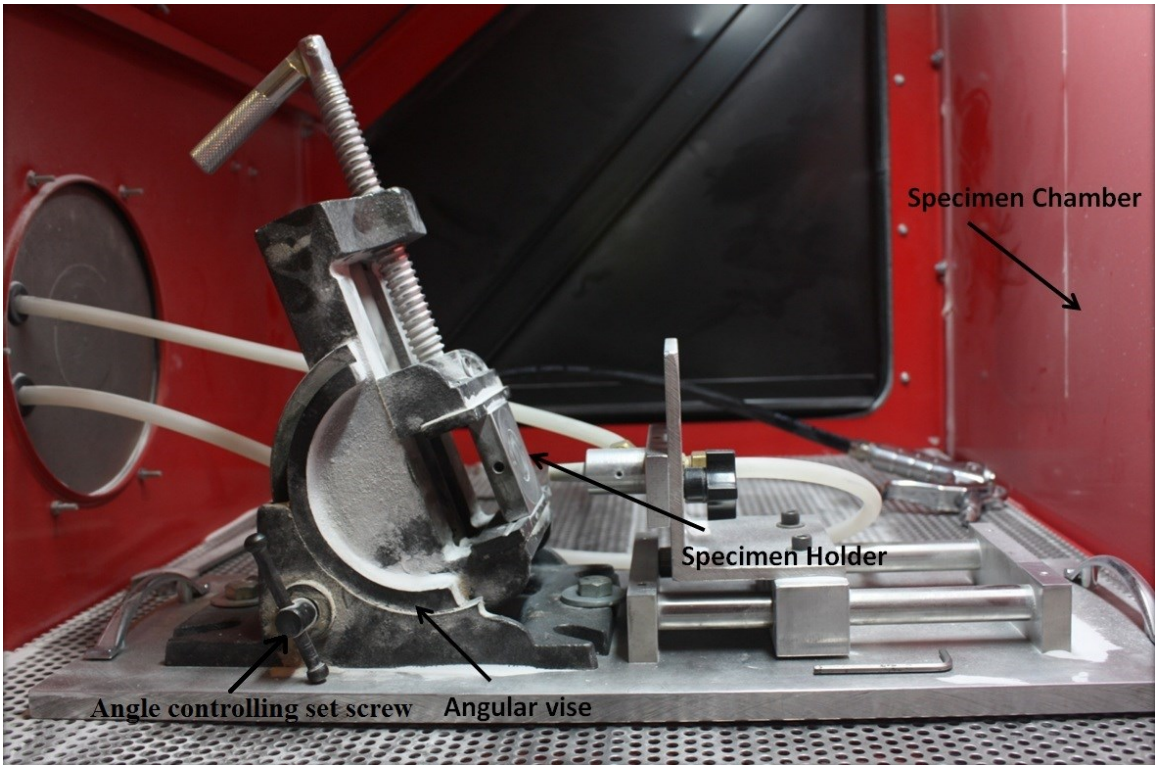

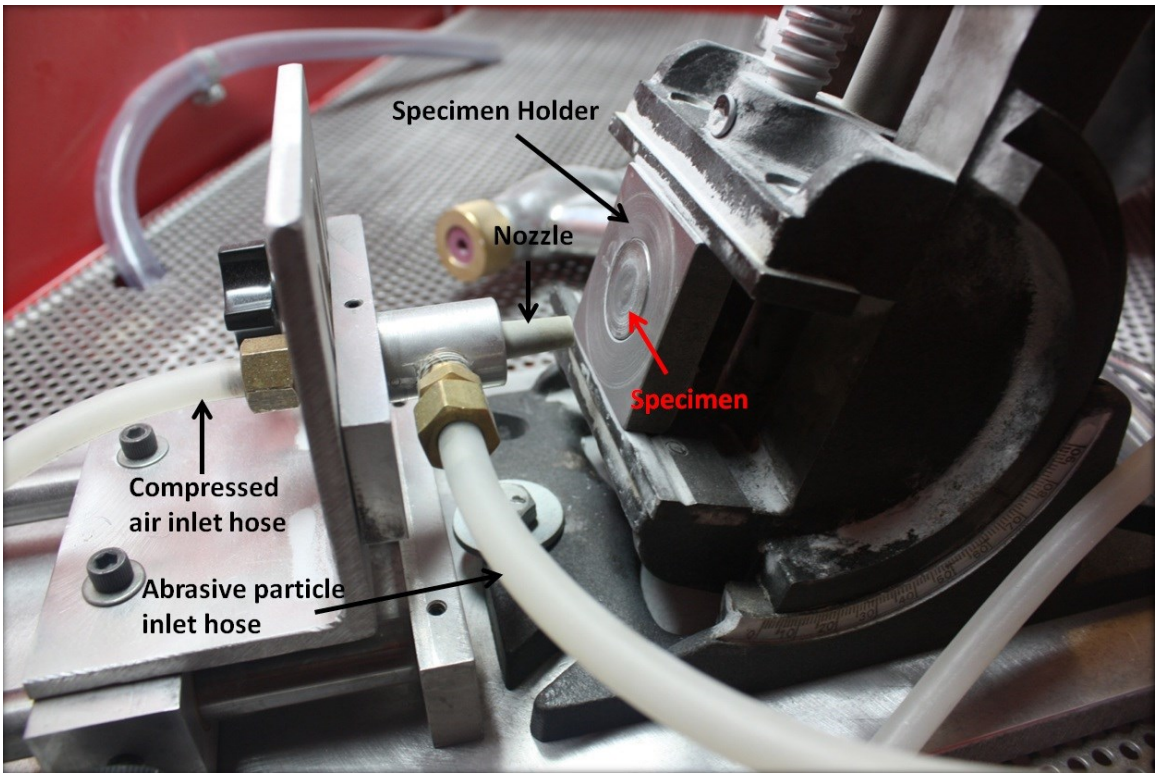

Figure 3-9 Specimen chamber of the erosion tester.

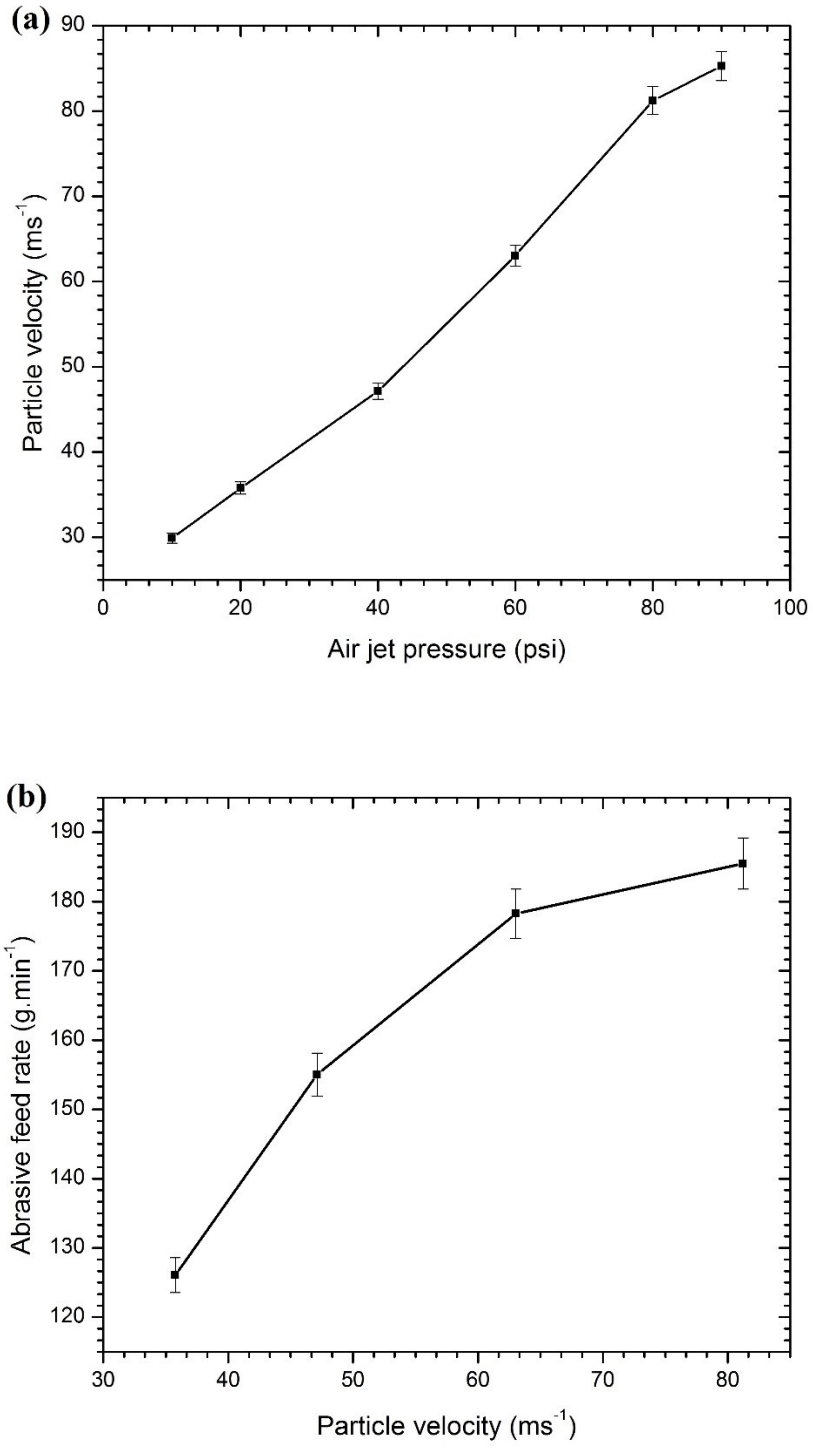

Figure 3-10 Calibration curves for the erosion tester, (a) air jet pressure vs particle velocity and (b) particle velocity vs abrasive feed rate.

3.2.2 Corrosion

Corrosion of steels were monitored using electrochemical and immersion test. Pertinent information regarding electrochemical and immersion corrosion tests are outlined in this section.

3.2.2.1 Electrochemical Test

A conventional three-electrode electrochemical glass cell with a graphite counter electrode and a saturated calomel reference electrode (SCE) was used for electrochemical measurements according to ASTM G59 [313]. All potentials are reported in SCE scale. Polarization curves were generated by changing the electrode potential using a Uniscan potentiostat PG581, at a sweep rate (scan rate) of 0.166 mV s^{-1}. Prior to electrochemical tests, the working electrode was kept in the solution and allowed to attain a stable open circuit potential (OCP). Measurements indicate that a stable OCP was achieved after 1.5 hrs of immersion. Figure 3-11 shows the OCP vs time curves as a representative example. After stabilization, potentiodynamic polarization curves were generated by changing the working electrode potential from an initial value of 250 mV below OCP up to 250 mV above OCP.

Corrosion tests were conducted in a one liter solution containing 2 g NaCl (0.03 M). CO_2 gas was purged through the cell until saturation. At saturation, the pH of the solution reached a value of 4.3. The flow of CO_2 was turned off during the experiment to avoid turbulence or gas bubble formation at the surface of the specimen. The pH of CO_2 saturated solution was monitored continuously during corrosion tests and was maintained at a constant value throughout the experiments. All tests were performed at room temperature. Specimens were weighed before and after each corrosion test. Corrosion rate

in absence of erosion (C_0) (μm s^{-1}) based on weight loss was calculated using the following equation [288],

$$C_0 = \left[\frac{\Delta W}{A\ d\ t}\right] K_2 \qquad \text{Equation 3-3}$$

where, ΔW is the weight loss (g) of the specimen, A is the surface area (mm^2), d is the density (g cm^{-3}), t is test duration (hr) and K_2 is a constant (277.78 μm hr cm^{-1} s^{-1}).

Corrosion rate in the absence of erosion (C_0) (μm s^{-1}) based on potentiodynamic polarization corrosion current (I_{corr}) was calculated using the following equation [288],

$$C_0 = \frac{K_3\ I_{corr}\ EW}{d} \qquad \text{Equation 3-4}$$

where, K_3 is a constant (1.03×10^{-7} μm g μA^{-1} cm^{-1} yr^{-1}), I_{corr} is the corrosion current density (μA cm^{-2}), EW is the equivalent weight and d is the density (g cm^{-3}). The operating conditions for corrosion tests are given in Table 3-7.

Table 3-7 Operating conditions for electrochemical corrosion tests.

Parameter	Operating condition
Test solution	1 liter distilled water + 2 g NaCl
Corroded surface area	100 mm^2
Test duration	2.5 hr
Test temperature	Room temperature ± 3°C
Sweep rate	0.166 mV s^{-1}
Poteniodynamic sweep	From -250 to 250 mV (vs OCP)
Bulk pH	4.3
Pressure	100 kPa CO_2
Velocity	Stagnant

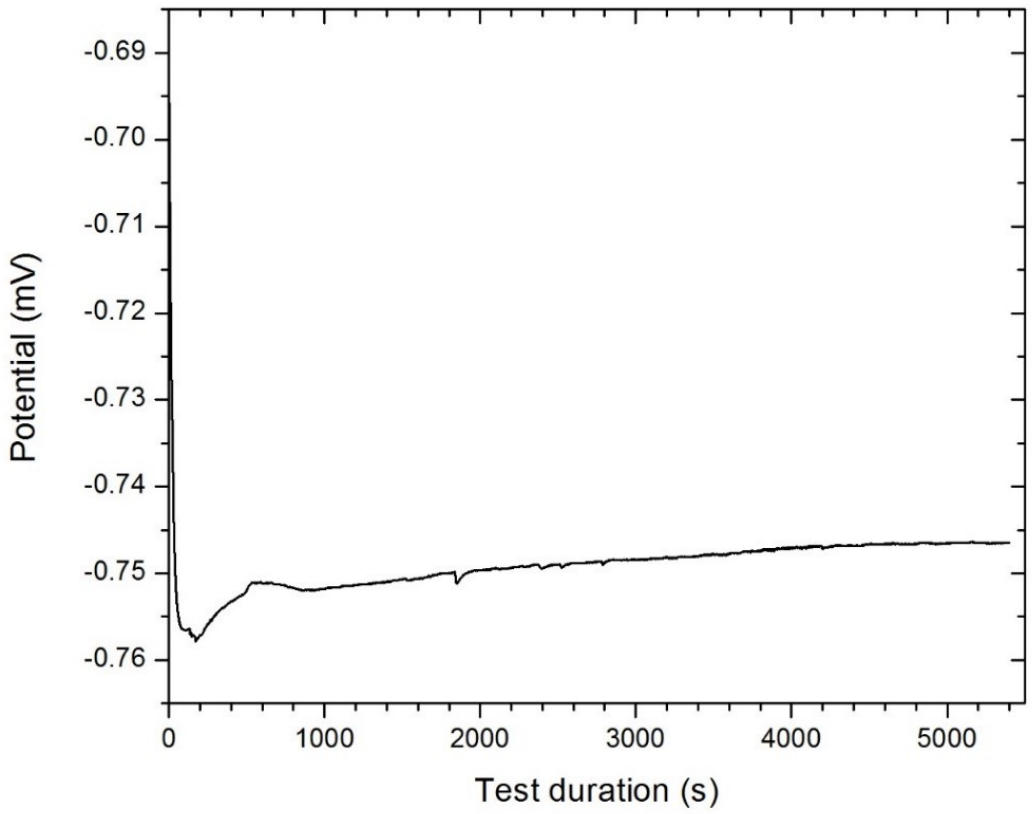

Figure 3-11 Evolution of open circuit potential vs exposure time in 2 g l^{-1} NaCl solution.

3.2.2.2 Immersion Test

Immersion corrosion tests were performed according to ASTM G31 standard [314]. The corrosion apparatus consists of a 400 mL flask (without an atmospheric seal), a thermometer, pH meter and a specimen holder. A schematic diagram of the immersion corrosion setup is shown in Figure 3-12. Corrosion in pipelines is reported to be due to the presence of CO_2 and H_2O. Depending on the operating conditions used for enhanced oil recovery, the bicarbonate concentration varies from 0.02 to 2 M [315]–[317]. Eliyan et al., [318] studied the effect of bicarbonate concentration (0.02, 0.1, 0.5 and 1 M) on corrosion of API steel and found that the film formation process is more effective with increased bicarbonate concentration. Bicarbonate in small concentrations reduces the dissolution and impedes the passivation, but in higher concentrations, it is a protective agent and makes the passive films grow faster. In this study a 2 g l^{-1} NaCl (0.03M) solution saturated with CO_2 was used as a test solution in order to ensure slow and steady growth of the corrosion layer. An open system (Figure 3-12) was used in order to better simulate real field conditions. Constant purging of the CO_2 to the solution was avoided as bubbles form on steel surface and interface with film formation. It is found that under the experimental condition used in this study solute evaporation was insignificant. According to ASTM standard [314] the recommended minimum ratio of test solution volume to test specimen surface area is 0.20 ml mm^{-2} to avoid any appreciable change in the test solution's corrosiveness. In this study, the ratio of test solution volume to test specimen surface area was 0.58 ml mm^{-2}. Polished coupons (15.8 mm diameter and 4.7 mm thick) were immersed into the solution for 15, 45, 100 and 185 hours. Test specimens were cleaned using distilled water in an ultrasonic bath in order to remove loosely adhering corrosion products. It is important to note that as the objective of this experiment is to characterize the corrosion layer, mechanical cleaning such as scrubbing, scraping and

brushing (which may lead to the removal of adherent corrosion layer) were avoided. Specimens were then dried and weighed, and the average corrosion rate was calculated using Equation 3-3.

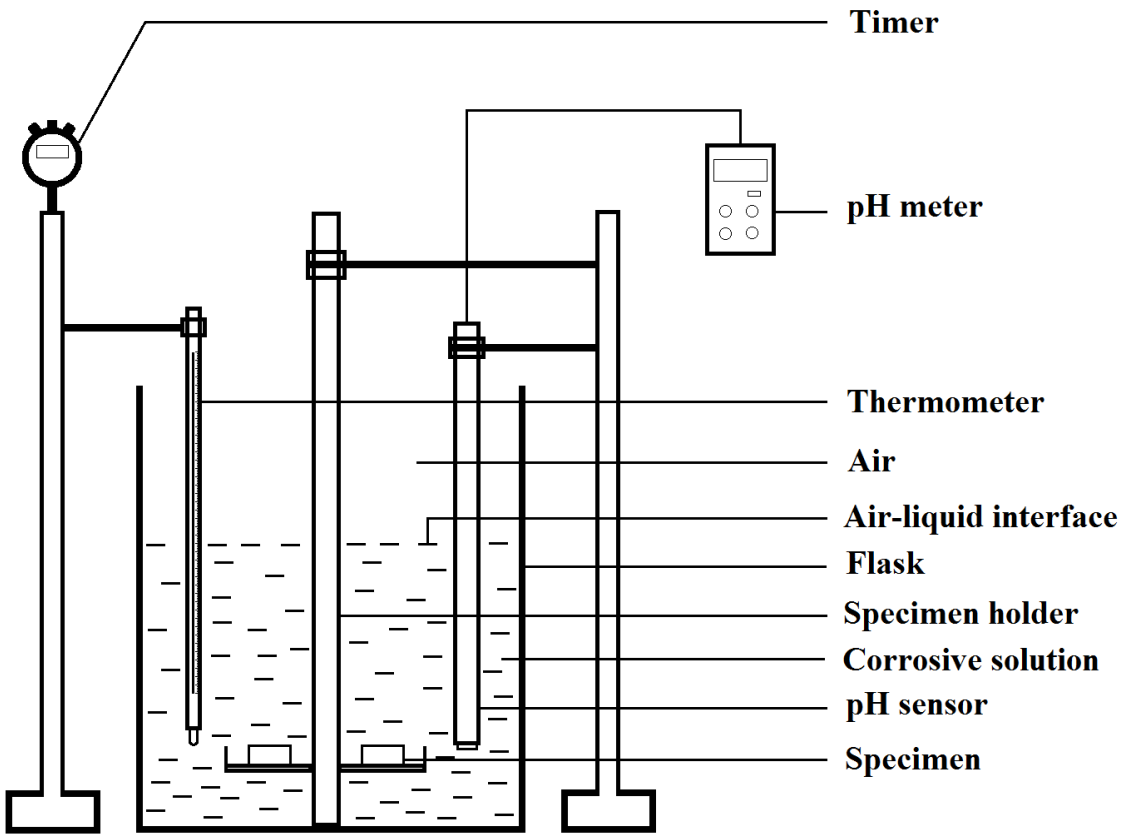

Figure 3-12 Schematic diagram of the immersion corrosion setup.

In this study, immersion tests were performed at ambient temperature and pressure without agitation. Typical field conditions are 500 psi pressure and 70°C temperature. The aim of this research is to establish the fundamentals of pipeline corrosion at ambient conditions. The pH of the solution was monitored at regular intervals, and test conditions were controlled throughout the test in order to ensure the reproducibility of results. Specimens were handled with gloves and tongs (before and after corrosion) to

avoid contamination. Two test specimens were exposed in each test condition. The measured corrosion rate (based on weight loss) of specimens was within ±5%. The test specimens were stored in a sealed container and were kept in a desiccator at an ambient temperature prior for further analysis to avoid any oxidation after corrosion. The operating conditions for immersion corrosion tests are given in Table 3-8.

X-ray photoelectron spectroscopy (XPS) is a semi-quantitative technique for surface chemical analysis. It determines the atomic percentage of the various elements present in a given specimen. This technique coupled with ion sputtering allows analyzing superficial layers and interfaces as well as establishing depth profiles of atomic concentrations within a specimen. XPS analysis was performed on the corrosion layers of specimens after immersion. The samples were mounted on a stainless steel stub using adhesive copper tape. With the sample loaded in the analysis chamber, a base pressure of 2×10^{-10} torr was achieved after approximately 16 hours of pumping. A survey scan was performed covering a wide binding energy range followed by high resolution scans over the following regions of interest: Fe 2p, O 1s and C 1s. Measurement conditions for XPS analysis are given in Table 3-9. Surface charging effects were compensated by referencing the binding energy (BE) to the C 1s line of residual carbon set at 284.8 eV BE [319]. Spectral decomposition assumed mixed Gaussian – Lorenzian curves and was performed using background subtraction and least square fitting.

Table 3-8 Operating conditions for immersion corrosion tests.

Parameter	Operating condition
Test solution	1 liter distilled water + 2 g NaCl saturated with CO_2*
Solution volume	250 ml
Exposed surface area	429.36 mm^2
Solution volume to surface area ratio	0.58 ml mm^{-2}
Test duration	15, 45, 100 and 185 hours
Test temperature	Room temperature ± 3°C
Velocity	Stagnant

*CO_2 was bubbled in the solution prior to the start of the immersion test.

Table 3-9 Measurement conditions for XPS analysis.

Parameter	Operating condition
X–ray source	Al kα (1486.6 eV)
X–ray power	14.7 kV, 26 mA
Pressure	5×10^{-10} – 2×10^{-9} torr (analysis), 6×10^{-8} torr (sputtering)
Pass energy	50 eV (survey), 20 eV (high resolution scans)
Energy step	1 eV (survey), 0.1 eV (high resolution scans)
Analysis spot	600 μm
Sampling depth	3–10 nm
Integration time	1000 ms (survey), 1200 ms (high resolution scans)
Sputtering source	Ar^+ ion
Sputtering time	10 min, 30 min and 150 min

3.2.3 Erosion-Corrosion

Different researchers have used different test facilities to simulate erosion-corrosion of steels in a CO_2 environment with abrasive particles. Shadley et al., [320], [321] constructed a mini loop composed of a diaphragm pump, a test section, a cyclone separator, a sand injector and a sump. A CO_2 saturated test solution was circulated by the pump. Sand was injected into the liquid at the sand injector below the cyclone separator and carried into the test section by the circulating solution. The test cell was connected to a potentiostat with reference and counter electrodes and linear polarization measurements were performed to determine whether and when $FeCO_3$ corrosion product formed. Neville et al., [66], [322]–[325] used an impinging jet apparatus (recirculation rig) coupled with an electrochemical setup in a sealed vessel for erosion-corrosion study. To determine material loss due to pure erosion, the test solution was prepared using tap water and N_2 was bubbled through the solution to reduce oxygen content. During erosion-corrosion, the test solution (NaCl + water) was purged with CO_2 before experiments. Stack et al., [271], [289] constructed an apparatus consisting of a large plastic tank used as a test chamber. The solution was delivered with high pressure through a flex vent. When the solution entered the ejector at high speed, it produced a partial vacuum due to the venturi effect and the slurry underneath the tube was mixed with the flowing solution by means of suction. An electrochemical cell was incorporated into the test rig to enable in-situ electrochemical tests and to control the potential of the specimen. The erosion-corrosion rate was obtained by mass loss techniques while corrosion contribution during the erosion-corrosion process was estimated by integration within the area under the current-time curve. Wood et al., [326], [327] performed erosion-corrosion experiments in a slurry pot erosion tester driven by a motor. The rig assembly was enclosed within a Faraday cage which allows electrochemical measurements. For pure erosion experiments, 0.1 M NaOH was used as the

test solution with the addition of silica sand. Pure corrosion experiments were performed using 3.5 wt% NaCl. Erosion-corrosion experiments were performed using similar corrosive solutions as used in pure corrosion with the addition of silica sand. Xie et al., [328] showed that by increasing frequency of the intermittent erosion-corrosion cycle, it is possible to obtain close results as if erosion and corrosion happened together. This test method provides more stable electrochemical measurements and is employed to mitigate the limitations of the in-situ method [64], [66], including the difficulty of controlling fluctuation in electrochemical data due to bubble formation and turbulence.

In this study the method employed by Xie et al., [328] was adopted. In order to calculate the rate of material loss contributions from erosion, corrosion and their interactions, specimens were subjected to erosion for 10 s and erosion rates were calculated using Equation 3-1. Eroded specimens were then subjected to corrosion for 2.5 hour and the corrosion rate was then calculated from both potentiodynamic polarization (Equation 3-4) and weight loss (Equation 3-3). In the present work, erosion followed by corrosion is termed 'cycle'. Five erosion-corrosion cycles (starting with erosion and finishing with corrosion) were performed, which made a total of 50 s of erosion and 12.5 hr of corrosion. Total erosion component (E_c) and total corrosion component (C_e) are averages of five consecutive erosion and corrosion cycles, respectively. Erosion rate in the absence of corrosion (E_0) and corrosion rate in the absence of erosion (C_0) were calculated from pure erosion for 50 s and pure corrosion for 12.5 hr, respectively. The synergy was then calculated using Equation 2-6, Equation 2-7, Equation 2-8 and Equation 2-9. The synergistic effect of erosion-corrosion in this work refers to the result of the cyclic erosion and corrosion tests.

During erosion-corrosion, entire surface area (A_1) exposed to corrosion, surface area (A_2) exposed only to corrosion and surface area (A_3) exposed to

both erosion-corrosion are 100, 91.34 and 8.66 mm^2, respectively. The following steps were followed in order to calculate the erosion enhanced corrosion current density (I_{corr, A_3}) for API steels. The surface (A_3) of the specimen exposed to erosion and corrosion is calculated using the following equation,

$$A_1 = A_2 + A_3 \qquad \text{Equation 3-5}$$

where, A_1 = entire surface of the specimen exposed to corrosion and A_2 = surface area exposed to corrosion only. The corrosion current density (I_{corr, A_2}) contribution from A_2 surface area is calculated from pure corrosion (potentiodynamic polarization) experiment using the following equation,

$$I_{corr, A_2} = \frac{I_{corr}\ A_2}{A_1} \qquad \text{Equation 3-6}$$

where, I_{corr} is the corrosion current density (μA cm^{-2}) during pure corrosion from the entire surface area (A_1). During erosion-corrosion experiment, I^*_{corr} (corrosion current density during erosion-corrosion) calculated from potentiodynamic data has contributions from both pure corrosion (A_2) and erosion-corrosion (A_3) areas. Therefore, erosion enhanced corrosion current density (I_{corr, A_3}) can be calculated using the following equation,

$$I_{corr, A_3} = I^*_{corr} - I_{corr, A_2} \qquad \text{Equation 3-7}$$

Erosion enhanced corrosion rate is then calculated using Equation 3-4. The operating conditions for pure erosion, pure corrosion and erosion-corrosion experiments are given in Table 3-10, Table 3-11 and Table 3-12, respectively.

Table 3-10 Operating conditions for pure erosion.

Parameter	Operating condition
Nozzle diameter	2.3 mm
Eroded surface area	8.66 mm^2
Standoff distance	3 mm
Test gas	Dry compressed air
Test duration	50 s
Test temperature	Room temperature ± 3°C
Angle of incidence	90°
Particle velocity	36, 47, 63 and 81 m s^{-1}

Table 3-11 Operating conditions for pure corrosion.

Parameter	Operating condition
Test solution	1 liter distilled water + 2 g NaCl
Corroded surface area	100 mm^2
Test duration	12.5 hr
Test temperature	Room temperature ± 3°C
Sweep rate	0.166 mV s^{-1}
Poteniodynamic sweep	From -250 to 250 mV (vs OCP)
Bulk pH	4.3
Pressure	100 kPa CO_2
Velocity	Stagnant

Table 3-12 Operating conditions for erosion-corrosion.

Erosion cycle		Corrosion cycle	
Nozzle diameter	2.3 mm	Test solution	2 g l^{-1} NaCl
Standoff distance	3 mm	Sweep rate	0.166 mV s^{-1}
Test gas	Dry compressed air	Poteniodynamic sweep	-250 to 250 mV (vs OCP)
Test duration	10 s for each cycle	Test duration	2.5 hr for each cycle
Number of cycles	5	Number of cycles	5
Angle of incidence	90°	Pressure	100 kPa CO_2
Particle velocity	36, 47, 63 and 81 m s^{-1}	Velocity	Stagnant

Chapter 4

Results and Discussion

In this chapter an attempt is made to untangle some of the complexities associated with erosion, corrosion and erosion-corrosion damage of pipeline steels.

4.1 Erosion

This section discusses the erosion behavior of steels. Operative erosion mechanisms are identified and an attempt is made to correlate the erosion behavior of steels to their microstructure. Empirical erosion mechanism maps are constructed and discussed at the end of this section.

4.1.1 Erosion Behavior of Steels

Weight loss of all steel specimens was measured after exposure to an abrasive stream for 10, 180, 420 and 600 s at different angles of incidence. A representative plot of how weight loss increases with increasing test duration is shown in Figure 4-1 for AISI 1018 steel at 47 m s^{-1} particle velocity. As evident from Figure 4-1, no significant change in slope is observed, which may indicate that no wear transition has taken place throughout the test duration. Normally, a transition in wear mechanism is associated with a change in wear rate, which would be represented by a change in the slope of

weight loss vs time. It is clearly seen that the weight loss of the steel increases with decreasing impact angle. Depending upon the angles of incidence, different erosion mechanisms may operate, resulting in the measured weight loss. Dominant erosion mechanisms will be discussed in a later section.

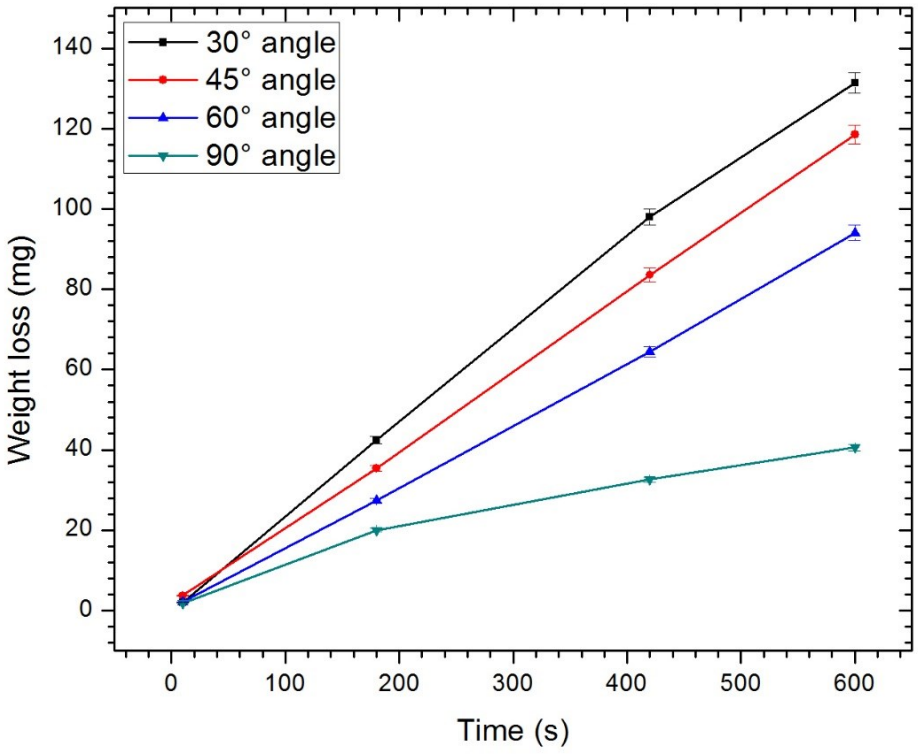

Figure 4-1 **Weight loss vs time for AISI 1018 steel at 47 m s^{-1} particle velocity as a function of impact angle.**

4.1.1.1 Profilometry Analysis

Profilometry scans were performed on individual specimens after erosion at 30° angle of incidence for different time intervals. Scanned profiles were then stitched together for comparison (aspect ratio of 1:1:2). Figure 4-2 shows the optical profilometry analysis for AISI 1018 steel as a representative example.

Particle impact direction is indicated by an arrow. Abrasive particles impacted the surface along the indicated direction at a 30° angle to the surface. 2D depth profiles (Figure 4-2 (b)) were taken at the maximum depths of the 3D erosion scars (Figure 4-2 (a)). As shown in the figure, the erosion scar maximum depth of attack varied from 0.06 ± 0.03 mm to 1.2 ± 0.03 mm for 10 and 600 s test durations, respectively, at 63 m s^{-1} particle velocity. The maximum depth of attack (Z axis) is the distance from the deepest point in the damaged zone to the unaffected surface of the specimen.

The localized plastic deformation increased surface roughness, which may have changed the localized impact angle with time. However, the mean surface roughness of the eroded AISI 1018 specimens was around 9.1 ± 2 μm and the average abrasive particle size used in this study was around 57 ± 3 μm. Hence, localized surface roughness didn't affect the global impact angle and is not expected to have significant influence on the total erosion rate. Figure 4-2 (a) is presented with an aspect ratio of 1:1:2 for enhanced visualization, *i.e.*, the z-axes (depth direction) is doubled with respect to the x and y directions. If the scans were plotted with 1:1:1 scale it would be clear that the crater depth is shallow compared to the size of the crater in the x and y directions. Based on this argument, the crater was shallow enough (the sidewall slope of the crater is low) with respect to the abrasive stream even for the deepest crater. That is, the local impact angle of the particles reasonably close to the incident angle of the particle jet.

At 30° impact angle, the shape of the projected area of the erosion scar was elliptical (Figure 4-2 (a)) due to the divergence of the particle stream. As the impact angle increased, the shape of the erosion scar became circular. The sizes of the erosion scar along the longitudinal and lateral direction (at different impact angles and 63 m s^{-1} particle velocity) are given in Table 4-1.

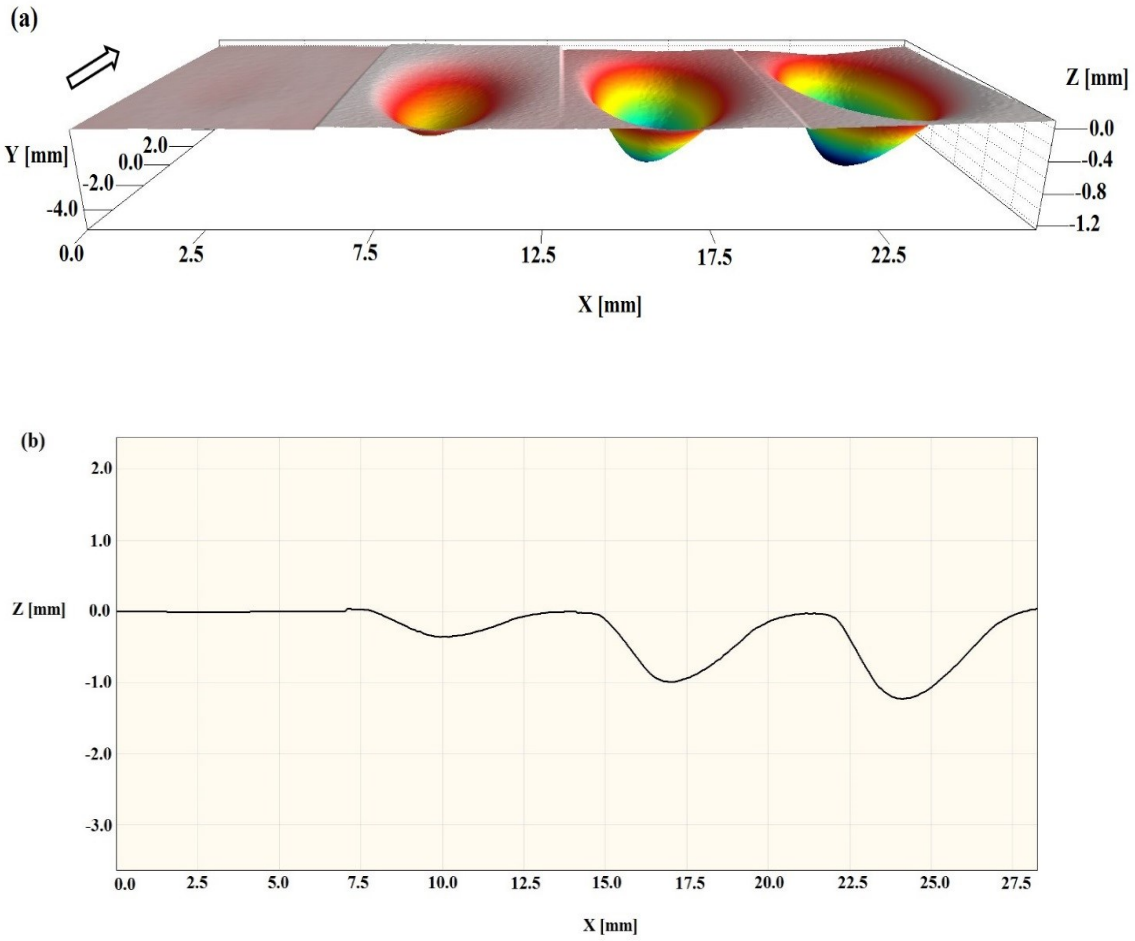

Figure 4-2 Erosion scar of AISI 1018 at 30° angle of incidence for different time intervals (from left to right, 10, 180, 420 and 600 s) and 63 m s^{-1} velocity (a) profilometry scan (aspect ratio, 1:1:2) and (b) profile depth comparison (aspect ratio, 1:2).

Table 4-1 Relative comparison of the erosion scar length at different impact angles.

Impact angle	Longitudinal direction (mm)	Lateral direction (mm)
30° angle	10.2 ± 0.5	5.2 ± 0.5
45° angle	6.9 ± 0.5	5.2 ± 0.5
60° angle	5.8 ± 0.5	5.2 ± 0.5
90° angle	5.2 ± 0.5	5.2 ± 0.5

4.1.1.2 Effect of Particle Velocity

Erosion rates (mg s^{-1}) of the steel specimens were measured from the slope of the weight loss vs time plots. Normalized erosion rates were calculated by dividing erosion rate (mg s^{-1}) by the abrasive particle flow rate (mg s^{-1}) using Equation 3-2. A representative plot of the normalized erosion rate vs particle velocity for API X42 is shown in Figure 4-3. Normalized erosion rate as a function of particle velocity plots for AISI 1018, AISI 1080, API X70 and API X100 are included in the appendices.

The normalized erosion rate of API X42 steel increases with increasing particle velocity as shown in Figure 4-3. As expected, higher particle velocity led to higher material removal from the surface in agreement with other erosion studies [279], [329], [330]. This is because of the fact that higher particle velocity is associated with higher kinetic energy, which leads to more material removal. It is interesting to note that at low velocity, the effect of the impact angle is less significant than at high velocity. The effect of impact angle on erosion rate gradually increases with particle velocity. It is believed that when the particle velocity is low, hence, low kinetic energy, only a small fraction of the abrasive particles have high enough velocity and mass to induce plastic deformation on the steel surface. The majority of particles have low energy, below a threshold value, which only results in elastic deformation of the steel. As the velocity increases more particles attain the required critical energy to result in deformation and material removal. That is, at low particle velocity, most of the impact is elastic and doesn't contribute to the measured erosion rate. This makes erosion almost independent of the impact angle. The dependence of erosion on the impact angle becomes evident at high particle velocity. Moreover, erosion is higher at low angles as it is believed that the energy required to remove material by cutting and ploughing mechanism (which are more dominant at low angles) is lower than

that at high angles. At high angles the steel surface deforms significantly before any material removal takes place.

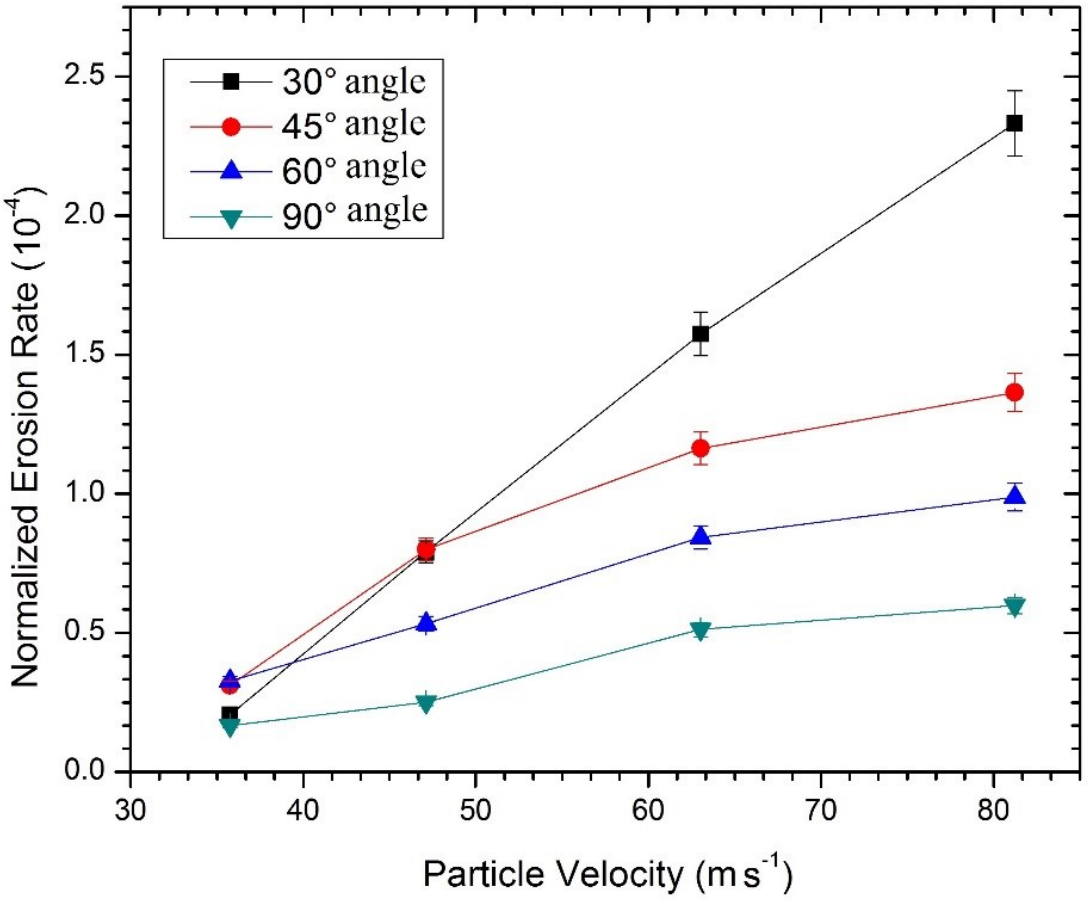

Figure 4-3 **Normalized erosion rate as a function of particle velocity for API X42 steel.**

4.1.1.3 Effect of Impact Angle

The normalized erosion rate of API X42 steel drops with increasing impact angle as shown in Figure 4-4. Several phenomena are responsible for the higher erosion rate at the low impact angle. First, abrasive particles come in contact with more surface area as compared to high incidence angle. At 30° impact angle, the shape of the projected area of the erosion scar is elliptical (Figure 4-2) due to high divergence of the particle stream. But for 90° impact angle the shape of the projected area of the scar is circular as shown in

Figure 4-5 (a). Figure 4-5 (b) compares the erosion scar (at 81 m s^{-1} and 10 s) profile for 30° and 90° impact angles. Erosion scar volume was measured and it is found that the scar volume for 30° and 90° impact angles are 1.02 ± 0.05 mm^3 and 0.54 ± 0.05 mm^3, respectively. Second, at low impact angle (30°) abrasive particles strike and reflect without affecting the forthcoming particle stream. On the other hand, at 90° impact angle, abrasive particles strike and reflect in the same direction inhibiting the motion of the approaching particle stream. Third, at high impact angle, an extensive amount of Al_2O_3 particles are embedded in the surface. These embedded particles contribute to some weight increase and slow down the erosion rate by protecting the eroded surface. Fourth, at low impact angle, the metal is removed predominantly by cutting and ploughing. While at high angle, the steel is plastically deformed and material is squeezed to the sides of the erosion scar without being totally removed.

Furthermore, in order to evaluate the effect of impact angle on velocity exponent *'n'*, normalized erosion data in Figure 4-3 was curve fit using nonlinear least square method. It is found that for 30°, 45°, 60° and 90° impact angles, the values of *'n'* are 2.1, 1.3, 1.2 and 1.1, respectively. A velocity exponent *'n'* having a value less than 2 has also been observed in previous studies [26], [331]. Here, the velocity exponent *'n'* decreases with increase in impact angle. This might be attributed to the fact that (under the high particle feed rate used in this study) with increase in impact angle more abrasive particles embed in the surface and act as a barrier for further erosion. SEM observations revel that, with an increase in impact angle from 30° to 90° the amount of embedded Al_2O_3 particles are significantly increased. These embedded particles reduce the specific erosion rate resulting in lower velocity exponent at higher impact angle. It can be concluded that, contrary to accepted belief for low particle feed rate, the *'n'* value is dependent on the erosion mechanism(s) and the eroded surface evolution

during the erosion process. This result is not in agreement with a previous study [330] that suggested that although erosion rate depends on erosion mechanisms, the velocity exponent *'n'* is independent of erosion mechanisms and only depends on velocity and particle feed rate. This discrepancy can be explained in terms of the particle feed rate used in the two studies. It could be argued that at high particle feed rates such the one employed in this study, the erosion mechanism plays a more significant role in determining the *'n'* value.

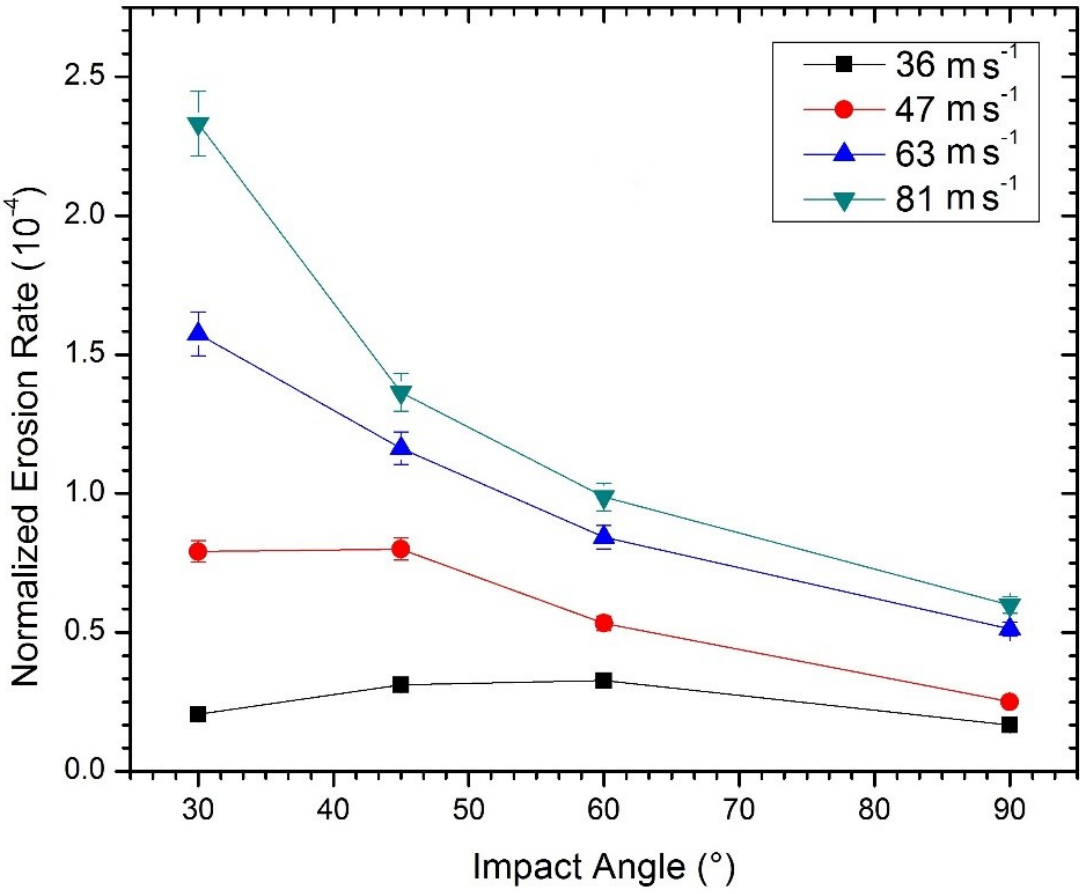

Figure 4-4 **Normalized erosion rate as a function of impact angle for API X42 steel.**

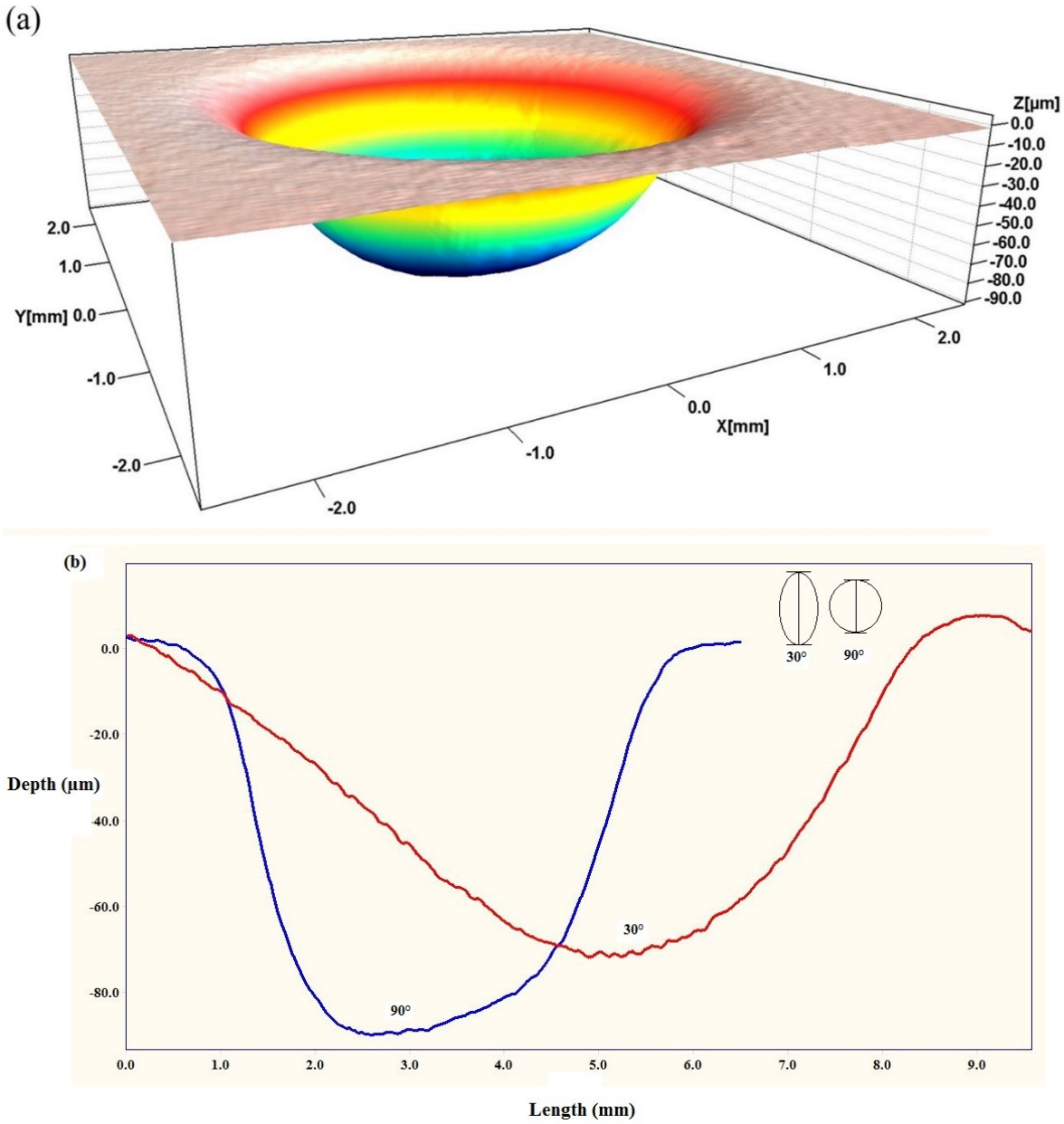

Figure 4-5 (a) Erosion scar topography for API X42 at 90° angle of incidence and 81 m s^{-1} particle velocity (aspect ratio, 1:1:50) and (b) erosion scar profile comparison for 30° and 90° angle of incidence after 10 s test duration and 81 m s^{-1} particle velocity measured along the line shown in the insert (aspect ratio, 1:50).

4.1.1.4 Normalized Erosion Rate as a Function of Impact Angle and Particle Velocity

Representative erosion data as a function of particle velocity and impact angle for API X42 steel is shown in Figure 4-6. It is evident from the erosion rate surface that the normalized erosion rate exhibits a non-linear relationship with both impact angle and particle velocity. Normalized erosion rates presented in a three dimensional space provide critical impact angle and threshold velocity data. For example, in the case of API X42 steel, a transition in erosion rate (Figure 4-6), was observed when the particle velocity was above a threshold of 47 m s^{-1}. On the other hand, critical impact angle is a function of particle velocity and shifts from low to high impact angle with increasing particle velocity at a normalized erosion rate of about 0.5×10^{-4}, where the transition in normalized erosion rate is observed. Other investigators [332]–[335] have also shown similar transitions in erosion behavior. Normalized erosion rate as a function of particle velocity and impact angle for AISI 1018, AISI 1080, API X70 and API X100 are included in the appendices (Figure B-7, Figure B-8, Figure B-9 and Figure B-10, respectively).

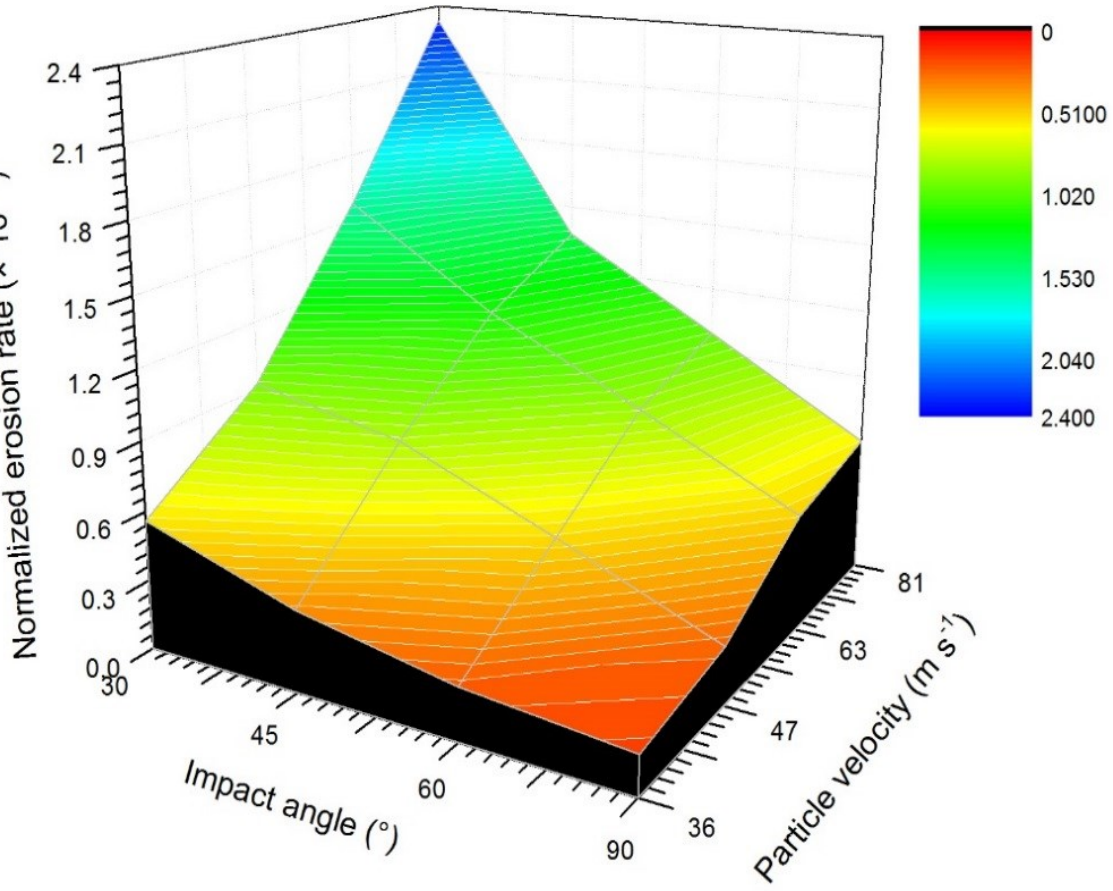

Figure 4-6 Normalized erosion rate as a function of impact angle and particle velocity for API X42 steel.

4.1.2 Erosion Mechanisms

Erosion is a complex time dependent phenomena. Different erosion mechanisms operate simultaneously and interact with one another, which makes the identification of these mechanisms a challenging task. The measured erosion rate is determined by the relative contributions of the different mechanisms. SEM micrographs were taken at the center of the erosion scar (heavily damaged region) and at the less damaged regions (on the periphery of the erosion scar) where the damage caused by individual particle impact could be seen. It is important to note that erosion mechanisms are a function of the impingement angle and velocity of the impacting particles. Steels in this study show similar erosion mechanisms. However, the extent of metal loss and conditions (contact angle and particle velocity) under which these mechanism operate are different as will be discussed in the erosion mechanism maps section below. In this section, erosion mechanisms are divided based on particle impact angle (low (30°), intermediate (45°-60°) and high (90°)) as discussed next.

4.1.2.1 Low Impact Angle

At low impact angle (30°) and low particle velocity (36 m s^{-1}), Al_2O_3 particles strike the surface and form dimples by locally micro-forging the surface (Figure 4-7 (a)). Under these conditions, Al_2O_3 particles are observed to embed into the steel surface (Figure 4-7 (b)), this has also been observed in earlier studies [279], [310]. However, ploughing by the abrasive particles, which has also been confirmed by others [68], [99], [329], [336], seems to be the dominant erosion mechanism under low impact angle and low particle velocity (Figure 4-7 (c)). Under these conditions, the vertical component of the kinetic energy ($KE\ sin\alpha$) of the impinging particles is consumed to penetrate the surface, while the horizontal component ($KE\ cos\alpha$) is used to plough the specimen surface as the abrasive particle slides on it; where *'α'* is the particle

angle of impact (between the particle direction of motion and the specimen surface). Figure 4-7 (c) shows deep long grooves as evidence of ploughing by the abrasive particles. As the particles slide on the surface, they squeeze the metal ahead and to the sides to form ridges. Subsequent attack by incoming particles cause the ridges to flatten, fracture and from erosion debris. Metal removal under low impact angle and high velocity (30°, 81 m s^{-1}) condition is controlled by 'low angle metal cutting' mechanism. Here, instead of embedding itself deeply into the surface, abrasive particles attain the required critical energy to cut the metal in the form of small metallic chips (3 – 5 μm) as shown in Figure 4-7 (d).

Under condition of low impact angle and high particle velocity, material removal also occurs by fracture of ridges around dimples, particularly, at the later stages of the erosion process. Here, material removal is a result of repeated impact by the energetic abrasive particles of the work hardened ridges, leading to brittle fracture of these ridges, as seen in Figure 4-8. Figure 4-8 is the cross-section of an erosion scar revealing stages of the deformed layer removal in the course of the erosion process (at low impact angle). The figures (Figure 4-8 (a), (b)) show the deformed surface layer and the undeformed base material. A number of other investigators have also reported the formation of a work hardened layer during erosion [122], [337], [338]. In this study the removal of this work hardened layer at different impact angles is confirmed from SEM observations. The direction of the impinging particle stream is shown by an arrow. Crack initiation takes place at the edge of the ridge as shown in Figure 4-8 (c). Upon further particle impact, cracks propagate through the deformed layer followed by complete removal of large fragments (Figure 4-8 (d)). A Schematic diagram illustrating metal removal by this mechanism is shown in Figure 4-9 (a). Removal of ridges at high angle in Figure 4-9 (b) will be discussed below.

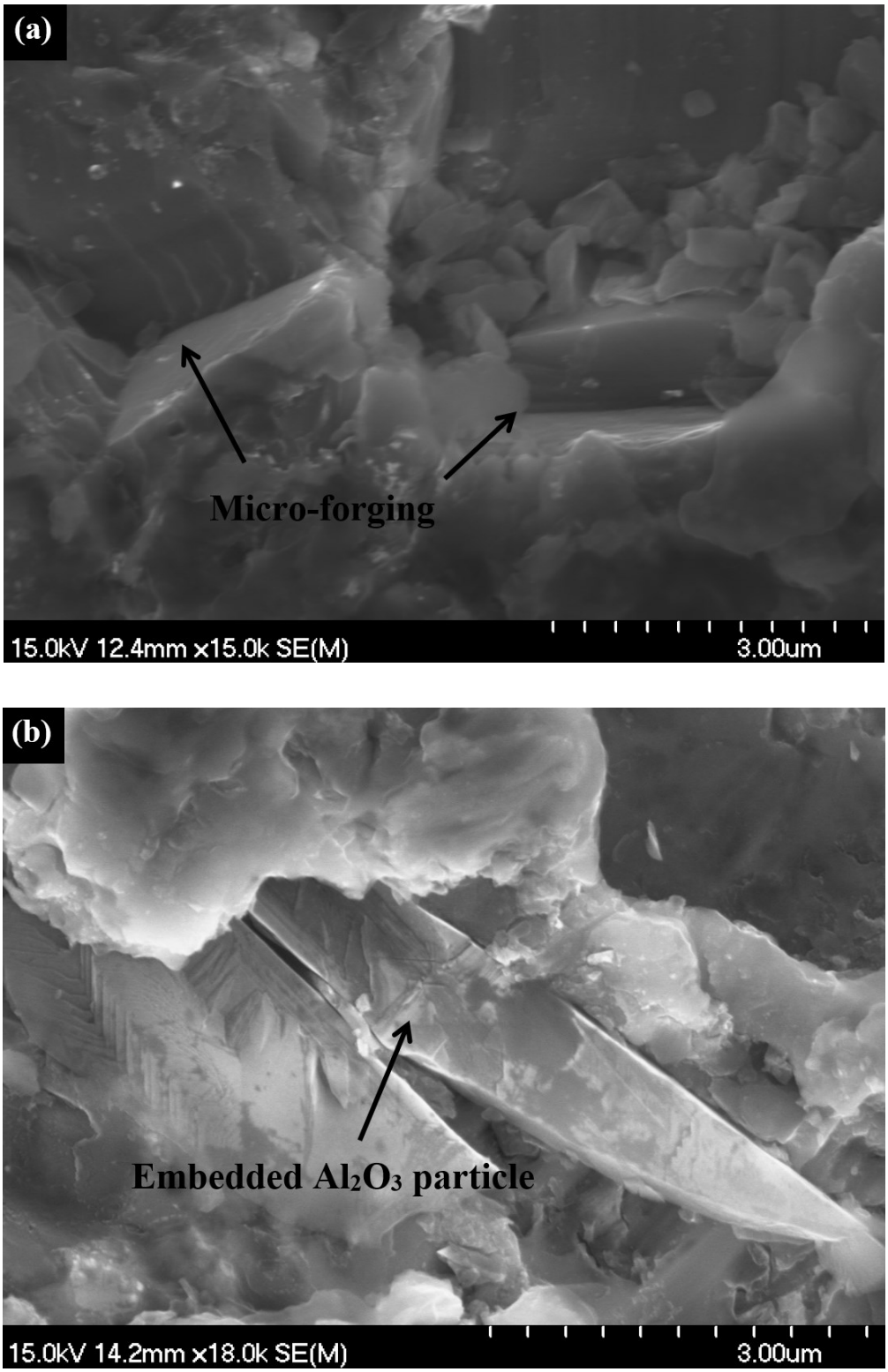

Figure 4-7 SEM micrograph of steel specimen after erosion at 30° impact angle (a) micro-forging of the surface (API X42, 36 m s^{-1}) and (b) embedded Al_2O_3 particle (API X42, 36 m s^{-1}).

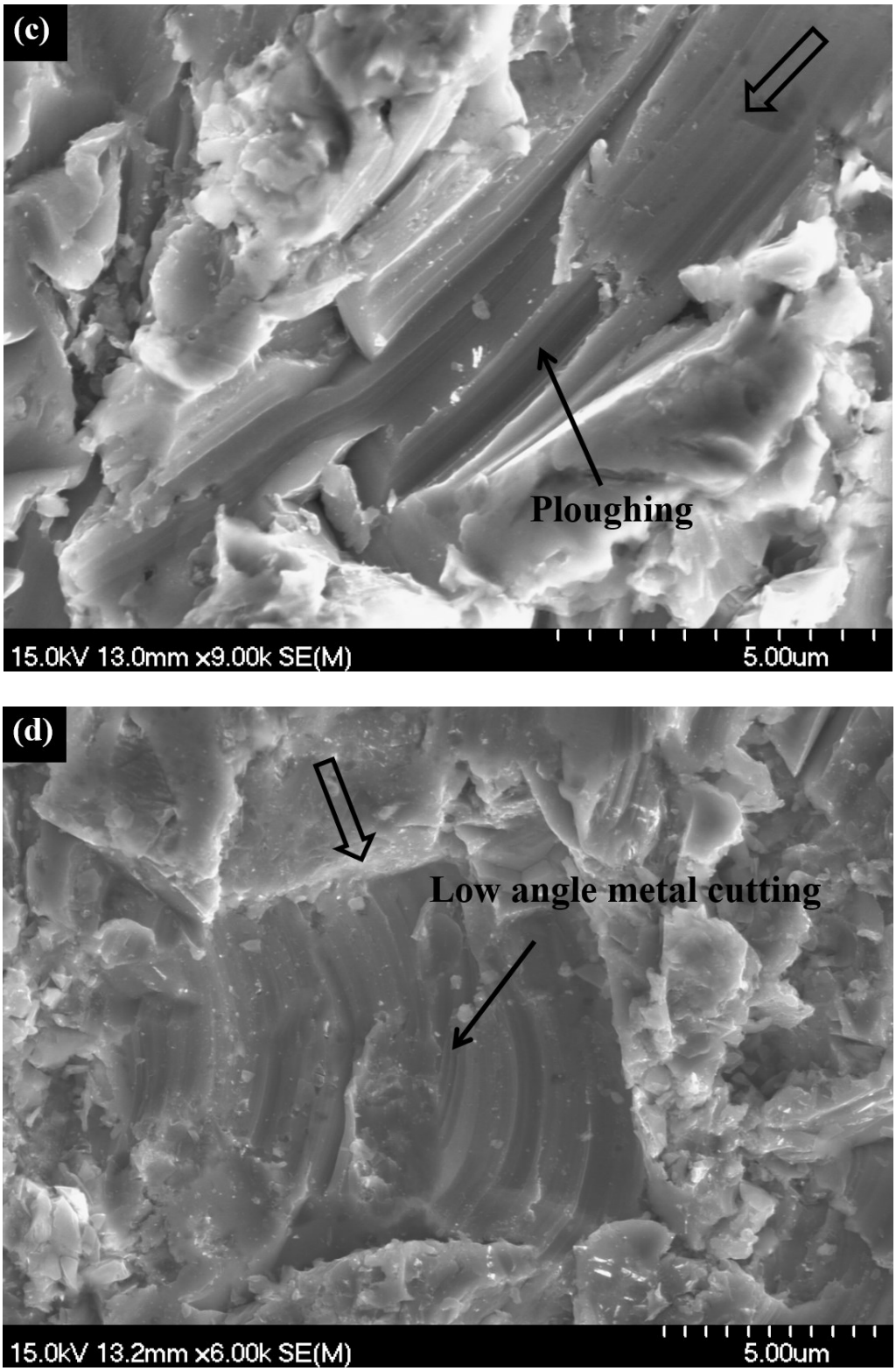

Figure 4-7 SEM micrograph of steel specimen after erosion at 30° impact angle (c) ploughing (AISI 1018, 36 m s^{-1}) and (d) low angle metal cutting (API X70, 81 m s^{-1}).

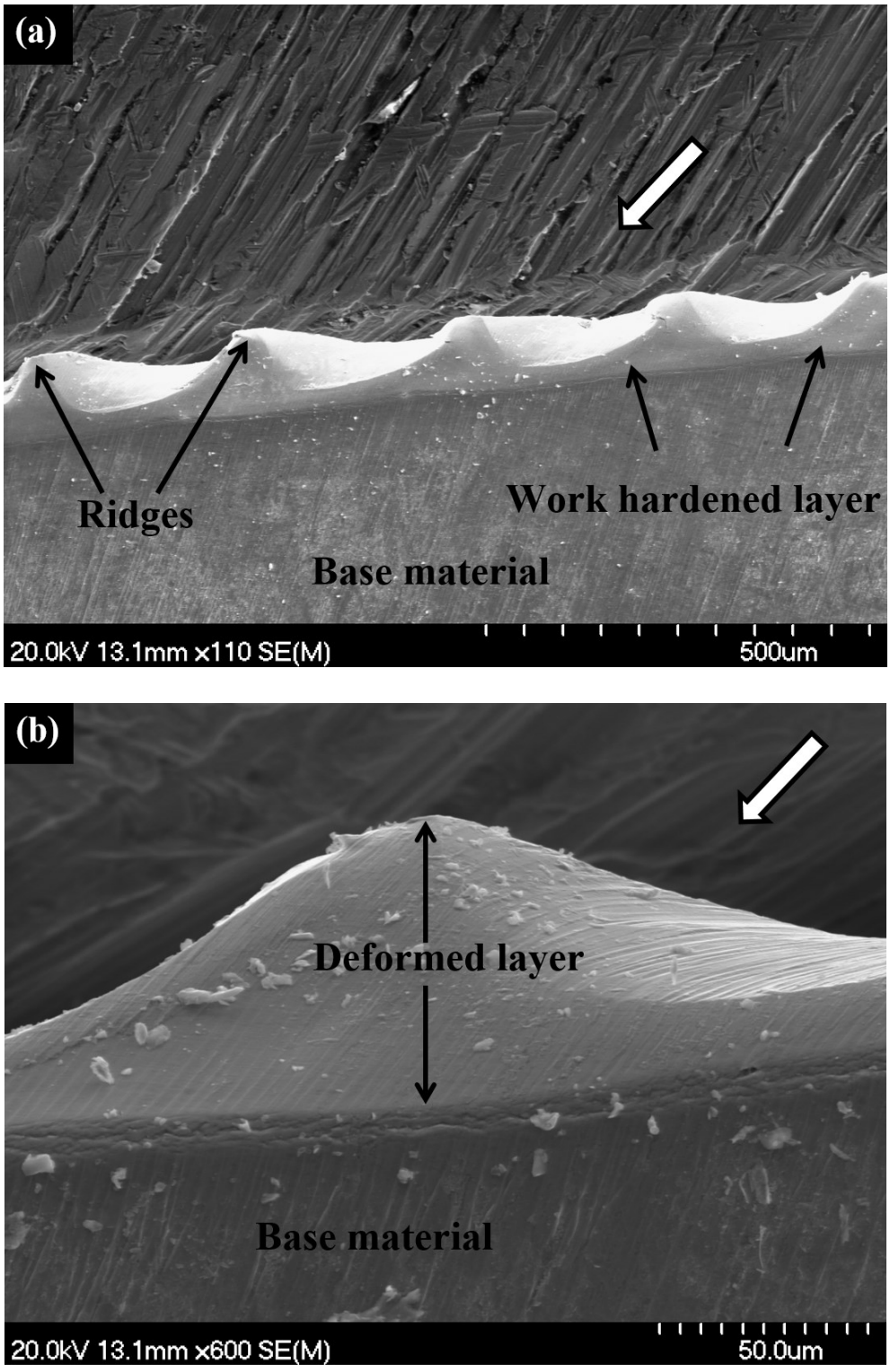

Figure 4-8 SEM micrograph of the cross sectioned layer of erosion scar (API X42). Particle flow direction is indicated by an arrow. (a) a series of ridges due to the formation of dimples on the eroded surface and (b) deformed layer and base material.

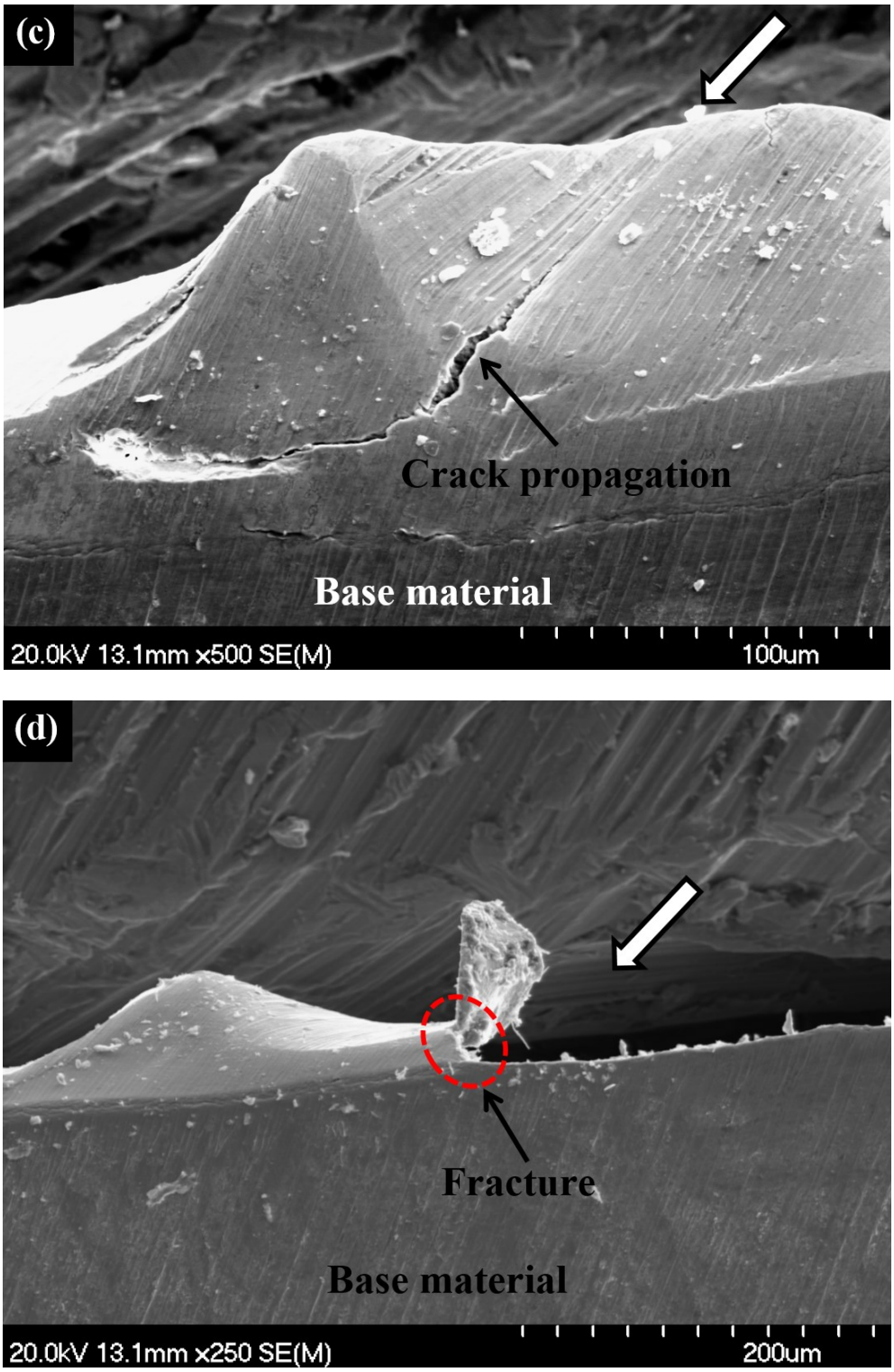

Figure 4-8 SEM micrograph of the cross sectioned layer of erosion scar (API X42). Particle flow direction is indicated by an arrow. (c) sub-surface crack propagation and (d) fracture of deformed layer.

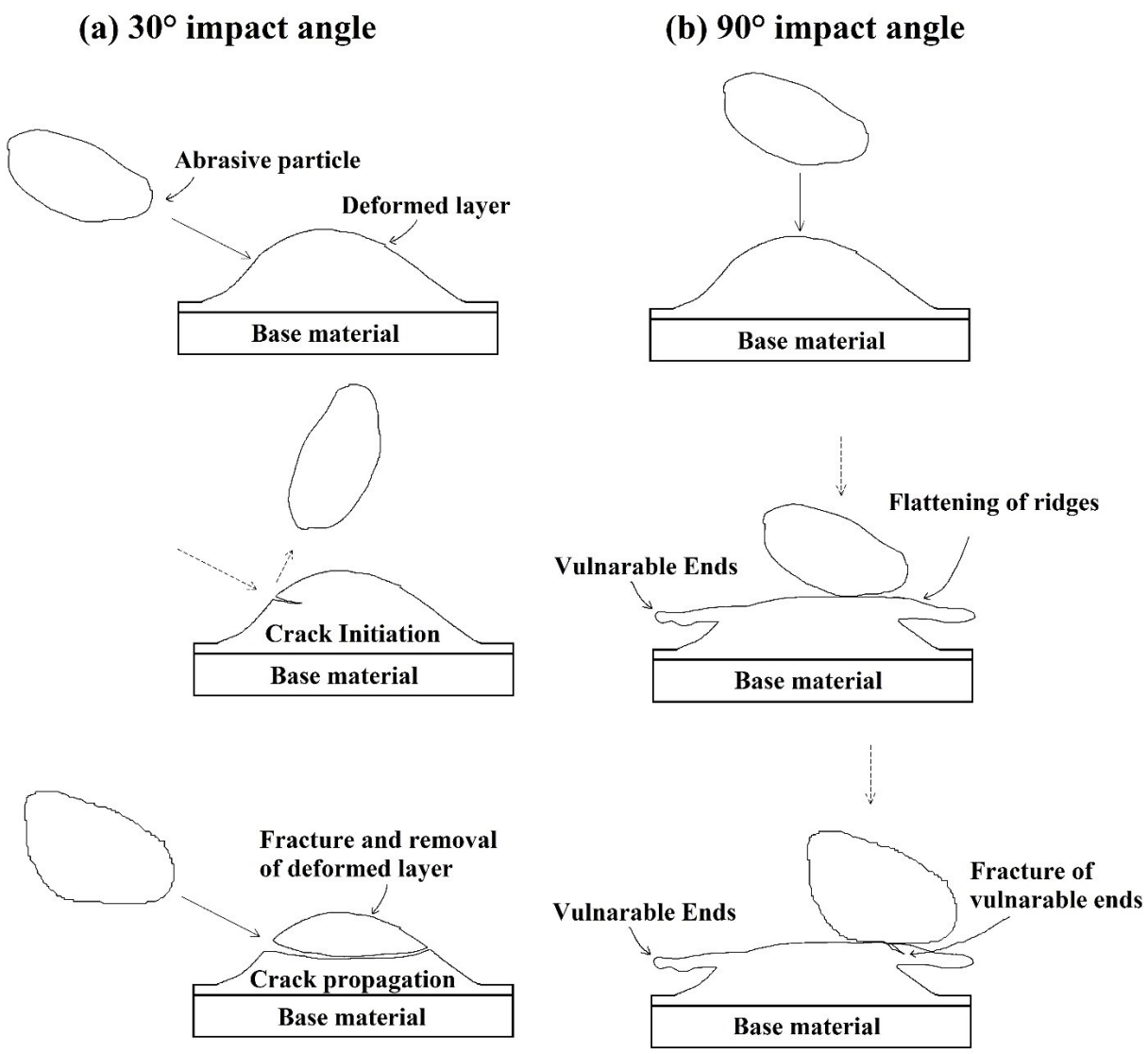

Figure 4-9 Schematic diagram illustrates stages of metal removal, (a) at 30° impact angle and (b) at 90° impact angle.

4.1.2.2 Intermediate Impact Angle

At intermediate impact angle (45°), with increasing particle velocity (63-81 m s^{-1}), abrasive particles cut the surface to the end of the cutting path but the cut chip remain attached to the surface and forms a ridge (*i.e.*, the chip is not completely cut and removed from the surface) (Figure 4-10 (a)). The chip is then removed due to subsequent impact. This mode of material removal is designated as cutting mode II [339]. It is important to distinguish cutting mode II mechanism from ploughing. In ploughing, the material is extruded (by plastic deformation) ahead of an abrasive particle, but in cutting mode II the metal is cut and forms a chip that remains attached at the end of the cutting scar. Furthermore, in ploughing the material is normally squeezed to the sides of the groove and form ridges on both sides, while in cutting mode II the material is accumulated at the end of the cutting scar. Also, the scar in cutting mode II is shorter and deeper than in ploughing.

At 60° angle of incidence, with increasing particle velocity (47-63 m s^{-1}), chips (about 10 μm) are cut from the surface by the abrasive particles without dragging the material ahead (Figure 4-10 (b)). The abrasive particles do not form significant ridges at the end of the cutting path as in cutting mode II, but they penetrate deeper into the metal surface and form sharp edges that are vulnerable to subsequent particles impact. This mode of erosion seems to be analogous to Type I cutting proposed by Hutchings [339]. This mode of deformation is termed as cutting mode I.

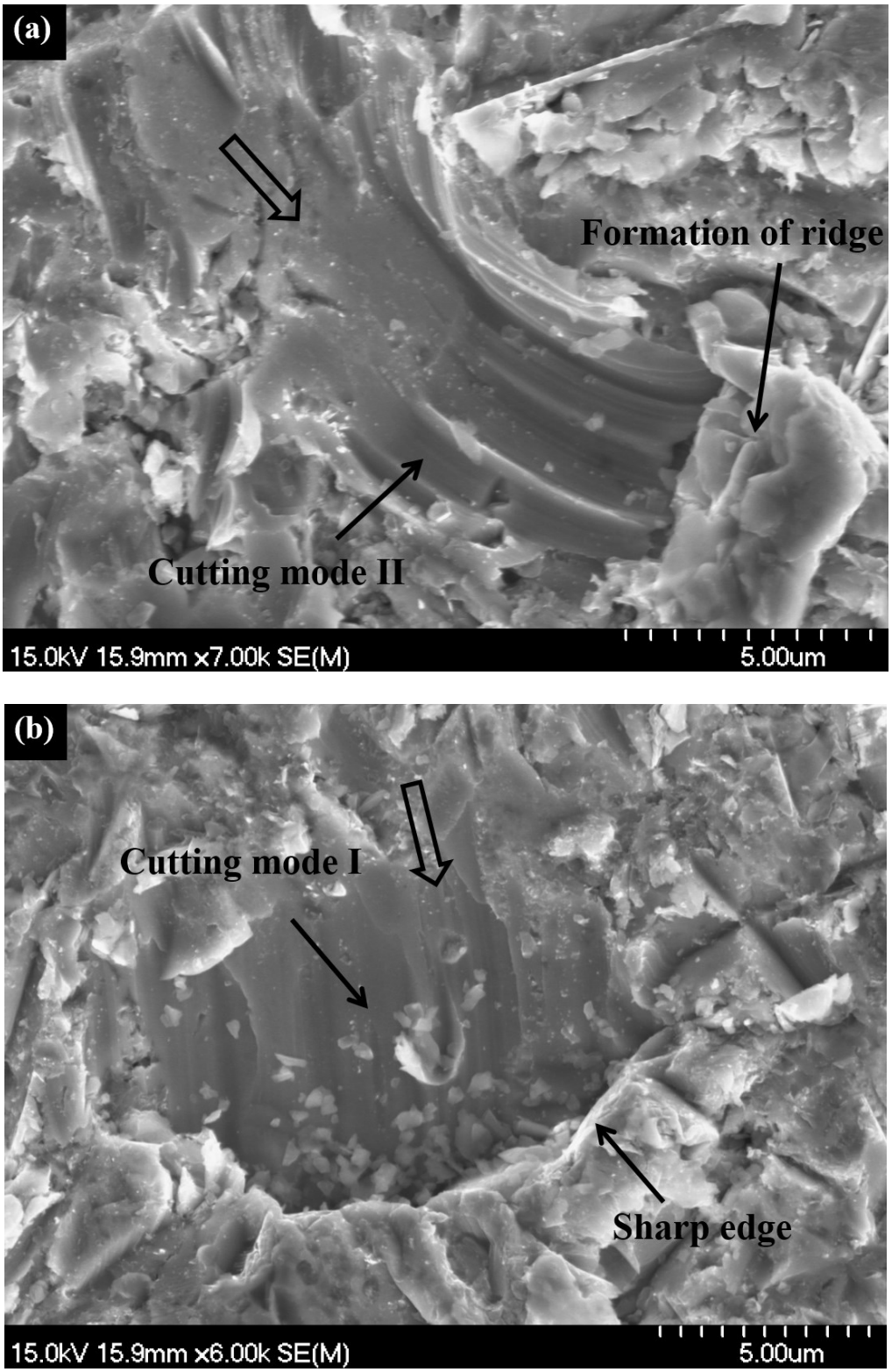

Figure 4-10 SEM micrograph of API X70 steel, (a) cutting mode II (45°, 81 m s^{-1}) and (b) cutting mode I (60°, 63 m s^{-1}).

4.1.2.3 High Impact Angle

At high impact angle (90°) and low particle velocity (36 m s^{-1}), most of the abrasive particles kinetic energy is used to penetrate the surface resulting in dimple formation and penetration by Al_2O_3 particles (as shown in Figure 4-11 (a)). Metal is squeezed out of the dimples to form ridges which are then removed by fracture due to plastic deformation and flattening of ridges around dimples. A schematic diagram illustrating stages of metal removal by this mechanism is given in Figure 4-9 (b), which illustrate the removal of ridges due to plastic deformation and fracture caused by the abrasive particle impact. This process of metal removal is observed at low particle velocity and more so at high velocity. Under condition of high impact angle and low particle velocity, material removal also occurs by delamination. Figure 4-11 (b) shows the cross-section of the erosion scar. Repeated impact by the abrasive particles generate high shear stresses in the sub-surface region which cause initiation and propagation of sub-surface cracks. The propagation of subsurface cracks parallel to and eventually up to the surface results in the formation of flake-like debris. Material removal due to delamination was also observed in earlier studies [110], [121].

At high particle velocity (81 m s^{-1}), embedded Al_2O_3 undergone repeated impact by the incoming particle stream which leads to particle fracture (Figure 4-11 (c)). Fractured particles are then removed from the surface leaving behind vulnerable lips (Figure 4-11 (d)). Material removal typically involves the flattening of a protrusion (lips) and fracture upon subsequent impacts. The higher the impact velocity, the deeper the abrasive particles penetrate into the surface and more material is removed. This metal removal process seems to dominate under conditions of high particle velocity and high impact angle. In addition, secondary metal cutting is also observed at high impact angle and high velocity (Figure 4-11 (e)) and contributes to metal loss. In 'secondary metal cutting' Al_2O_3 particles strike and deflected by the

previously embedded particles and erode a small portion of metal (2 – 3 μm). As illustrated in the Figure 4-11 (e), an abrasive particle deflects from an embedded Al_2O_3 particle and erodes a small portion of metal from the adjacent area where there is no embedded particle.

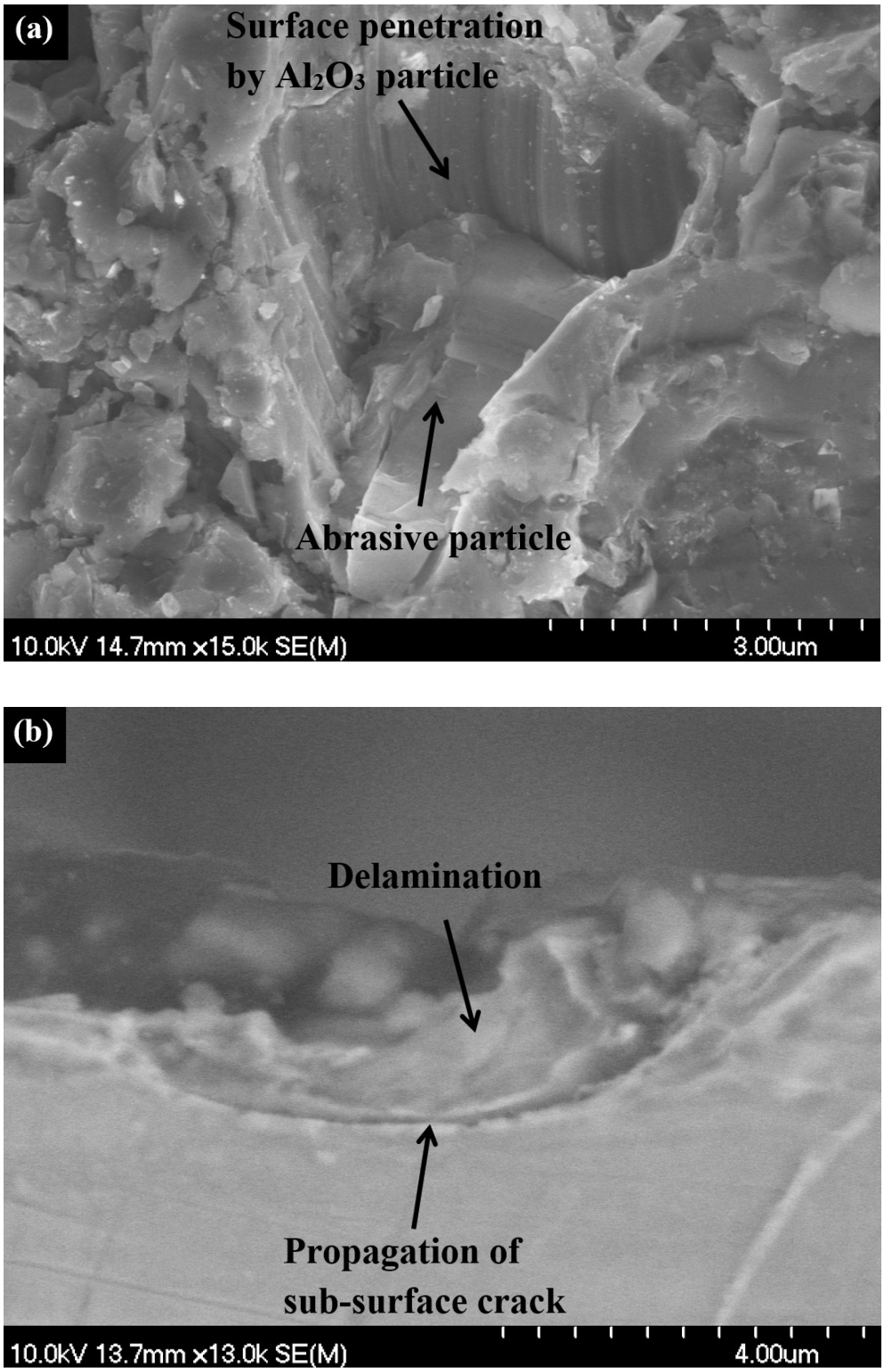

Figure 4-11 SEM micrograph of AISI 1018 steel, (a) embedded particle (90°, 36 m s^{-1}) and (b) cross-section of erosion scar shows the propagation of sub-surface crack (90°, 36 m s^{-1}).

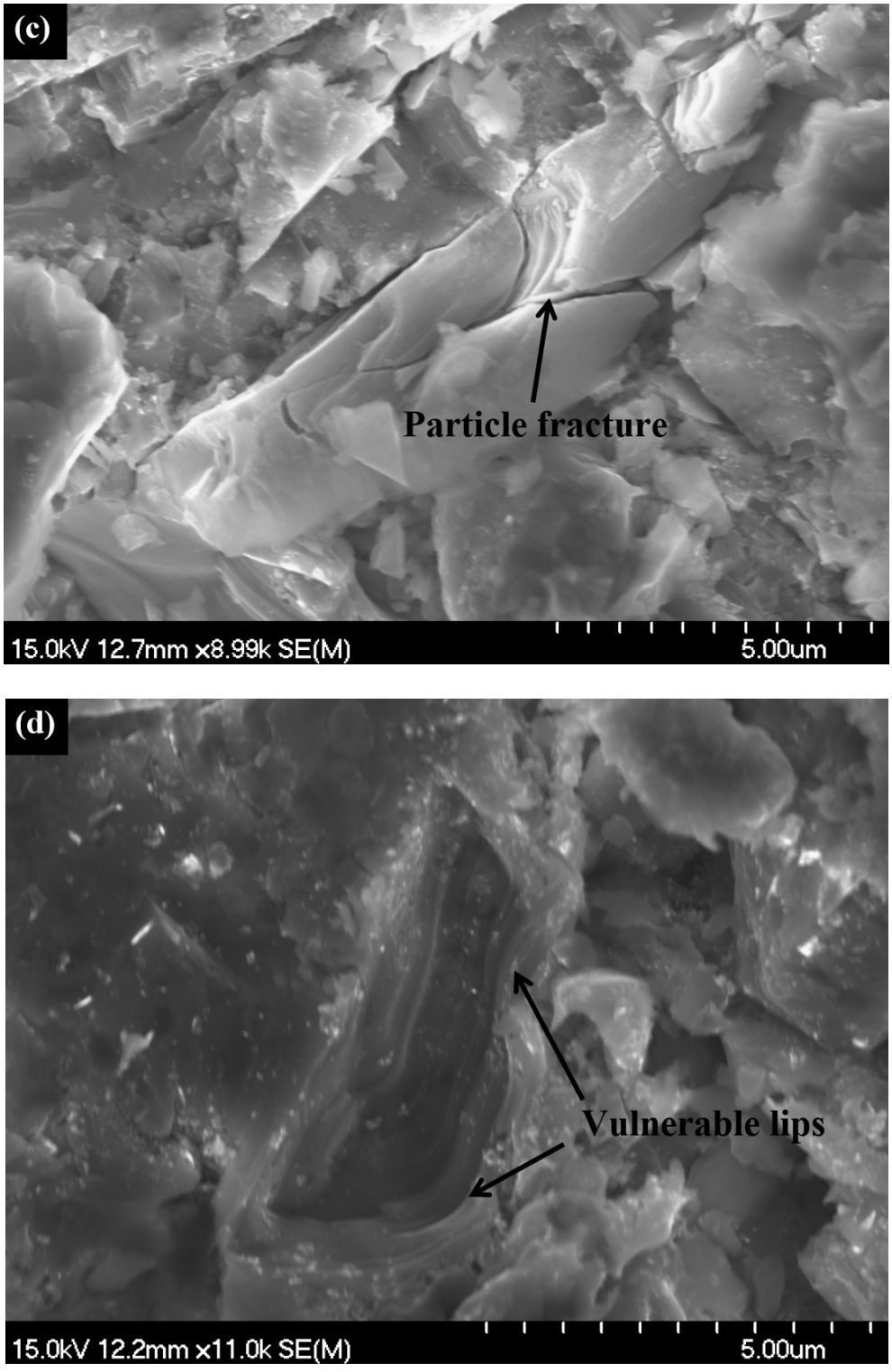

Figure 4-11 SEM micrograph of API X42, (c) fracture of embedded Al_2O_3 particle (90°, 81 m s^{-1}) and (d) formation of vulnerable lips (90°, 81 m s^{-1}).

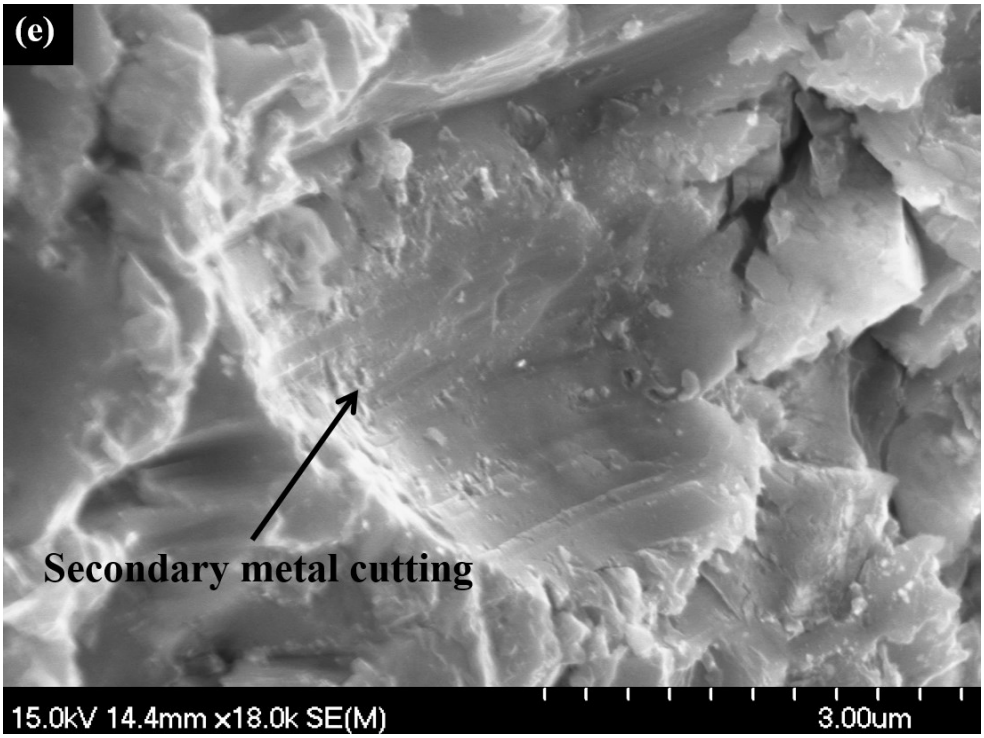

Figure 4-11 SEM micrograph of API X42, (e) secondary metal cutting due to deflection (90°, 81 m s^{-1}).

It is important to note that, the identification of low angle metal cutting, cutting mode II, cutting mode I and secondary metal cutting is a challenging task. Not only is the appearance, but also the test condition is required to identify them correctly. Schematic diagrams illustrating low angle metal cutting, cutting mode II, cutting mode I and secondary metal cutting are shown in Figure 4-12. Low angle metal cutting is usually observed at low impact angle (30°) and high velocity (81 m s^{-1}), where the abrasive particle completely cut a small portion of material (Figure 4-12 (a)). Low angle metal cutting does not form a ridge at the end of the eroded scar. Abrasive particles have the required critical energy to cut the metal in the form of small metallic chips. However, cutting mode II usually forms ridges at the end of the scar. In cutting mode II (usually occurs at 45° angle and 63-81 m s^{-1} particle velocity), abrasive particles cut the surface but the chip remains attached at the end of the particle path and form a ridge (Figure 4-12 (b)). In

cutting mode I (occurs at 60° angle and 47-63 m s^{-1} particle velocity), the depth of particle penetration is higher and the cutting scar is shorter than in cutting mode II. Here, the cutting action form a sharp edge at the end of the cutting scar as shown in Figure 4-12 (c). In secondary metal cutting, abrasive particles get deflected by the previously embedded particles and erode a small portion of metal from the sides of the eroded scar (Figure 4-12 (d)). Table 4-2 summarizes the significant features observed during erosion.

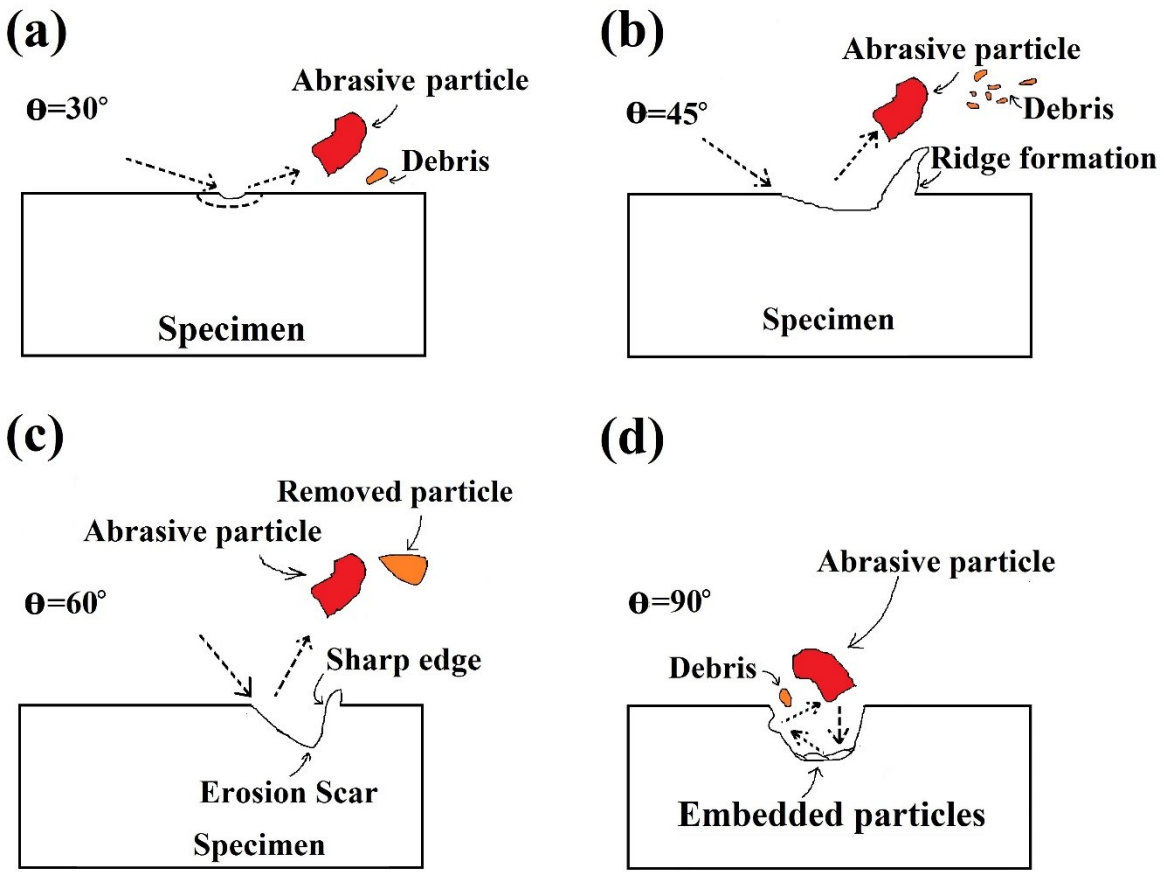

Figure 4-12 Schematic diagram of (a) low angle metal cutting, (b) cutting mode II, (c) cutting mode I and (d) secondary metal cutting.

Table 4-2 Summary of the dominant features observed during erosion.

Particle velocity	Impact angle		
	Low impact angle (30°)	Intermediate impact angle (45-60°)	High impact angle (90°)
Low velocity	● Metal removal by ploughing	● Metal removal by cutting mode I	● Flattening and fracture of ridges around dimples by Al_2O_3 particles ● Metal removal by delamination due to sub-surface crack propagation
High velocity	● Metal removal by cutting (low angle metal cutting) ● Removal of ridges around dimples	● Metal removal by cutting mode II	● Vulnerable lips formation due to fracture and removal of embedded particles ● Metal cutting due to deflection (secondary metal cutting) ● Deep dimple formation and flattening of ridges and fracture

4.1.3 Effect of Microstructure on Erosion Mechanisms

The erosion response of various steel microstructures is different depending on phases present in the steel and their orientation with respect to eroding particles impact angle. In this section, erosion responses of two common steel microstructures (pearlite and ferrite) are examined.

Figure 4-13 shows SEM micrographs of AISI 1018 steel after erosion at 30° impact angle and 36 m s^{-1} particle velocity. The particle impact direction is indicated by an arrow on the micrographs. Figure 4-13 (a) shows a deep groove on the ferrite phase as a result of abrasive particles penetrating and ploughing the steel surface. The depth and width of the groove seem to be somewhat constant throughout the length of the groove. Figure 4-13 (b) shows a groove extending from the pearlitic phase towards the ferritic phase as a result of an abrasive particle ploughing the surface. As clearly depicted by the figure, the groove is narrow and shallow as it extends over the pearlite phase and becomes deeper and wider as it encounters the ferrite phase. This behavior can also be seen in Figure 4-13 (c) where the Al_2O_3 abrasive particle has induced a deep groove in ferrite but not in the pearlite phase which appears on both ends of the groove. This presents clear evidence that pearlite is more effective in resisting ploughing and deformation during erosion than ferrite.

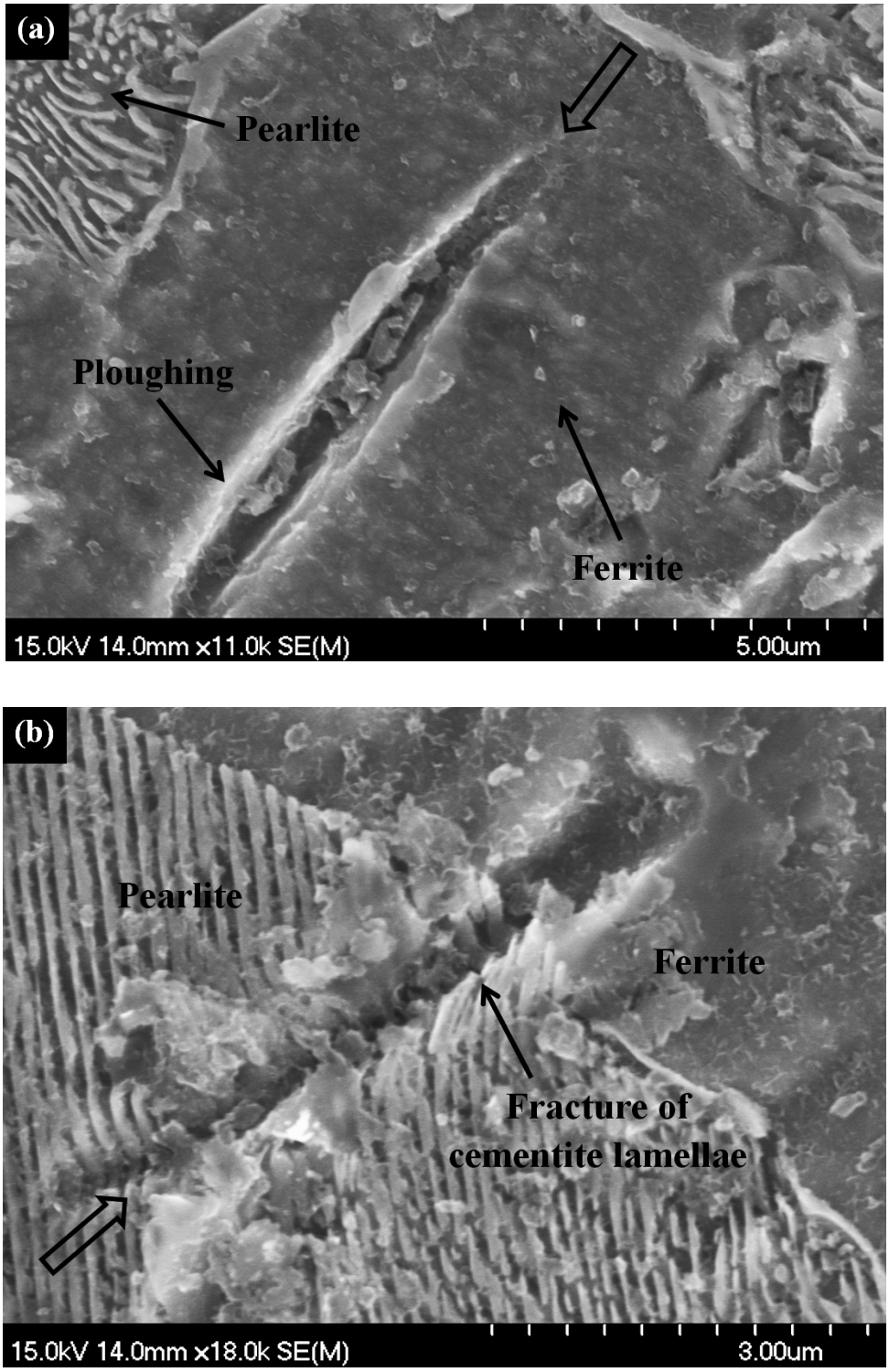

Figure 4-13 SEM micrograph of AISI 1018 steel at 30° impact angle, (a) ploughing on ferrite and (b) abrasive particle impacts pearlite and slides towards ferrite.

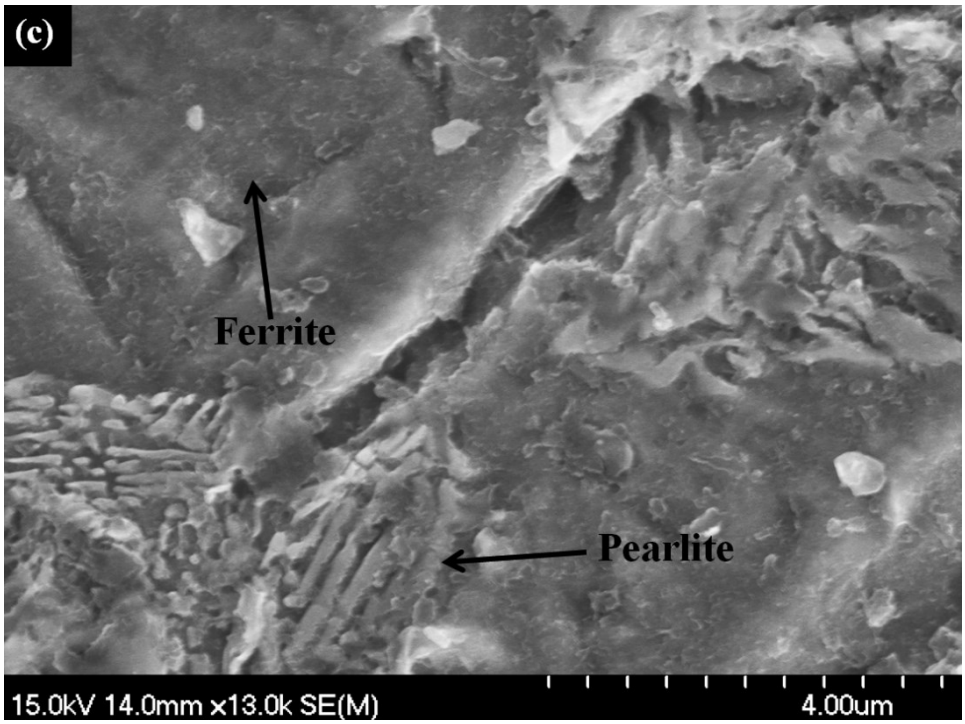

Figure 4-13 **SEM micrograph of AISI 1018 steel at 30° impact angle, (c) Al_2O_3 abrasive particle has induced a deep groove in ferrite but not in the pearlite.**

When an abrasive particle strikes a pearlitic microstructure, the extent of damage depends on the orientation of the cementite lamellae relative to the impacting particle. Abrasive particles may impact parallel to the cementite layer, at an angle to the cementite layer or perpendicular to the cementite layer. Figure 4-14 (a)-(g) shows etched SEM micrographs of AISI 1080 steel (at 30° impact angle and 36 m s^{-1} particle velocity) where abrasive particles strike the pearlitic phase. Figure 4-14 (a) shows an abrasive particle striking a pearlite grain at almost 90° angle to the cementite plates. It is clearly seen how the pearlite plates deform ahead of the abrasive particle and stack together preventing further deformation by the particle. The deformation of the pearlite plates around the tip of an Al_2O_3 abrasive particle is also seen in Figure 4-14 (b) and (c). The pearlitic plates seem to absorb the energy of the particle effectively and prevent further damage to the steel surface. It is also

clear from these micrographs that the interlamellar spacing between the pearlite plates shortens as a result of the particle impact. In Figure 4-14 (d) the abrasive particle impacting the pearlite grain is somewhat parallel to the cementite plates. It appears that the particle has encountered less resistance than the previous case (particle at right angle to pearlite plates). The abrasive particle seems to slide a longer distance parallel to the cementite plates than perpendicular to the plates. This can also be seen in Figure 4-14 (e), where a long and deep groove appears parallel to the cementite plates as compared to the groove perpendicular to the cementite plates. It seems that when particles strike the pearlite phase in a direction parallel to the cementite plates, shearing of the plates occurs. The shearing process requires less energy than deforming the cementite plates when the abrasive particle is at a right angle to the cementite plates. Furthermore, the plates in the pearlite phase slow down crack propagation perpendicular to the plate structure as seen in Figure 4-14 (f) and (g). Figure 4-14 (f) and (g) shows how the cementite lamellae in pearlite prevent the propagation of a surface crack. The cementite layers act as barriers in front of crack tips and inhibit crack propagation.

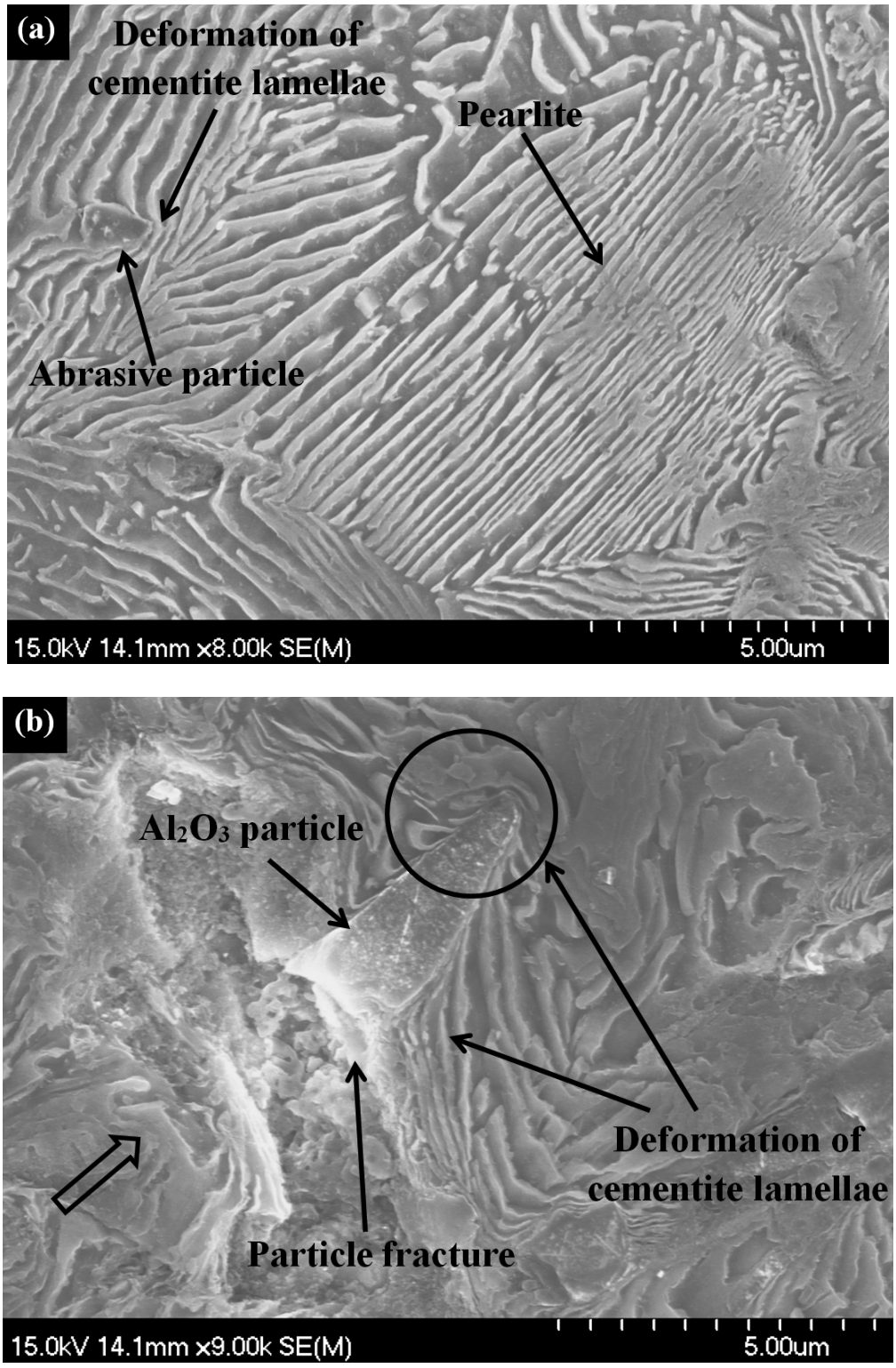

Figure 4-14 SEM micrograph of AISI 1080 steel at 30° impact angle, (a) abrasive particle impacting perpendicular to the cementite lamellae and (b) deformation of cementite lamellae around abrasive particle.

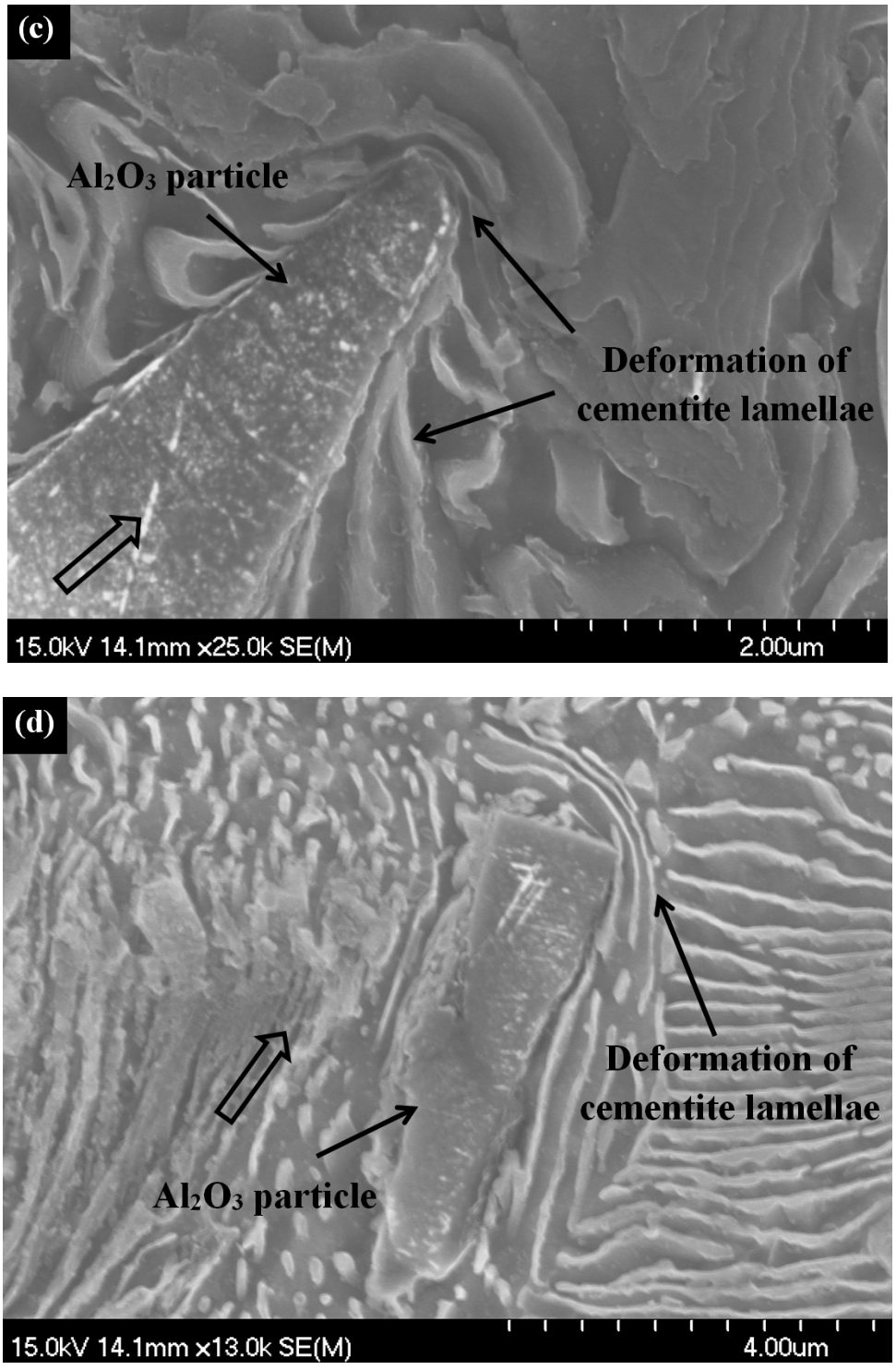

Figure 4-14 SEM micrograph of AISI 1080 steel at 30° impact angle, (c) magnified image of Figure 4-14 (b), deformation of cementite lamellae around abrasive particle and (d) abrasive particle impacting at parallel to the cementite lamellae.

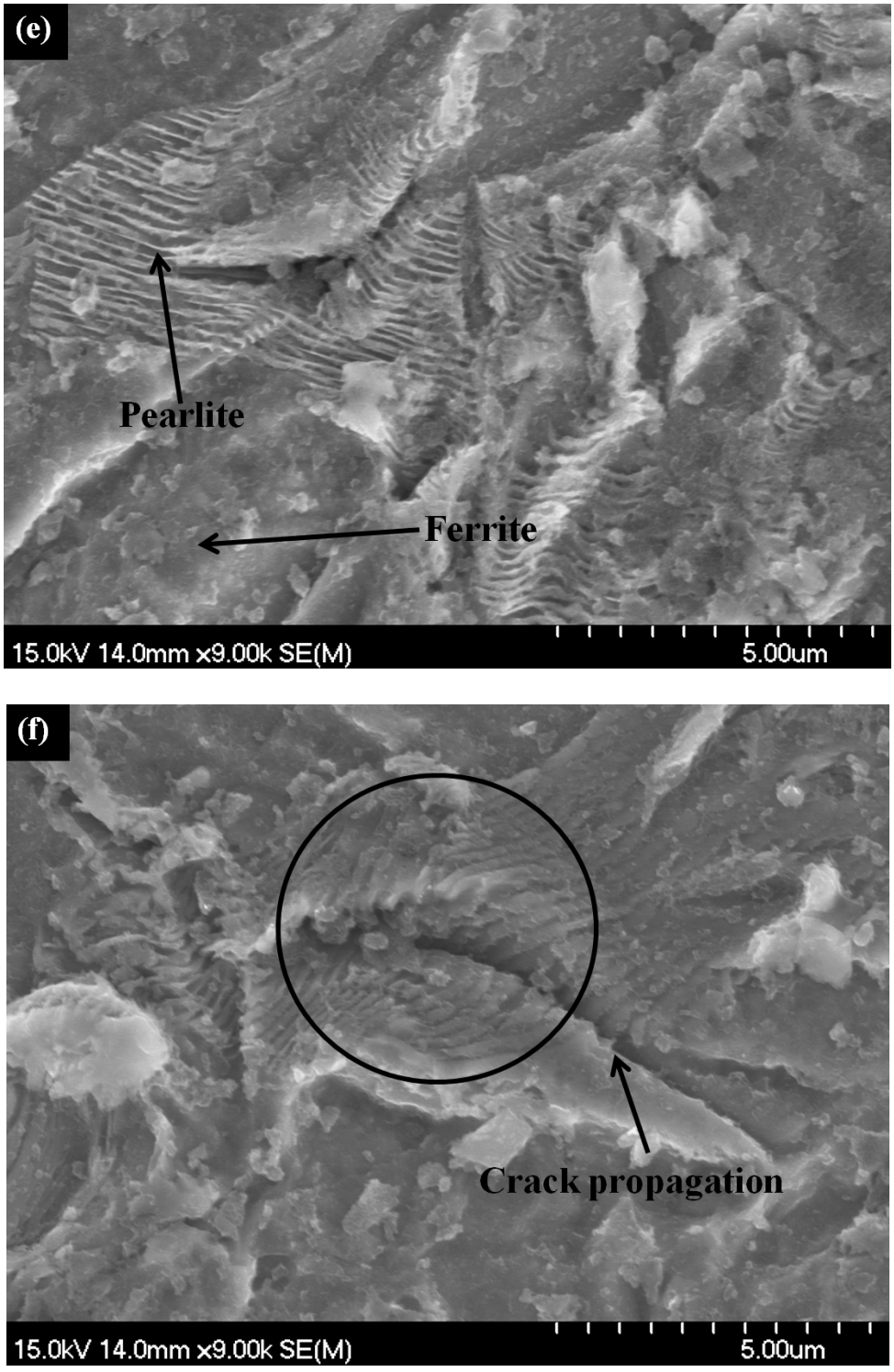

Figure 4-14 SEM micrograph of AISI 1080 steel at 30° impact angle, (e) abrasive particle impacting parallel and perpendicular to the cementite plates and (f) cementite lamellae in pearlite prevent the propagation of surface crack.

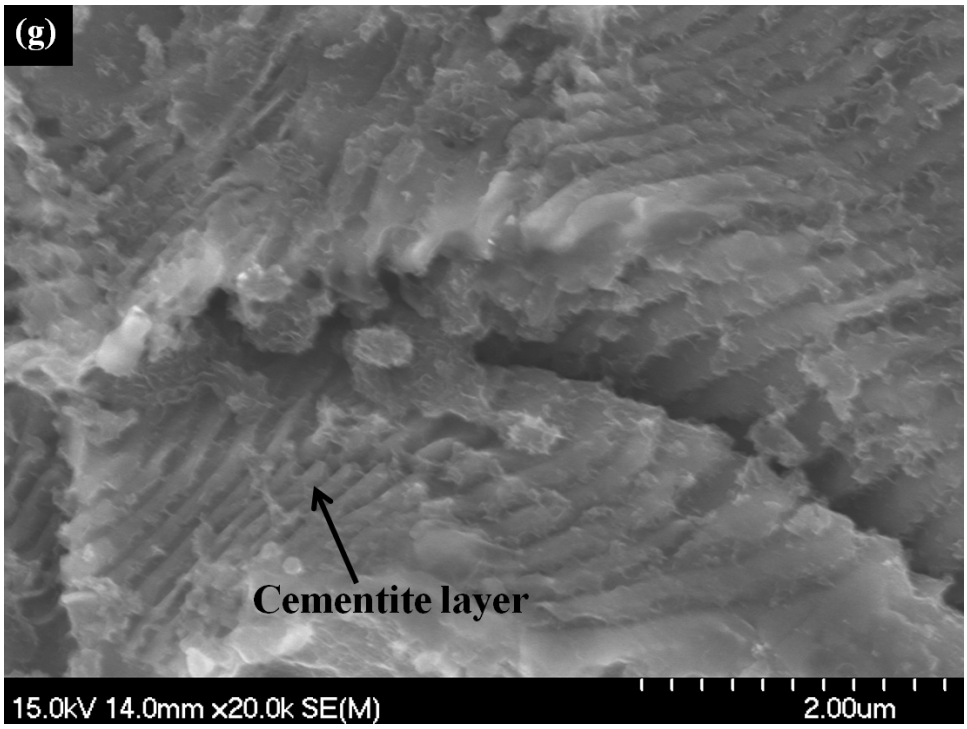

Figure 4-14 SEM micrograph of AISI 1080 steel at 30° impact angle, (g) magnified image of Figure 4-14 (f).

Eroded specimens were cross-sectioned along the longitudinal direction of the erosion scar. Specimens were etched (5% Nital) and SEM observations were performed on the sub-surface of the erosion scar. Figure 4-15 (a)-(d) shows the sub-surface of AISI 1018 steel after erosion at 30° impact angle and 63 m s^{-1} particle velocity. Figure 4-15 (a) and (b) shows the difference in erosion behavior of ferritic and pearlitic microstructures. As we see from the micrograph, ferrite erodes faster relative to pearlite. As indicated in the figure, more material removal was observed from ferrite compared to pearlite. However, the erosive behavior of pearlite is sensitive to the orientation of the cementite layers. Figure 4-15 (c) is a magnified image of Figure 4-15 (b) (marked as a circle) illustrating the erosion response of pearlite when the abrasive particle impacts at an angle perpendicular to the

cementite layer. The kinetic energy of the abrasive particle deforms the cementite layers instead of removing the material completely. On the other hand, when the cementite layers are oriented parallel to the abrasive particle direction, material is removed at higher rate as shown in Figure 4-15 (d).

It is interesting to note that, although pearlite is more effective in resisting ploughing and plastic deformation, AISI 1018 steel exhibits higher erosion resistance at 30° impact angle compared to AISI 1080 steel (Figure B-2). At a low impact angle, the indenting component of the kinetic energy is small and a small percentage of the abrasive particles attain the critical energy required to penetrate the steel surface. Due to its lower hardness, the required critical energy for AISI 1018 is low. Hence, AISI 1018 steel exhibits significant Al_2O_3 embedded particles (which act as surface enforcements), resulting in less material loss and lower erosion rate as compared to AISI 1080. It is important to note that embedded Al_2O_3 are more effective in resisting erosion compared to pearlite in the AISI 1080 steel. This behavior is not observed at higher angles because as the incident angle increases the particles indenting energy becomes higher, which results in the fracture of embedded particles by the subsequent incoming particle stream.

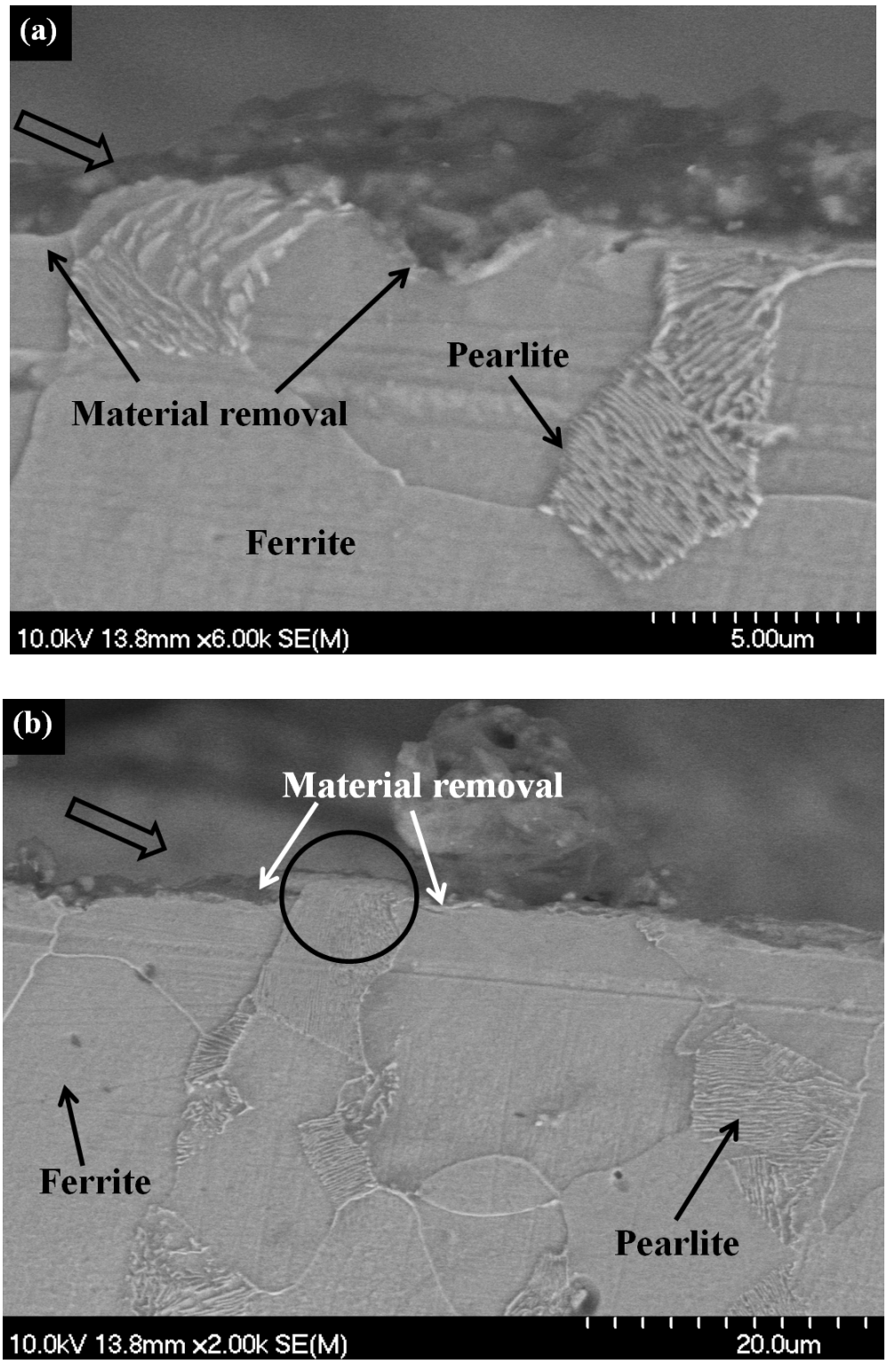

Figure 4-15 SEM micrograph of the cross-section of AISI 1018 steel at 30° angle, (a)-(b) abrasive particle impacting at an angle and different erosive behavior of pearlitic and ferritic microstructure.

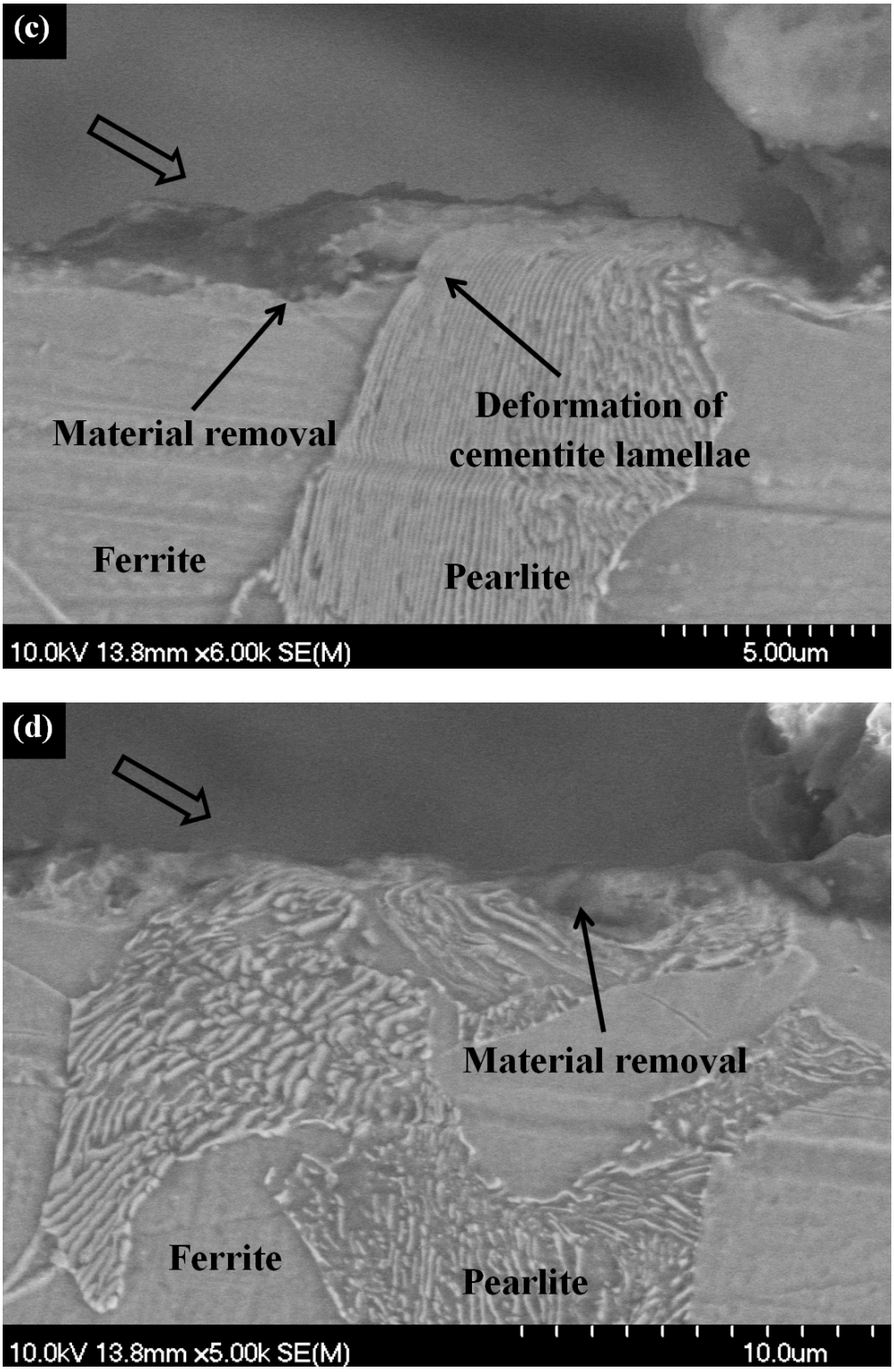

Figure 4-15 SEM micrograph of the cross-section of AISI 1018 steel at 30° angle, (c) magnified image of Figure 4-15 (b) (marked as circle) and (d) delamination of cementite layer due to abrasive impact.

4.1.4 Erosion Mechanism Maps

Researchers involved in the development of wear, erosion or erosion-corrosion mechanism maps have their individual approaches in the construction of these maps [110], [161], [280], [289], [291]–[298], [340]. In this study, the following common approach is followed to construct the erosion mechanism maps for carbon and pipeline steels:

i. In order for an erosion map to be constructed, it is essential to define the pair of materials of interest, their mode of contact, contact geometry and the environment in which they interact. In this study, solid particle erosion was performed using AISI 1018, AISI 1080, API X42, API X70 and API X100 as test specimens and alpha aluminum oxide particles as erodent.

ii. Operative erosion mechanisms are a function of test conditions. Earlier studies [162], [163] have shown that the most important factors which influence erosion are the angle of impingement and the velocity of the impacting particles. In this study, impact angle and normalized particle velocity were selected as axes for the two-dimensional erosion map. In-house erosion tests were carried out covering a wide range of particle velocities (36-81 m s^{-1}) and impact angles (30°-90°).

iii. Empirical erosion maps were constructed by grouping erosion data according to the mode and mechanism of erosion. Erosion rate and erosion mechanism data, appropriately classified, are then plotted onto a two-dimensional space defining the map. The measured erosion rate is determined by the relative contributions of different mechanisms, while, the erosion mechanisms are identified through SEM observations. Although, different erosion mechanisms operate simultaneously and interact with one another, the dominant

mechanism is the one which, for a given angle and velocity, leads to the greatest metal loss. The field of dominance of each mechanism is then defined using field boundaries and the approximate locations of the contours of constant erosion rates are located.

Normalized particle velocity ($\dot{V}$) is used as y-axis for the present erosion maps and is calculated using Equation 4-1 [340], where the thermal diffusivity of alumina is 1.2×10^{-5} m^2 s^{-1} [341]–[344].

$$\text{Normalized velocity}, V = \frac{\text{Particle velocity, } v\ (\text{m s}^{-1}) \times \text{Radius of the erodent, } r_0\ (\text{m})}{\text{Thermal diffusivity of the erodent, } a\ (\text{m}^2\ \text{s}^{-1})}$$

Equation 4-1

Based on SEM observations, identified dominant erosion mechanisms are given in Table 4-3. It is important to note that dominant erosion mechanism is the one that is observed more than 50% of the time at specific impact angle and velocity condition. Plotting the data in Table 4-3 provides regions of dominant erosion mechanisms. Within the experimental conditions used in this study, ploughing occurs at low impact angle regardless of particle velocity. However, low angle metal cutting and secondary metal cutting only occur at high particle velocity, when the impact angle is 30° and 90°, respectively. Plastic deformation and fracture occur at low impact angle and intermediate velocity condition. Fracture of ridges around dimples dominates within a range of intermediate impact angle and low particle velocity conditions, while, cutting mode I and II mechanisms appear at specific velocity and impact angle condition. Material is removed by delamination at high impact angle and low particle velocity condition [110], [121].

Table 4-3 Identified erosion mechanisms (based on SEM examination) at different impact angles and particle velocities.

Erosion mechanism	Impact angle (°)	Particle velocity (m s^{-1})
Ploughing	30° ~ 45°	36-81 m s^{-1}
Low angle metal cutting	30°	63-81 m s^{-1}
Plastic deformation and fracture	30° ~ 45°	47-63 m s^{-1}
Cutting mode II	45°	63-81 m s^{-1}
Dimple formation and fracture of ridges	45° ~ 60°	36-47 m s^{-1}
Cutting mode I	60°	47-63 m s^{-1}
Secondary metal cutting	60° ~ 90°	47-81 m s^{-1}
Delamination	90°	36-47 m s^{-1}

The normalized erosion rate is plotted as a function of impact angle and normalized velocity. Abrasive particle velocity in m s^{-1} is shown on a secondary axes. Contours of normalized erosion rate are plotted at 3×10^{-6} intervals.

The next step in constructing the erosion map is identifying erosion modes based on the normalized erosion rate. The following four broad classes of erosion modes are identified:

1. Ultra-mild erosion
2. Mild erosion
3. Moderate erosion and
4. Severe erosion

The erosion levels at which these limits are set depend on the desired lifetime of a material under various exposure conditions. For example, fittings such as elbows and tees that redirect the flow field usually experience severe erosion for particle velocity more than 10 m s^{-1}, which results in maximum allowable erosion rate of 0.1 mm yr^{-1} for fittings [345]–[347]. Due to the severity of problems to components in service, different researchers have performed erosion tests covering a wide range of impact angle and particle velocity for different material pairs of interest [56], [62], [70], [72], [104], [131], [311],

[348], [349]. In order to define the boundaries of different erosion modes, a literature review was conducted to arrive at a common classification. To be able to compare erosion rate data collected from literature, it is essential to calculate normalized erosion rate and normalized particle velocity. Data collected from the literature is given in appendix (Table B-1). Table 4-4 is generated based on literature data, and represents typical erosion boundaries. Figure 4-16 to Figure 4-20 show empirical erosion mechanism maps for AISI 1018, AISI 1080, API X42, API X70 and API X100 steel, respectively, showing regions of different erosion modes and mechanisms.

Table 4-4 Classification of different erosion modes based on normalized erosion rate.

Erosion mode	Range of normalized erosion rate
Ultra-mild erosion	$\leq 2.1 \times 10^{-5}$
Mild erosion	$2.1 \times 10^{-5} \leq$ mild erosion $\leq 4.8 \times 10^{-5}$
Moderate erosion	$4.8 \times 10^{-5} \leq$ moderate erosion $\leq 1.2 \times 10^{-4}$
Severe erosion	$\geq 1.2 \times 10^{-4}$

Ultra-mild erosion is a regime in the erosion map where erosion is insignificant ($\leq 2.1 \times 10^{-5}$) and for all steels used in this study it emerges at high impact angle and low velocity condition. At high impact angle the kinetic energy of the abrasive particles is used to penetrate the surface resulting in embedded Al_2O_3 particles. These embedded particles enforce and protect the surface from further erosion. Compared to all steels, AISI 1018 and API X100 show the smallest and largest ultra-mild erosion regions, respectively. The yield strength of API X100 (690 MPa) is almost double that of AISI 1018 (310 MPa), therefore, as expected, API X100 provides better erosion resistance because of its higher yield strength. API X70 also shows good erosion resistance at high impact angle and low particle velocity. Delamination seem to be the dominant erosion mechanism in the ultra-mild regime for API X70 and API X100 steel.

When the normalized erosion rate is in between 2.1×10^{-5} and 4.8×10^{-5} (mild erosion regime), delamination and fracture of ridges around dimples are the dominant erosion mechanisms for AISI 1018, AISI 1080 and API X42 steel. In addition, secondary metal cutting (at high impact angle and high velocity) is the dominant erosion mechanism for AISI 1080 steel. On the other hand, fracture of ridges around dimple, cutting mode I and secondary metal cutting seem to be the dominant mechanisms for API X70 and API X100 steel with increasing velocity. Carbon and API steels experience mild erosion at high impact angle (60°– 90°), when the abrasive particle velocity is at or above 47 m s^{-1}. API X42 exhibits smaller mild erosion region compared to API X70 and API X100 and for application where particle velocity is above 63 m s^{-1}, API X42 can be replaced with either API X70 or API X100 for better erosion resistance.

Moderate erosion regime (in between 4.8×10^{-5} and 1.2×10^{-4}) occupies a large area in the erosion mechanism map. Depending upon the impact angle, carbon and API steels may experience moderate degradation at all particle velocities employed in this study. It is interesting to note that moderate erosion is the largest region in AISI 1018 erosion map and in application, where erosion is a major concern, AISI 1018 will undergo moderate erosion under almost all conditions. Depending upon impact angle and particle velocity, ploughing, plastic deformation and fracture and cutting mode II are the dominant erosion mechanisms for carbon and API steels. Moreover, cutting mode I and secondary metal cutting are also dominant mechanisms for AISI 1018 and API X42 in the moderate erosion regime.

Severe erosion ($\geq 1.2 \times 10^{-4}$) usually occurs at low impact angle and high velocity condition, where material is typically removed due to the combined effect of ploughing and low angle metal cutting. It is important to note that, AISI 1018 exhibits better erosion resistance at low impact angle and high velocity compared to API X100. At low impact angle (30°) the indenting

component ($KE\ sin\alpha$) of the abrasive particle is small and a limited amount of abrasive particles embed into the surface. Because of its low hardness, AISI 1018 exhibits more embedded alumina particles compared to other steels resulting in better erosion resistance. Assuming regions where mild and ultra-mild erosion dominate are acceptable for steel pipes. Then API X100 would be the best choice as the mild and ultra-mild regions are the largest compared to other steels.

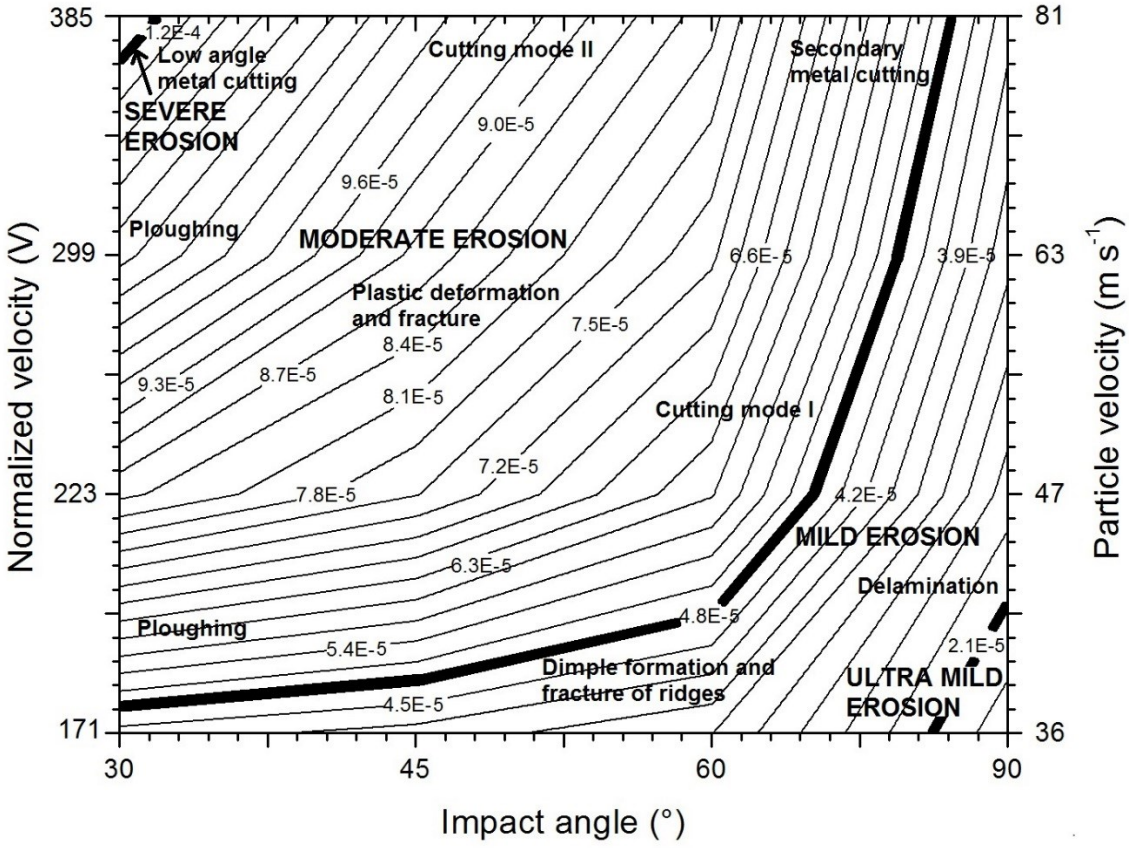

Figure 4-16 Empirical erosion mechanism map for AISI 1018 steel as a function of impact angle and normalized velocity. Contours of constant normalized erosion rates are superimposed on fields showing the regimes of dominances of different erosion mechanisms.

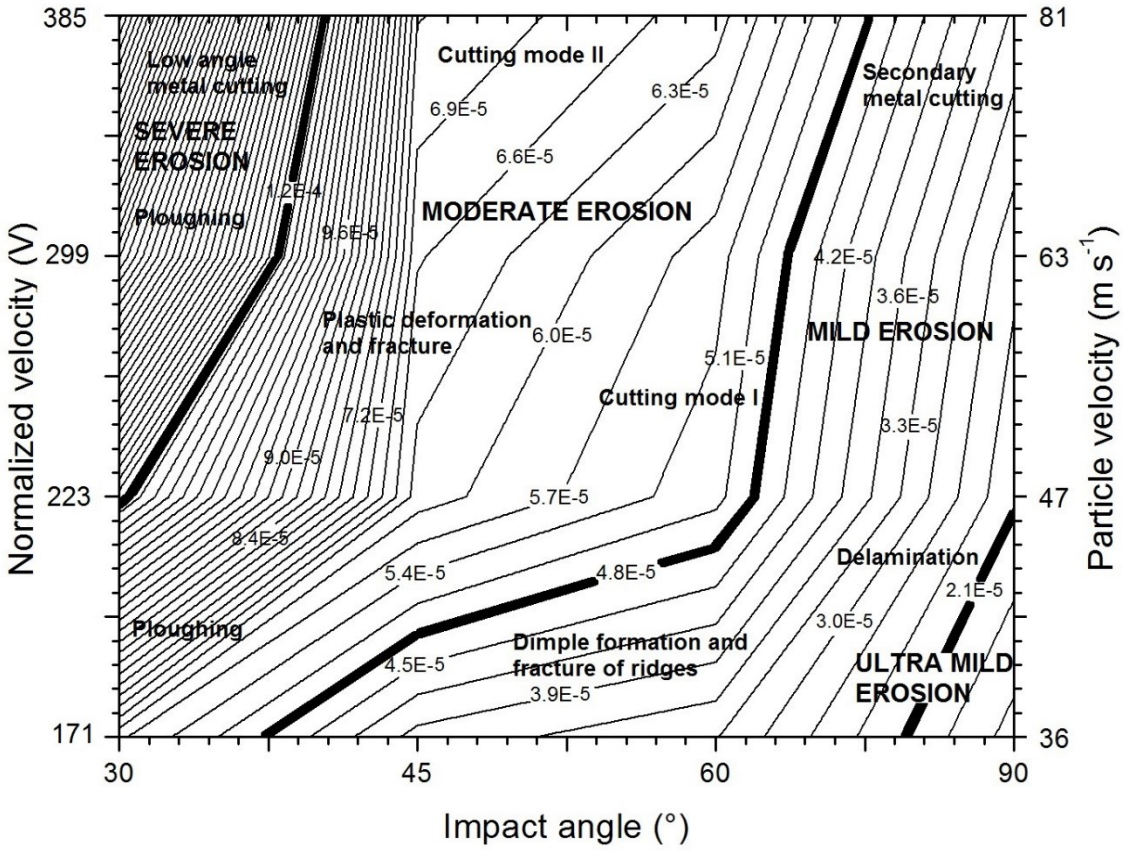

Figure 4-17 Empirical erosion mechanism map for AISI 1080 steel as a function of impact angle and normalized velocity. Contours of constant normalized erosion rates are superimposed on fields showing the regimes of dominances of different erosion mechanisms.

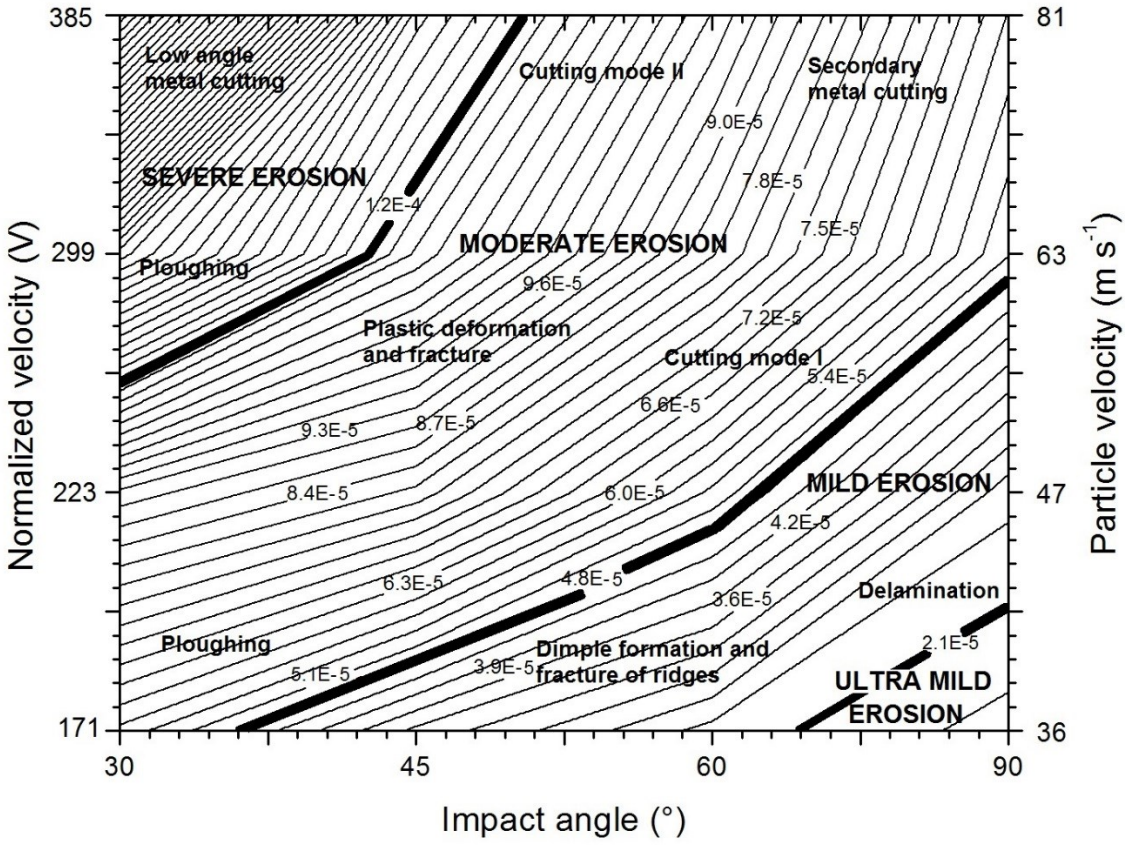

Figure 4-18 Empirical erosion mechanism map for API X42 steel as a function of impact angle and normalized velocity. Contours of constant normalized erosion rates are superimposed on fields showing the regimes of dominances of different erosion mechanisms.

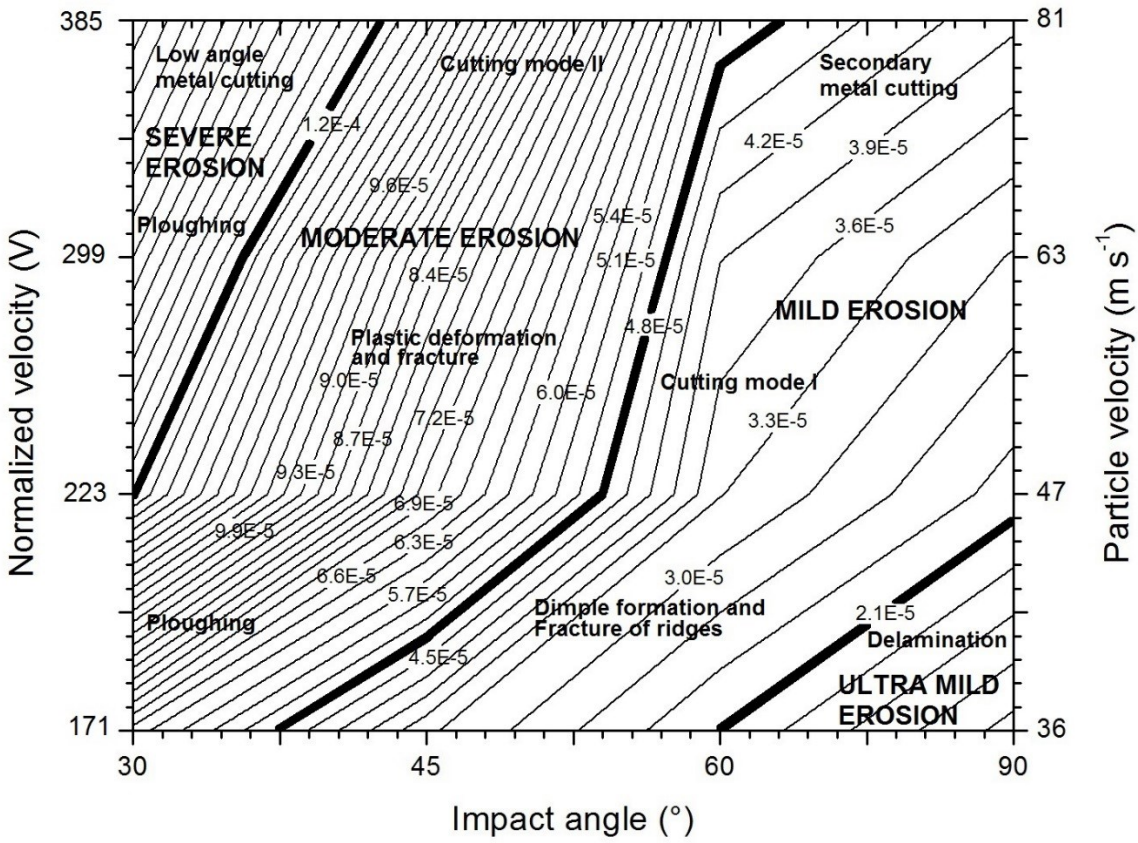

Figure 4-19 Empirical erosion mechanism map for API X70 steel as a function of impact angle and normalized velocity. Contours of constant normalized erosion rates are superimposed on fields showing the regimes of dominances of different erosion mechanisms.

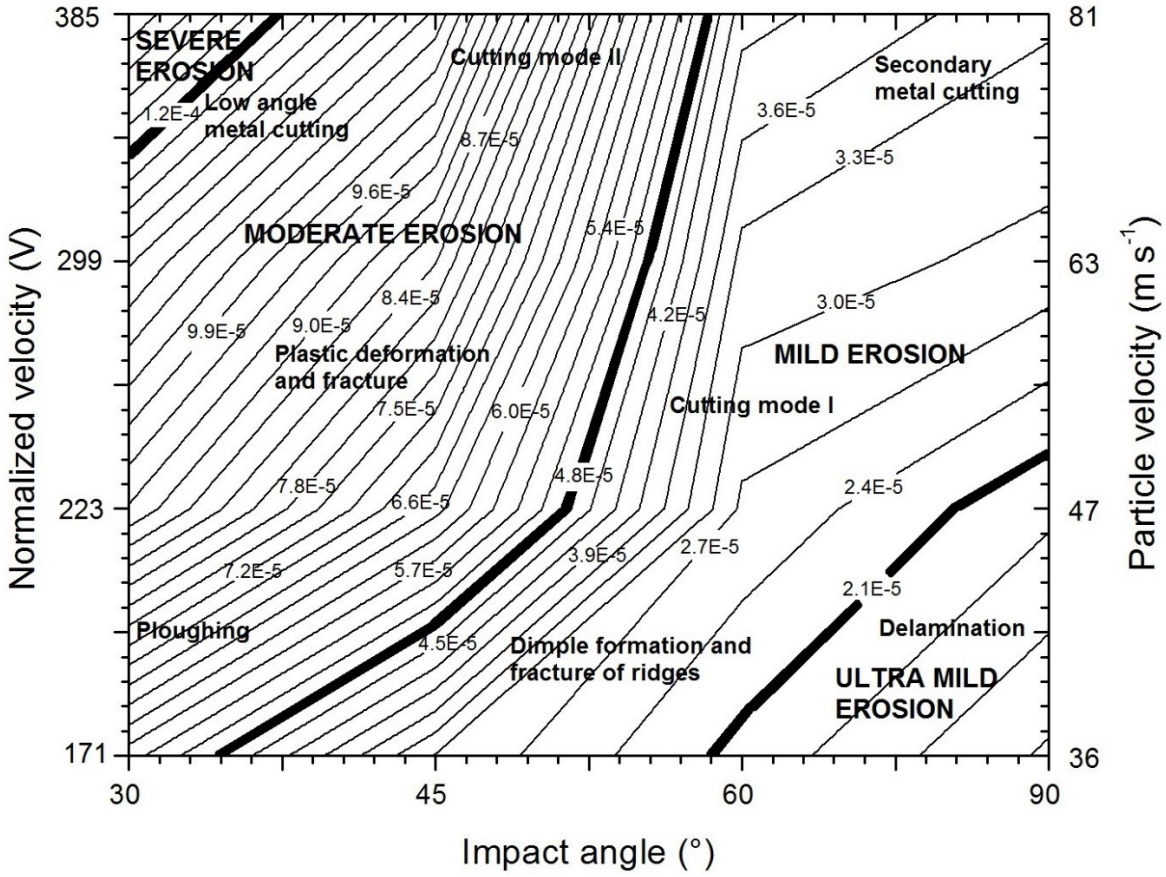

Figure 4-20 Empirical erosion mechanism map for API X100 steel as a function of impact angle and normalized velocity. Contours of constant normalized erosion rates are superimposed on fields showing the regimes of dominances of different erosion mechanisms.

4.1.5 Summary

Erosion mechanism maps for carbon and API pipeline steels were constructed. These maps show the erosion rate and the region of dominance of each competing erosion mechanism. Erosion mechanism maps are a useful material selection tool to designers, engineers, steel makers and pipeline operators.

The normalized erosion rate of carbon and API steels increases with increasing particle velocity and decreases with increasing impact angle. AISI 1080 steel exhibits higher erosion resistance compared to AISI 1018 steel at 45°, 60° and 90° impact angle. However, AISI 1018 steel shows better erosion resistance at low impact angle (30°). API X100 exhibits higher erosion resistance compared to API X42 and API X70 steel for all impact angle and velocity conditions. The dominant operative erosion mechanisms are found to be significantly different depending on particle impact angle and velocity. However, on all maps, regions where ultra-mild erosion and severe erosion dominant are the two extreme corners of the map. That is, severe erosion dominants at low angle and high velocity and ultra-mild erosion dominates at high angle and low velocity for all steels. At low impact angle and low particle velocity, ploughing is the dominant mechanism and a combination of low angle metal cutting and ridge removal are dominant at low impact angle and high velocity condition. However, at high impact angle, secondary metal cutting and flattening of ridges and fracture seems to be the dominant process of metal removal at high velocity. At low particle velocity, deformation and fracture of ridges around dimples is dominant. Most of the impact at low particle velocity is elastic and doesn't contribute to the measured erosion rate. This makes erosion almost independent of the impact angle. The dependence of erosion on impact angle becomes evident at high particle velocities. Several phenomena are responsible for lower erosion rate at high impact angle: (i) particle interference, which prevents some particles

from reaching the surface; (ii) embedded abrasive particles protect the steel surface from incoming particles and (iii) heavy plastic deformation of the surface and less actual material removal.

The erosion response of pearlite and ferrite are different depending upon the particle impact location and the orientation of the pearlite relative to the impinging particle. The pearlite phase is more effective in resisting erosion than ferrite phase due to its lamellar structure. However, embedded Al_2O_3 are more effective in resisting erosion than pearlite. At low impact angle (30°), because of its low hardness, AISI 1018 exhibits more embedded particles resulting in better erosion resistance. The orientation of the pearlite plates with respect to the impacting particle plays a significant role in resisting deformation. When the pearlite plates are at right angle to the striking particle, the resistance to deformation is at its maximum.

4.2 Corrosion

This section examines the corrosion behavior of API steels in sweet environment and the characterization of the corrosion layer. Microstructural effects on the formation of the corrosion layer are also discussed at the end of this section.

4.2.1 Electrochemical Corrosion

Electrochemical corrosion tests for API X42, API X70 and API X100 were performed in 2 g l^{-1} NaCl solution saturated with CO_2 for 2.5 hr. A typical poteniodynamic polarization curve for API X42 steel is given in Figure 4-21. The corrosion current density (I_{corr}) of the system was measured from Tafel extrapolation. Statistical analysis was performed to measure the accuracy of the fit, which gives an accuracy of the fit at 95% confidence level. The corrosion potential (E_{corr}), corrosion current density (I_{corr}), anodic (β_a) and cathodic (β_c) beta for API X42, API X70 and API X100 steels are given in Table 4-5. The specimens were weighed before and after the corrosion tests and the corrosion rates were calculated from weight loss using Equation 3-3. Equation 3-4 is used to calculate the corrosion rate from I_{corr}. Table 4-6 summarizes the corrosion rate data for these steels. Figure 4-22 shows the relative comparison of corrosion rates for API X42, API X70 and API X100 based on weight loss and I_{corr}. API X100 shows better corrosion resistance in CO_2 containing salt solution compared to API X42 and API X70. The differences in the corrosion characteristics may have resulted from the variation in the alloying content with respect to chromium, molybdenum, copper and nickel. Chromium is a reactive element, and forms a protective metal oxide layer [350]–[352]. Hence, higher chromium content in API X100 provides better corrosion resistance compared to API X42 and API X70 steels.

It was found that when copper is present as an alloying element in low carbon steel, it forms copper oxide in the corrosion product layer. Because copper oxide is less soluble in solution than iron oxide, it provides better protections to the steel [353], [354]. Accordingly, API X100 has more protective corrosion product films than API X42 and API X70 [355]–[357]. Moreover, bainitic microstructure (due to higher amount of molybdenum and nickel) in API X100 provides compact and nonporous oxide layer and yields better corrosion resistance in marine environment compared to ferritic/pearlitic microstructure [358]–[361].

It is interesting to note that corrosion rate calculated from weight loss is higher than the corrosion rate calculated from I_{corr}. This is because, I_{corr} was calculated from Tafel slope which measures the rate of dissolution of iron ions. However, in addition to iron dissolution, weight loss also includes material removal due to second phase particles and removal of corrosion product from the surface during cleaning. Similar results was also observed in previous studies [362]–[364].

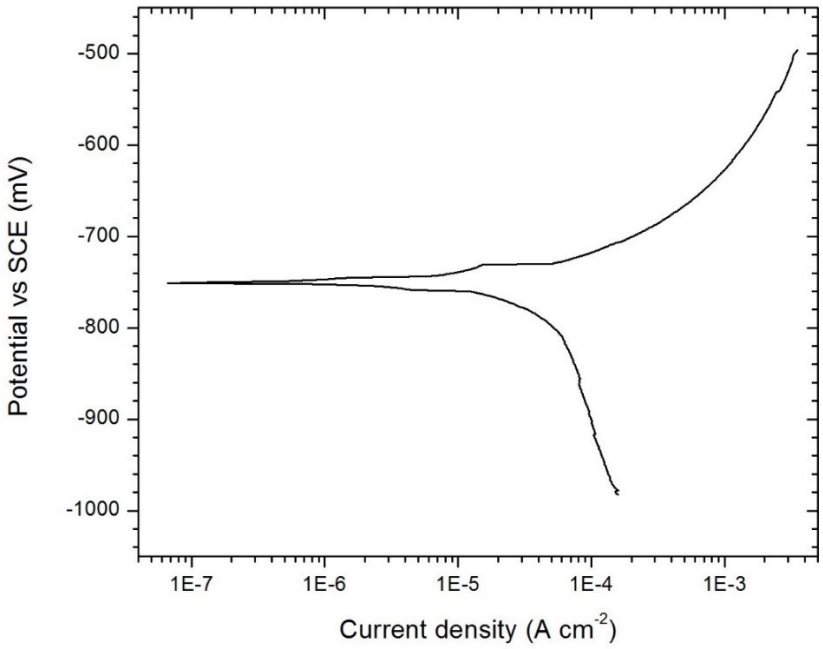

Figure 4-21 Potentiodynamic polarization curve for API X42 steel in 2 g l^{-1} NaCl saturated with CO_2.

Table 4-5 Electrochemical parameters for API X42, API X70 and API X100 steels.

Steel	E_{corr} (mV) vs SCE	I_{corr} (μA cm^{-2})	Anodic beta (β_a) (mV $decade^{-1}$)	Cathodic beta (β_c) (mV $decade^{-1}$)
API X42	-754.2	52.5	79.2	-507.2
API X70	-730.9	43.2	65.6	-527.3
API X100	-726.9	22.0	62.2	-227.9

Table 4-6 Corrosion rate calculated from electrochemical measurement and weight loss.

Steel	Weight loss (g mm^{-2})	Corrosion rate from weight loss (C_0), (μm s^{-1})	Corrosion rate from I_{corr} (μm s^{-1})
API X42	3.10×10^{-6}	4.39×10^{-5}	1.93×10^{-5}
API X70	2.84×10^{-6}	4.02×10^{-5}	1.58×10^{-5}
API X100	1.93×10^{-6}	2.73×10^{-5}	0.81×10^{-5}

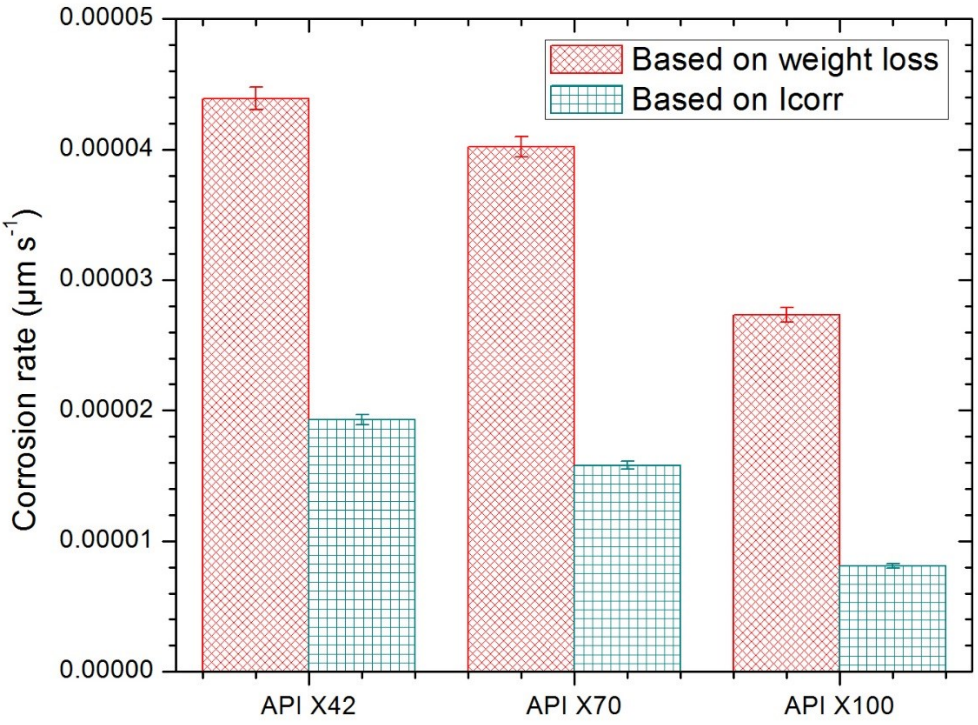

Figure 4-22 Relative comparison of corrosion rates for API X42, API X70 and API X100.

Profilometry scans were performed before and after corrosion of API X42 steel samples. Scanned profiles were then stitched together for comparison as shown in Figure 4-23. The surface roughness of the specimen was measured and is given in Table 4-7, where the error indicates standard deviation. It was found that there is around 54% increase in surface roughness after corrosion. This could be due to the existence of residual inhomogeneities and surface defects, e.g., impurities and stresses [365]. The surface inhomogenities promote micro-corrosion cells by which corrosion takes place, which, in turn raises the surface roughness of the steel. In addition, pitting corrosion that form on the metal surface also contributes to the increase in surface roughness [366].

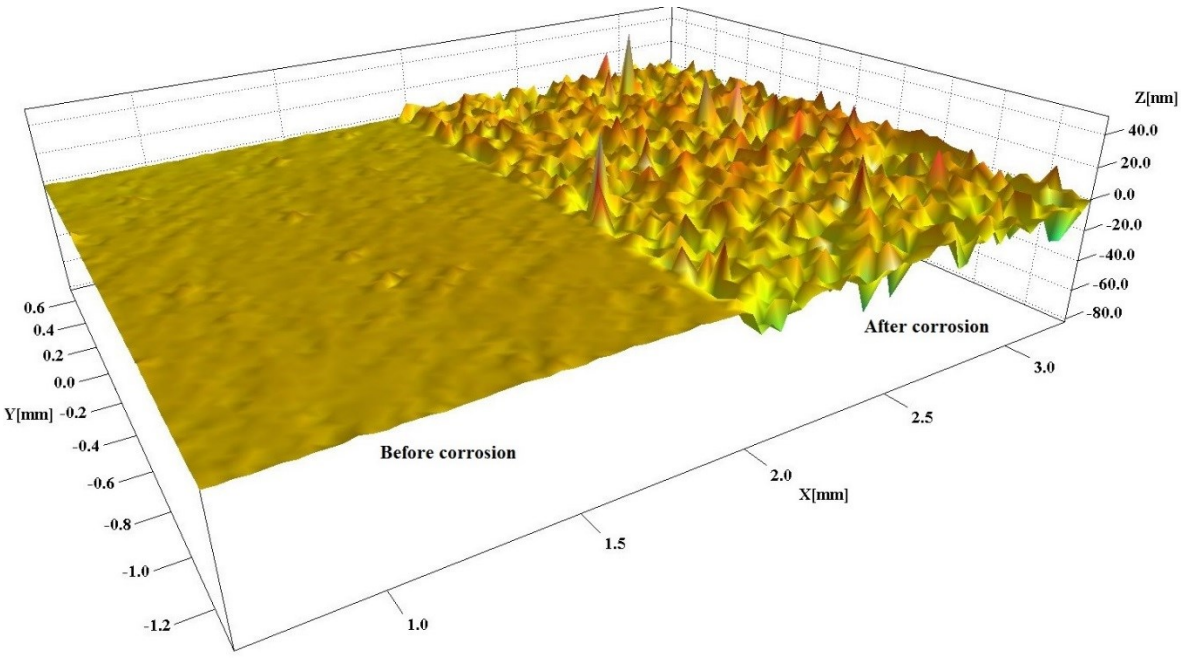

Figure 4-23 Profilometry scans of API X42 steel showing surface roughness profiles before and after pure corrosion.

Table 4-7 Roughness data for API X42 steel before and after pure corrosion.

	Before corrosion (nm)	After corrosion (nm)	% increase
Average roughness (R_a)	847 ± 5	1306 ± 5	54
Root mean square (RMS)	1081± 5	1674 ± 5	54

In order to assess the effect of the steel microstructure, API X42 steel (having proeutectoid ferrite and pearlite) is examined under corrosive conditions. Figure 4-24 (a) shows the SEM micrograph of etched as-received API X42 steel. Figure 4-24 (b) shows the magnified image (marked as a circle) of Figure 4-24 (a) illustrating the pearlitic and proeutectoid ferritic microstructure before corrosion. The pearlitic microstructure of the steel after it was exposed to the corrosive solution (2 g l^{-1} NaCl saturated with CO_2) for 12.5 hr is shown in Figure 4-24 (c). It is generally agreed that ferrite is anodic to cementite (Fe_3C) in CO_2 environment [367], [368], which leads to the dissolution of eutectoid ferrite into Fe^{2+} ion and leaving behind a cementite (Fe_3C) network in pearlite (Figure 4-24 (c)). It is believed that depending upon the morphology of these cementite (Fe_3C) networks, they can reinforce a protective layer by anchoring it to the steel surface [247]. Furthermore, the anodic reaction involving oxidation of iron to ferrous ion in the corrosive solution leads to the preferential dissolution of proeutectoid ferrite as shown by the wavy appearance in Figure 4-24 (d). The dissolution of iron provides a suitable chemical environment for the formation of iron carbonate ($FeCO_3$), which then precipitates on the steel surface due to its limited solubility [227], [242], [245], [247], [267], [368], [369]. Figure 4-25 shows the EDS analysis performed on the specimen before and after corrosion. An order of magnitude increase in carbon to iron concentration ratio and the presence of high oxygen content indicates the possibility of the formation of $FeCO_3$ on the corroded surface. The properties of the $FeCO_3$ layer play an important role in determining the corrosion rate of the steel. In general, it acts as a diffusion barrier covering the underlying metal and decreasing the corrosion rate by preventing electrochemical reactions at the surface [370]. The protectiveness of such corrosion layer determines the long term corrosion performance. It is interesting to note that while the bulk pH remained constant (Table 3-7) during the test (at 4.3) the local pH did not. Iron carbonate forms mostly locally, at sites where the pearlitic phase existed. As the concentration of the

Fe^{2+} increases locally between cementite plates, the local pH also rises [371]. The local increase in pH provides a suitable environment for $FeCO_3$ to form between cementite plates [228], as predicted by the $FeCO_3$ potential-pH diagram for Fe-H_2O-CO_2 at 25°C [267]. The iron carbonate then precipitates due to its lower solubility at higher pH [372]. In this work, it is believe that the iron carbonate we detected by EDS is due to this localized precipitation of $FeCO_3$. This argument is supported by a number of research papers [242], [245], [369].

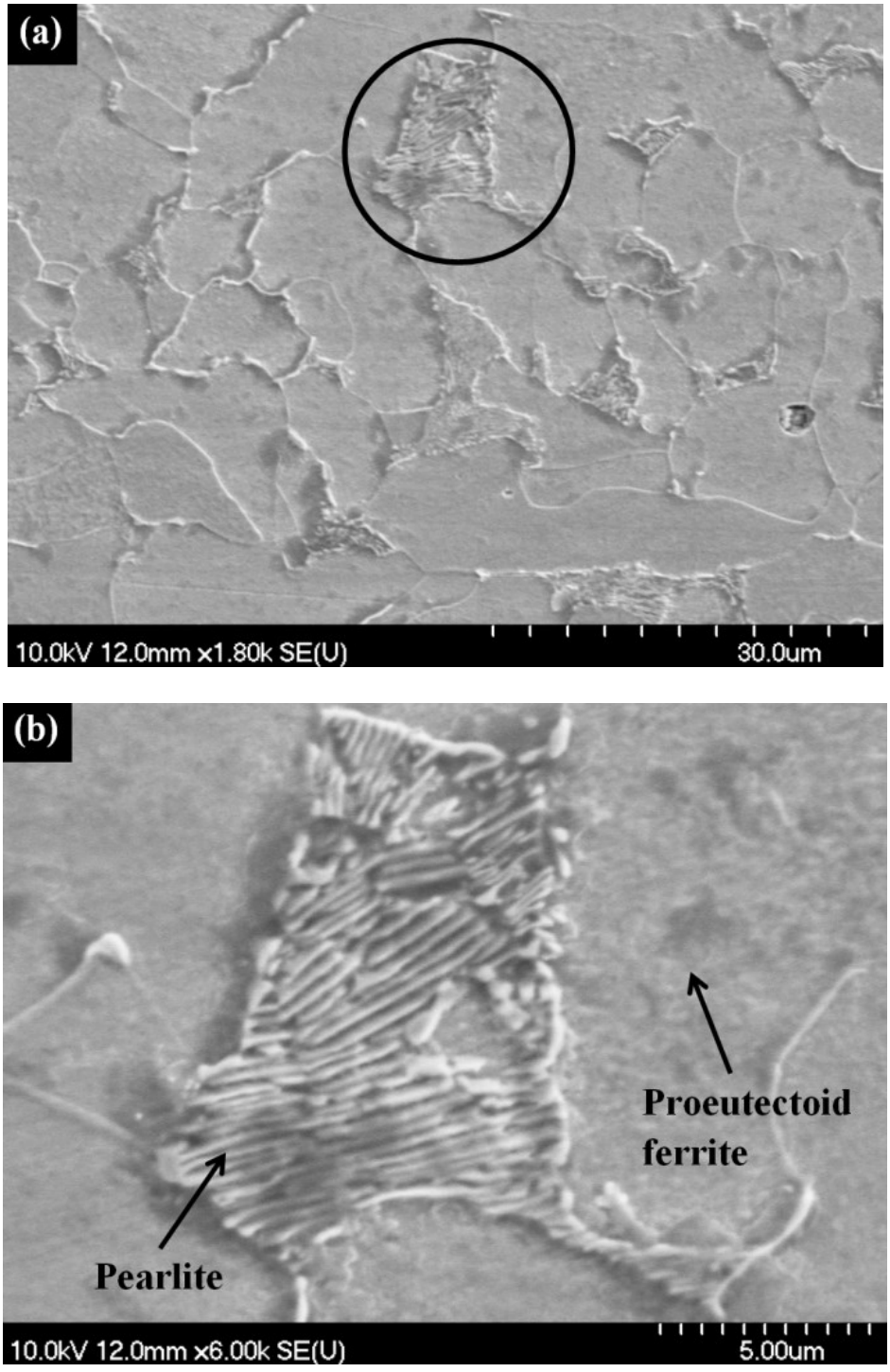

Figure 4-24 SEM images of (a) as received API X42 steel after etching and (b) pearlite and proeutectoid ferrite before corrosion.

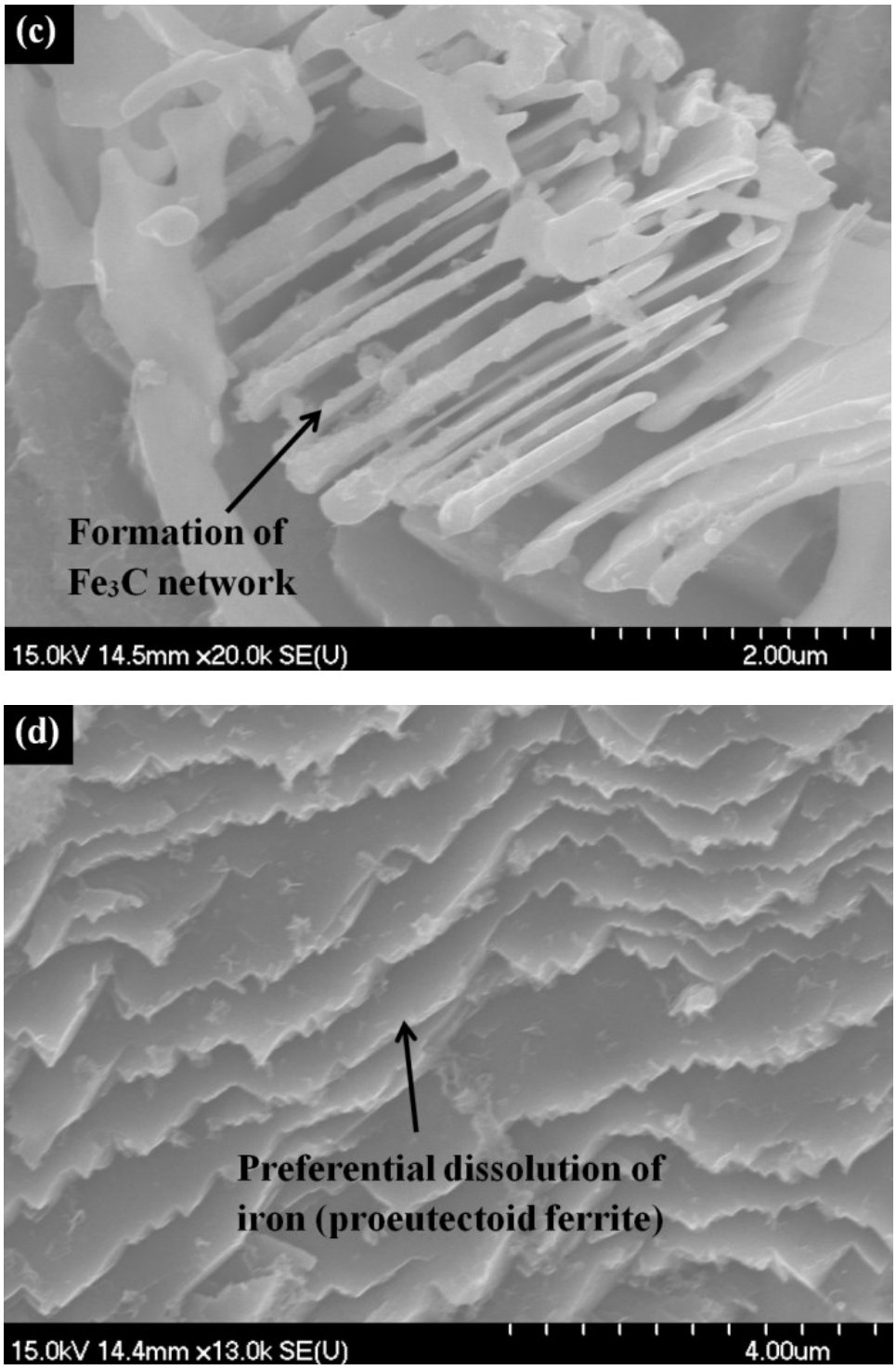

Figure 4-24 SEM images of (c) formation of cementite network due to the dissolution of eutectoid ferrite and (d) preferential dissolution of proeutectoid ferrite.

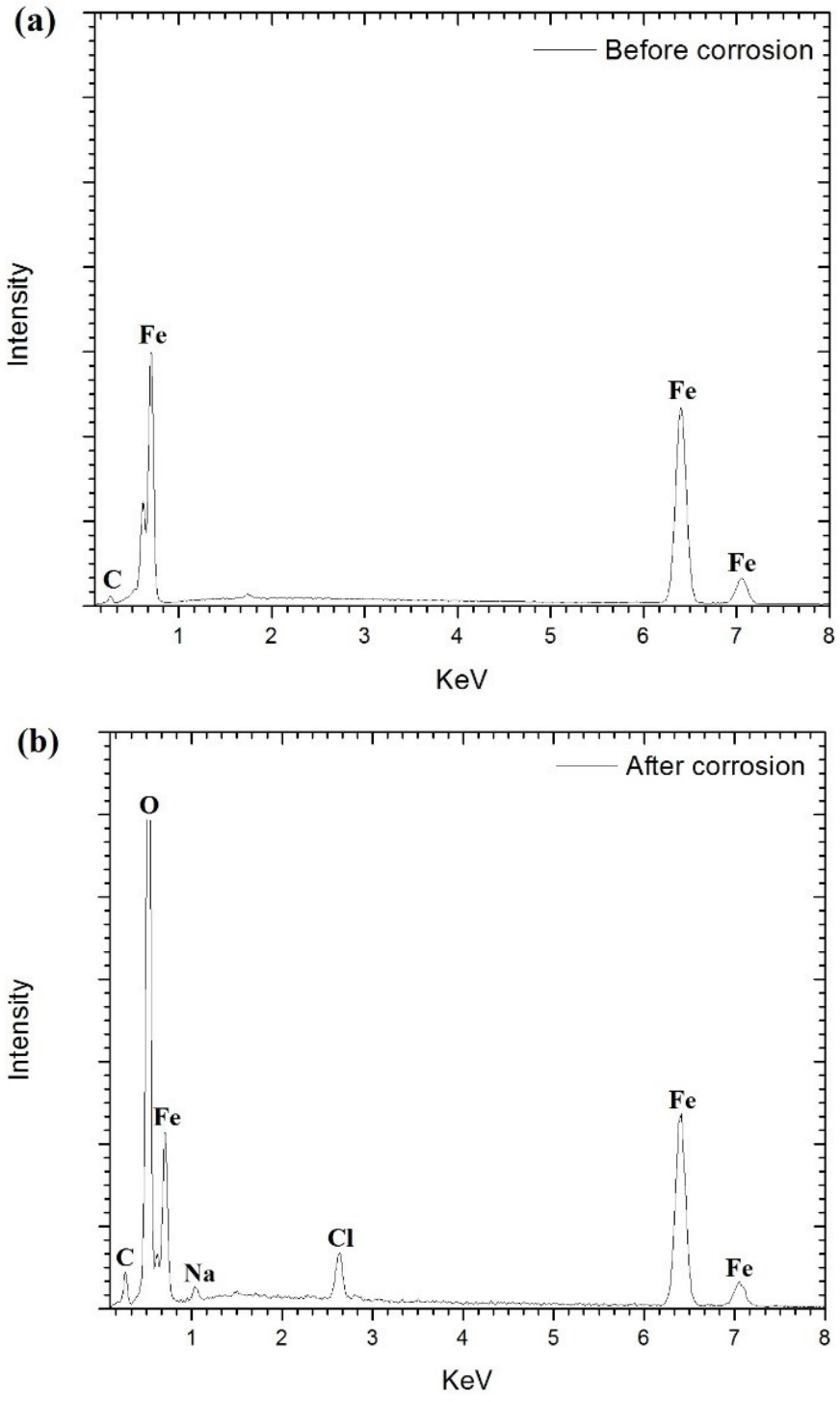

Figure 4-25 EDS analysis performed on the specimen, (a) before corrosion and (b) after corrosion.

4.2.2 Characterization of the Corrosion Layer

Corrosion of carbon steel in CO_2 containing environment is very complex and requires extensive attention. Various mechanisms have been proposed to explain the phenomenon. However, these mechanisms either apply to very specific conditions or have not received widespread recognition or acceptance. To establish a fundamental understanding of CO_2 attack on steel, it is essential to conduct further studies to investigate the formation, composition, microstructure and characteristics of the surface film induced by carbon dioxide corrosion. In order to characterize the corrosion layer, specimens were immersed in the corrosive solution (2 g l^{-1} NaCl solution purged with CO_2) for 15, 45, 100 and 185 hours (open system). Scanning electron microscopy (SEM), X-ray diffraction (XRD) and X-ray photoelectron spectroscopy (XPS) were employed systematically to characterize the composition, microstructure and formation of the surface film on API X42 steel.

The general (uniform) corrosion rates of specimens were calculated using Equation 3-3 and are plotted in Figure 4-26. Significant corrosion (0.25 mm yr^{-1}) was observed during the initial stage of immersion (after 15 hours) due to high dissolution of iron into Fe^{2+} ions. This is followed by a rapid drop in corrosion rate after 45 hours. The drop in corrosion rate is due to the formation of a passive film that provides a barrier between the steel surface and the corrosive environment. This passive layer partially protects the steel from corroding. There is around 46% decrease in corrosion rate observed as immersion time increased from 15 to 45 hours. After significant growth of the protective surface film, corrosion rate stabilizes where only around 2% and 5% decrease in corrosion rate was observed as immersion time increased from 45 to 100 hours and 100 to 185 hours, respectively.

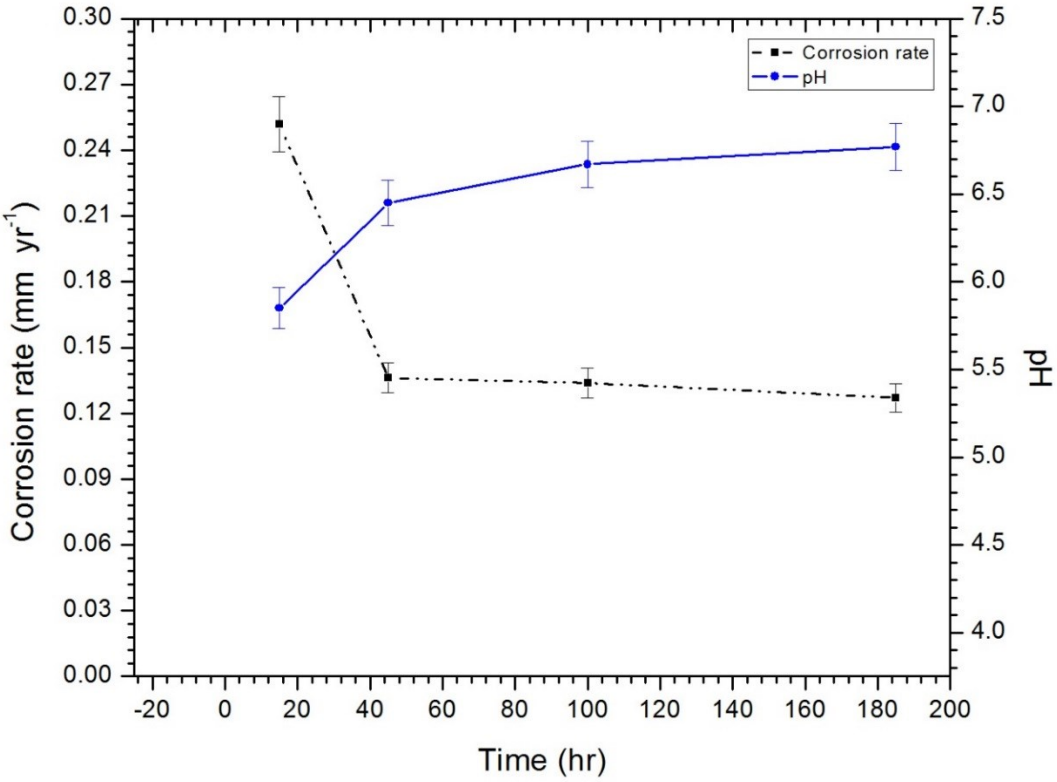

Figure 4-26 Corrosion rate and pH vs time for API X42 steel immerged in 2 g l^{-1} NaCl solution saturated with CO_2.

The pH of the solution was measured before immersing the samples and was monitored at regular time intervals (Figure 4-26). It took around half an hour to get a constant pH value. As shown in the figure, the pH of the solution increases with increasing test duration. There is around 48% increase in pH after 45 hours of immersion. Immersion corrosion test was performed in open environment (Figure 3-12). It is believed that, the rapid increase in pH at the initial stage of immersion is due to the escape of dissolved CO_2 from the test solution and the consumption of CO_2 in the electrochemical reactions. However, as time increases past 45 hours, the pH of the solution stabilizes and only 5% increase in pH was observed after 185 hours of immersion. With an increase in pH, the cathodic reaction (reduction of carbonic acid into

bicarbonate ions and reduction of bicarbonate ions into carbonate ions, Equation 2-5 (b) and (c)) rates decrease, which, in turn, slows down the anodic reaction (*i.e.*, oxidation of iron to Fe^{2+} ion, Equation 2-5 (e)). Moreover, the increase in pH value of the solution creates a favorable environment for carbonate deposition. The iron carbonate then precipitates (due to its lower solubility at higher pH) to form a protective surface film. Earlier studies have shown that a pH range of 5.6 to 6.3 is favorable for the formation of iron carbonate film [367], [368], [372]. The corrosion layer thickness of the specimens (after 15, 45, 100 and 185 hours of immersion) was measured and is plotted in Figure 4-27. As expected, the corrosion layer thickness increases with increasing test duration.

The relationship between corrosion rate and corrosion layer thickness is plotted in Figure 4-28. As expected, when the corrosion layer thickness increases the corrosion rate drops. However, it is interesting to note that, although the corrosion layer thickness almost doubled from 100 to 185 hours of immersion, the corrosion rate of the specimens after 185 hours (0.12 mm yr^{-1}) is slightly lower than the corrosion rate after 100 hours (0.13 mm yr^{-1}). This is because the relationship between corrosion rate and corrosion layer thickness resembles an exponential decay (Figure 4-28). That is, there is a critical thickness above which corrosion rate reduction becomes insignificant. In other words, above this critical thickness, corrosion rate reaches a minimum value.

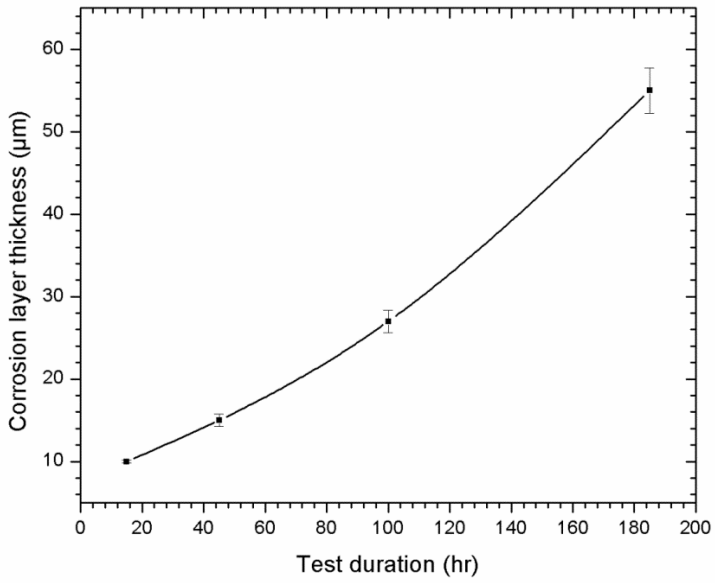

Figure 4-27 Test duration vs corrosion layer thickness of the API X42 steels immersed in the corrosive solution.

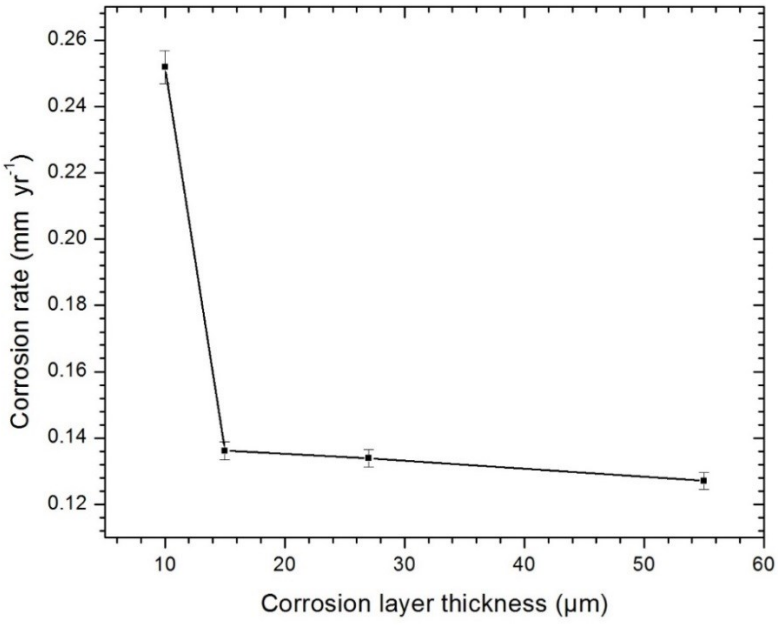

Figure 4-28 Corrosion rate vs corrosion layer thickness for API X42 steel.

4.2.2.1 SEM Analysis

Figure 4-29 shows SEM micrographs of API X42 steel illustrating the evolution of surface morphology after 15, 45, 100 and 185 hours of immersion. Few clusters of $FeCO_3$ crystals are observed in Figure 4-29 (a) after 15 hours of immersion. The plate-like iron carbonate crystals (insert in Figure 4-29 (a)) are around 5–7 μm long across the plate and about 500 nm thick and are found in random locations. Precipitation of $FeCO_3$ crystals were also observed by others [369]. EDS analysis on these crystals confirms the presence of iron, carbon and oxygen. As time progresses, a porous corrosion layer is formed (after 45 hours of immersion) due to the deposition of corrosion product (Figure 4-29 (b)). Deposition of the corrosion product gradually increases the thickness and uniformity of the corrosion layer. Figure 4-29 (c) and (d) show the surface morphology of the specimens after 100 and 185 hours of immersion, respectively.

Palacios et al., [245] describe two types of scales that form during CO_2 corrosion in brine solution. The primary scale, forms directly on the corroding metal surface, which is non-uniform (spotty), and adherent, while secondary scale forms on top of the primary scale. This secondary scale is porous and flaky (poor adhesion to the steel surface). Figure 4-30 (a) shows this type of primary and secondary corrosion layers. EDS analysis were performed on the primary and secondary corrosion layers, marked as location 'b' and 'c' respectively, in Figure 4-30 (a). Figure 4-30 (b), (c) show the EDS spectrum at locations 'b' and 'c', respectively. The results of the analysis are given in Table 4-8 (Na and Cl are the residue from the corrosive solution).

Both primary and secondary corrosion layers consist of Fe, C, O, Na and Cl. However, as compared to the primary corrosion layer, the secondary corrosion layer consists of about 39% more oxygen. It is believed that the higher oxygen

content in the secondary corrosion layer is due to the formation of different iron oxides during corrosion.

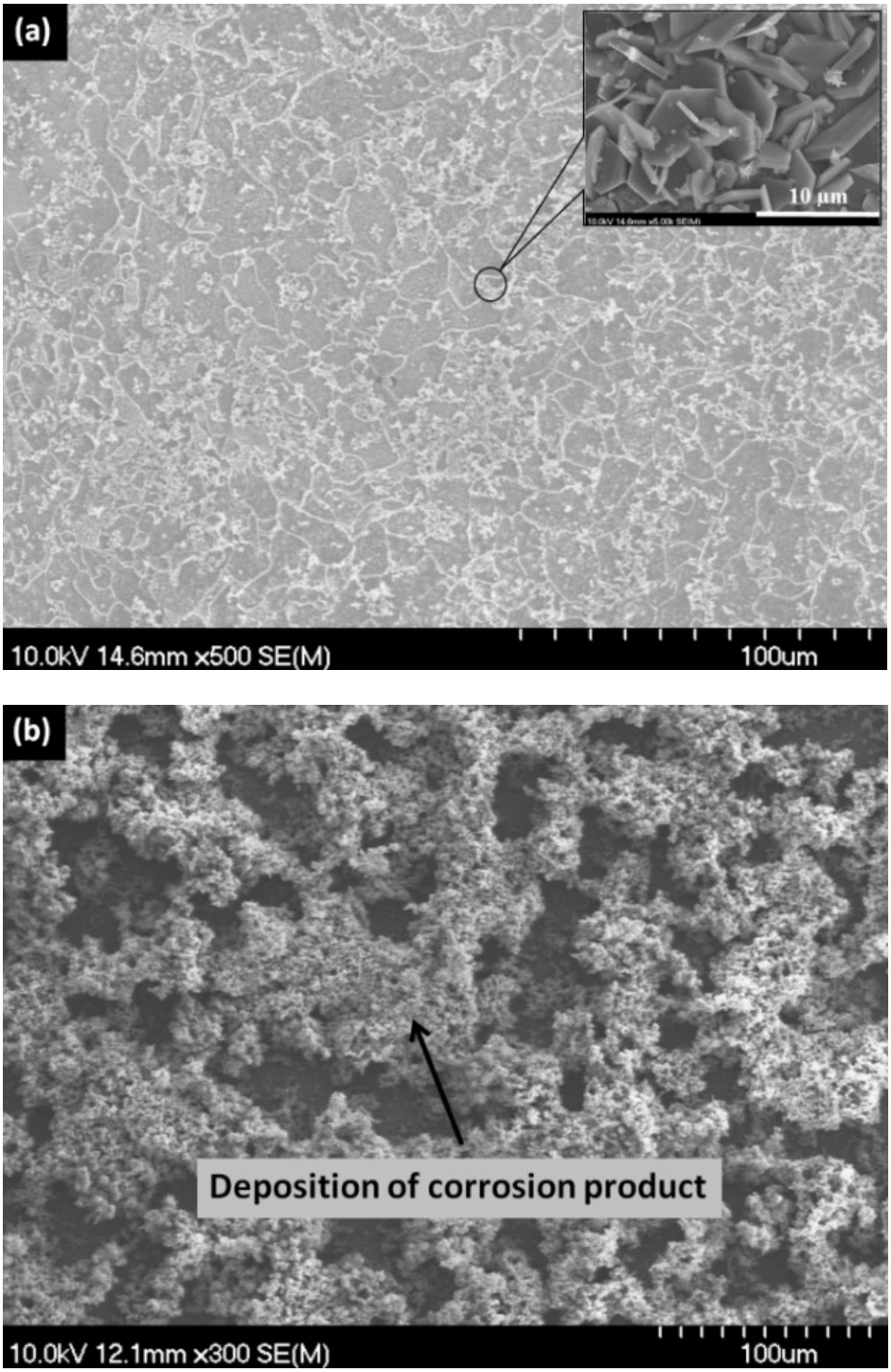

Figure 4-29 SEM micrograph of the API X42 steel after immersion tests (a) surface morphology after 15 hours of immersion and (b) surface morphology after 45 hours of immersion.

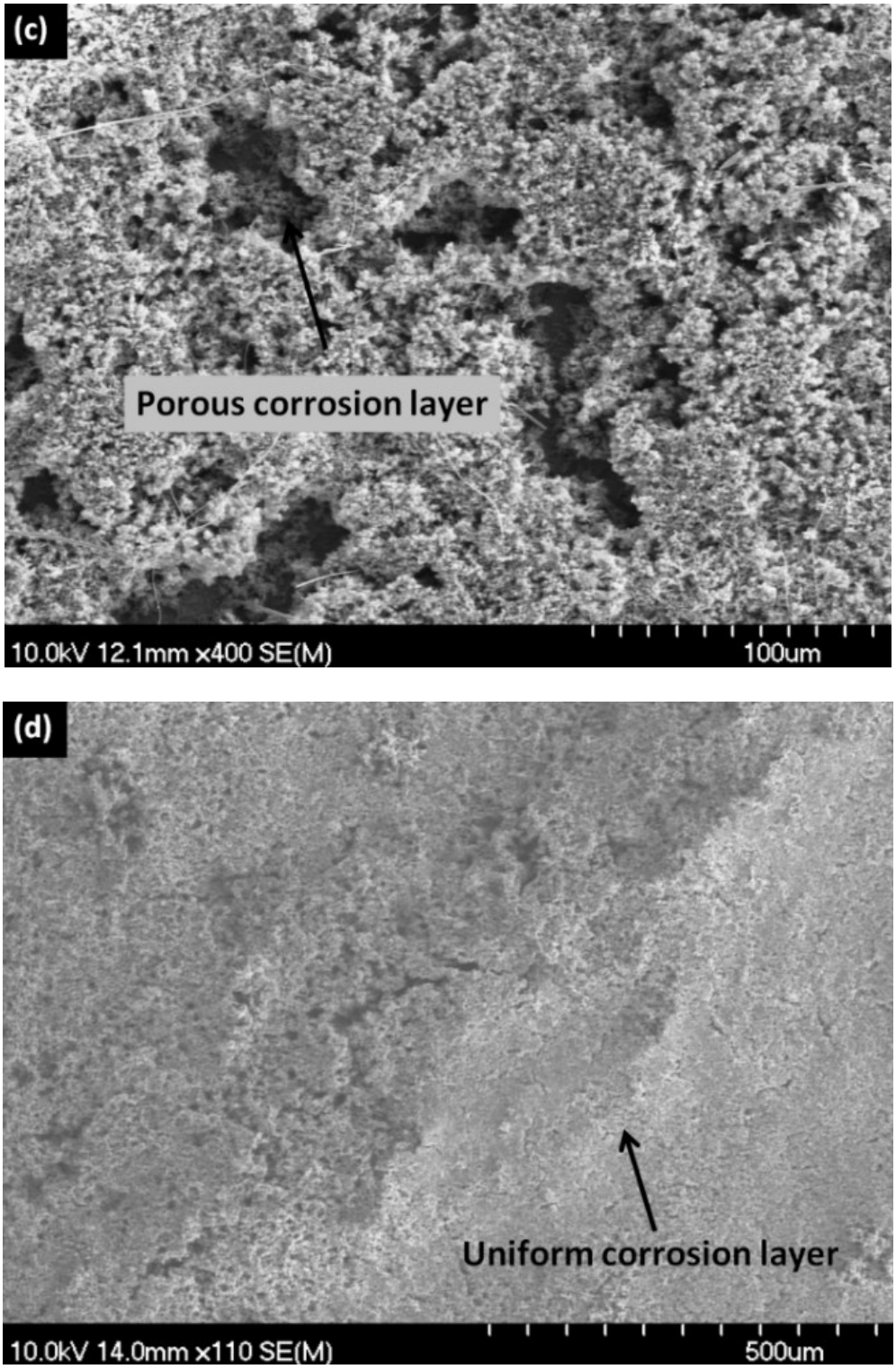

Figure 4-29 SEM micrograph of the API X42 steel after immersion tests, (c) surface morphology after 100 hours of immersion and (d) surface morphology after 185 hours of immersion.

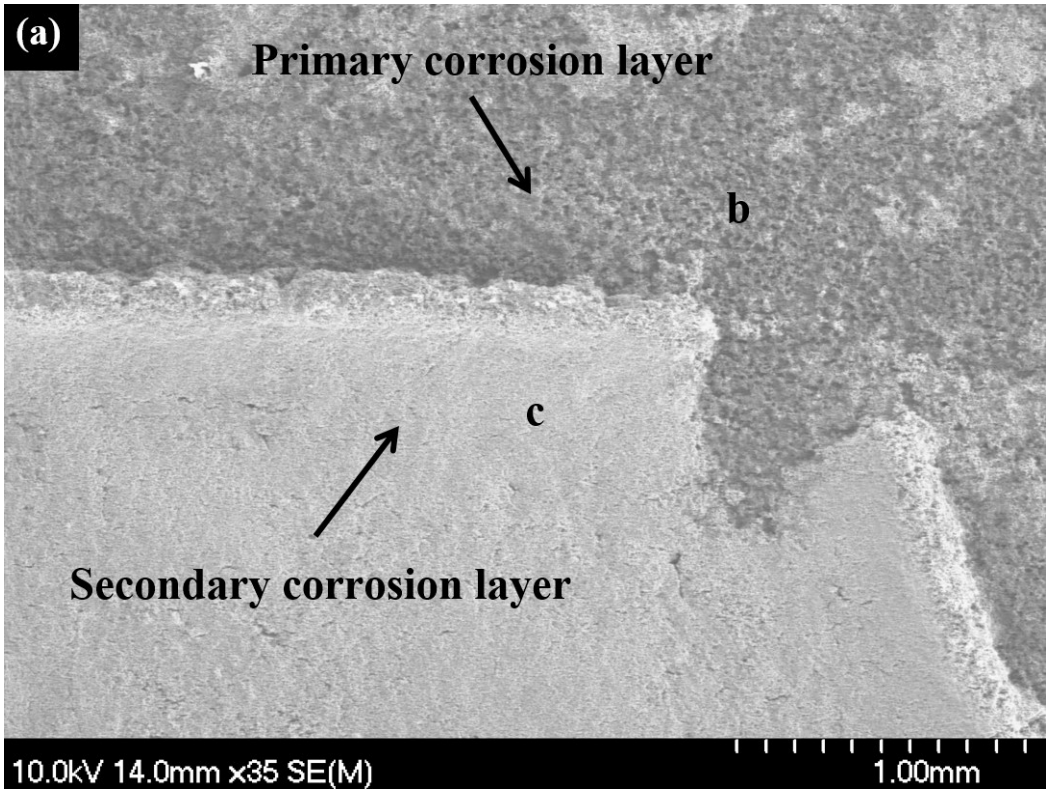

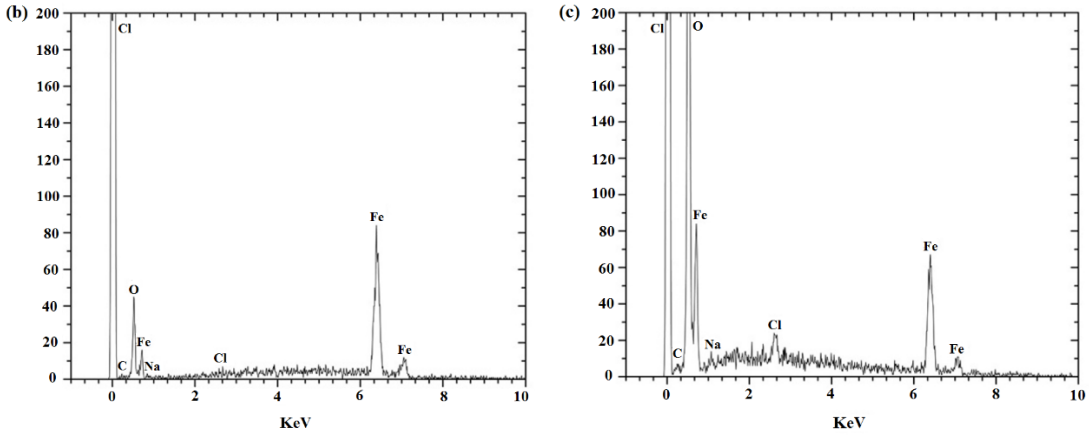

Figure 4-30 SEM micrograph of the corrosion layer after 45 hours of immersion,(a) fracture and partial detachment of the secondary corrosion layer, (b) EDS analysis on the primary corrosion layer (point b) and (c) EDS analysis on the secondary corrosion layer (point c).

Table 4-8 EDS elemental analysis of the primary and secondary corrosion layers.

Element	Primary corrosion layer (point b)		Secondary corrosion layer (point c)	
	Weight (%)	Atomic (%)	Weight (%)	Atomic (%)
C	0.84	2.13	0.96	2.07
O	31.92	60.66	44.32	71.86
Na	0.42	0.55	0.49	0.61
Cl	0.87	0.74	2.41	1.77
Fe	65.96	35.91	51.82	24.10

4.2.2.2 X-ray Diffraction

In order to identify the crystallographic structure and the composition of the corrosion layers, XRD experiments were carried out on the corroded surfaces and on the uncorroded base material as a reference. Figure 4-31, show the XRD diffraction patterns for API X42 steel prior to testing and after 15, 45 and 100 hours of immersion time. Diffraction patterns were then matched with reference patterns of pure substances from the powder diffraction database. Table 4-9 shows the identified compounds with their matched 2θ values, diffraction planes and crystallographic structures. A trace amount of NaCl was also identified in all of the corroded samples. With increasing the immersion duration, more peaks appear on the XRD pattern. According to XRD analysis, it can be concluded that a primary corrosion layer forms after 15 hours of immersion and mainly consists of a thin scale of $FeCO_3$. Secondary corrosion layer forms after 45 hours of immersion and consists of $FeCO_3$ and Fe_2O_3. After 100 hours of immersion, FeO starts to form on top of the secondary corrosion layer along with $FeCO_3$ and Fe_2O_3. This top layer has compact and flaky appearance and is termed, in the present work, as 'tertiary' corrosion layer.

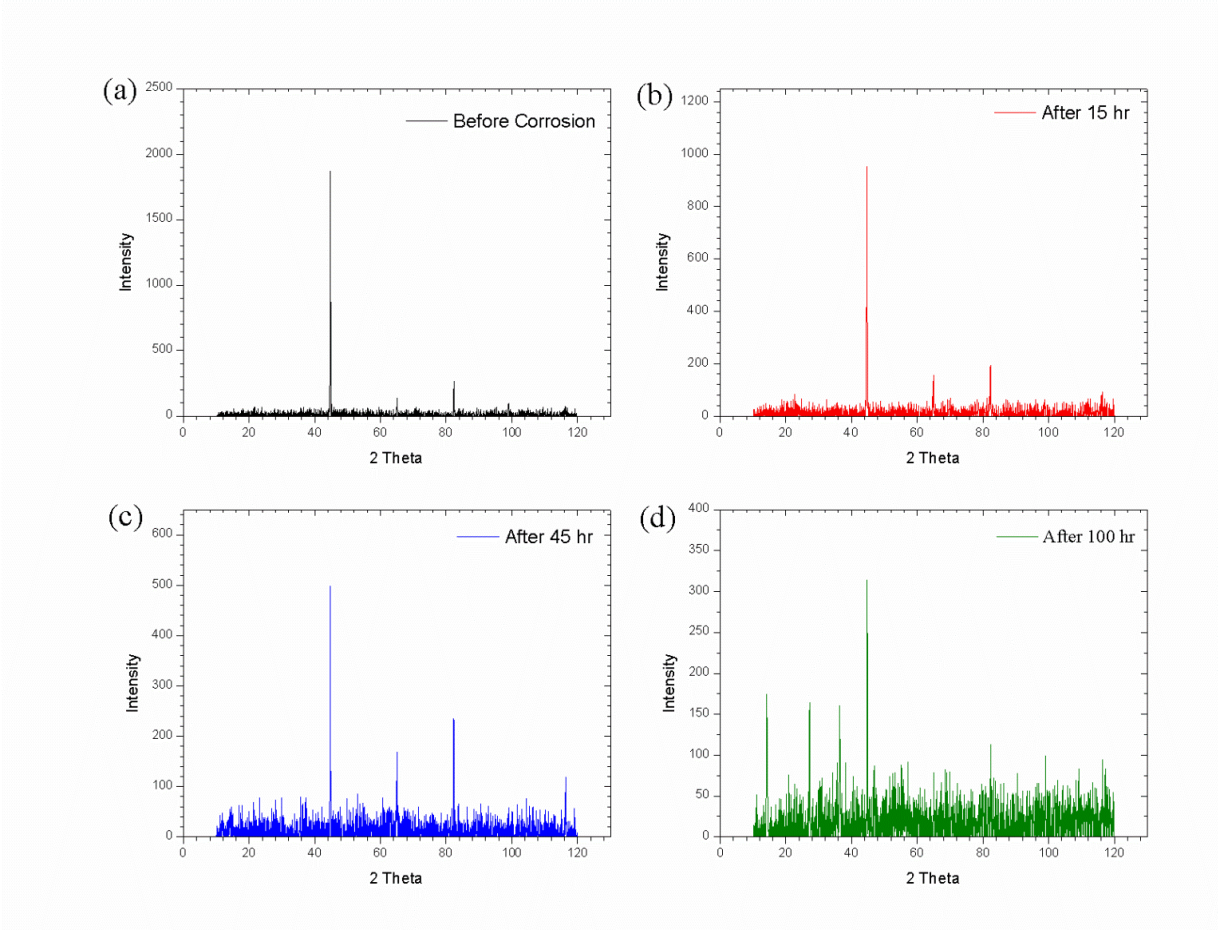

Figure 4-31 XRD analysis of API X42 steel, (a) before corrosion, (b) after 15 hours, (c) after 45 hours and (d) after 100 hours of immersion.

Table 4-9 Identification of elements and compounds in the corrosion layers of API X42 steel.

Test duration	Identified element	2θ values	Diffraction planes	Crystal structure
Before corrosion	Fe	44.6, 65.0, 82.3	(110), (200), (211)	BCC
After 15 hours	Fe	44.6, 65.0, 82.3	(110), (200), (211)	BCC
	$FeCO_3$	24.7, 32.0, 52.8	(012), (104), (116)	Rhombohedral
After 45 hours	Fe	44.6, 65.0, 82.3	(110), (200), (211)	BCC
	$FeCO_3$	24.7, 32.0, 52.8	(012), (104), (116)	Rhombohedral
	Fe_2O_3	30.2, 35.6, 62.9	(220), (311), (440)	Cubic
After 100 hours	Fe	44.6, 65.0, 82.3	(110), (200), (211)	BCC
	$FeCO_3$	24.7, 32.0, 52.8	(012), (104), (116)	Rhombohedral
	Fe_2O_3	30.2, 35.6, 62.9	(220), (311), (440)	Cubic
	FeO	35.9, 41.7, 60.4	(111), (200), (220)	FCC

4.2.2.3 EDS Mapping

In order to define the nature of the corrosion layers more accurately, elemental mapping of C, O and Fe on the cross-section of the corrosion layer was performed using EDS. Figure 4-32 shows the EDS mapping done on the cross-section of the specimen after 15 hours of immersion in the corrosive solution. The distribution of the elements is inhomogeneous, showing a thin corrosion layer on the surface enriched in oxygen and carbon and depleted in iron. Point and ID analysis on the cross-section of the specimens were performed to identify the composition (as relative percentage) of these elements. Three arbitrary locations on the corrosion layer (after 100 hours of immersion) and three on the base material were selected for this analysis as shown in Figure 4-33. Figure 4-34 shows the relative comparison of C, O and Fe in the base material and corrosion layer. It is evident that the percentages of carbon and oxygen in the corrosion film are higher than in the base material due to the formation of iron carbonate and different forms of iron oxides in the corrosion layer.

Although, the corrosion film is enriched in C and O, the compositions of C, O and Fe are not uniform across the layer. Point and ID analysis on the cross-section of the specimen across the corrosion layer were performed to identify the % change in composition of these elements. Figure 4-35 shows six different points where the EDS analysis was performed, in which point 1 is on the base material (reference) and points 2-6 are on the corrosion layer at an incremental distance from the base material. Analysis results are given in Table 4-10, which shows the distribution of C, O and Fe along the corrosion layer. There is an increase in oxygen content observed with increasing distance from the base material. Immersion corrosion tests were performed in open environment and the presence of higher oxygen content away from base metal suggests the existence of dissolved oxygen in the solution. Baek et al., [373] studied the effect of dissolved oxygen on the corrosion film of low carbon

steel and concluded that dissolved oxygen in the solution acts as an oxidant and transforms Fe_3O_4 to Fe_2O_3. It also accelerates the transformation of FeO to Fe_2O_3. Hence, it may be concluded that, secondary and tertiary corrosion layers (away from base), in addition to $FeCO_3$, may contain iron oxides (Fe_2O_3 or FeO) compared to the primary corrosion layer (close to the base). These results are in good agreement with XRD results discussed above.

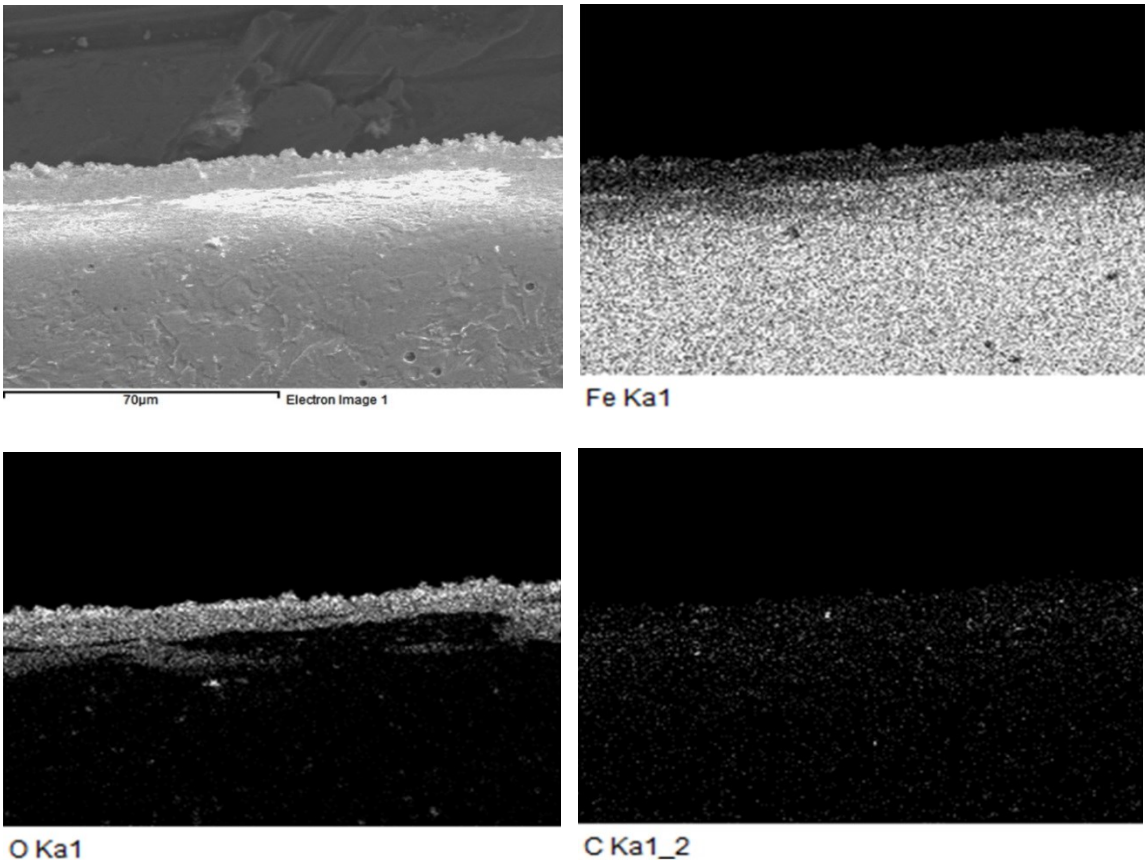

Figure 4-32 **EDS mapping of the cross-section of the specimen after immersion in the corrosive solution for 15 hours. Elemental mapping of iron, oxygen and carbon on the cross-section of the corrosion layer.**

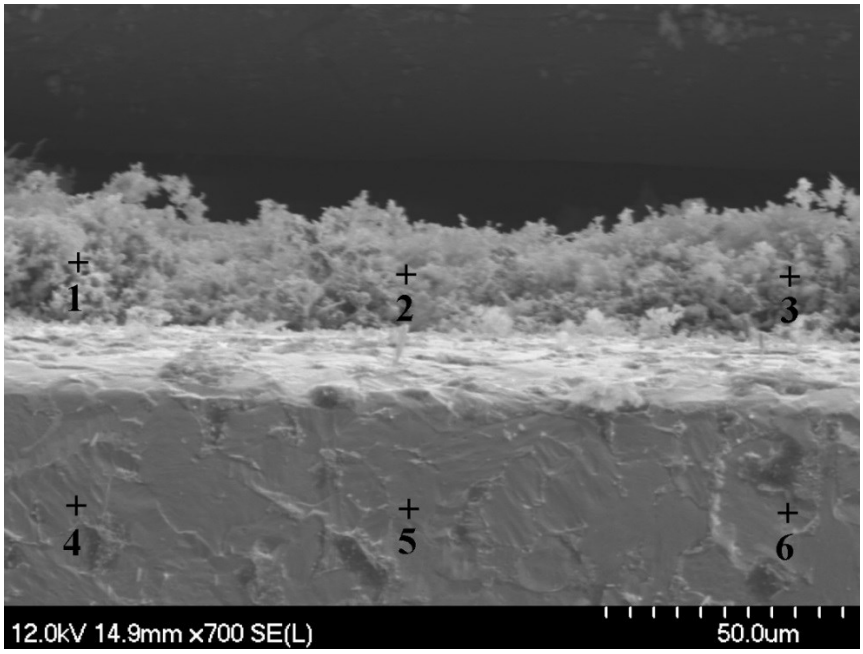

Figure 4-33 EDS (point and ID) analysis on the cross-section of the specimen after 100 hours of immersion in the corrosive solution.

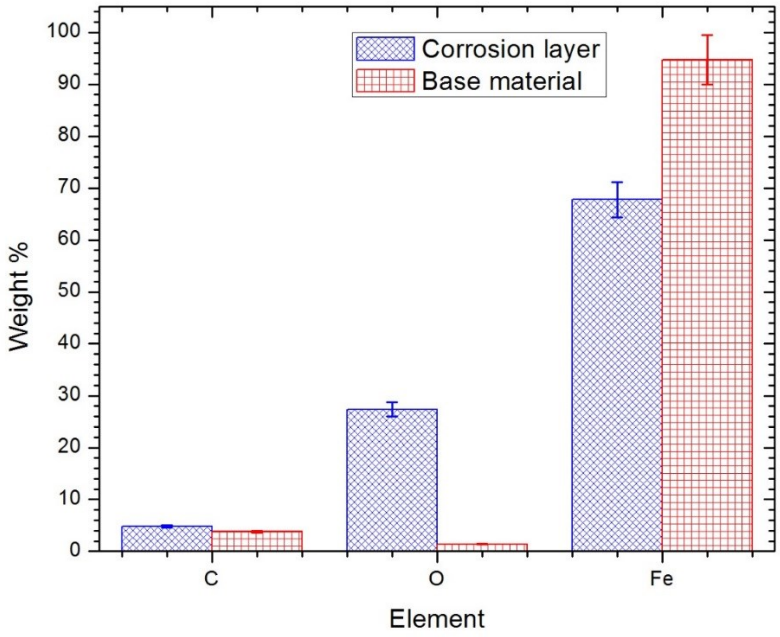

Figure 4-34 Relative comparison of C, O and Fe in the base material and corrosion layer after 100 hours of immersion.

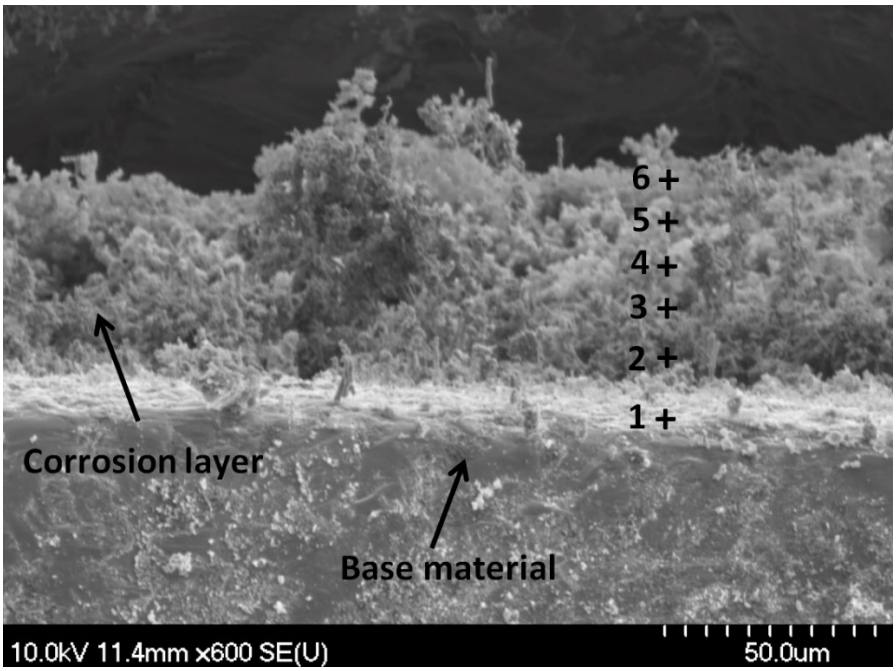

Figure 4-35 EDS (point and ID) analysis on the cross-section of the specimen along the corrosion layer after 185 hours of immersion in the corrosive solution.

Table 4-10 EDS analysis results of the cross-section of the specimen along a line perpendicular to the corrosion layer after immersion in the corrosive fluid for 185 hours.

Spectrum location	Spectrum no	Element					
		C		O		Fe	
		Weight %	Atomic %	Weight %	Atomic %	Weight %	Atomic %
Base material	1	6.47	24.09	0.52	1.45	93.01	74.44
Corrosion layer	2	8.55	16.53	43.93	63.71	47.52	19.74
	3	8.93	17.07	44.47	63.77	46.60	19.14
	4	8.59	16.41	45.05	64.55	46.36	19.03
	5	8.12	15.13	48.18	67.35	43.70	17.50
	6	7.71	13.56	54.74	72.23	37.55	14.19

4.2.2.4 XPS Analysis

EDS analysis performed on the corrosion films revealed the presence of significant amounts of iron and oxygen. However, several iron products contain these elements including iron carbonate ($FeCO_3$), ferrous oxide (FeO), hematite (Fe_2O_3) and magnetite (Fe_3O_4). XPS can reveal chemical state information of a substance and therefore, was performed on the corrosion layers to identify the corrosion products present. A survey scan (1 eV steps) covering a wide binding energy range was performed. All major peaks in the survey scan have been identified. Figure 4-36 shows the survey scan on the secondary corrosion layer of API X42 steel. As expected, strong iron, oxygen, and carbon spikes were observed. High resolution scans were performed with 0.1 eV steps over the following regions of interest: C 1s, O 1s and Fe 2p, before and after 10, 30 and 150 min Ar^+ sputtering cleaning process. Argon ion sputtering for different time intervals was performed in an attempt to identify the relative amount of different compounds as a function of depth within the corrosion layers.

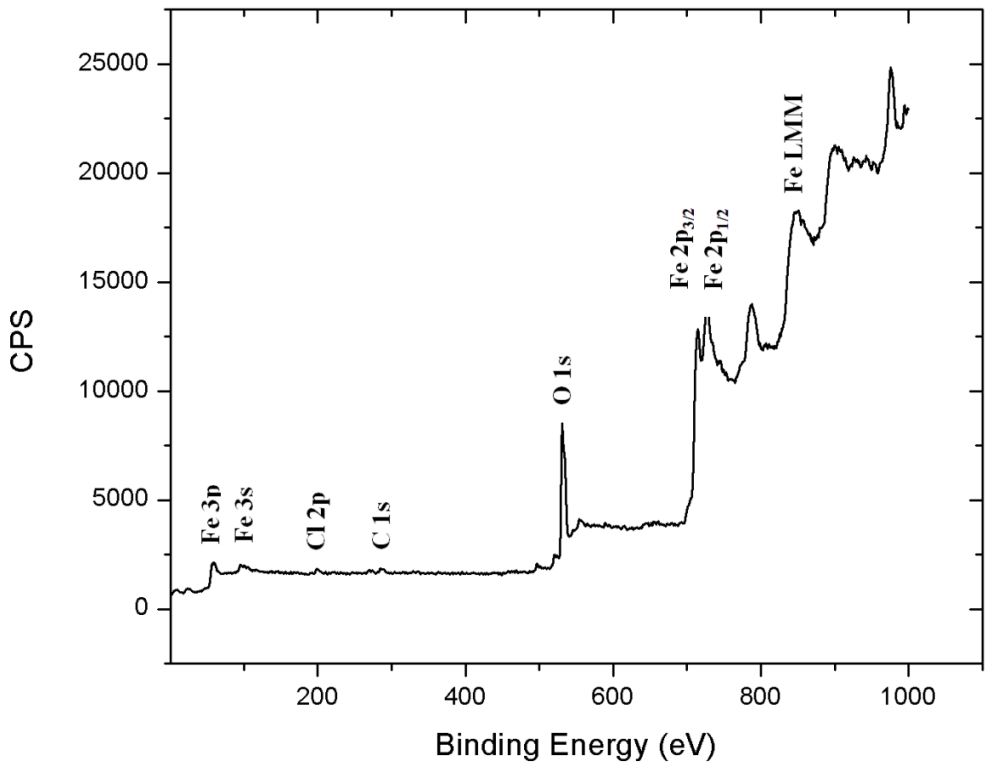

Figure 4-36 Survey scan on the corrosion layer of API X42 after 45 hours of immersion.

4.2.2.4.1 C 1s Spectra

Figure 4-37 shows the C 1s high resolution XPS scans on the corrosion layer of API X42 steel for different Ar^+ sputtering times. Decomposition of multiple peaks in the C 1s region were performed, and the results are shown in Figure 4-37 (a)-(d) after 0, 10, 30 and 150 min Ar^+ sputtering. Binding energies and relative intensities are listed in Table 4-11. Two peaks are evident near 285.2 eV and 289 eV BE before the sputter-cleaning process. The one at 285.2 eV corresponds to residual carbon [319], [374], and the small peak at about 289 eV is attributed to iron carbonate [242]. For all the scans before and after sputtering, the peak labeled as (i), is associated with carbon and the peak labeled as (ii), is associated with $FeCO_3$. Based on the XPS data, we can conclude that, the corrosion layer consists of different proportions of the same chemical compounds at various distances from the base material.

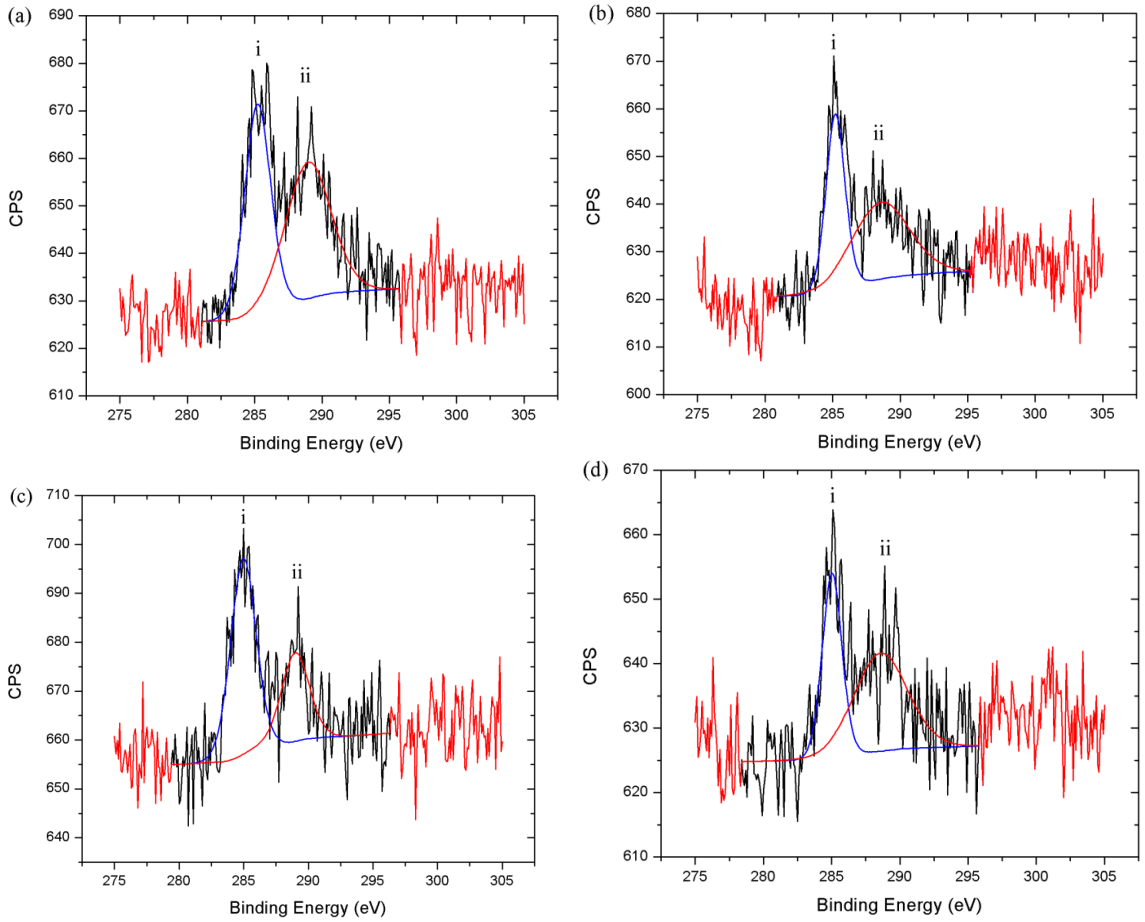

Figure 4-37 XPS spectra for C 1s region after 45 hours of immersion for different sputtering times, (a) after 0 min Ar^+ sputtering, (b) after 10 min Ar^+ sputtering, (c) after 30 min Ar^+ sputtering and (d) after 150 min Ar^+ sputtering.

Table 4-11 Binding energies and relative intensities of the C 1s signals.

Sample	BE (eV)	Weight %	Peak
0 min Ar^+	285.2	46.7	(i) Graphitic
	289.0	53.3	(ii) $FeCO_3$
10 min Ar^+	285.2	43.5	(i) Graphitic
	288.6	56.5	(ii) $FeCO_3$
30 min Ar^+	285.0	66.7	(i) Graphitic
	289.0	33.3	(ii) $FeCO_3$
150 min Ar^+	285.0	40.1	(i) Graphitic
	288.6	59.0	(ii) $FeCO_3$

4.2.2.4.2 O 1s Spectra

XPS spectra corresponding to the O 1s region for different sputtering times and the decomposition of the peaks are shown in Figure 4-38. Table 4-12 presents the binding energies and relative intensities corresponding to each peak. The peak associated with iron carbonate in the O 1s region is at 531.9 eV [242], [374] is superimposed on the dominant hydroxyle peak at 531.6 eV due to the chemisorption of water or oxygen [242], [319], [374]. This makes the identification of $FeCO_3$ difficult. For all the scans before and after sputtering, the peak (i) is attributed to oxidized species (O^{2-}), the peak labeled as (ii), is assigned to hydroxyle species (HO^-) and the peak labeled as (iii) is associated with H_2O. The Ar^+ sputtering for 30 and 150 min does not show peak (iii) corresponding to adsorbed water [375], [376].

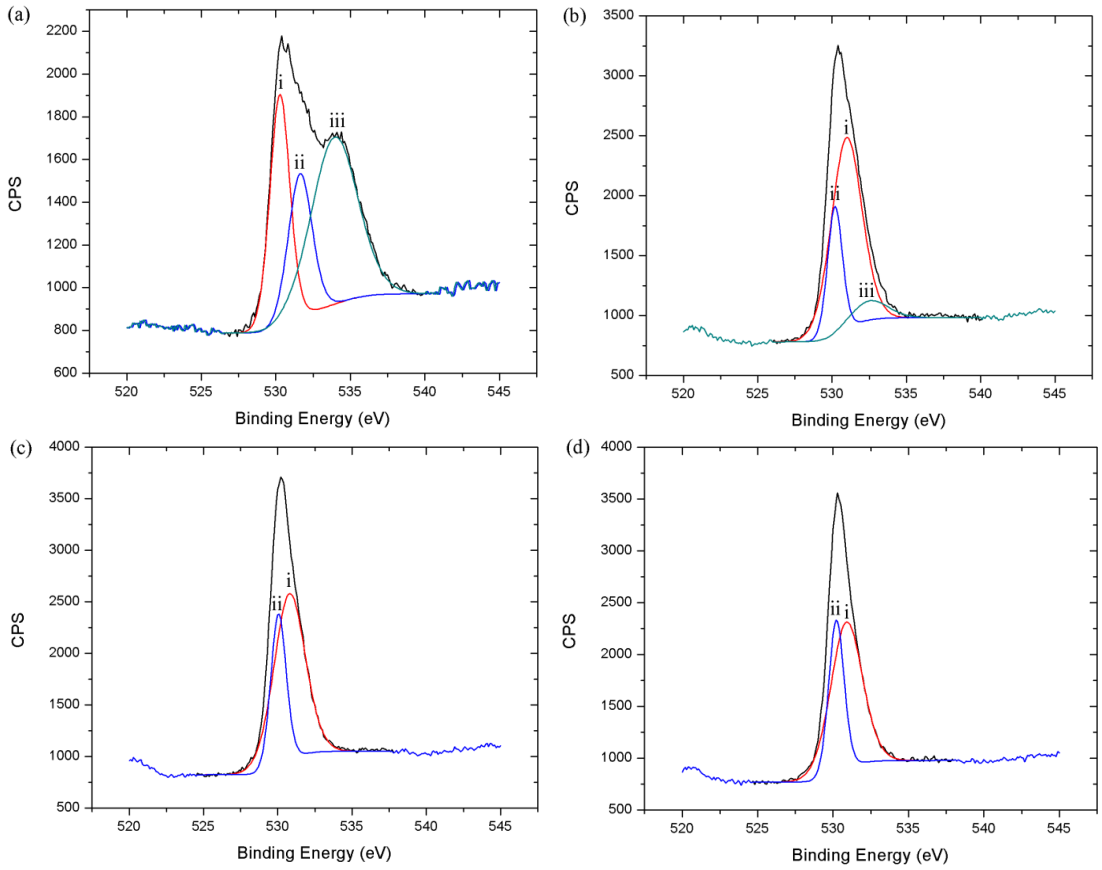

Figure 4-38 XPS spectra for O 1s region after 45 hours of immersion for different sputtering times, (a) after 0 min Ar^+ sputtering, (b) after 10 min Ar^+ sputtering, (c) after 30 min Ar^+ sputtering and (d) after 150 min Ar^+ sputtering.

Table 4-12 Binding energies and relative intensities of the O 1s signals.

Sample	BE (eV)	Weight %	Peak
0 min Ar^+	530.3	29.4	(i) O^{2-}
	531.6	21.7	(ii) HO^-
	534.0	48.9	(iii) H_2O
10 min Ar^+	530.2	22.5	(i) O^{2-}
	531.0	69.3	(ii) HO^-
	532.5	8.2	(iii) H_2O
30 min Ar^+	530.0	31.1	(i) O^{2-}
	530.8	68.9	(ii) HO^-
150 min Ar^+	530.2	33.7	(i) O^{2-}
	530.9	66.3	(ii) HO^-

4.2.2.4.3 Fe 2p Spectra

XPS spectra and the decomposition of peaks in the region of Fe $2p_{3/2}$ at various sputtering times (0, 10, 30 and 150 min) are shown in Figure 4-39. Binding energies and relative intensities for these peaks are given in Table 4-13.

The presence of iron carbonate and oxidized species are evidenced from the XPS spectra. Two Fe $2p_{3/2}$ peaks were observed near 711 eV (peak (i)) and around 719.1 eV (peak (iii)). These Fe $2p_{3/2}$ peaks (711 eV and 719.1 eV) and the O 1s peak at 530.3 eV both fall in the binding energy range covered by Fe_2O_3 [319], [374]. The peak at around 714.1 eV (peak (ii)) is associated with $FeCO_3$. The corrosion reactions (Equation 2-5) do not predict the formation of Fe_2O_3. This may suggest that, Fe_2O_3 forms by partial decomposition of $FeCO_3$ as evident from XPS analysis [242]. The decomposition process that iron carbonate may undergo at temperatures below 100° C (leading to Fe_2O_3) is shown in Equation 4-2 (a)-(e) [242]. Dissolved oxygen in the solution (as evident from EDS analysis) promotes the formation of Fe_2O_3 during the decomposition process.

$$FeCO_3 = FeO + CO_2 \qquad \text{Equation 4-2 (a)}$$

$$4FeO + O_2 = 2Fe_2O_3 \qquad \text{Equation 4-2 (b)}$$

$$3FeO + CO_2 = Fe_3O_4 + CO \qquad \text{Equation 4-2 (c)}$$

$$3FeO + H_2O = Fe_3O_4 + H_2 \qquad \text{Equation 4-2 (d)}$$

$$4Fe_3O_4 + O_2 = 6Fe_2O_3 \qquad \text{Equation 4-2 (e)}$$

The intensity of carbonate peak (ii) decreases significantly after the sputter-cleaning process. All the peaks corresponding to (i), (ii) and (iii), shifted to lower binding energy from 711 eV, 714.1 eV and 719.1 eV to 710.3 eV, 712.7 eV and 717.5 eV respectively, after 150 min Ar^+ sputtering. However, in the current study, there was no peak observed at around 709.7 eV (characteristic

of FeO), which is in agreement with the XRD data confirming the absence of FeO in the secondary corrosion layer.

The appearance of an additional peak at 707 eV for the metallic iron after sputtering is frequently used in order to estimate the thickness of the oxide layers by XPS [377], [378]. However, in this study, the thicknesses of the corrosion layers is greater than the depth of the XPS analysis even after long periods of Ar^+ sputtering (100 nm / hour). Therefore, the appearance of the peak corresponding to metallic iron didn't appear in the XPS spectrum.

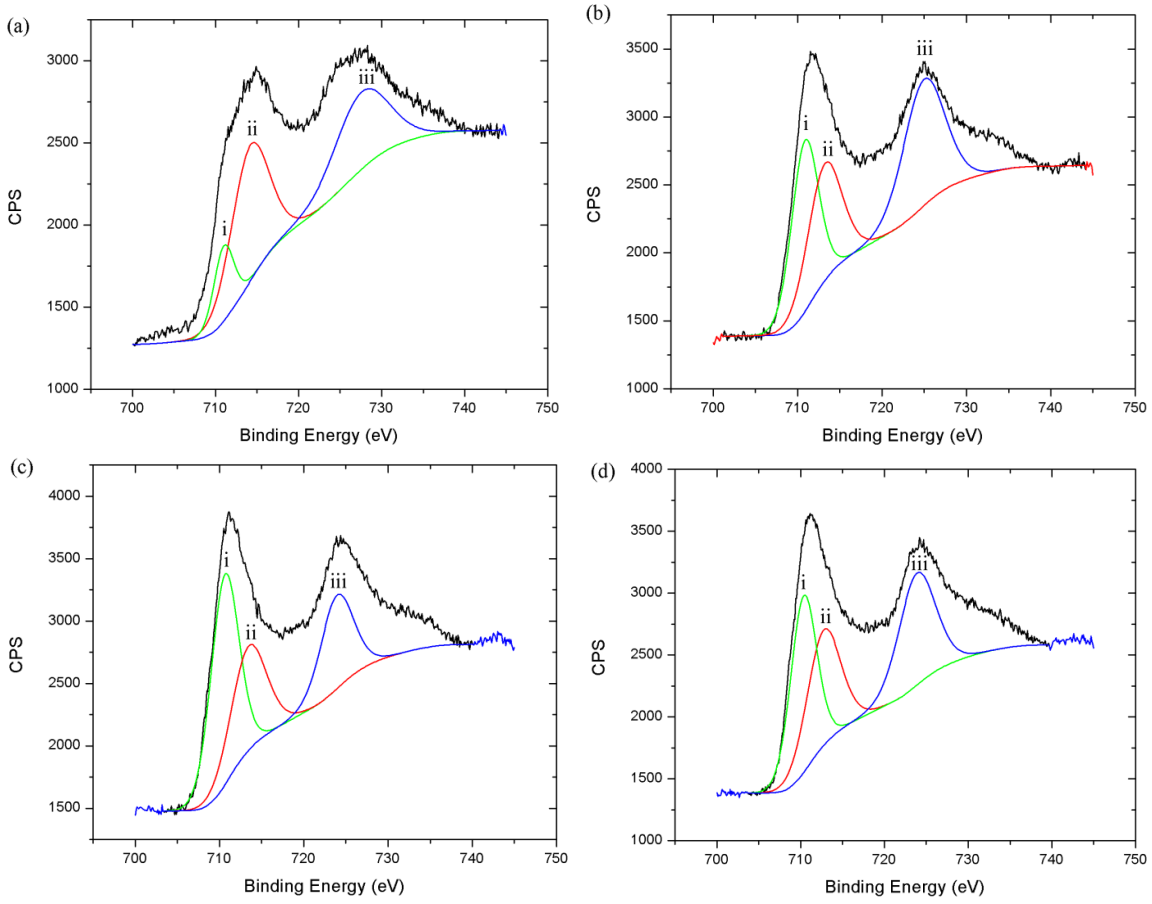

Figure 4-39 **XPS spectra for Fe $2p_{3/2}$ region after 45 hours of immersion for different sputtering times, (a) after 0 min Ar^+ sputtering, (b) after 10 min Ar^+ sputtering, (c) after 30 min Ar^+ sputtering and (d) after 150 min Ar^+ sputtering.**

Table 4-13 Binding energies and relative intensities of the Fe $2p_{3/2}$ signals.

Sample	BE (eV)	Weight %	Peak
0 min Ar^+	711.0	9.4	(i) Fe_2O_3
	714.1	32.0	(ii) $FeCO_3$
	719.1	58.6	(iii) Fe_2O_3
10 min Ar^+	710.8	36.4	(i) Fe_2O_3
	713.2	31.5	(ii) $FeCO_3$
	718.4	32.0	(iii) Fe_2O_3
30 min Ar^+	710.6	44.6	(i) Fe_2O_3
	713.4	28.1	(ii) $FeCO_3$
	718.5	27.3	(iii) Fe_2O_3
150 min Ar^+	710.3	37.3	(i) Fe_2O_3
	712.7	31.6	(ii) $FeCO_3$
	717.5	31.1	(iii) Fe_2O_3

4.2.2.5 Microstructural Factors

It is believed that the reason behind the good adhesion of the primary layer is the anchoring of corrosion layer by the pearlite phase. Figure 4-24 (a) shows an SEM micrograph of etched as-received API X42 steel, while Figure 4-24 (b) shows a magnified image (within the circle) of Figure 4-24 (a) illustrating the pearlitic and proeutectoid ferritic microstructure before corrosion. The surface morphology of the steel after it was immersed in the corrosive solution (2 g l^{-1} NaCl saturated with CO_2) for 15 hours is shown in Figure 4-40 (a). Figure 4-40 (b) shows the magnified image (within the circle) of Figure 4-40 (a). Here, preferential dissolution of eutectoid ferrite (within pearlite) takes place leaving behind a cementite network along with corrosion products. It is generally agreed that ferrite is anodic to cementite (Fe_3C) in CO_2 environment [367], [368].

Preferential dissolution of eutectoid ferrite increases the local concentration of ferrous ions in the cavities between the cementite platelets. Higher local

Fe^{2+} ion concentration allows the formation of $FeCO_3$ crystals between the cementite platelets. The iron carbonate layer that forms on the pearlite phase is well adherent to the surface as the cementite networks help to anchor it down. The film formed on the proeutectoid phase is believed to be less adherent. Similar behavior has been reported in the literature [245], [379]. It is concluded that the anchoring effect induced by the pearlitic structure gives the primary corrosion layer its good adhesion properties. However, since pearlite is only present in random locations along the steel surface, the primary corrosion layer appears to be non-uniform (spotty).

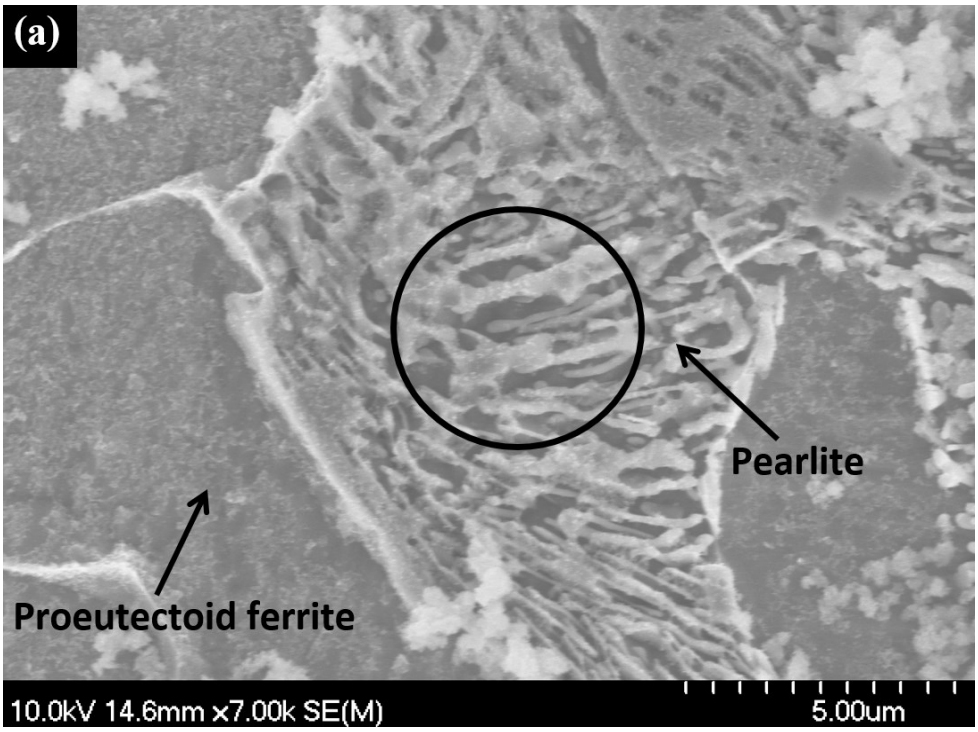

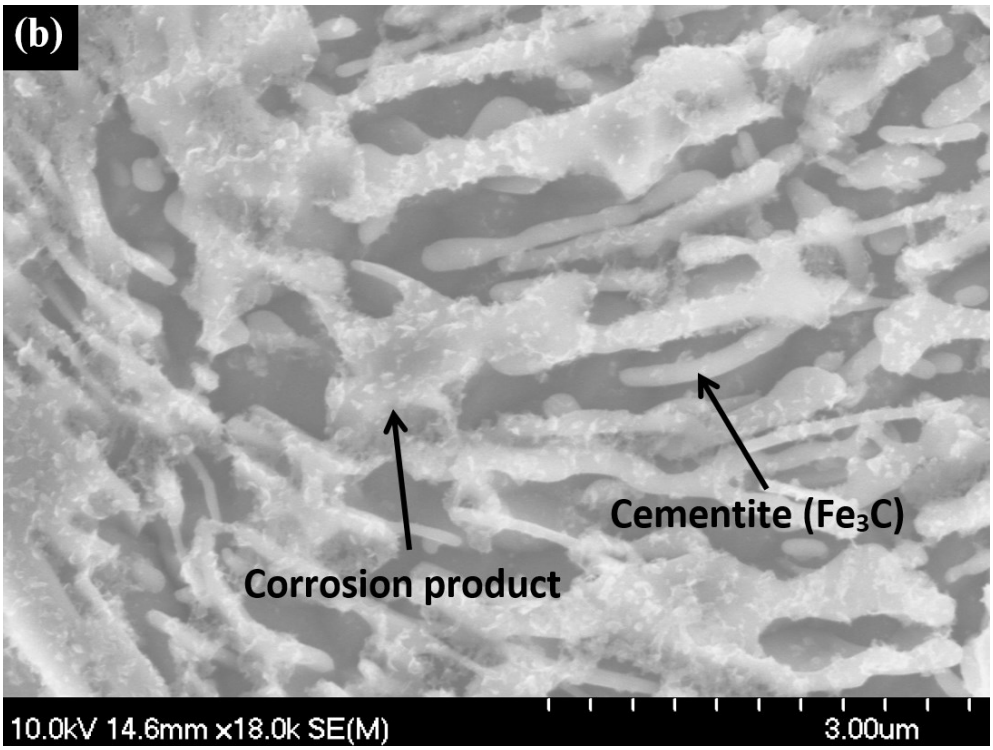

Figure 4-40 SEM images of (a) surface morphology after 15 hours of immersion and (b) magnified image of Figure 4-40 (a) (marked as a circle). Dissolution of eutectoid ferrite creates cementite network in pearlite and corrosion products deposit on the cementite network.

4.2.3 Summary

The pH of the solution plays an important role during corrosion. The pH of the solution increases with increasing test duration due to the escape of CO_2 from the test solution. At the initial stage of corrosion (low pH), increase in pH of the solution leads to the reduction in corrosion rate by influencing the electrochemical mechanisms. However, as the pH reaches a steady state value after 100 hours of immersion (as observed in this study), it reduces the corrosion rate by creating a favorable condition (the solution becomes saturated with Fe^{2+} ions) for the precipitation of iron carbonate ($FeCO_3$). Corrosion rate decreases with increasing test duration due to the formation of protective surface film.

Corrosion scale consists of primary, secondary and tertiary layers. Figure 4-41 shows a schematic diagram illustrating the formation and composition of primary, secondary and tertiary corrosion layers. Primary corrosion layer is non-uniform (spotty) and adherent to the surface. However, secondary corrosion layer is porous, flaky and tertiary corrosion layer is compact and flaky. XRD, EDS and XPS analysis confirms the presence of primary corrosion layer having a thickness of around 10 μm (after 15 hours of immersion) and consists mainly of a thin layer of iron carbonate. The iron carbonate layer that forms on the pearlite phase is well adherent to the surface as the cementite networks helps to anchor it down. The film formed on the proeutectoid phase is believed to be less adherent. Primary corrosion layer significantly decreases the corrosion rate. Deposition of corrosion products on top of the primary corrosion layer forms a porous, flaky secondary corrosion layer. Secondary corrosion layer is observed after 45 hours of immersion and mainly consists of $FeCO_3$ and Fe_2O_3. The thickness of the secondary corrosion layer is around 10-27 μm. Tertiary corrosion layer forms due to the re-deposition of corrosion product on top of the secondary corrosion layer. It forms after 100 hours of immersion and has a thickness

greater than 27 μm. The thickness of the tertiary corrosion layer is a function of time and usually increases with increasing test duration but at a decreasing rate. Tertiary corrosion layer is found to consist of $FeCO_3$, Fe_2O_3 and FeO. Secondary and tertiary corrosion layers are found to form due to the decomposition of $FeCO_3$ to Fe_2O_3 and FeO. Dissolved oxygen in the solution assists the decomposition process during corrosion.

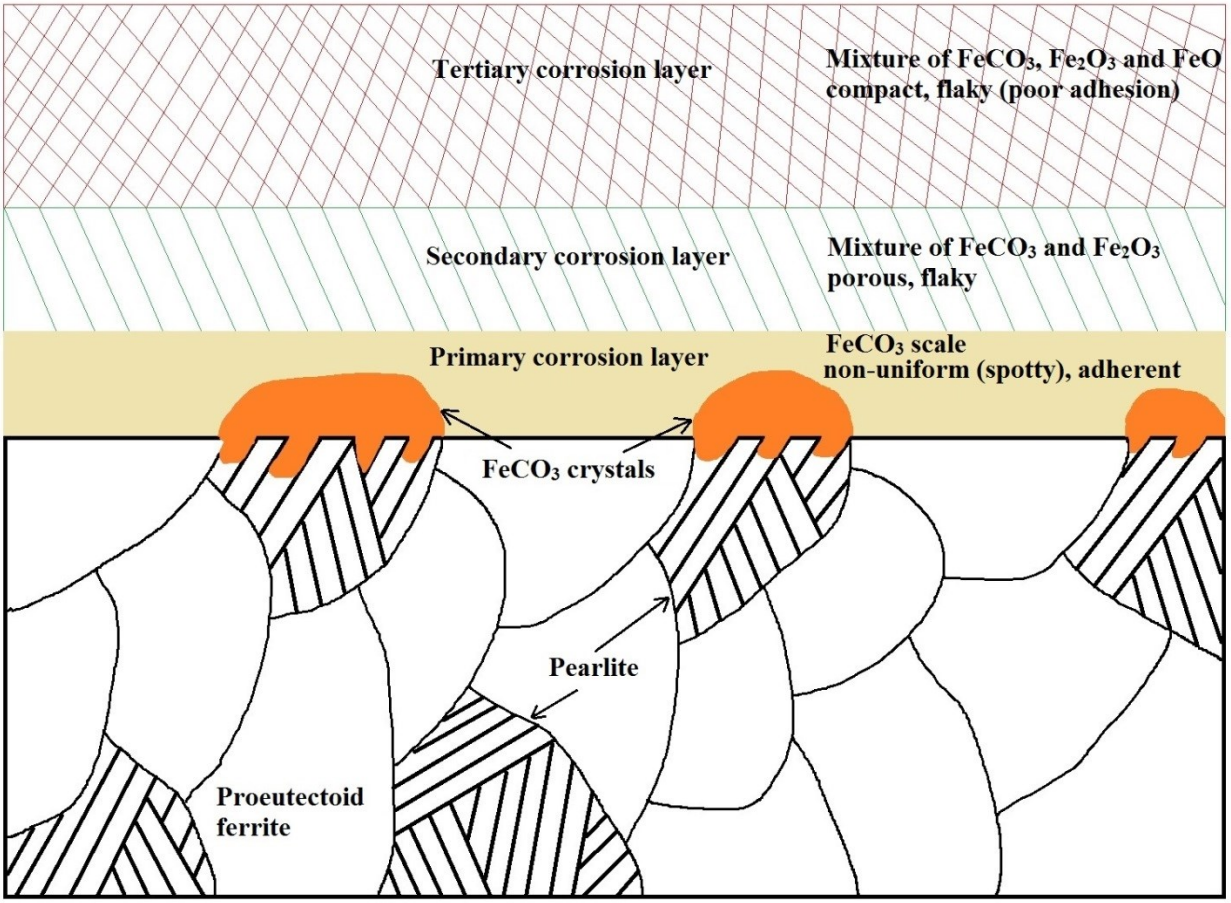

Figure 4-41 Schematic diagram illustrating the formation of primary, secondary and tertiary corrosion layer.

4.3 Erosion-Corrosion

Erosion-corrosion behavior of API steels and the synergistic effect between erosion and corrosion are discussed in this section.

4.3.1 Erosion-Corrosion of API Steels

During pure erosion, API X42, API X70 and API X100 steels were exposed to an abrasive stream for 50 s at 90° angle of incidence and different particle velocities (36, 47, 63 and 81 m s^{-1}). Erosion rate in the absence of corrosion (E_0) was calculated using Equation 3-1. Calculated erosion rate (pure erosion) (E_0) based on 50 s of erosion as a function of abrasive particle velocity for API X42 steel is shown in Figure 4-42, as a representative example. As expected, higher particle velocity leads to higher material removal from the surface as observed in other erosion studies [123]. During pure corrosion, API X42, API X70 and API X100 steels were exposed to corrosive solution (2 g l^{-1} NaCl saturated with CO_2) for 12.5 hr and corrosion rate in the absence of erosion (pure corrosion) (C_0) was calculated using Equation 3-3. Pure corrosion rates for API X42, API X70 and API X100 are shown in Figure 4-43. There is around 8% and 32% decrease in corrosion rate of API X42 and API X70 as compared to API X70 and API X100, respectively. It interesting to note that, pure corrosion rate (C_0) (calculated from weight loss) after 12.5 hr (Figure 4-43) is lower than the corrosion rate obtained after 2.5 hr (Figure 4-22), which confirms the formation of protective surface layer on the steel surface.

During erosion-corrosion process, five erosion cycles (10 s each) were performed for a total of 50 s of erosion time (same duration as pure erosion) for 36, 47, 63 and 81 m s^{-1} particle velocity and 90° impingement angle. Figure 4-44 shows changes in average erosion rate (total erosion component)

(E_c) with particle velocity for API X42 steel, in which each data point is an average of five erosion cycles. As shown in the figure, erosion rate increases with increasing particle velocity as observed previously for pure erosion (Figure 4-42). Figure 4-45 shows the average corrosion rate (total corrosion component) (C_e) of 5 cycles for API X42 steel. Abrasive particles partially or completely remove the protective surface film and expose the fresh surface for further corrosion. High particle velocity results in more protective film removal from the surface. Partial removal of the protective surface film creates favorable conditions for accelerated corrosion. Again, as observed from pure erosion, high particle velocity leads to higher material removal creating more effective surface area for corrosion. Moreover, it is believed that due to high particle velocity, the sharp edges of the abrasive particles create micro-cracks and provide additional surface area for corrosion. Figure 4-46 shows total material loss as a function of velocity for API X42, API X70 and API X100 steel. As expected, total material loss increases with increasing particle velocity for API steels. There are around 4.8, 5.0 and 3.4 times increase in material loss observed for API X42, API X70 and API X100 steel, respectively, with an increase in particle velocity from 36 m s^{-1} to 81 m s^{-1}. It is important to note that API X100 exhibits better erosion-corrosion resistance than API X42 and API X70 (Figure 4-46). As discussed earlier (section 4.1.4), higher yield strength of API X100 (690 MPa) compared to API X42 (290 MPa) and API X70 (482 MPa), provides better erosion resistance at high impact angle (90°). In addition, API X100 shows better corrosion resistance due to its bainitic microstructure and higher chromium and copper content (section 4.2.1). As a consequence, API X100 exhibits enhanced erosion-corrosion resistance compared to API X42 and API X70 in the test conditions employed in this study.

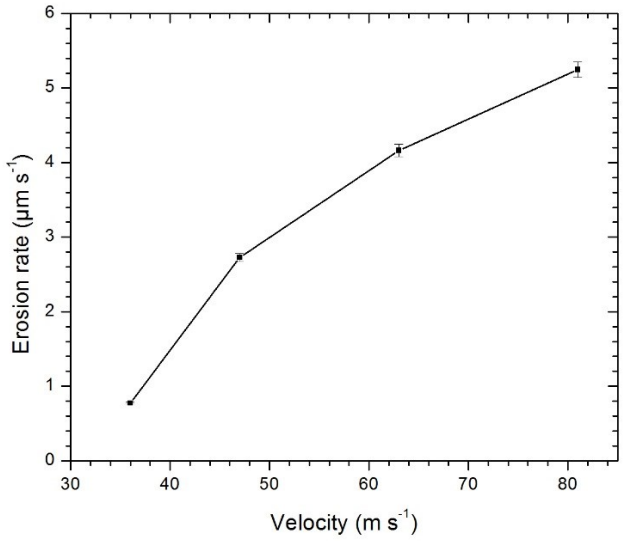

Figure 4-42 Pure erosion rate (E_0) (based on 50 s of erosion) vs abrasive particle velocity for API X42 steel showing an increase in erosion rate with particle velocity.

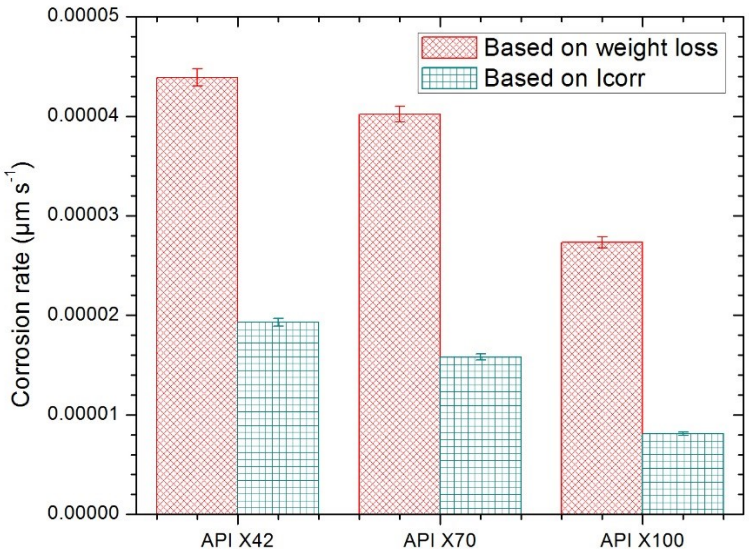

Figure 4-43 Pure corrosion rate (C_0) (based on weight loss after 12.5 hr of corrosion) for API X42, API X70 and API X100 steel in 2 g l^{-1} NaCl solution saturated with CO_2.

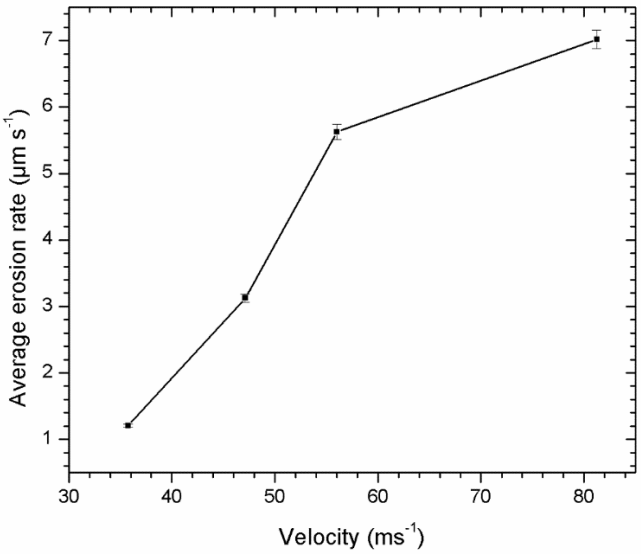

Figure 4-44 Average erosion rate (E_c) vs particle velocity for API X42 steel during erosion-corrosion process. Each data point is an average of five erosion cycles.

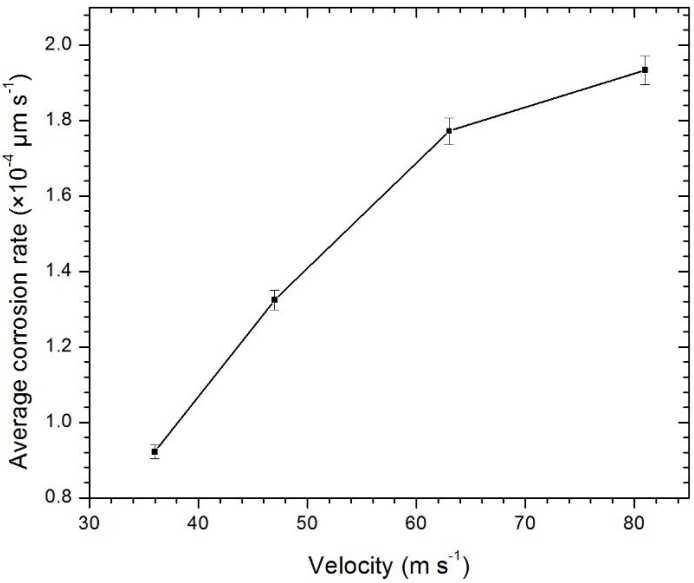

Figure 4-45 Average corrosion rate (C_e) (based on weight loss) vs particle velocity for API X42 steel during erosion-corrosion test in which each data point is an average of five corrosion cycles.

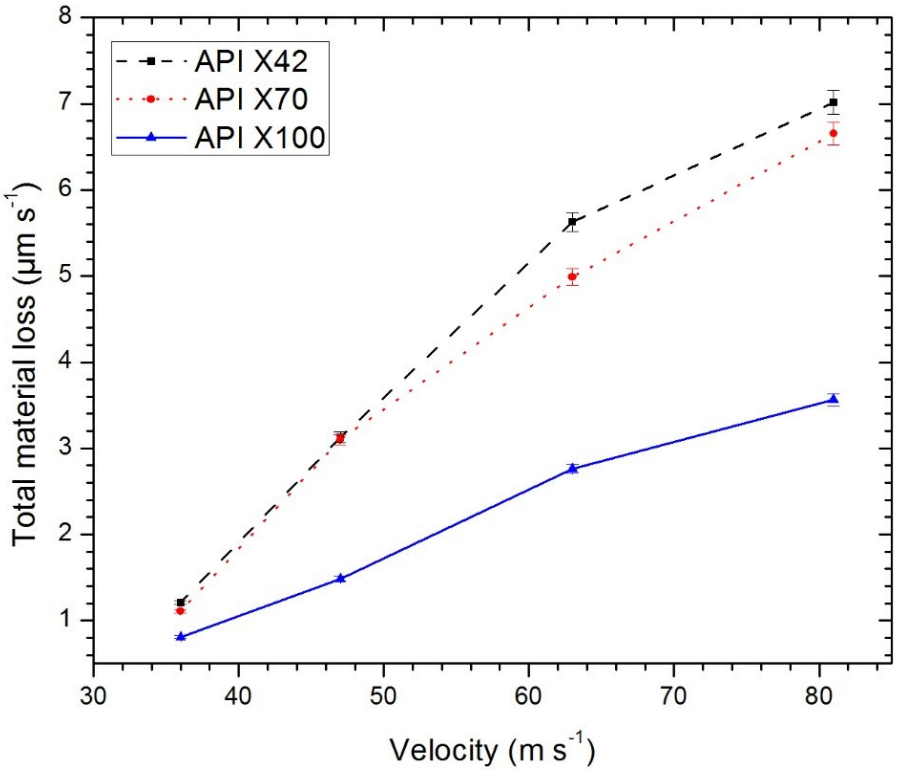

Figure 4-46 Total material loss vs velocity for API X42, API X70 and API X100 steel.

4.3.2 Erosion-Corrosion Mechanisms

SEM micrographs of the API X42 steel after erosion-corrosion are shown in Figure 4-47. Figure 4-47 (a) shows the general surface morphology after the steel surface was exposed to five consecutive erosion-corrosion cycles (a total of 50 s erosion and 12.5 hr corrosion). Simultaneous action of erosion and corrosion leads to high material removal during this process. A magnified image of Figure 4-47 (a) (marked as a circle) is shown in Figure 4-47 (b). Upon impact, abrasive particles locally micro-forge the surface during the erosion cycle and form a work hardened layer due to plastic deformation as observed in pure erosion. This work hardened layer is highly susceptible to corrosion (more anodic) and experiences rapid corrosion during the corrosion cycle.

Al_2O_3 particles are observed to embed into the steel surface and in some cases act as barriers and protect the surface underneath from corrosion. These embedded Al_2O_3 particles may also act as nucleation sites for pits formation and surfaces adjacent to these embedded particles undergo preferential dissolution as shown in Figure 4-47 (c). After sufficient dissolution (around the particles) in the same corrosion cycle, embedded particles are removed from the surface and create fresh surfaces (cavities) for further corrosion. These cavities may act as initiation sites for pitting corrosion. Previous studies [380]–[382] showed that pits almost always initiate at some chemical and physical heterogeneity, such as second phase particles, inclusions, dislocations and flaws. Figure 4-47 (d) shows accelerated dissolution of iron inside the cavity where the adjacent surface area is protected by a corrosion film formed at the initial stage of corrosion.

Pits are often initiated at the steel surface (Figure 4-47 (e)) due to the breakdown of the passive film by the abrasive particles. These micro sized pits are often considered as metastable pits and under certain conditions,

they continue to grow to form large pits. These pits are often covered with corrosion products [181] which makes visual detection extremely difficult. Burstein [335] suggested that a cover over the pit mouth is required during a metastable state to maintain the diffusion controlled mechanism. Without the cover in this early growth stage, the pit would repassivate and die. Figure 4-47 (f) shows the fracture of such pit cover during the erosion-corrosion process.

Figure 4-47 (g) shows the fracture of Fe_3C network by the abrasive particles. The damage to the Fe_3C network significantly decreases the adherence of the protective surface film. Moreover, due to high particle velocity, the sharp edges of the abrasive particles create micro-cracks. During corrosion, corrosive solution penetrates through these cracks into the sub-surface region and extends these cracks further. Figure 4-47 (h) shows the cross-section of the specimen after erosion-corrosion illustrating the propagation of sub-surface crack. The propagation of sub-surface cracks during corrosion promotes delamination in the next erosion cycle.

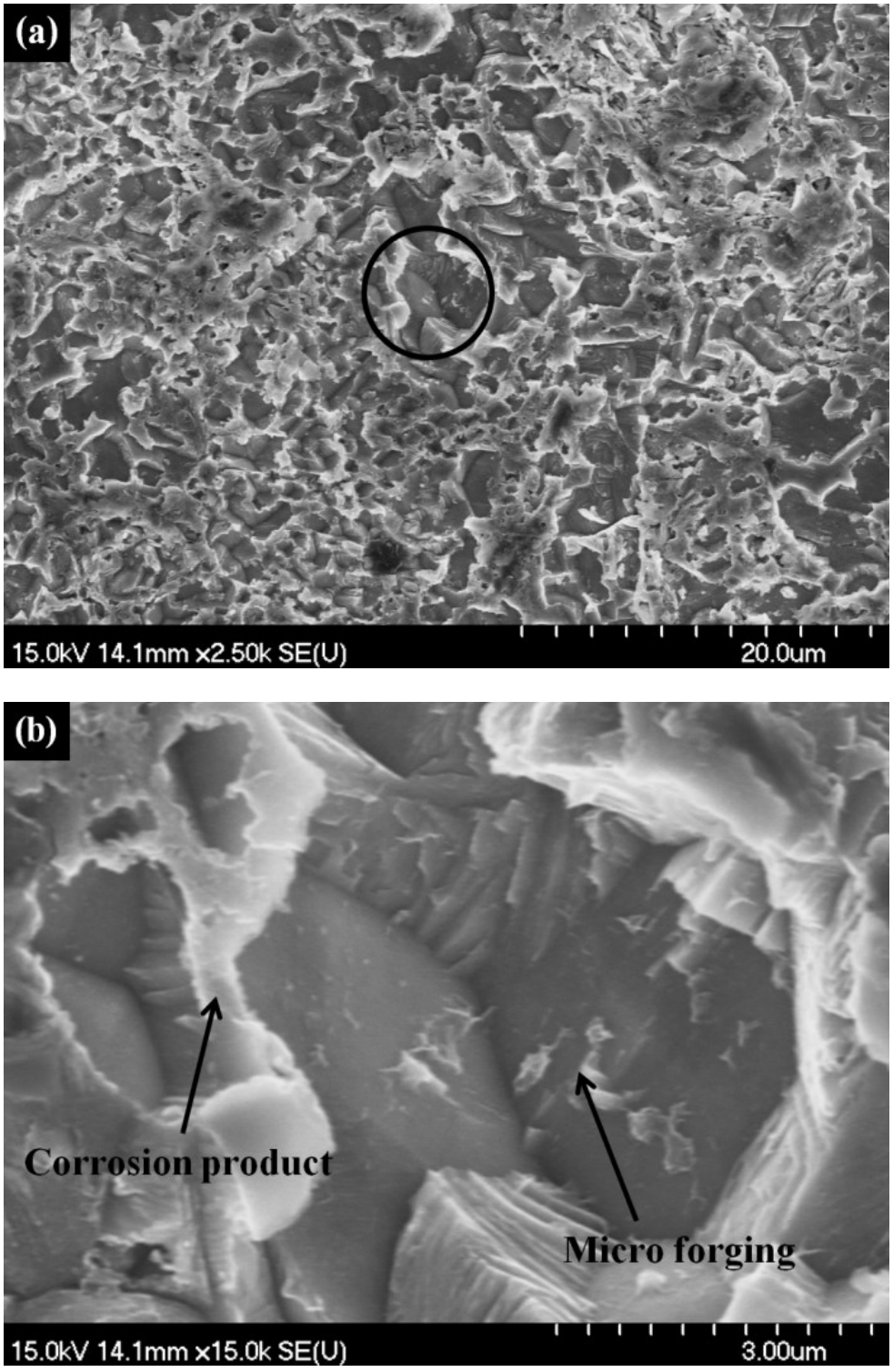

Figure 4-47 SEM micrographs of (a) surface morphology after erosion-corrosion and (b) magnified image of figure (a) (marked as a circle) showing corrosion of work hardened layer.

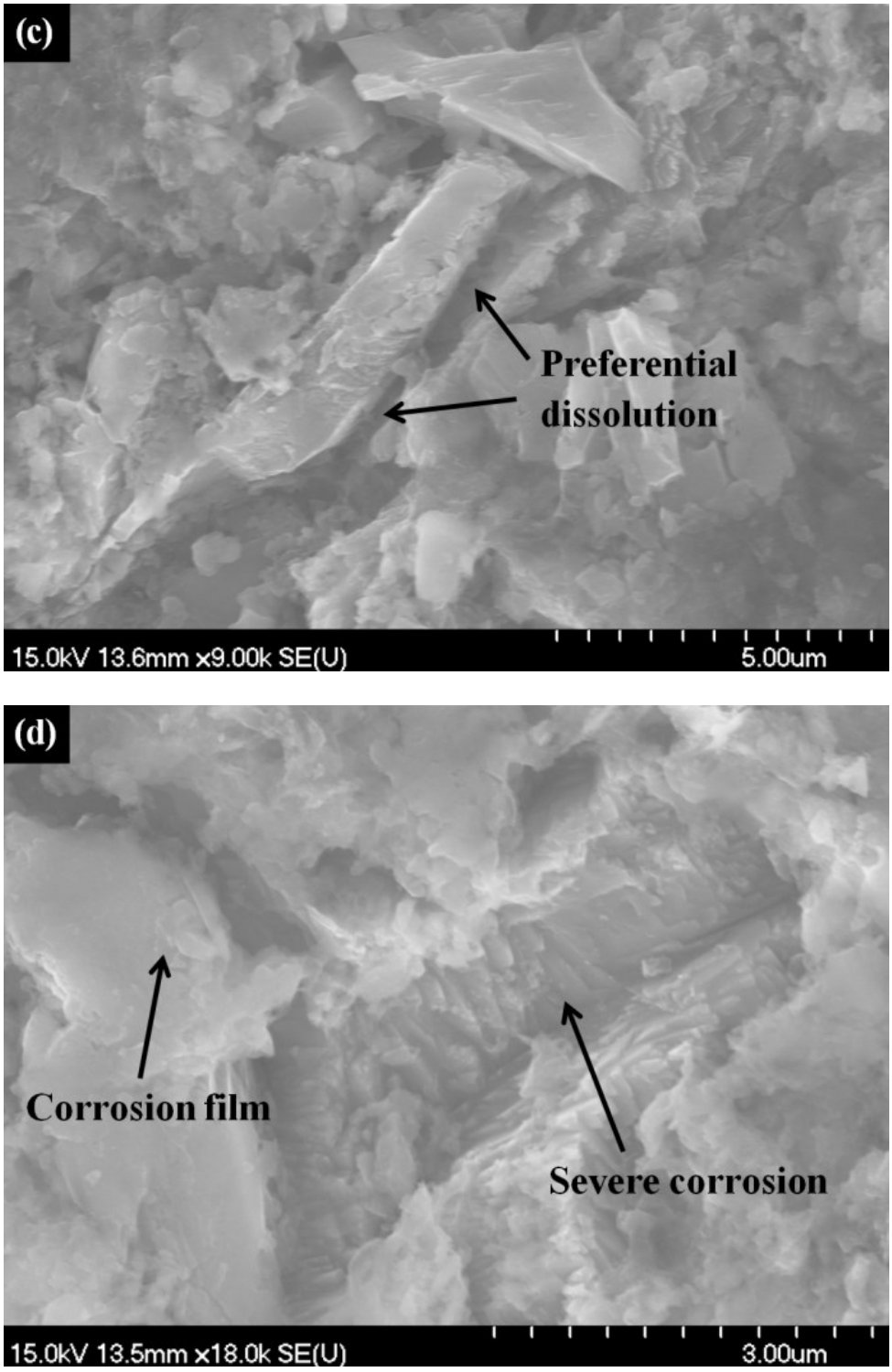

Figure 4-47 SEM micrographs of (c) preferential dissolution of iron around an embedded particle and (d) accelerated corrosion inside a cavity while the adjacent surface area is protected by a corrosion film.

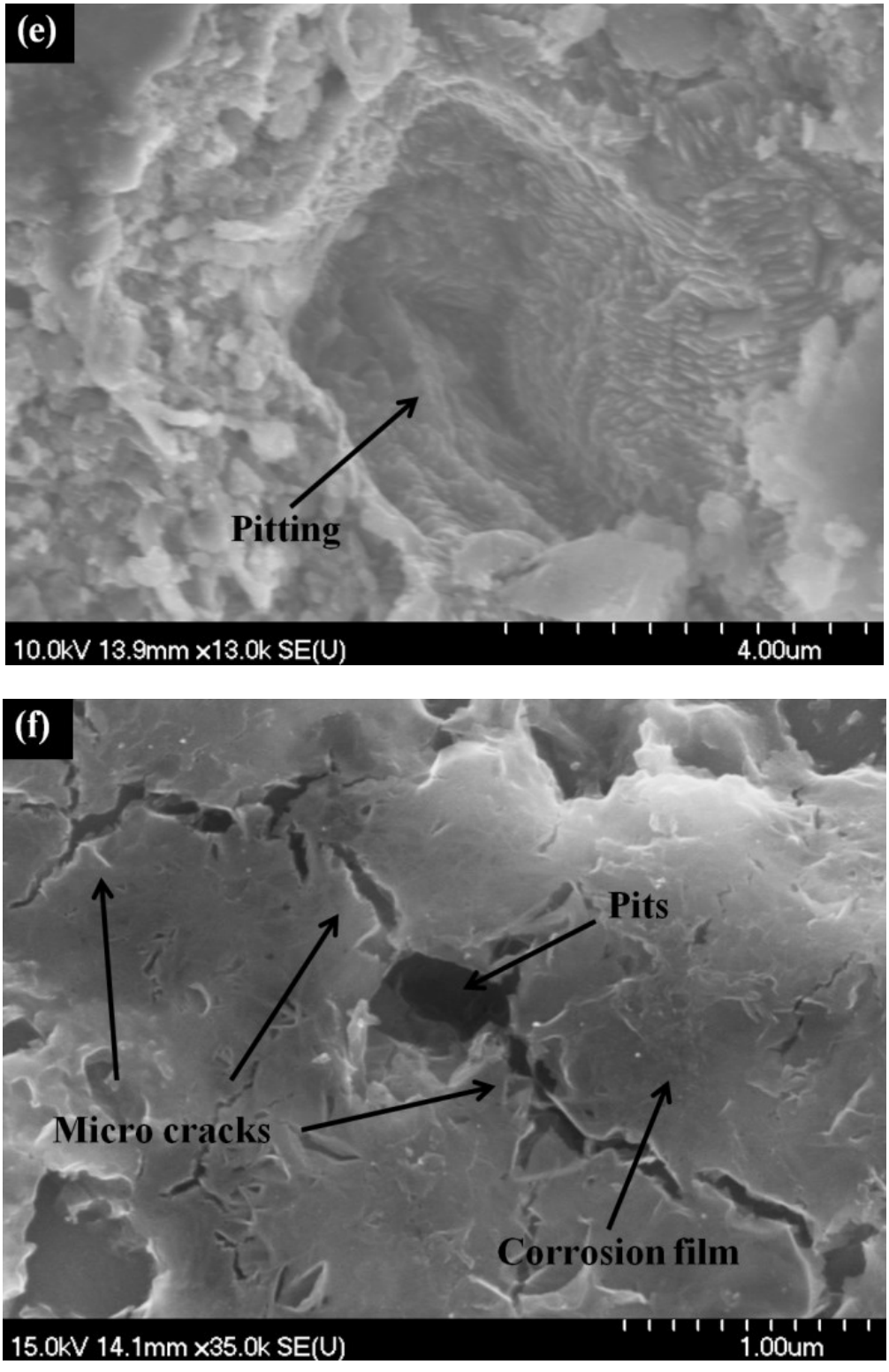

Figure 4-47 SEM micrographs of (e) pitting corrosion due to the breakdown of passive film and (f) fracture of pit cover after sufficient growth of the pit underneath.

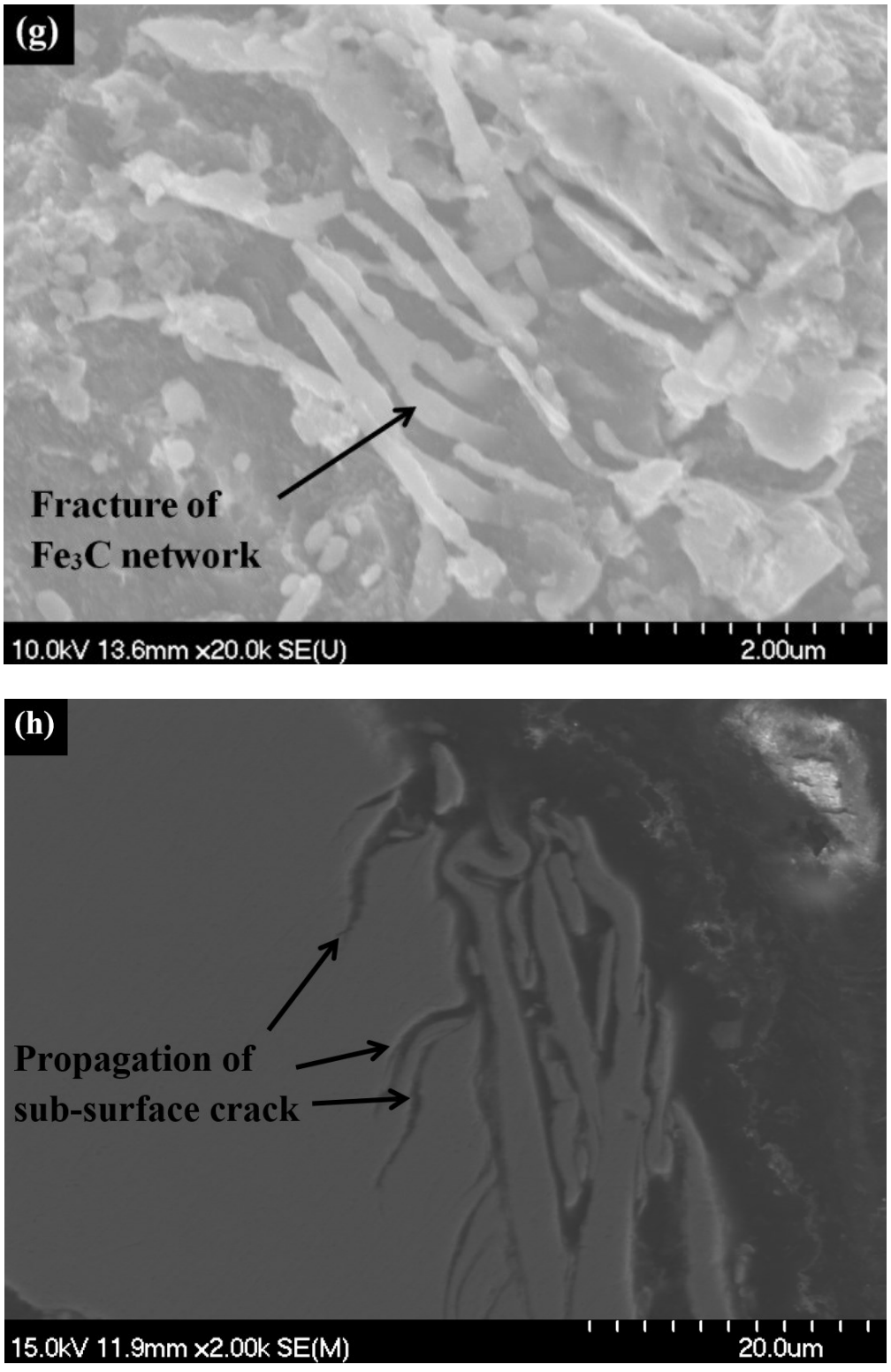

Figure 4-47 SEM micrographs of (g) fracture of cementite network by abrasive particles during the erosion cycle and (h) cross-section of the damaged surface showing propagation of sub-surface crack.

4.3.3 Synergistic Effect between Erosion and Corrosion

The effect of erosion on corrosion and vice-versa is discussed in the following section. Summary of erosion-corrosion, pure erosion and pure corrosion data (based on weight loss) for API X42, API X70 and API X100 steel is provided in the appendices (Table D-1, Table D-2 and Table D-3).

4.3.3.1 Effect of Erosion on Corrosion

Relative comparison of corrosion components for API X42, API X70 and API X100 steel is shown in Figure 4-48 (a), (b) and (c), respectively. The figures indicate that the effect of erosion on corrosion is significant. This increase in corrosion rate during erosion-corrosion is because the work hardened layer formed after the erosion cycle is more anodic and makes the eroded surface highly susceptible to corrosion [328], [383]. Throughout the corrosion process, the precipitation of iron carbonate ($FeCO_3$) forms a passive film which acts as a diffusion barrier by covering the underlying metal and decreasing corrosion rate [370]. This layer is weakly bonded to the steel surface and can be easily removed by erosive particles which expose a fresh surface to the corrosive environment. Additionally, disruptions in Fe_3C network in pearlite (due to erosion) significantly decrease the adherence of the protective film. Removal of the protective layer promotes accelerated pitting corrosion. During erosion, abrasive particles are embedded within the surface. These embedded particles also act as nucleation sites for pit formation. Pits are often initiated on the steel surface due to the breakdown of passive film by the abrasive particles. Moreover, the increase in surface roughness due to abrasive particles impact increases the effective (real) surface area, which leads to higher corrosion rate [221], [281]. It is interesting to note that, for API X42 steel, the velocity exponent *'n'* (Equation 2-1) decreases from 2.13 (Figure 4-42) to 2.03 (Figure 4-44) for pure erosion and erosion–corrosion,

respectively. This indicates that material loss rate becomes more dependent on the mechanisms involved during the erosion–corrosion process.

Figure 4-49 shows % $\Delta C_e/C_0$ for API X42, API X70 and API X100. API X70 exhibits lower % $\Delta C_e/C_0$ at all particle velocities compared to API X42. Percent increase in corrosion due to erosion (% $\Delta C_e/C_0$) increases with increasing particle velocity. Higher particle velocity causes more damage to the passive film and exposes fresh surface to the solution. Also, high velocity causes more embedded particles (creates more nucleation sites for pitting), more micro-cracks and deeper penetration into the steel. After removal of these embedded particles, more effective surface area is exposed to the corrosive media. Furthermore, the thickness of the work hardened layer increases with increasing particle velocity, which significantly increases the overall corrosion rate. Hence, it can be concluded that the effect of erosion on corrosion is more prominent at high particle velocity.

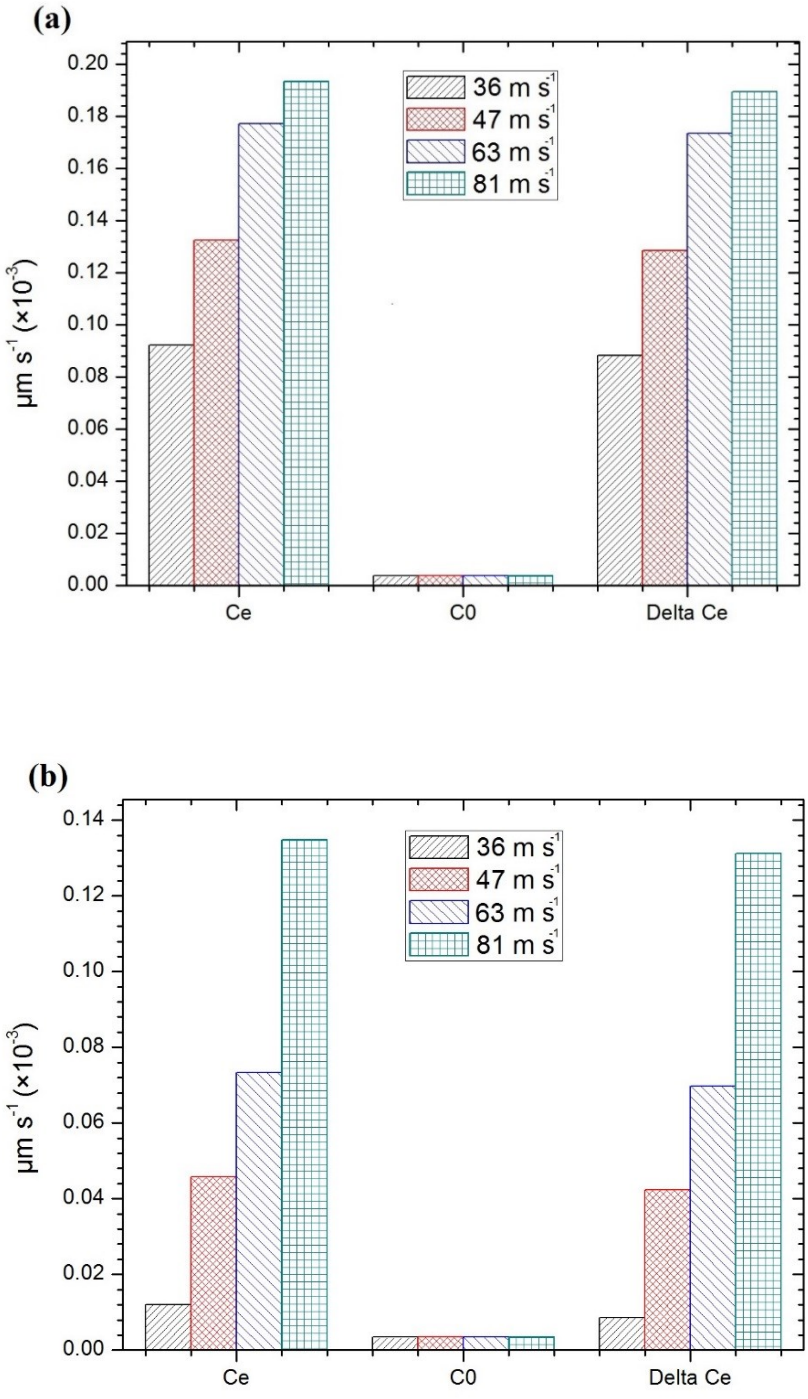

Figure 4-48 Relative comparison of total corrosion component (C_e), corrosion rate in absence of erosion (C_0) and change in corrosion rate due to erosion ΔC_e, (a) API X42 steel and (b) API X70.

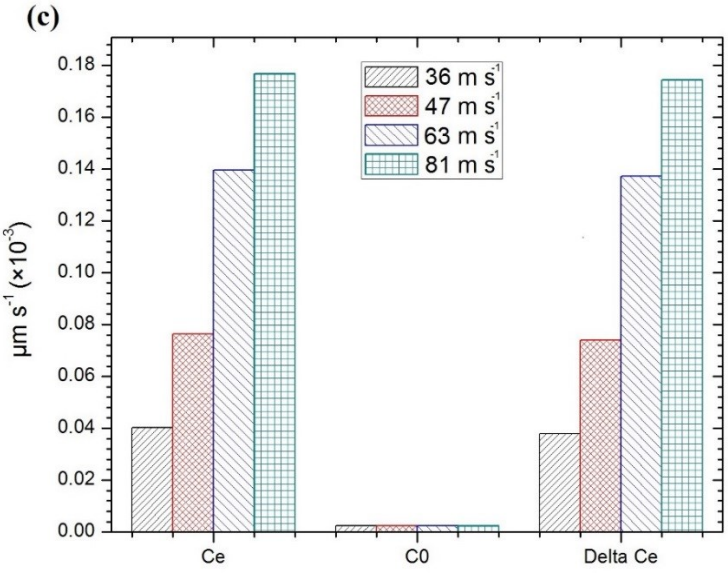

Figure 4-48 Relative comparison of total corrosion component (C_e), corrosion rate in absence of erosion (C_0) and change in corrosion rate due to erosion ΔC_e, (c) API X100 steel.

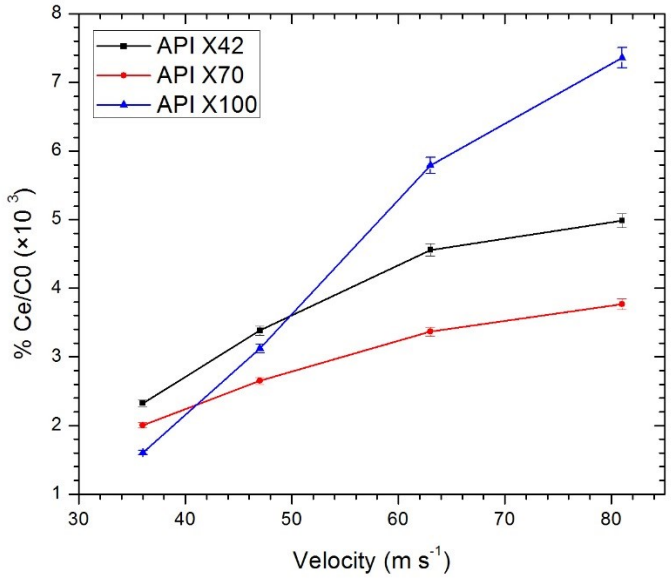

Figure 4-49 Percent increase in corrosion due to erosion (% $\Delta C_e/C_0$) for API X42, API X70 and API X100.

4.3.3.2 Effect of Corrosion on Erosion

Relative comparison of erosion components for API X42, API X70 and API X100 steel are shown in Figure 4-50 (a), (b) and (c), respectively. The charts reveals that the effect of corrosion on erosion is significant. Surface roughness plays an important role during erosion. As described earlier, erosion is highly sensitive to impingement angle and an increase in surface roughness changes the local impact angle. Previous studies [128] showed that low angle metal cutting, ploughing and delamination predominates at low impingement angle leading to higher erosion rate. Moreover, an increase in the surface roughness creates vulnerable local peaks, which can then be easily removed during erosion. As discussed in section 4.2.1 (Table 4-7), surface roughness increases by about 54% (for API X42) as a result of corrosion, which, in turn, causes higher erosion rate during erosion-corrosion. It is believed that corrosion removes the work-hardened layer and exposes an unhardened surface for further erosion. At high impact angle (90°), extensive amount of Al_2O_3 particles embed in the surface and act as reinforcing particles and slow down the erosion rate by protecting the surface underneath from additional erosion. However, preferential dissolution around the embedded particles (during the corrosion cycle) accelerates the removal of these embedded particles and increases the erosion rate by exposing fresh surface and creating vulnerable lips. Furthermore, due to high particle velocity, the sharp edges of the abrasive particles create micro-cracks during the erosion cycle. During the corrosion cycle, corrosive fluid penetrates and corrosion products precipitate inside the micro-cracks, which generates tensile stresses leading to the propagation of these cracks. The propagation of these micro-cracks mainly promote delamination in the next erosion cycle. Schematic diagram illustrating the propagation of micro-cracks during the corrosion cycle is shown in Figure 4-51.

Percent increase in erosion due to corrosion decreases with increasing particle velocity. Figure 4-52 shows % $\Delta E_c/E_0$ with respect to particle velocity for API steels. For API X100, there are around 123, 108, 75 and 66% increase in % $\Delta E_c/E_0$ at 36, 47, 63 and 81 m s^{-1} particle velocity, respectively. This indicates that the effect of corrosion on erosion is more pronounced at low particle velocity. This is because, at high particle velocity, particles are embedded deep into the steel surface and work as barriers from further erosion. However, at low particle velocity, the particles are not embedded deep in the steel surface and can be easily removed by dissolution of the steel around these particles, hence, increasing the effect of corrosion on erosion. Moreover, high particle velocity creates a thicker work hardened layer that is not completely removed during the corrosion cycle, which slows down the material loss rate during the erosion cycle.

Synergy ($S = \Delta E_c + \Delta C_e$) (Equation 2-7) due to erosion-corrosion for API X42, API X70 and API X100 is shown in Figure 4-53. In general, API X100 provides better erosion-corrosion resistance at all particle velocities compared to API X42 and API X70 steels. The synergistic components (S) for API X100 at 36, 47, 63 and 81 m s^{-1} are 0.45, 0.77, 1.19 and 1.42 μm s^{-1}, respectively, and increases with increasing particle velocity. It is interesting to note that, although total material loss for API X70 is lower than API X42 (Figure 4-46), the synergistic component (S) for API X70 is around 1.5 times higher than API X42 (Figure 4-53). Which indicates that in applications where erosion-corrosion is a major concern, material degradation in API X70 will be faster than API X100 and API X42.

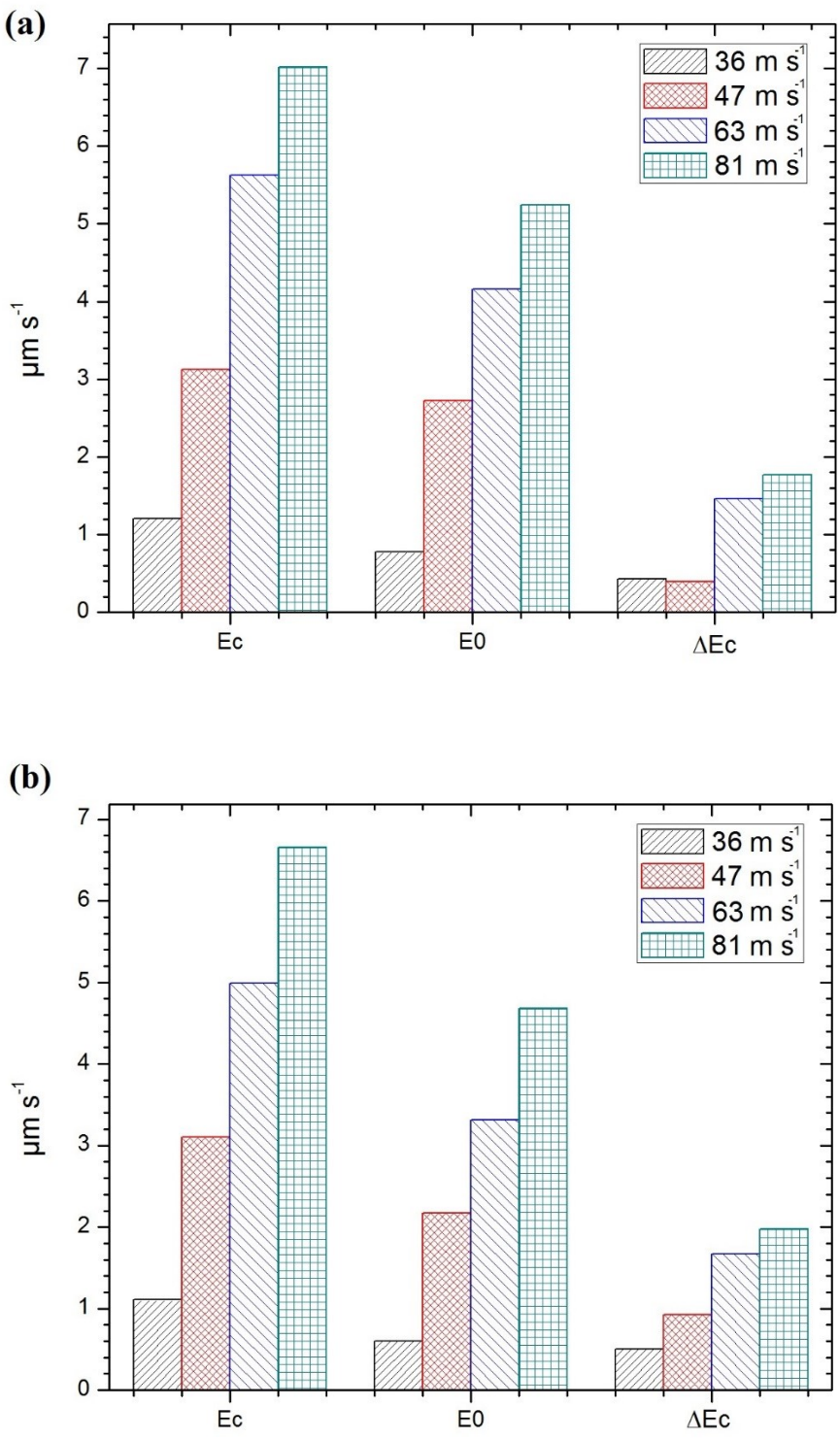

Figure 4-50 Relative comparison of total Erosion component (E_c), Erosion rate in absence of corrosion (E_0) and change in erosion rate due to corrosion ΔE_c, (a) API X42 steel and (b) API X70.

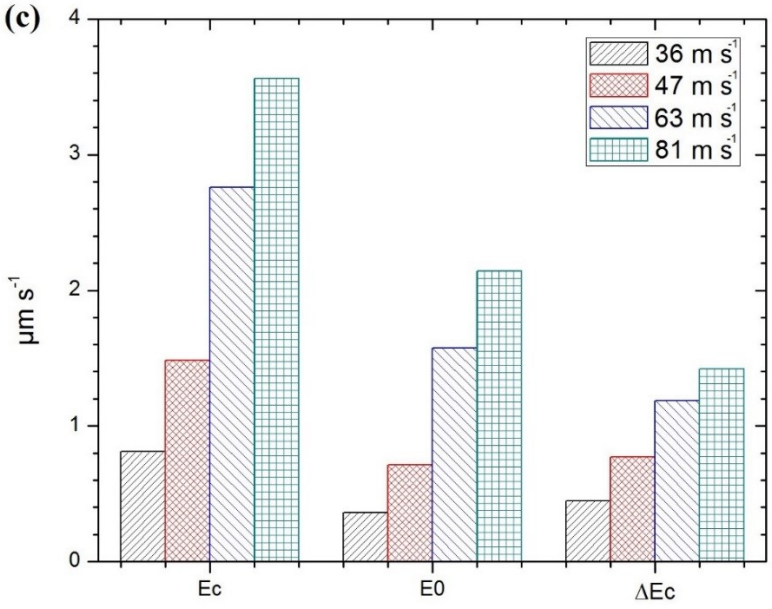

Figure 4-50 Relative comparison of total erosion component (E_c), erosion rate in absence of corrosion (E_0) and change in erosion rate due to corrosion ΔE_c, (c) API X100 steel.

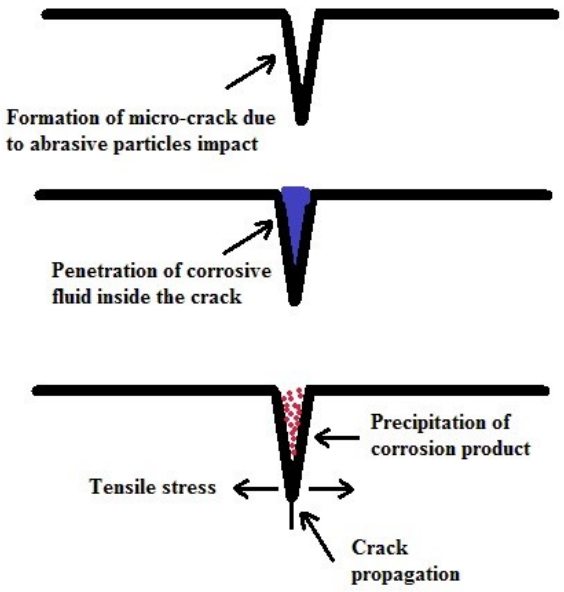

Figure 4-51 Schematic diagram showing the propagation of micro-crack during corrosion cycle. Precipitation of corrosion products inside the cracks generates tensile stress in front of the crack tip and extends the micro-cracks.

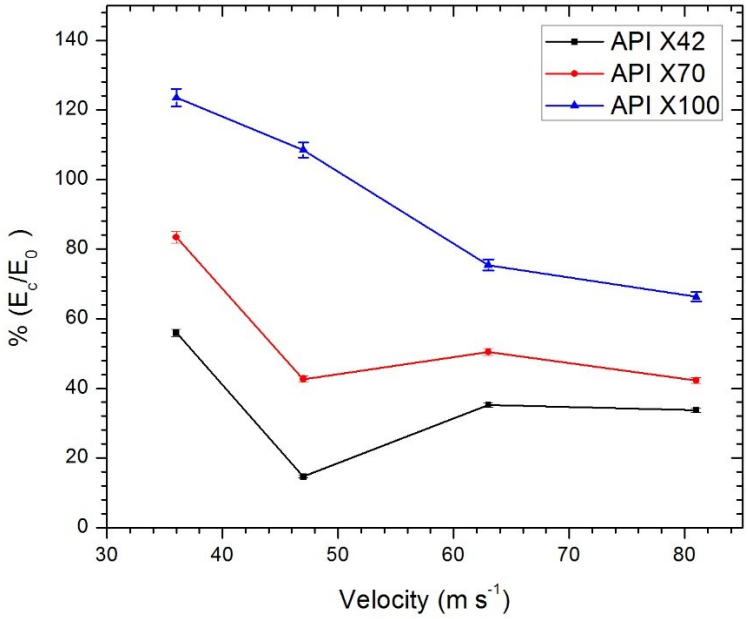

Figure 4-52 Percent increase in erosion due to corrosion (% $\Delta E_c/E_0$) for API X42, API X70 and API X100.

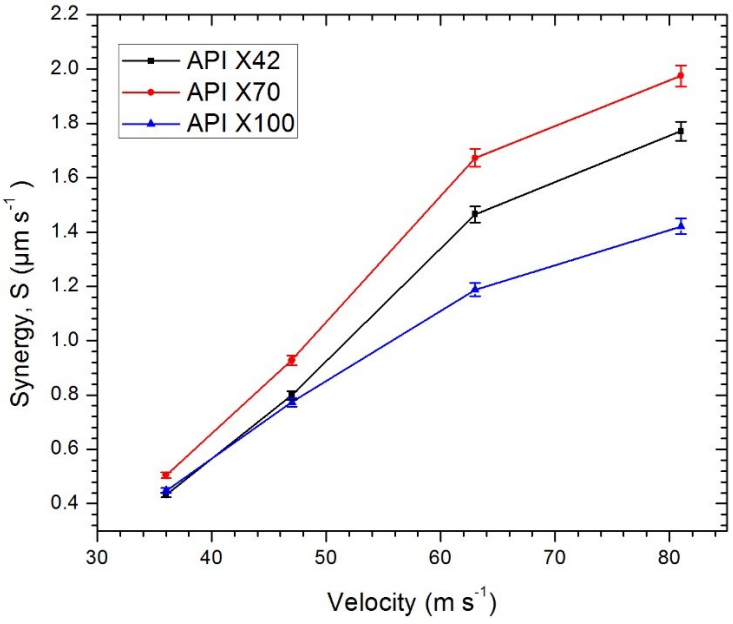

Figure 4-53 Synergy ($\Delta E_c + \Delta C_e$) due to erosion-corrosion for API X42, API X70 and API X100.

4.3.4 Summary

Throughout the erosion-corrosion process, significant increase in erosion was observed due to corrosion. Corrosion increases surface roughness, removes work hardened layer and accelerates the removal of embedded particles. It also promotes delamination by extending sub-surface cracks. Similarly, a significant increase in corrosion was observed due to erosion. Erosion removes the passive film from the surface, breaks the cementite network, provides favorable conditions for pitting and increases the effective surface area by increasing the surface roughness. In addition, erosion creates sub-surface cracks and deformed work hardened layers, which increases corrosion kinetics. The effect of corrosion on erosion is significant at low particle velocity, while, the effect of erosion on corrosion is more prominent at high particle velocity.

Chapter 5

Conclusions

In this study, erosion, corrosion and erosion-corrosion experiments were performed on various carbon and API pipeline steels to evaluate the synergistic effect between erosion and corrosion. Erosion mechanism maps were developed for the steels and the effect of microstructure on erosion behavior was examined. The effect of the steel microstructure on corrosion film formation was also studied. The following conclusions can be made from the current work:

1. Normalized erosion rate increases with increasing particle velocity and decreases with increasing impact angle. At low impact angle and low particle velocity, ploughing is the dominant mechanism and a combination of low angle metal cutting and ridge removal are dominant at low impact angle and high velocity condition. At high particle impact angle, secondary metal cutting and flattening of ridges and fracture was found to be the dominant process of metal removal at high velocity. At low velocity, plastic deformation and fracture of ridges around dimples is dominant.

2. Under the high particle feed rate employed in this study, contrary to expectations, the velocity exponent *'n'* decreases with increase in impact angle. This is because of the fact that with an increase in impact angle abrasive particles embed in the matrix and act as

barriers to further erosion. That is, under such conditions, the velocity exponent *'n'* becomes mechanism dependent.

3. At low particle velocity most of the impact is elastic and doesn't contribute to the measured erosion rate. This makes erosion almost independent of the impact angle. The dependence of erosion on impact angle becomes evident at high particle velocities.

4. Pearlite is more effective in resisting erosion than ferrite due to its lamellar structure. When the pearlite plates are at right angles to the striking particles, the resistance to deformation is at its maximum.

5. The developed erosion mechanism maps summarize erosion behavior over a wide range of impact angle and particle velocity, identifying the dominant mechanism and providing the overall erosion rate. Morphologies of the worn surfaces, in the various regimes, provide insight into the physical mechanisms of material removal.

6. During corrosion, preferential dissolution of eutectoid ferrite provides a suitable chemical environment for the formation of protective surface film on pearlite. Cementite (Fe_3C) network in pearlite anchors the passive film to the surface.

7. Corrosion rate decreases with increasing test duration due to the formation of protective surface film. The corrosion scale consists of primary, secondary and tertiary layers. Primary corrosion layer consists of $FeCO_3$ and is non-uniform (spotty) and adherent to the surface. However, secondary corrosion layer was found to consist of $FeCO_3$ and Fe_2O_3 and is porous, flaky and tertiary corrosion layer ($FeCO_3$, Fe_2O_3 and FeO) is compact and flaky. Tertiary corrosion layers form due to the decomposition of $FeCO_3$ to Fe_2O_3 and FeO.

8. The effect of corrosion on erosion and erosion on corrosion is significant due to synergy between the two modes of degradation. The effect of corrosion on erosion is significant at low particle velocity, while, the effect of erosion on corrosion is more prominent at high particle velocity.

9. During erosion-corrosion, erosion removes the passive film from the surface, breaks the cementite network, provides favorable conditions for pitting and increases the effective surface area by increasing the surface roughness. In addition, erosion creates sub-surface cracks and deformed work hardened layer, which increases corrosion kinetics.

10. Throughout the erosion-corrosion process, corrosion increases surface roughness, removes work hardened layer and accelerates the removal of embedded particle. It also promotes delamination by extending sub-surface cracks.

11. API X100 provides better erosion-corrosion resistance than both API X42 and API X70.

5.1 Contributions

This research is original and expands our knowledge in the area of erosion and tribo-corrosion of API X-series pipeline steels. The following is a list of contributions resulting from this research work:

1. The effect of impact angle and particle velocity on erosion were investigated and different erosion mechanisms were identified.

2. Successfully explored the effect of microstructure on erosion behavior of steel.

3. Empirical erosion mechanism maps (as a function of operating conditions) for AISI 1018, AISI 1080, API X42, API X70 and API X100 were constructed. These mechanism maps can be a useful tool to steel and piping manufacturers.

4. Effectively characterized the corrosion layer that formed in sweet environment and its role in the degradation of oil and gas pipeline steels.

5. The synergistic effect of erosion-corrosion for API X42, API X70 and API X100 was quantified and successfully identified erosion-corrosion mechanisms.

It is important to note that the findings of this research have resulted in 19 conference presentations/posters and in the following 9 papers:

1. Islam, Md. Aminul, Alam, Tahrim, Farhat, Z; '*Erosion Mechanism Map for API X70 Pipeline Steel*' Canadian Metallurgical Quarterly (2015). (Under Review)

2. Islam, Md. Aminul, Farhat, Z; '*Erosion-Corrosion Behavior of Pipeline Steel*' Materials Performance, NACE International, 54 (11) (2015) 2-5.

3. Islam, Md. Aminul, Farhat, Z; '*Mechanical and Electrochemical Synergism of API X42 Pipeline Steel during Erosion-Corrosion*' Journal of Bio and Tribo-Corrosion, 1 (4) (2015) 1-18.

4. Islam, Md. Aminul, Farhat, Z; '*Characterization of the Corrosion layer on Pipeline Steel in Sweet Environment*' Journal of Materials Engineering and Performance, 24 (8) (2015) 3142-3158.

5. Islam, Md. Aminul, Alam, Tahrim, Farhat, Z, Mohamed, Adel, Alfantazi, Akram; '*Effect of Microstructure on the Erosion Behavior of Carbon Steel*' Wear, 332-333 (2015) 1080–1089.

6. Islam, Md. Aminul, Farhat, Z; '*Effect of Impact Angle and Velocity on Erosion of API X42 Pipeline Steel under High Abrasive Feed Rate*' Wear, 311 (2014) 180-190.

7. Islam, Md. Aminul, Farhat, Z; '*The Synergistic Effect between Erosion and Corrosion of API Pipeline in CO_2 and Saline Medium*' Tribology International, 68 (2013) 26-34.

8. Islam, Md. Aminul, Farhat, Z, E. M. Ahmed, A.M. Alfantazi; '*Erosion Enhanced Corrosion and Corrosion Enhanced Erosion of API X70 Pipeline Steel*' Wear, 302 (2013) 1592-1601.

Other Refereed Contribution (Full Paper)

9. Islam, Md. Aminul, Farhat, Z, E. M. Ahmed, '*Influence of Impact Angle and Velocity on Erosion of AISI 1018 Steel Under Jet Impingement*' Proceedings of the 3rd Gas Processing Symposium, (2012) 274-279.

5.2 Recommendations for Future Work

The following are recommendations for future work:

1. Generate more erosion data covering wider range of particle velocity and impact angle to extend the maps developed in this work.

2. Develop erosion-corrosion mechanism maps for the API steels under sweet environment.

3. Develop an in-situ erosion-corrosion test method that addresses the limitations encountered in current methods.

4. Develop a comprehensive erosion model that takes microstructural effects and erosion micro-mechanics into consideration.

5. Develop surface treatments, such as coating/hardfacing on API steels in an attempt to provide protection to structures in oil, gas and mining industry.

References

[1] J. Davidson and R. V. Jewell, "K-sea Transportation," *United States Securities and Exchange Commission*, 2003. [Online]. Available: https://www.nasdaq.com/markets/ipos/filing.ashx?filingid=2247105. [Accessed: 30-Sep-2015].

[2] D. Furchtgott, "Pipelines Are Safest For Transportation Of Oil And Gas," *Manhattan Institute*, 2003. [Online]. Available: http://www.manhattan-institute.org/html/ib_23.htm#.Vg1VE7QyFUU. [Accessed: 01-Oct-2015].

[3] A. C. on C. and A. Steels, *ASM Metals Handbook: Volume 3*, 9th ed. 1980.

[4] R. M. Andrews and A. D. Batte, "Developments in fracture control technology for gas pipelines utilising high strength steels.," *Korean Gas Union*, pp. 1–11, 2011.

[5] D. Fairchild, "High strength steels - beyond X80," in *Application and Evaluation of High Grade Linepipe in Hostile Enlivenments*, 2002, p. 307.

[6] A. Glover, "Application of grade 555 (X80) and 690 (X100) in Arctic climates," in *Application and Evaluation of High Grade in Hostile Environments*, 2002, p. 33.

[7] L. Barsanti, "From X80 to X100: Know-how reached by ENI Group on high strength steel," in *Application and Evaluation of High Grade in Hostile Environments*, 2002, p. 231.

[8] N. America and U. States, "Research and Development (R & D) at TransCanada," 2013. [Online]. Available: http://www.transcanada.com/docs/About_Us/TransCanada-research-and-development.pdf.

[9] M. Mohitpour, A. Murray, M. McManus, and I. Colquhoun, *Pipeline Integrity Assurance: A Practical Approach*. Amer Soc Mechanical Engineers, 2010.

[10] G. H. Koch, M. P. H. Brongers, N. G. Thompson, Y. P. Virmani, and J. H. Payer, "Corrosion cost and preventive strategies in the United States," *National Climatic Data Center*, 2002. .

[11] T. Ross and N. Lott, "Billion Dollar U.S. Weather Disasters, 1980–2001," *National Climatic Data Center*, 2001. [Online]. Available: http://www.infoplease.com/ipa/A0882823.html. [Accessed: 09-Aug-2015].

[12] ISO, "Carbon steel tubes suitable for screwing," *Int. Organ. Stand.*, vol. 65, pp. 1–3, 1981.

[13] ISO, "Hot-rolled steel sections - Part 1: Equal-leg angles - Dimensions," *Int. Organ. Stand.*, vol. 657–1, pp. 1–4, 1989.

[14] ISO, "Hot-rolled steel sections - Part 2: Unequal-leg angles - Dimensions," *Int. Organ. Stand.*, vol. 657–2, pp. 1–5, 1989.

[15] ISO, "Mechanical properties of fasteners made of carbon steel and alloy steel -- Part 1: Bolts, screws and studs with specified property classes - Coarse thread and fine pitch thread," *Int. Organ. Stand.*, vol. 898–1, pp. 1–57, 2013.

[16] ISO, "Mechanical properties of fasteners made of carbon steel and alloy steel - Part 2: Nuts with specified property classes - Coarse thread and fine pitch thread," *Int. Organ. Stand.*, vol. 898–2, pp. 1–21, 2012.

[17] ISO, "Stainless steel clamp pipe couplings for the food industry," *Int. Organ. Stand.*, vol. 2852, pp. 1–12, 1993.

[18] ISO, "Classification of steels into unalloyed and alloy steels based on chemical composition," *Int. Organ. Stand.*, pp. 1–2, 1982.

[19] ISO, "Preparation of steel substrates before application of paints and related products - Visual assessment of surface cleanliness - Part 1: Rust grades and preparation grades of uncoated steel substrates and of steel substrates after overal," *Int. Organ. Stand.*, vol. 8501–1, pp. 1–74, 2007.

[20] ISO, "Mechanical properties of corrosion-resistant stainless steel fasteners - Part 1: Bolts, screws and studs," *Int. Organ. Stand.*, vol. 3506–1, pp. 1–27, 2009.

[21] SAE, "Carbon and Alloy Steels," *SAE International*, 2015. [Online]. Available: http://standards.sae.org/j411_201501/. [Accessed: 05-Aug-2015].

[22] SAE, "Carbon Steel, Sheet, Strip, and Plate, (SAE 1020 and 1025), Annealed," *SAE International*, 2012. [Online]. Available: http://standards.sae.org/ams5046d/. [Accessed: 05-Aug-2015].

[23] SAE, "Carburizing, Carbon and Low-Alloy Steel Parts," *SAE International*, 2013. [Online]. Available: http://standards.sae.org/ams2762b/. [Accessed: 05-Aug-2015].

[24] SAE, "Chemical Compositions of SAE Wrought Stainless Steels," *SAE International*, 1998. [Online]. Available: http://standards.sae.org/j405_199806/. [Accessed: 05-Aug-2015].

[25] P. Cunat, "Stainless Steel In Structural Automotive Applications," *SAE Tech. Pap.*, pp. 1–10, 2002.

[26] R. J. K. Wood, "Erosion–corrosion interactions and their effect on marine and offshore materials," *Wear*, vol. 261, no. 9, pp. 1012–1023, Nov. 2006.

[27] P. Santacreu, J. Glez, N. Roulet, and T. Fröhlich, "Austenitic Stainless Steels For Automotive Structural Parts," *SAE Tech. Pap.*, pp. 1–8, 2006.

[28] S. H. Avner, *Introduction to physical metallurgy*. McGraw-Hill, 1964.

[29] ASTM, "Standard Specification for Forged or Rolled UNS N06030 , UNS N06022 , UNS N06035 , N06045 , UNS N06025 , and UNS R20033 Alloy Pipe Flanges , Forged Fittings , and Valves and Parts for Corrosive High-Temperature Service," *ASTM Int.*, pp. 1–5, 2011.

[30] ASTM, "UNS N08925, UNS N08031, UNS N08932, UNS N08926, UNS N08354, UNS N08830, and UNS R20033 Plate, Sheet, and Strip," *ASTM Int.*, vol. B625 − 14, pp. 8925–8927, 2015.

[31] ASTM, "Standard Specification for UNS N08031, UNS N08354 and UNS N08926, and Cr-Ni-Fe-N Low-Carbon Alloy (UNS R20033) Bar and Wire, and Ni-Cr-Fe-Mo-N Alloy (UNS N08936) Wire," *ASTM Int.*, vol. B649−06, pp. 1–7, 2011.

[32] ASTM, "Standard Specification for UNS N06002, UNS N06230, UNS N12160, and UNS R30556," *ASTM Int.*, vol. B435 − 06, pp. 5–7, 2011.

[33] ASTM, "Standard Specification for UNS N08925, UNS N08354, and UNS N08926 Seamless Pipe," *ASTM Int.*, vol. B677 − 05, pp. 1–2, 2010.

[34] S. W. Thompson, D. J. Colvin, and G. Krauss, "Continuous Cooling transformatios and Microstructures in Low-carbon, High-Strength Low Alloy Plate Steel," *Metall. Trans. A*, vol. 21A, pp. 1493–1497, 1990.

[35] W.-S. Lee and T.-T. Su, "Mechanical properties and microstructural features of AISI 4340 high-strength alloy steel under quenched and tempered conditions," *J. Mater. Process. Technol.*, vol. 87, no. 1–3, pp. 198–206, Mar. 1999.

[36] B. Hirosh, N. Yamada, and H. Matsuda, "Effect of the Thermo-Mechnical control process on the properties of hig hstrength low alloy steel," *Trans. ISIJ*, vol. 25, no. 54, pp. 54–61, 1985.

[37] C. L. Davis and J. E. King, "Effect of cooling rate on intercritically reheated microstructure and toughness in high strength low alloy steel," *Mater. Sci. Technol.*, vol. 9, no. 1, pp. 8–15, Jan. 1993.

[38] F. B. Pickering, "High Strength Low Alloy Steels," in *Materials Science and Technology*, Wiley-VCH Verlag GmbH & Co. KGaA, 2006.

[39] C. Y. Chen, H. W. Yen, F. H. Kao, W. C. Li, C. Y. Huang, J. R. Yang, and S. H. Wang, "Precipitation hardening of high-strength low-alloy steels by nanometer-sized carbides," *Mater. Sci. Eng. A*, vol. 499, no. 1–2, pp. 162–166, Jan. 2009.

[40] V. Stephanie, "Control of the Non-Recrystallization Temperature in High Strength Low Alloy (HSLA) Steels," Ghent University, 2010.

[41] H. G. Hillenbrand, A. Liessem, K. Bierman, C. J. Heckman, and V. Schwinn, "Development of high strength material and pipe production technology for grade X120 line pipe," in *2004 International Pipeline Conference*, 2004, pp. 1743–1749.

[42] H. . Hillenbrand, A. Liessem, C. Kalwa, M. Erdelen-Peppler, and C. Stallybrass, "Technological solutions for high strength gas pipelines.," in *1st International Conference on Super-High Strength Steels*, 2008, pp. 1–16.

[43] J. T. Black and R. A. Kohser, *Degarmo's Materials and Processes in Manufacturing*, 11 th. Wiley, 2011.

[44] D. G. Stalheim and G. Muralidharan, "The Role of Continuous Cooling Transformation Diagrams in Material Design for High Strength Oil and Gas Transmission Pipeline Steels," in *International Pipeline Conference*, 2006.

[45] M. Shome and O. N. Mohanty, "Continuous cooling transformation diagrams applicable to the heat-affected zone of HSLA-80 and HSLA-100 steels," *Metall. Mater. Trans. A Phys. Metall. Mater. Sci.*, vol. 37, no. 7, pp. 2159–2169, 2006.

[46] J. T. Mcgrath, J. A. Gianetto, and R. F. Orr, "Microstructure / Mechanical Property Relationships of Submerged Arc Welds in HSLA 80 Steel," in *Welding Research Supplement*, 1989, pp. 112–120.

[47] P. A. Peters and H. G. Hillendbrand, "Experience in Supply of Arctic Grdae Line Pipe for Soviet Construction Projects," in *World Materials Congress*, 1988.

[48] W. F. Smith, *Structure and Properties of Engineering Alloys*, 2nd ed. McGraw-Hill, 1993.

[49] H. G. Hillenbrand and P. Schwaab, "Quantitative determination of the microstructure of high strength structural steels for correlation with their mechanical properties," *Mater. Sci. Eng.*, vol. 94, pp. 71–78, Oct. 1987.

[50] D. B. Rosado, W. D. Waele, D. Vanderschueren, and S. Hertelé, "Latest developments in mechanical properties and metallurgical features of high strength line pipe steels," *Int. J. Sustain. Constr. Des.*, vol. 4, no. 1, p. 10, 2013.

[51] H. Asahi, N. R. V Bangaru, T. Hara, J. Koo, M. J. Luton, C. W. Petersen, H. Tamehiro, and Y. Terada, "Ultra-high strength, weldable steels with excellent ultra-low temperature toughness," 06-May-1999.

[52] A. Liessem, G. Knauf, and S. Zimmermann, "Strain Based Design—What the Contribution of a Pipe Manufacturer Can Be," in *The Seventeenth International Offshore and Polar Engineering Conference*, 2007.

[53] P. A. Peters, M. K. Graef, H.-G. Hillenbrand, and K. A. Niederhoff, "Modern line pipe steels for offshore use," in *3R International*, 1988.

[54] A. Neville and T. Hodgkiess, “Study of effect of liquid corrosivity in liquid-solid impingement on cast iron and austenitic stainless steel,” *Br. Corros. J.*, vol. 32, no. 3, pp. 197–205, 1997.

[55] D. J. O’Flynn, M. S. Bingley, M. S. A. Bradley, and A. J. Burnett, “A model to predict the solid particle erosion rate of metals and its assessment using heat-treated steels,” *Wear*, vol. 248, no. 1–2, pp. 162–177, Mar. 2001.

[56] J. R. Laguna-Camacho, A. Marquina-Chávez, J. V. Méndez-Méndez, M. Vite-Torres, and E. A. Gallardo-Hernández, “Solid particle erosion of AISI 304, 316 and 420 stainless steels,” *Wear*, vol. 301, no. 1–2, pp. 398–405, Apr. 2013.

[57] Y. I. Oka, K. Okamura, and T. Yoshida, “Practical estimation of erosion damage caused by solid particle impact,” *Wear*, vol. 259, no. 1–6, pp. 95–101, Jul. 2005.

[58] J. I. Ukpai, R. Barker, X. Hu, and A. Neville, “Exploring the erosive wear of X65 carbon steel by acoustic emission method,” *Wear*, vol. 301, no. 1–2, pp. 370–382, Apr. 2013.

[59] Y. I. Oka, S. Mihara, and T. Yoshida, “Impact-angle dependence and estimation of erosion damage to ceramic materials caused by solid particle impact,” *Wear*, vol. 267, no. 1–4, pp. 129–135, Jun. 2009.

[60] H. S. Grewal, H. Singh, and A. Agrawal, “Understanding Liquid Impingement erosion behaviour of nickel–alumina based thermal spray coatings,” *Wear*, vol. 301, no. 1–2, pp. 424–433, Apr. 2013.

[61] R. G. Rateick, K. R. Karasek, A. J. Cunningham, K. C. Goretta, and J. L. Routbort, “Solid-particle erosion of tungsten carbide/cobalt cermet and hardened 440C stainless steel—A comparison,” *Wear*, vol. 261, no. 7–8, pp. 773–778, Oct. 2006.

[62] M. Vite-Torres, J. R. Laguna-Camacho, R. E. Baldenebro-Castillo, E. A. Gallardo-Hernández, E. E. Vera-Cárdenas, and J. Vite-Torres, “Study of solid particle erosion on AISI 420 stainless steel using angular silicon carbide and steel round grit particles,” *Wear*, vol. 301, no. 1–2, pp. 383–389, Apr. 2013.

[63] T. H. Mccloskey and C. Bellanca, “Minimizing solid particle erosion in power plant steam turbines,” *Power Eng.*, vol. 93, no. 8, pp. 35–38, 1989.

[64] R. Malka, S. Nešić, and D. A. Gulino, “Erosion–corrosion and synergistic effects in disturbed liquid-particle flow,” *Wear*, vol. 262, no. 7–8, pp. 791–799, Mar. 2007.

[65] Y. P. Wang, D. Y. Li, L. Parent, and H. Tian, “Performances of hybrid high-entropy high-Cr cast irons during sliding wear and air-jet solid-particle erosion,” *Wear*, vol. 301, no. 1–2, pp. 390–397, Apr. 2013.

[66] X. Hu and A. Neville, “CO2 erosion–corrosion of pipeline steel (API X65) in oil and gas conditions—A systematic approach,” *Wear*, vol. 267, no. 11, pp. 2027–2032, Oct. 2009.

[67] Y. I. Oka and T. Yoshida, “Practical estimation of erosion damage caused by solid particle impact,” *Wear*, vol. 259, no. 1–6, pp. 102–109, Jul. 2005.

[68] M. A. Al-Bukhaiti, S. M. Ahmed, F. M. F. Badran, and K. M. Emara, “Effect of impingement angle on slurry erosion behaviour and mechanisms of 1017 steel and high-chromium white cast iron,” *Wear*, vol. 262, no. 9–10, pp. 1187–1198, Apr. 2007.

[69] M. A. Islam, T. Alam, Z. N. Farhat, A. Mohamed, and A. Alfantazi, “Effect of microstructure on the erosion behavior of carbon steel,” *Wear*, vol. 332–333, pp. 1080–1089, May 2015.

[70] L. P. McCabe, G. A. Sargent, and H. Conrad, “Effect of microstructure on the erosion of steel by solid particles,” *Wear*, vol. 105, no. 3, pp. 257–277, Oct. 1985.

[71] A. V. Levy, “The solid particle erosion behavior of steel as a function of microstructure,” *Wear*, vol. 68, no. 3, pp. 269–287, May 1981.

[72] R. Sahoo, B. B. Jha, T. K. Sahoo, and S. Mantry, “Effect of Microstructural Degradation on Solid Particle Erosion Behavior of 2.25 Cr-1Mo Steel,” *Tribol. Trans.*, vol. 57, no. 4, pp. 679–689, 2014.

[73] B. B. Jha, B. K. Mishra, T. K. Sahoo, P. S. Mukherjee, and S. N. Ojha, “Effect of Microstructure upon the Wear Properties of 2.25 Cr-1Mo Steel,” in *Defect and Diffusion Forum*, 2010, vol. 303, pp. 85–97.

[74] R. Mohsin, Z. A. Majid, and M. Z. Yusof, “Multiple failures of API 5L X42 natural gas pipe: Experimental and computational analysis,” *Eng. Fail. Anal.*, vol. 34, pp. 10–23, Dec. 2013.

[75] Z. A. Majid, R. Mohsin, Z. Yaacob, and Z. Hassan, "Failure analysis of natural gas pipes," *Eng. Fail. Anal.*, vol. 17, no. 4, pp. 818–837, Jun. 2010.

[76] J. L. F. Freire, R. D. Vieira, and a. C. Benjamin, "Part 2: Experimental Strain Analysis of Metal Loss Defects in Pipeline," *Exp. Tech.*, vol. 30, no. 5, pp. 42–47, 2006.

[77] J. Postlethwaite, "Effect of Chromate Inhibitor on the Mechanical and Electrochemical Components of Erosion-Corrosion in Aqueous Slurries of Sand," *Corrosion*, vol. 37, no. 1, pp. 1–5, Jan. 1981.

[78] R. Bellman and A. Levy, "Erosion mechanism in ductile metals," *Wear*, vol. 70, no. 1, pp. 1–27, Jul. 1981.

[79] R. J. Llewellyn, S. K. Yick, and K. F. Dolman, "Scouring erosion resistance of metallic materials used in slurry pump service," *Wear*, vol. 256, no. 6, pp. 592–599, Mar. 2004.

[80] R. . Wellman and J. . Nicholls, "High temperature erosion–oxidation mechanisms, maps and models," *Wear*, vol. 256, no. 9–10, pp. 907–917, May 2004.

[81] R. Hamzah, D. J. Stephenson, and J. E. Strutt, "Erosion of material used in petroleum production," *Wear*, vol. 186–187, pp. 493–496, Aug. 1995.

[82] K. Haugen, O. Kvernvold, A. Ronold, and R. Sandberg, "Sand erosion of wear-resistant materials: Erosion in choke valves," *Wear*, vol. 186–187, pp. 179–188, Jul. 1995.

[83] H. M. Shalaby, W. T. Riad, A. A. Alhazza, and M. H. Behbehani, "Failure analysis of fuel supply pipeline," *Eng. Fail. Anal.*, vol. 13, no. 5, pp. 789–796, Jul. 2006.

[84] G. R. Desale, B. K. Gandhi, and S. C. Jain, "Slurry erosion of ductile materials under normal impact condition," *Wear*, vol. 264, no. 3–4, pp. 322–330, Feb. 2008.

[85] I. Finnie, G. R. Stevick, and J. R. Ridgely, "The influence of impingement angle on the erosion of ductile metals by angular abrasive particles," *Wear*, vol. 152, no. 1, pp. 91–98, Jan. 1992.

[86] G. W. Stachwick and A. W. Batchelor, *Engineering tribology*, 2nd ed. Boston: Butterworth-Heinemann, 2001.

[87] R. S. Lynn, K. K. Wong, and H. M. Clark, "On the particle size effect in slurry erosion," *Wear*, vol. 149, no. 1–2, pp. 55–71, Sep. 1991.

[88] A. Misra and I. Finnie, "On the size effect in abrasive and erosive wear," *Wear*, vol. 65, no. 3, pp. 359–373, Jan. 1981.

[89] H. M. Clark and R. B. Hartwich, "A re-examination of the 'particle size effect' in slurry erosion," *Wear*, vol. 248, no. 1–2, pp. 147–161, Mar. 2001.

[90] S. Bahadur and R. Badruddin, "Erodent particle characterization and the effect of particle size and shape on erosion," *Wear*, vol. 138, no. 1–2, pp. 189–208, Jun. 1990.

[91] G. T. Burstein and K. Sasaki, "Effect of impact angle on the slurry erosion–corrosion of 304L stainless steel," *Wear*, vol. 240, no. 1–2, pp. 80–94, May 2000.

[92] Y. I. Oka, H. Ohnogi, T. Hosokawa, and M. Matsumura, "The impact angle dependence of erosion damage caused by solid particle impact," *Wear*, vol. 203–204, pp. 573–579, Mar. 1997.

[93] K. C. Chen, J. L. He, W. H. Huang, and T. T. Yeh, "Study on the solid–liquid erosion resistance of ion-nitrided metal," *Wear*, vol. 252, no. 7–8, pp. 580–585, Apr. 2002.

[94] A. Yabuki, K. Matsuwaki, and M. Matsumura, "Critical impact velocity in the solid particles impact erosion of metallic materials," *Wear*, vol. 233–235, pp. 468–475, Dec. 1999.

[95] M. Liebhard and A. Levy, "The effect of erodent particle characteristics on the erosion of metals," *Wear*, vol. 151, no. 2, pp. 381–390, Dec. 1991.

[96] M. Divakar, V. K. Agarwal, and S. N. Singh, "Effect of the material surface hardness on the erosion of AISI316," *Wear*, vol. 259, no. 1–6, pp. 110–117, Jul. 2005.

[97] M. S. ElTobgy, E. Ng, and M. A. Elbestawi, "Finite element modeling of erosive wear," *Int. J. Mach. Tools Manuf.*, vol. 45, no. 11, pp. 1337–1346, Sep. 2005.

[98] R. J. K. Wood and T. F. Jones, "Investigations of sand–water induced erosive wear of AISI 304L stainless steel pipes by pilot-scale and laboratory-scale testing," *Wear*, vol. 255, no. 1–6, pp. 206–218, Aug. 2003.

[99] I. Finnie, "The Mechanism of Erosion of Ductile Metals," in *3rd U.S. Nat. Congress of Applied Mechanics*, 1958, pp. 527–532.

[100] I. Finnie, "Erosion of surfaces by solid particles," *Wear*, vol. 3, no. 2, pp. 87–103, Mar. 1960.

[101] I. Finnie and D. H. McFadden, "On the velocity dependence of the erosion of ductile metals by solid particles at low angles of incidence," *Wear*, vol. 48, no. 1, pp. 181–190, May 1978.

[102] J. Salik and D. Buckley, "Effects of Erodent Particle Shape and Various Heat Treatments on Erosion Resistance of Plain Carbon Steel," in *NASA Technical Paper*, 1981.

[103] G. A. Sargent, M. K. Keshavan, P. K. Mehrotra, and H. Conrad, "The Erosion of Plain Carbon Steels by Ash Particles From a Coal Gasifier," in *Proceedings of International Conference on Wear of Materials*, 1981.

[104] A. Levy and S. Jahanmir, "The Effects of the Microstructure of Ductile Alloys on Solid Particle Erosion Behavior," in *TMS-AIME*, 1978.

[105] A. Neville and C. Wang, "Inhibitor Performance on Corrosion and Erosion/Corrosion Under Turbulent Flow With Sand and CO2—An AC Impedance Study," *SPE Prod. Oper.*, vol. 23, no. 2, pp. 215–220, 2008.

[106] A. Neville and C. Wang, "Erosion–corrosion mitigation by corrosion inhibitors—An assessment of mechanisms," *Wear*, vol. 267, no. 1–4, pp. 195–203, Jun. 2009.

[107] A. Neville and C. Wang, "Erosion–corrosion of engineering steels—Can it be managed by use of chemicals?," *Wear*, vol. 267, no. 11, pp. 2018–2026, Oct. 2009.

[108] A. A. Torrance, "An explanation of the hardness differential needed for abrasion," *Wear*, vol. 68, no. 2, pp. 263–266, May 1981.

[109] A. Levy and P. Chik, "The effects of erodent composition and shape on the erosion of steel," *Wear*, vol. 89, no. 2, pp. 151–162, Aug. 1983.

[110] I. M. Hutchings, "A model for the erosion of metals by spherical particles at normal incidence," *Wear*, vol. 70, no. 3, pp. 269–281, Aug. 1981.

[111] A. Levy, J. Yan, and J. Patterson, "Elevated temperature erosion of steels," *Wear*, vol. 108, no. 1, pp. 43–60, Mar. 1986.

[112] A. Levy and S. Jahanmir, “Corrosion-erosion behavior of materials,” in *Metallurgical society of AIME*, New York, 1980, pp. 177–190.

[113] A. A. Gadhikar, C. P. Sharma, and D. B. Goel, “Effect of carbides on erosion resistance of 23-8-N steel,” *Bull. Mater. Sci.*, vol. 37, no. 2, pp. 315–319, 2014.

[114] H. U. Hong, B. S. Rho, and S. W. Nam, “Correlation of the M23C6 precipitation morphology with grain boundary characteristics in austenitic stainless steel,” *Mater. Sci. Eng. A*, vol. 318, no. 1–2, pp. 285–292, Nov. 2001.

[115] D. R. Andrews and N. Horsfield, “Particle collisions in the vicinity of an eroding surface,” *J. Phys. D. Appl. Phys.*, vol. 16, no. 4, pp. 525–538, 2000.

[116] P. H. Shipway and I. M. Hutchings, “The rôle of particle properties in the erosion of brittle materials,” *Wear*, vol. 193, no. 1, pp. 105–113, Apr. 1996.

[117] J. F. Molinari and M. Ortiz, “A study of solid-particle erosion of metallic targets,” *Int. J. Impact Eng.*, vol. 27, no. 4, pp. 347–358, Apr. 2002.

[118] J. G. A. Bitter, “A study of erosion phenomena part I,” *Wear*, vol. 6, no. 1, pp. 5–21, Jan. 1963.

[119] J. G. A. Bitter, “A study of erosion phenomena part II,” *Wear*, vol. 6, no. 3, pp. 169–190, May 1963.

[120] I. M. Hutchings, *Tribology: Friction and Wear of Engineering Materials*. London, 1992.

[121] I. M. Hutchings and R. E. Winter, “Particle erosion of ductile metals: A mechanism of material removal,” *Wear*, vol. 27, no. 1, pp. 121–128, Jan. 1974.

[122] A. Levy, “The platelet mechanism of erosion of ductile metals,” *Wear*, vol. 108, no. 1, pp. 1–21, Mar. 1986.

[123] D. A. López, J. P. Congote, J. R. Cano, A. Toro, and A. P. Tschiptschin, “Effect of particle velocity and impact angle on the corrosion–erosion of AISI 304 and AISI 420 stainless steels,” *Wear*, vol. 259, no. 1–6, pp. 118–124, Jul. 2005.

[124] G. P. Tilly, “A two stage mechanism of ductile erosion,” *Wear*, vol. 23, no. 1, pp. 87–96, Jan. 1973.

[125] A. N. J. Stevenson and I. M. Hutchings, “Scaling laws for particle velocity in the gas-blast erosion test,” *Wear*, vol. 181–183, pp. 56–62, Feb. 1995.

[126] J. . Mbabazi, T. . Sheer, and R. Shandu, “A model to predict erosion on mild steel surfaces impacted by boiler fly ash particles,” *Wear*, vol. 257, no. 5–6, pp. 612–624, Sep. 2004.

[127] E. Akbarzadeh, E. Elsaadawy, A. M. Sherik, J. K. Spelt, and M. Papini, “The solid particle erosion of 12 metals using magnetite erodent,” *Wear*, vol. 282–283, pp. 40–51, Apr. 2012.

[128] M. A. Islam and Z. N. Farhat, “Effect of impact angle and velocity on erosion of API X42 pipeline steel under high abrasive feed rate,” *Wear*, vol. 311, no. 1–2, pp. 180–190, Mar. 2014.

[129] P. Blau, *Friction, Lubrication, and Wear Technology*, vol. 18. ASM International, 1992.

[130] H. M. Clark, “The influence of the flow field in slurry erosion,” *Wear*, vol. 152, no. 2, pp. 223–240, Jan. 1992.

[131] I. M. Hutchings, R. E. Winter, and J. E. Field, “Solid particle erosion of metals: the removal of surface material by spherical projectiles,” in *Proceedings of the Royal Society of London A: Mathematical, Physical and Engineering Sciences*, 1976, vol. 348, no. 1654, pp. 379–392.

[132] D. G. Rickerby and N. H. MacMillan, “Erosion of Aluminum and Magnesium Oxide by Spherical Particles,” in *Wear of Materials*, 1981, pp. 548–563.

[133] D. G. Rickerby and N. H. Macmillan, “On the oblique impact of a rigid sphere against a rigid-plastic solid,” *Int. J. Mech. Sci.*, vol. 22, no. 8, pp. 491–494, Jan. 1980.

[134] I. M. Hutchings, N. H. Macmillan, and D. G. Rickerby, “Further studies of the oblique impact of a hard sphere against a ductile solid,” *Int. J. Mech. Sci.*, vol. 23, no. 11, pp. 639–646, Jan. 1981.

[135] N. Gane, “The direct measurement of the strength of metals on a sub-micrometre scale,” in *Proceedings of the Royal Society of London A:*

Mathematical, Physical and Engineering Sciences, 1970, vol. 317, no. 1530, pp. 367–391.

[136] N. Gane and J. M. Cox, "The micro-hardness of metals at very low loads," *Philos. Mag.*, vol. 22, no. 179, pp. 881–891, 1970.

[137] R. Brown, E. J. Jun, and J. W. Edington, "Mechanisms of Erosive Wear for 90° Impact on Copper and Iron Targets," in *Wear of Materials*, 1981, pp. 583–591.

[138] J. Maji and G. L. Sheldon, "Mechanisms of Erosion of a Ductile Material by Solid Particles," in *Erosion: Prevention and Useful Applications*, 1979, pp. 136–147.

[139] K. Wellinger and H. Uetz, "Gleit-, Spül- und strahlverschleiss-prüfung," *Wear*, vol. 1, no. 3, pp. 225–231, Dec. 1957.

[140] I. Finnie, "Some observations on the erosion of ductile metals," *Wear*, vol. 19, no. 1, pp. 81–90, Jan. 1972.

[141] T. Deng, A. R. Chaudhry, M. Patel, I. Hutchings, and A. J. Burnett, "Effect of particle concentration on erosion rate of mild steel bends in a pneumatic conveyor," *Wear*, vol. 248, pp. 162–177, 2001.

[142] H. Uuemõis and I. Kleis, "A critical analysis of erosion problems which have been little studied," *Wear*, vol. 31, no. 2, pp. 359–371, Feb. 1975.

[143] G. P. Tilly and W. Sage, "The interaction of particle and material behaviour in erosion processes," *Wear*, vol. 16, no. 6, pp. 447–465, Dec. 1970.

[144] P. H. Shipway and I. M. Hutchings, "A method for optimizing the particle flux in erosion testing with a gas-blast apparatus," *Wear*, vol. 174, no. 1–2, pp. 169–175, May 1994.

[145] T. Burzynski and M. Papini, "Analytical models of the interference between incident and rebounding particles within an abrasive jet: Comparison with computer simulation," *Wear*, vol. 263, no. 7–12, pp. 1593–1601, Sep. 2007.

[146] K. Anand, S. K. Hovis, H. Conrad, and R. O. Scattergood, "Flux effects in solid particle erosion," *Wear*, vol. 118, no. 2, pp. 243–257, Aug. 1987.

[147] H. M. Clark and K. K. Wong, "Impact angle, particle energy and mass loss in erosion by dilute slurries," *Wear*, vol. 186–187, pp. 454–464, Aug. 1995.

[148] Q. Fang, H. Xu, P. S. Sidky, and M. G. Hocking, "Erosion of ceramic materials by a sand/water slurry jet," *Wear*, vol. 224, no. 2, pp. 183–193, Feb. 1999.

[149] I. M. Hutchings, "Deformation of metal surfaces by the oblique impact of square plates," *Int. J. Mech. Sci.*, vol. 19, no. 1, pp. 45–52, Jan. 1977.

[150] R. E. Winter and I. M. Hutchings, "Solid particle erosion studies using single angular particles," *Wear*, vol. 29, no. 2, pp. 181–194, Aug. 1974.

[151] I. M. Hutchings, "Mechanisms of the erosion of metals by solid particles," *Eros. Prev. Useful Appl. ASTM STP*, vol. 664, pp. 59–76, 1979.

[152] I. Finnie, A. Levy, D. H. McFadden, S. M. Wolf, and N. H. Macmillan, "Fundamental mechanisms of the erosive wear of ductile metals by solid particles. Discussion," *ASTM Spec. Tech. Publ.*, no. 664, pp. 36–58, 1979.

[153] R. A. Mayville, "Mechanisms of material removal in the solid particle erosion of ductile materials," *Lawrence Berkeley Natl. Lab.*, 2011.

[154] T. H. Kosel, Z. Y. Mao, and S. V Prasad, "Erosion debris particle observations and the micromachining mechanism of erosion," *ASLE Trans.*, vol. 28, no. 2, pp. 268–276, 1985.

[155] A. Hammarsten, S. Soderberg, and S. Hogmark, "Study of Erosion Mechanisms of Recovery and Analysis of Wear Fragments," in *Proceedings of International Conference on Wear of Materials*, 1983, pp. 373–381.

[156] A. Levy, "The Erosion of Metal Alloys and Their Scales, Proceedings of Conference on Corrosion-Erosion-Wear of Materials in Emerging Fossil Energy Systems," in *National Association of Corrosion Engineers*, 1982, pp. 298–376.

[157] I. M. Hutchings and A. V. Levy, "Thermal effects in the erosion of ductile metals," *Wear*, vol. 131, no. 1, pp. 105–121, May 1989.

[158] J. H. Neilson and A. Gilchrist, "Erosion by a stream of solid particles," *Wear*, vol. 11, no. 2, pp. 111–122, Feb. 1968.

[159] T. Singh and G. Sundararajan, "The erosion behavior of 304 stainless steel at elevated temperatures," *Metall. Trans. A*, vol. 21, no. 12, pp. 3187–3199, 1990.

[160] C. T. Morrison, R. O. Scattergood, and J. L. Routbort, "Erosion of 304 stainless steel," *Wear*, vol. 111, no. 1, pp. 1–13, Aug. 1986.

[161] I. M. Hutchings, "Ductile-brittle transitions and wear maps for the erosion and abrasion of brittle materials," *J. Phys. D. Appl. Phys.*, vol. 25, pp. 212–221, 1992.

[162] G. Sundararajan and P. G. Shewmon, "A new model for the erosion of metals at normal incidence," *Wear*, vol. 84, no. 2, pp. 237–258, Jan. 1983.

[163] A. W. Ruff and S. . Wiederhorn, "Erosion by solid particle impact," *Treatise Mater. Sci. Technol.*, vol. 16, pp. 69–126, 1979.

[164] M. G. Fontana, *Corrosion engineering*. Tata McGraw-Hill Education, 2005.

[165] M. G. Fontana, "The Eight Forms of Corrosion," in *Process Industries Corrosion*, 1975, pp. 1–39.

[166] M. G. Fontana and N. D. Greene, *Corrosion Engineering*, 2nd ed. 1978.

[167] R. W. Revie, *Corrosion and corrosion control*. John Wiley & Sons, 2008.

[168] U. R. Evans, *The Corrosion and Oxidation of Metals: Scientific Principles and Practical Applications*. Hodder Arnold, 1960.

[169] C. X. Li and T. Bell, "Corrosion properties of active screen plasma nitrided 316 austenitic stainless steel," *Corros. Sci.*, vol. 46, no. 6, pp. 1527–1547, 2004.

[170] S.-J. Lee and J.-J. Lai, "The effects of electropolishing (EP) process parameters on corrosion resistance of 316L stainless steel," *J. Mater. Process. Technol.*, vol. 140, no. 1, pp. 206–210, 2003.

[171] C. Ren, D. Liu, Z. Bai, and T. Li, "Corrosion behavior of oil tube steel in simulant solution with hydrogen sulfide and carbon dioxide," *Mater. Chem. Phys.*, vol. 93, no. 2, pp. 305–309, 2005.

[172] A. D. Mercer and E. A. Lumbard, "Corrosion of mild steel in water," *Br. Corros. J.*, vol. 30, no. 1, pp. 43–55, 1995.

[173] W.-T. Tsai and J.-R. Chen, "Galvanic corrosion between the constituent phases in duplex stainless steel," *Corros. Sci.*, vol. 49, no. 9, pp. 3659–3668, 2007.

[174] M. J. Pryor and D. S. Keir, "Galvanic Corrosion II. Effect of pH and Dissolved Oxygen Concentration on the Aluminum- Steel Couple," *J. Electrochem. Soc.*, vol. 105, no. 11, pp. 629–635, 1958.

[175] B. Tsujino and S. Miyase, "The galvanic corrosion of steel in sodium chloride solution," *Corrosion*, vol. 38, no. 4, pp. 226–230, 1982.

[176] X. G. Zhang and E. M. Valeriote, "Galvanic protection of steel and galvanic corrosion of zinc under thin layer electrolytes," *Corros. Sci.*, vol. 34, no. 12, pp. 1957–1972, 1993.

[177] M. Tavakkolizadeh and H. Saadatmanesh, "Galvanic corrosion of carbon and steel in aggressive environments," *J. Compos. Constr.*, vol. 5, no. 3, pp. 200–210, 2001.

[178] Z. Szklarska-Smialowska and J. Mankowski, "Crevice corrosion of stainless steels in sodium chloride solution," *Corros. Sci.*, vol. 18, no. 11, pp. 953–960, 1978.

[179] J. W. Oldfield and W. H. Sutton, "Crevice Corrosion of Stainless Steels: I. A Mathematical Model," *Br. Corros. J.*, vol. 13, no. 1, pp. 13–22, 1978.

[180] Z. Li, F. Gan, and X. Mao, "A study on cathodic protection against crevice corrosion in dilute NaCl solutions," *Corros. Sci.*, vol. 44, no. 4, pp. 689–701, 2002.

[181] G. S. Frankel, L. Stockert, F. Hunkeler, and H. Boehni, "Metastable Pitting of Stainless Steel," *Corrosion*, vol. 43, no. 7, pp. 429–436, Jul. 1987.

[182] M. A. Streicher, "Pitting Corrosion of 18Cr- 8Ni Stainless Steel," *J. Electrochem. Soc.*, vol. 103, no. 7, pp. 375–390, 1956.

[183] Y. Tsutsumi, A. Nishikata, and T. Tsuru, "Pitting corrosion mechanism of Type 304 stainless steel under a droplet of chloride solutions," *Corros. Sci.*, vol. 49, no. 3, pp. 1394–1407, 2007.

[184] Y. Zhu and D. E. Williams, "Scanning electrochemical microscopic observation of a precursor state to pitting corrosion of stainless steel," *J. Electrochem. Soc.*, vol. 144, no. 3, pp. L43–L45, 1997.

[185] C. S. Tedmon, D. A. Vermilyea, and J. H. Rosolowski, "Intergranular corrosion of austenitic stainless steel," *J. Electrochem. Soc.*, vol. 118, no. 2, pp. 192–202, 1971.

[186] C. L. Briant, "The effects of sulfur and phosphorus on the intergranular corrosion of 304 stainless steel," *Corrosion*, vol. 36, no. 9, pp. 497–509, 1980.

[187] T. M. Devine, "Mechanism of intergranular corrosion and pitting corrosion of austenitic and duplex 308 stainless steel," *J. Electrochem. Soc.*, vol. 126, no. 3, pp. 374–385, 1979.

[188] M. Matula, L. Hyspecka, M. Svoboda, V. Vodarek, C. Dagbert, J. Galland, Z. Stonawska, and L. Tuma, "Intergranular corrosion of AISI 316L steel," *Mater. Charact.*, vol. 46, no. 2, pp. 203–210, 2001.

[189] A. Y. Kina, V. M. Souza, S. S. M. Tavares, J. M. Pardal, and J. A. Souza, "Microstructure and intergranular corrosion resistance evaluation of AISI 304 steel for high temperature service," *Mater. Charact.*, vol. 59, no. 5, pp. 651–655, 2008.

[190] R. P. Frankenthal and H. W. Pickering, "Intergranular corrosion of a ferritic stainless steel," *J. Electrochem. Soc.*, vol. 120, no. 1, pp. 23–26, 1973.

[191] J. K. Kim, Y. H. Kim, S. H. Uhm, J. S. Lee, and K. Y. Kim, "Intergranular corrosion of Ti-stabilized 11wt% Cr ferritic stainless steel for automotive exhaust systems," *Corros. Sci.*, vol. 51, no. 11, pp. 2716–2723, 2009.

[192] M. Terada, M. Saiki, I. Costa, and A. F. Padilha, "Microstructure and intergranular corrosion of the austenitic stainless steel 1.4970," *J. Nucl. Mater.*, vol. 358, no. 1, pp. 40–46, 2006.

[193] V. Ganesan and V. Ganesan, "Corrosion of annealed AISI 316 stainless steel in sodium environment," *J. Nucl. Mater.*, vol. 256, no. 1, pp. 69–77, 1998.

[194] R. E. Seebold, L. S. Birks, and E. J. Brooks, "Selective Removal of Chromium From Type 304 Stainless Steel by Air-Contaminated Lithium," *Corrosion*, vol. 16, no. 9, p. 468t–470t, 1960.

[195] R. Venkatesan, M. A. Venkatasamy, T. A. Bhaskaran, E. S. Dwarakadasa, and M. Ravindran, "Corrosion of ferrous alloys in deep sea environments," *Br. Corros. J.*, vol. 37, no. 4, pp. 257–266, 2002.

[196] J. A. Gonzalez, E. Ramırez, and A. Bautista, "Protection of steel embedded in chloride-containing concrete by means of inhibitors," *Cem. Concr. Res.*, vol. 28, no. 4, pp. 577–589, 1998.

[197] A. Neville, T. Hodgkiess, and J. T. Dallas, "A study of the erosion-corrosion behaviour of engineering steels for marine pumping applications," *Wear*, vol. 186, pp. 497–507, 1995.

[198] Y. Zheng, Z. Yao, X. Wei, and W. Ke, "The synergistic effect between erosion and corrosion in acidic slurry medium," *Wear*, vol. 186, pp. 555–561, 1995.

[199] E. A. M. Hussain and M. J. Robinson, "Erosion–corrosion of 2205 duplex stainless steel in flowing seawater containing sand particles," *Corros. Sci.*, vol. 49, no. 4, pp. 1737–1754, 2007.

[200] S. Nešić, J. Postlethwaite, and D. L. Olson, "An Electrochemical Model for Prediction of Corrosion of Mild Steel in Aqueous Carbon Dioxide Solutions," *Corros.*, vol. 52, no. 4, pp. 280–294, 1996.

[201] Y. Xi, D. Liu, and D. Han, "Improvement of erosion and erosion–corrosion resistance of AISI 420 stainless steel by low temperature plasma nitriding," *Appl. Surf. Sci.*, vol. 254, no. 18, pp. 5953–5958, 2008.

[202] M.-D. Bermúdez, F. J. Carrión, G. Martínez-Nicolás, and R. López, "Erosion–corrosion of stainless steels, titanium, tantalum and zirconium," *Wear*, vol. 258, no. 1, pp. 693–700, 2005.

[203] U. Lotz and J. Postlethwaite, "Erosion-corrosion in disturbed two phase liquid/particle flow," *Corros. Sci.*, vol. 30, no. 1, pp. 95–106, 1990.

[204] C. T. Kwok, F. T. Cheng, and H. C. Man, "Synergistic effect of cavitation erosion and corrosion of various engineering alloys in 3.5% NaCl solution," *Mater. Sci. Eng. A*, vol. 290, no. 1, pp. 145–154, 2000.

[205] J. A. Smith, M. H. Peterson, and B. F. Brown, "Electrochemical conditions at the tip of an advancing stress corrosion crack in AISI 4340 steel," *Corrosion*, vol. 26, no. 12, pp. 539–542, 1970.

[206] J. D. Harston and J. C. Scully, "Stress corrosion of type 304 steel in H2SO4/NaCl environments at room temperature," *Corrosion*, vol. 25, no. 12, pp. 493–501, 1969.

[207] D. A. Vaughan, D. I. Phalen, C. L. Peterson, and W. K. Boyd, "Relationship between hydrogen pickup and susceptible paths in stress corrosion cracking of type 304 stainless steel," *Corrosion*, vol. 19, no. 9, p. 315t–326t, 1963.

[208] J. F. Newman, "The stress corrosion of steel in sodium hydroxide solution: a film-rupture model," *Corros. Sci.*, vol. 21, no. 7, pp. 487–503, 1981.

[209] R. A. Oriani, "Hydrogen embrittlement of steels," *Annu. Rev. Mater. Sci.*, vol. 8, no. 1, pp. 327–357, 1978.

[210] L. S. Moroz and T. E. Mingin, "Hydrogen embrittlement of steel," *Met. Sci. Heat Treat.*, vol. 4, no. 3, pp. 135–137, 1962.

[211] M. B. Whiteman and A. R. Troiano, "Hydrogen embrittlement of austenitic stainless steel," *Corrosion*, vol. 21, no. 2, pp. 53–56, 1965.

[212] B. J. Berkowitz and H. H. Horowitz, "The role of H2S in the corrosion and hydrogen embrittlement of steel," *J. Electrochem. Soc.*, vol. 129, no. 3, pp. 468–474, 1982.

[213] M. R. Todd and G. V Grand, "Enhanced oil recovery using carbon dioxide," *Energy Convers. Manag.*, vol. 34, no. 9, pp. 1157–1164, 1993.

[214] G. Zhao, X. Lu, J. Xiang, and Y. Han, "Formation Characteristic of CO2 Corrosion Product Layer of P110 Steel Investigated by SEM and Electrochemical Techniques," *J. Iron Steel Res. Int.*, vol. 16, no. 4, pp. 89–94, Jul. 2009.

[215] E. Sadeghi Meresht, T. Shahrabi Farahani, and J. Neshati, "2-Butyne-1,4-diol as a novel corrosion inhibitor for API X65 steel pipeline in carbonate/bicarbonate solution," *Corros. Sci.*, vol. 54, pp. 36–44, Jan. 2012.

[216] D. G. Li, Y. R. Feng, Z. Q. Bai, and M. S. Zheng, "Characteristics of CO2 corrosion scale formed on N80 steel in stratum water with saturated CO2," *Appl. Surf. Sci.*, vol. 253, no. 20, pp. 8371–8376, Aug. 2007.

[217] B. Wang, M. Du, J. Zhang, and C. J. Gao, "Electrochemical and surface analysis studies on corrosion inhibition of Q235 steel by imidazoline derivative against CO2 corrosion," *Corros. Sci.*, vol. 53, no. 1, pp. 353–361, Jan. 2011.

[218] S. Guo, L. Xu, L. Zhang, W. Chang, and M. Lu, "Corrosion of alloy steels containing 2% chromium in CO2 environments," *Corros. Sci.*, vol. 63, pp. 246–258, Oct. 2012.

[219] F. Eliyan, E.-S. Mahdi, and A. Alfantazi, "Electrochemical evaluation of the corrosion behaviour of API-X100 pipeline steel in aerated bicarbonate solutions," *Corros. Sci.*, vol. 58, pp. 181–191, May 2012.

[220] Y. Xie, L. Xu, C. Gao, W. Chang, and M. Lu, "Corrosion behavior of novel 3%Cr pipeline steel in CO2 Top-of-Line Corrosion environment," *Mater. Des.*, vol. 36, pp. 54–57, Apr. 2012.

[221] G. A. Zhang and Y. F. Cheng, "Electrochemical corrosion of X65 pipe steel in oil/water emulsion," *Corros. Sci.*, vol. 51, no. 4, pp. 901–907, Apr. 2009.

[222] Q. M. Malik and M. R. Islam, "CO2 Injection in the Weyburn field of Canada: optimization of enhanced oil recovery and greenhouse gas storage with horizontal wells," in *SPE/DOE improved oil recovery symposium*, 2000.

[223] T. L. Watson and S. Bachu, "Identification of wells with high CO2-leakage potential in mature oil fields developed for CO2-enhanced oil recovery," in *SPE Symposium on Improved Oil Recovery*, 2008.

[224] R. K. Srivastava, S. S. Huang, and M. Dong, "Comparative effectiveness of CO2 produced gas, and flue gas for enhanced heavy-oil recovery," *SPE Reserv. Eval. Eng.*, vol. 2, no. 03, pp. 238–247, 1999.

[225] E. Dayalan, G. Vani, J. R. Shadley, S. A. Shirazi, and E. F. Rybicki, "Modelling CO2 corrosion of carbon steel in pipe flow," in *Corrosion*, 1995, p. Paper no 118.

[226] M. Heydari and M. Javidi, "Corrosion inhibition and adsorption behaviour of an amido-imidazoline derivative on API 5L X52 steel in CO2-saturated solution and synergistic effect of iodide ions," *Corros. Sci.*, vol. 61, pp. 148–155, Aug. 2012.

[227] D. R. Lide, *Handbook of chemistry and physics*. CRS Press, 1998.

[228] M. Ueda and H. Takabe, "Effect of Environmental Factor and Microstructure on Morphology of Corrosion Products in CO2 Environments," *Corrosion*, vol. Paper no 1, 1999.

[229] A. Dugstad, L. Lunde, and K. Videm, "Parametric Study of CO2 Corrosion of Carbon Steel," *Corrosion*, vol. Paper no 1, 1994.

[230] Y. Sun and S. Nešić, "A Parametric Study and Modelling on Localized CO2 Corrosion in Horizontal Wet Gas Flow," *Corrosion*, vol. Paper no 3, 2004.

[231] E. W. J. Hunnik, B. F. M. Pots, and E. L. J. A. Hendriksen, "The formation of protective FeCO3 corrosion product layers in CO2 corrosion," *Corrosion*, vol. Paper no 6, 1996.

[232] F. D. Moraes, S. A. Petrobras, J. R. Shadley, J. Chen, and E. F. Rybicki, "Characterization of CO2 Corrosion Product Scales related to Environmental Conditions," in *Corrosion*, 2000, p. Paper no 30.

[233] S. Nešić and L. Lunde, "Carbon Dioxide Corrosion of Carbon Steel in Two-Phase Flow," *Corrosion*, vol. 50, no. 9, pp. 717–727, 1994.

[234] K. Videm, "The influence of composition of carbon steels on anodic and cathodic reaction rate in CO2 corrosion," in *Corrosion*, 1998, p. Paper no 30.

[235] K. Videm and A. Dugstad, "Corrosion of carbon steel in an aqueous carbon dioxide environment. Part II: film formation," *Mater. Perform.*, vol. 28, pp. 46–49, 1989.

[236] B. Mishra, S. Al-Hassan, D. L. Olson, and M. M. Salama, "Development of a Predictive Model for Activation-Controlled Corrosion of Steel in Solutions Containing Carbon Dioxide," *Corrosion*, vol. 53, no. 11, pp. 852–859, 1997.

[237] C. DeWaard and D. E. Milliams, "Carbonic Acid Corrosion of Steel.," *Corrosion*, vol. 31, no. 5, pp. 177–181, 1975.

[238] C. DeWaard, U. Lotz, and D. E. Milliams, "Predictive Model for CO2 Corrosion Engineering in Wet Natural Gas Pipelines," *Corrosion*, vol. 47, no. 12, pp. 976–985, 1991.

[239] A. Neville, X. Hu, and I. M. Ismail, "Investigation of Pitting Corrosion and Inhibition in Sweet Conditions," in *Corrosion*, 2013, p. Paper no 2361.

[240] U. Lotz and T. Sydberger, "CO2 corrosion of carbon steel and 13Cr steel in particle-laden fluid," *Corrosion*, vol. 44, no. 11, pp. 800–809, 1988.

[241] J. C. C. Filho and M. E. Orazem, "Application of a Submerged Impinging Jet to Investigate the Influence of Temperature, Dissolved C02, and Fluid Velocity on Corrosion of Pipeline-Grade Steel in Brine," in *Corrosion*, 2001, p. Paper no 01058.

[242] J. K. Heuer and J. F. Stubbins, "An XPS characterization of FeCO3 films from CO2 corrosion," *Corros. Sci.*, vol. 41, no. 7, pp. 1231–1243, Jul. 1999.

[243] E. Gulbrandsen, J. Kvarekval, and H. Miland, "Effect of oxygen contamination on the inhibition of CO2 corrosion," in *Corrosion*, 2001, p. Paper no 01054.

[244] R. E. Reed-Hill, *Physical Metallurgy Principles*, 2nd ed. Mexico: Litton Educational Publishing International, 1979.

[245] C. A. Palacios and J. R. Shadley, "Characteristics of corrosion scales on steels in a CO2-saturated NaCl brine," *Corrosion*, vol. 47, no. 2, pp. 122–127, Feb. 1991.

[246] J. L. Crolet, N. Thevenot, and S. Nešić, "Role of Conductive Corrosion Products in the Protectiveness of Corrosion Layers," *Corrosion*, vol. 54, no. 3, pp. 194–203, Mar. 1998.

[247] A. Dugstad, H. Hemmer, and M. Seiersten, "Effect of Steel Microstructure on Corrosion Rate and Protective Iron Carbonate Film Formation," *Corrosion*, vol. 57, no. 4, pp. 369–378, Apr. 2001.

[248] R. Jasinski, "Corrosion of N80-Type Steel by CO2/Water Mixtures," *Corrosion*, vol. 43, no. 4, pp. 214–218, Apr. 1987.

[249] A. K. Pilkey, S. B. Lambert, and A. Plumtree, "Stress Corrosion Cracking of X-60 Line Pipe Steel in a Carbonate-Bicarbonate Solution," *Corrosion*, vol. 51, no. 2, pp. 91–96, Feb. 1995.

[250] C. A. Palacios and J. R. Shadley, "CO2 Corrosion of N-80 Steel at 71°C in a Two-Phase Flow System," *Corrosion*, vol. 49, no. 8, pp. 686–693, Aug. 1993.

[251] D. A. López, W. H. Schreiner, S. R. de Sánchez, and S. . Simison, "The influence of inhibitors molecular structure and steel microstructure on corrosion layers in CO2 corrosion," *Appl. Surf. Sci.*, vol. 236, no. 1–4, pp. 77–97, Sep. 2004.

[252] S. L. Wu, Z. D. Cui, F. He, Z. Q. Bai, S. L. Zhu, and X. J. Yang, "Characterization of the surface film formed from carbon dioxide corrosion on N80 steel," *Mater. Lett.*, vol. 58, no. 6, pp. 1076–1081, Feb. 2004.

[253] Y. Li, G. T. Burstein, and I. M. Hutchings, "Influence of environmental composition and electrochemical potential on the slurry erosion-corrosion of aluminium," *Wear*, vol. 181–183, pp. 70–79, Feb. 1995.

[254] X. Hu and A. Neville, "The electrochemical response of stainless steels in liquid–solid impingement," *Wear*, vol. 258, no. 1–4, pp. 641–648, Jan. 2005.

[255] G. Liang, X. Peng, L. Xu, and Y. F. Cheng, "Erosion-corrosion of carbon steel pipes in oil sands slurry studied by weight-loss testing and CFD simulation," *J. Mater. Eng. Perform.*, vol. 22, no. 10, pp. 3043–3048, 2013.

[256] S. Aribo, M. Bryant, A. Neville, and X. Hu, "Erosion-Corrosion of Lean Duplex Stainless Steel (UNS S32101) in a CO2-Saturated Oilfield Brine," in *Corrosion*, 2013.

[257] D. D. Macdonald and G. A. Cragnolino, "Corrosion of Steam Cycle Materials," *ASME Handb. Water Technol. Therm. Power Syst.*, vol. 8, no. Chapter 9, 1989.

[258] Y. Li, G. T. Burstein, and I. M. Hutchings, "The influence of corrosion on the erosion of aluminium by aqueous silica slurries," *Wear*, vol. 186–187, pp. 515–522, Aug. 1995.

[259] S. Zhou, M. M. Stack, and R. C. Newman, "Characterization of Synergistic Effects Between Erosion and Corrosion in an Aqueous Environment Using Electrochemical Techniques," *Corrosion*, vol. 52, no. 12, pp. 934–946, Dec. 1996.

[260] S. W. Watson, F. J. Friedersdorf, B. W. Madsen, and S. D. Cramer, "Methods of measuring wear-corrosion synergism," *Wear*, vol. 181–183, pp. 476–484, Mar. 1995.

[261] C. Wang, A. Neville, S. Ramachandran, and V. Jovancicevic, "Alleviation of erosion–corrosion damage by liquid–sand impact through use of chemicals," *Wear*, vol. 258, no. 1–4, pp. 649–658, Jan. 2005.

[262] A. Neville and T. Hodgkiess, “Characterisation of high-grade alloy behaviour in severe erosion–corrosion conditions,” *Wear*, vol. 233–235, pp. 596–607, Dec. 1999.

[263] M. B. Kermani and A. Morshed, “Carbon Dioxide Corrosion in Oil and Gas Production—A Compendium,” *Corrosion*, vol. 59, no. 8, pp. 659–683, Aug. 2003.

[264] A. Levy and Y.-F. Man, “Elevated temperature erosion-corrosion of 9Cr-1Mo steel,” *Wear*, vol. 111, no. 2, pp. 135–159, Sep. 1986.

[265] A. V. Levy and M. Yong-Fa, “Erosion-corrosion mechanisms and rates in fe-cr steels,” *Wear*, vol. 131, no. 1, pp. 39–51, May 1989.

[266] H. Meng, X. Hu, and A. Neville, “A systematic erosion–corrosion study of two stainless steels in marine conditions via experimental design,” *Wear*, vol. 263, no. 1–6, pp. 355–362, Sep. 2007.

[267] G. I. Ogundele and W. E. White, “Some Observations on Corrosion of Carbon Steel in Aqueous Environments Containing Carbon Dioxide,” *Corrosion*, vol. 42, no. 2, pp. 71–78, Feb. 1986.

[268] X.-P. Guo and Y. Tomoe, “The effect of corrosion product layers on the anodic and cathodic reactions of carbon steel in CO2-saturated mdea solutions at 100°C,” *Corros. Sci.*, vol. 41, no. 7, pp. 1391–1402, Jul. 1999.

[269] J. Amri, E. Gulbrandsen, and R. P. Nogueira, “The effect of acetic acid on the pit propagation in CO2 corrosion of carbon steel,” *Electrochem. commun.*, vol. 10, no. 2, pp. 200–203, Feb. 2008.

[270] J. Villarreal, D. Laverde, and C. Fuentes, “Carbon-steel corrosion in multiphase slug flow and CO2,” *Corros. Sci.*, vol. 48, no. 9, pp. 2363–2379, Sep. 2006.

[271] M. M. Stack and G. H. Abdulrahman, “Mapping erosion–corrosion of carbon steel in oil–water solutions: Effects of velocity and applied potential,” *Wear*, vol. 274–275, pp. 401–413, Jan. 2012.

[272] X. Tang, L. Y. Xu, and Y. F. Cheng, “Electrochemical corrosion behavior of X-65 steel in the simulated oil–sand slurry. II: Synergism of erosion and corrosion,” *Corros. Sci.*, vol. 50, no. 5, pp. 1469–1474, May 2008.

[273] S. Hassani, K. P. Roberts, S. Shirazi, J. R. Shadley, E. F. Rybicki, and C. Joia, “A New Approach for Predicting Inhibited Erosion-Corrosion in

CO2-Saturated Oil/Brine Flow Condition," *SPE Prod. Oper.*, vol. 28, no. 2, p. SPE–155136–PA, 2013.

[274] B. Saleh and S. M. Ahmed, "Slurry erosion-corrosion of carburized AISI 5117 steel," *Tribol. Lett.*, vol. 51, no. 1, pp. 135–142, 2013.

[275] Y. H. Dou, Y. Li, Z. G. Wang, and Z. Li, "Study of the Erosion-Corrosion Behavior of P110, N80 and VM140 Steel in 3.5 wt.% NaCl Solutions with Sand," in *Advanced Materials Research*, 2013, vol. 683, pp. 353–356.

[276] X. C. Lu, S. Z. Li, X. X. Jiang, and T. C. Zhang, "Effect of γ Phase on Corrosive Wear of Duplex Stainless Steel in Sulfuric Acid Solution," *Corrosion*, vol. 51, no. 6, pp. 456–462, Jun. 1995.

[277] T. C. Zhang, X. X. Jiang, and S. Z. Li, "Acceleration of corrosive wear of duplex stainless steel by chloride in 69% H3PO4 solution," *Wear*, vol. 199, no. 2, pp. 253–259, Nov. 1996.

[278] FanAiming, LongJinming, and TaoZiyun, "An investigation of the corrosive wear of stainless steels in aqueous slurries," *Wear*, vol. 193, no. 1, pp. 73–77, Apr. 1996.

[279] M. A. Islam and Z. N. Farhat, "The synergistic effect between erosion and corrosion of API pipeline in CO2 and saline medium," *Tribol. Int.*, vol. 68, pp. 26–34, Dec. 2013.

[280] M. M. Stack and B. D. Jana, "Modelling particulate erosion–corrosion in aqueous slurries: some views on the construction of erosion–corrosion maps for a range of pure metals," *Wear*, vol. 256, no. 9–10, pp. 986–1004, May 2004.

[281] B. R. Tian and Y. F. Cheng, "Electrochemical corrosion behavior of X-65 steel in the simulated oil sand slurry. I: Effects of hydrodynamic condition," *Corros. Sci.*, vol. 50, no. 3, pp. 773–779, Mar. 2008.

[282] K. Sasaki and G. T. Burstein, "Erosion–corrosion of stainless steel under impingement by a fluid jet," *Corros. Sci.*, vol. 49, no. 1, pp. 92–102, Jan. 2007.

[283] A. Gnanavelu, N. Kapur, A. Neville, and J. F. Flores, "An integrated methodology for predicting material wear rates due to erosion," *Wear*, vol. 267, no. 11, pp. 1935–1944, Oct. 2009.

[284] S. S. Rajahram, T. J. Harvey, and R. J. K. Wood, "Full factorial investigation on the erosion–corrosion resistance of UNS S31603," *Tribol. Int.*, vol. 43, no. 11, pp. 2072–2083, Nov. 2010.

[285] S. S. Rajahram, T. J. Harvey, and R. J. K. Wood, "Electrochemical investigation of erosion–corrosion using a slurry pot erosion tester," *Tribol. Int.*, vol. 44, no. 3, pp. 232–240, Mar. 2011.

[286] Y. M. Chang and C. H. Pitt, "Corrosive-Erosive Wear of Grinding Ball Metals at High Jet Velocities," *Corrosion*, vol. 43, no. 10, pp. 599–605, Oct. 1987.

[287] H. X. Guo, B. T. Lu, and J. L. Luo, "Interaction of mechanical and electrochemical factors in erosion–corrosion of carbon steel," *Electrochim. Acta*, vol. 51, no. 2, pp. 315–323, Oct. 2005.

[288] B. Madsen, "Standard guide for determining amount of synergism between wear and corrosion," *Wear Erosion, Met. Corros.*, vol. G119–09, pp. 1–7, 1994.

[289] M. M. Stack and N. Pungwiwat, "Erosion–corrosion mapping of Fe in aqueous slurries: some views on a new rationale for defining the erosion–corrosion interaction," *Wear*, vol. 256, no. 5, pp. 565–576, Mar. 2004.

[290] W. J. Schumacher, "Corrosive wear synergy of alloy and stainless steel," *Wear*, pp. 558–566, 1985.

[291] S. C. Lim and M. F. Ashby, "Overview no. 55 Wear-Mechanism maps," *Acta Metall.*, vol. 35, no. 1, pp. 1–24, Jan. 1987.

[292] I. M. Hutchings, "Transitions, threshold effects and erosion maps," *Key Eng. Mater.*, vol. 71, pp. 75–92, 1992.

[293] M. M. Stack and G. H. Abdulrahman, "Mapping erosion-corrosion of carbon steel in oil exploration conditions: Some new approaches to characterizing mechanisms and synergies," *Tribol. Int.*, vol. 43, no. 7, pp. 1268–1277, Jul. 2010.

[294] J. Jiang, M. M. Stack, and A. Neville, "Modelling the tribo-corrosion interaction in aqueous sliding conditions," *Tribol. Int.*, vol. 35, no. 10, pp. 669–679, Oct. 2002.

[295] M. M. Stack, N. Corlett, and S. Zhou, "A methodology for the construction of the erosion-corrosion map in aqueous environments," *Wear*, vol. 203–204, pp. 474–488, Mar. 1997.

[296] M. M. Stack and T. M. Abd El Badia, "Some comments on mapping the combined effects of slurry concentration, impact velocity and electrochemical potential on the erosion–corrosion of WC/Co–Cr coatings," *Wear*, vol. 264, no. 9–10, pp. 826–837, Apr. 2008.

[297] M. M. Stack, H. Jawan, and M. T. Mathew, "On the construction of micro-abrasion maps for a steel/polymer couple in corrosive environments," *Tribol. Int.*, vol. 38, no. 9, pp. 848–856, Sep. 2005.

[298] M. M. Stack and T. M. Abd El Badia, "Mapping erosion–corrosion of WC/Co–Cr based composite coatings: Particle velocity and applied potential effects," *Surf. Coatings Technol.*, vol. 201, no. 3–4, pp. 1335–1347, Oct. 2006.

[299] M. M. Stack, S. Zhou, and R. C. Newman, "Identification of transitions in erosion-corrosion regimes in aqueous environments," *Wear*, vol. 186–187, pp. 523–532, Aug. 1995.

[300] W. C. Oliver and G. M. Pharr, "An improved technique for determining hardness and elastic modulus using load and displacement sensing indentation experiments," *J. Mater. Res.*, vol. 7, no. 06, pp. 1564–1583, 1992.

[301] ISO, "Particle size analysis - Laser diffraction methods," *Int. Organ. Stand.*, vol. 13320, pp. 1–51, 2009.

[302] P. H. P. Darcis, C. N. McCowan, J. D. McColskey, and R. Fields, "Crack tip opening angle measurement through a girth weld in an X100 steel pipeline section," *Fatigue Fract. Eng. Mater. Struct.*, vol. 31, no. 12, pp. 1065–1078, 2008.

[303] M. Almansour, "Sulfide stress cracking resistance of API X100 high strength low alloy steel in H2S environments," University of British Columbia, 2007.

[304] J. Capeiie, J. Gilgert, and G. Pluvinage, "Hydrogen Effect on Fatigue and Fracture of Pipe Steels," in *Ecole Nationale d'Ingénieurs de Metz*, 2009, pp. 1–12.

[305] "API 5L Line Pipe Physical Properties," *Woodco USA*, 2014. [Online]. Available: http://www.woodcousa.com/line_pipe_properties.htm. [Accessed: 29-Sep-2015].

[306] "White Aluminum Oxide (AOW)." [Online]. Available: http://catalog.agsco.com/item/all-categories/industrial-minerals/pn-1035. [Accessed: 30-Sep-2015].

[307] J.-Y. Yoo, S.-S. Ahn, D.-H. Seo, W.-H. Song, and K.-B. Kang, "New Development of High Grade X80 to X120 Pipeline Steels," *Mater. Manuf. Process.*, vol. 26, no. 1, pp. 154–160, 2011.

[308] D. Lyn, S. Einav, W. Rodi, and H. Park, "A laser-Doppler velocimetry study of ensemble-averaged characteristics of the turbulent near wake of a square cylinder," *J. Fluid Mech.*, vol. 304, pp. 285–319, 1995.

[309] S. L. Chen, P. Siitonen, and P. Kettunen, "A method for measuring particle velocity in thermal spraying," *Surf. Coatings Technol.*, vol. 64, no. 1, pp. 17–20, Apr. 1994.

[310] A. W. Ruff and L. K. Ives, "Measurement of solid particle velocity in erosive wear," *Wear*, vol. 35, no. 1, pp. 195–199, Nov. 1975.

[311] L. C. Chang, I. C. Hsui, L. H. Chen, and T. S. Lui, "A study on particle erosion behavior of ductile irons," *Scr. Mater.*, vol. 52, no. 7, pp. 609–613, Apr. 2005.

[312] ASTM, "Standard Test Method for Conducting Erosion Tests by Solid Particle Impingement Using Gas Jets," *ASTM Int.*, vol. G76–07, pp. 1–6, 2013.

[313] ASTM, "Standard test method for conducting potentiodynamic polarization resistance measurements," *ASTM Int.*, vol. G59–97, pp. 1–4, 2014.

[314] ASTM, "Standard guide for laboratory immersion corrosion testing of metals," *ASTM Int.*, vol. G31–12a, pp. 1–10, 2012.

[315] A. Dugstad, "Importance of FeCO3 supersaturation on the CO2 corrosion of carbon steels," in *Corrosion*, 1992, vol. Paper no 1.

[316] A. Dugstad, "Mechanism of protective film formation during CO2 corrosion of carbon steel," in *Corrosion*, 1998.

[317] L. G. Llongueras, J. Hernandez, A. Munoz, and J. M. Flores, "Mechanism of FeCO3 Formation on API X70 Pipeline Steel in Brine Solutions Containing CO2," *Corrosion*, no. 05457, pp. 1–13, 2005.

[318] F. Eliyan and A. Alfantazi, "Effect of bicarbonate concentration on corrosion of high strength steel," *Corros. Eng. Sci. Technol.*, vol. 50, pp. 178–185, 2015.

[319] J. F. Moulder, W. F. Stickle, P. E. Sobol, and K. D. Bomben, *Handbook of X-ray Photoelectron Spectroscopy*. Minnesota: Physical Electronics, Inc., 1995.

[320] J. R. Shadley, S. A. Shirazi, E. Dayalan, M. Ismail, and E. F. Rybicki, "Erosion-Corrosion of a Carbon Steel Elbow in a Carbon Dioxide Environment," *Corrosion*, vol. 52, no. 9, pp. 714–723, Sep. 1996.

[321] J. R. Shadley, S. A. Shirazi, E. Dayalan, and E. F. Rybicki, "Prediction of Erosion-Corrosion Penetration Rate in a Carbon Dioxide Environment with Sand," *Corrosion*, vol. 54, no. 12, pp. 972–978, Dec. 1998.

[322] X. Hu, A. Neville, J. Wells, and V. De Souza, "Prediction Of Erosion-Corrosion In Oil And Gas - A Systematic Approach," in *Corrosion*, 2008, p. Paper no 08540.

[323] C. Wang, A. Neville, and S. Ramachandran, "Understanding the Action of Inhibitors in Mitigating Erosion-Corrosion in Impinging Flows," in *Corrosion*, 2004, p. Paper no 04658.

[324] X. Hu and A. Neville, "An examination of the electrochemical characteristics of two stainless steels (UNS S32654 and UNS S31603) under liquid–solid impingement," *Wear*, vol. 256, no. 5, pp. 537–544, Mar. 2004.

[325] X. Hu, R. Barker, A. Neville, and A. Gnanavelu, "Case study on erosion–corrosion degradation of pipework located on an offshore oil and gas facility," *Wear*, vol. 271, no. 9–10, pp. 1295–1301, Jul. 2011.

[326] S. S. Rajahram, T. J. Harvey, and R. J. K. Wood, "Erosion–corrosion resistance of engineering materials in various test conditions," *Wear*, vol. 267, no. 1–4, pp. 244–254, Jun. 2009.

[327] T. J. Harvey, J. A. Wharton, and R. J. K. Wood, "Development of synergy model for erosion-corrosion of carbon steel in a slurry pot," *Tribol. Mater. Surfaces Interfaces*, vol. 1, no. 1, pp. 33–47, 2007.

[328] J. Xie, A. T. Alpas, and D. O. Northwood, "Mechano-electrochemical effect between erosion and corrosion," *J. Mater. Sci.*, vol. 38, no. 24, pp. 4849–4856, 2003.

[329] G. R. Desale, B. K. Gandhi, and S. C. Jain, "Effect of erodent properties on erosion wear of ductile type materials," *Wear*, vol. 261, no. 7–8, pp. 914–921, Oct. 2006.

[330] B. A. Lindsley and A. R. Marder, "The effect of velocity on the solid particle erosion rate of alloys," *Wear*, vol. 225–229, pp. 510–516, Apr. 1999.

[331] M. M. Stack, F. H. Stott, and G. C. Wood, "The significance of velocity exponents in identifying erosion-corrosion mechanisms," *Le J. Phys. IV*, vol. 3, no. C9, pp. 687–694, 1993.

[332] A. J. Sparks and I. M. Hutchings, "Transitions in the erosive wear behaviour of a glass ceramic," *Wear*, vol. 149, no. 1–2, pp. 99–110, Sep. 1991.

[333] R. O. Scattergood and J. L. Routbort, "Velocity and size dependences of the erosion rate in silicon," *Wear*, vol. 67, no. 2, pp. 227–232, Mar. 1981.

[334] J. L. Routbort and A. P. L. Turner, "The erosion rate of reaction-bonded SiC containing various amounts of free silicon," *Wear*, vol. 84, no. 3, pp. 381–385, Feb. 1983.

[335] K. Sasaki and G. T. Burstein, "The generation of surface roughness during slurry erosion-corrosion and its effect on the pitting potential," *Corros. Sci.*, vol. 38, no. 12, pp. 2111–2120, Dec. 1996.

[336] A. K. Chauhan, D. B. Goel, and S. Prakash, "Solid particle erosion behaviour of 13Cr–4Ni and 21Cr–4Ni–N steels," *J. Alloys Compd.*, vol. 467, no. 1–2, pp. 459–464, Jan. 2009.

[337] Y. I. Oka, M. Matsumura, and T. Kawabata, "Relationship between surface hardness and erosion damage caused by solid particle impact," *Wear*, vol. 162–164, pp. 688–695, Apr. 1993.

[338] G. Sundararajan, "The depth of plastic deformation beneath eroded surfaces: The influence of impact angle and velocity, particle shape and material properties," *Wear*, vol. 149, no. 1–2, pp. 129–153, Sep. 1991.

[339] I. M. Hutchings, "Prediction of the resistance of metals to erosion by solid particles," *Wear*, vol. 35, no. 2, pp. 371–374, Dec. 1975.

[340] M. F. Ashby and S. C. Lim, "Wear-mechanism maps," *Scr. Metall. Mater.*, vol. 24, no. 5, pp. 805–810, May 1990.

[341] F. P. I. Theodore L. Bergman, Adrienne S. Lavine, *Fundamentals of Heat and Mass Transfer*, 7th Editio. Wiley, 2011.

[342] V. Casalegno, P. Vavassori, M. Valle, M. Ferraris, M. Salvo, and G. Pintsuk, "Measurement of thermal properties of a ceramic/metal joint by laser flash method," *J. Nucl. Mater.*, vol. 407, pp. 83–87, 2010.

[343] P. Hofer and E. Kaschnitz, "Thermal diffusivity of the aluminium alloy Al-10Si-Mn-Mg (Silafont 36) in the solid and liquid states," *High Temp. Press.*, vol. 40, pp. 311–323, 2011.

[344] O. Koszor, A. Lindemann, F. Davin, and C. Balazsi, "Observation of thermophysical and tribological properties of CNT reinforced Si3 N4," *Key Eng. Mater.*, vol. 409, pp. 354–362, 2009.

[345] J. K. Edwards, B. S. McLaury, and S. A. Shirazi, "Modeling solid particle erosion in elbows and plugged tees," *J. Energy Resour. Technol.*, vol. 123, no. 4, pp. 277–284, 2001.

[346] B. S. McLaury, J. Wang, S. A. Shirazi, J. R. Shadley, and E. F. Rybicki, "Solid Particle Erosion in Long Radius Elbows and Straight Pipes," in *Society of Petroleum Engineers*, 1997, pp. 977–986.

[347] B. Merger, "Recommended Practices For Erosive Wear in Piping Systems," *Det Nor. Verit.*, no. January, 2007.

[348] J. J. Kim and S. K. Park, "Solid particle erosion of AISI 403 stainless steel," *J. Mater. Sci. Lett.*, vol. 17, no. 17, pp. 1503–1506, 1998.

[349] T. Deng, M. S. Bingley, and M. S. A. Bradley, "The influence of particle rotation on the solid particle erosion rate of metals," *Wear*, vol. 256, no. 11–12, pp. 1037–1049, Jun. 2004.

[350] Y. S. Choi, J. J. Shim, and J. G. Kim, "Effects of Cr, Cu, Ni and Ca on the corrosion behavior of low carbon steel in synthetic tap water," *J. Alloys Compd.*, vol. 391, no. 1–2, pp. 162–169, Apr. 2005.

[351] Y.-S. Choi, J.-J. Shim, and J.-G. Kim, "Corrosion behavior of low alloy steels containing Cr, Co and W in synthetic potable water," *Mater. Sci. Eng. A*, vol. 385, no. 1–2, pp. 148–156, Nov. 2004.

[352] M. Ueda and A. Ikeda, “Effect of Microstructure and Cr Content in Steel on CO2 Corrosion,” in *NACE Corrosion*, 1996, p. PAper ID: NACE 96013.

[353] B. Kermani, M. Dougan, J. C. Gonzalez, C. Linne, and R. Cochrane, “Development of low carbon Cr-Mo steels with exceptional corrosion resistance for oilfield applications,” in *Corrosion*, 2001.

[354] B. Chexal, J. Horowitz, and B. Dooley, “Flow-accelerated corrosion in power plants. Revision 1,” Electric Power Research Inst., Palo Alto, CA (United States), 1998.

[355] M. S. Alwaranbi, “Chloride pitting corrosion of API X-80 and X-100 high strength low alloy pipeline steels in bicarbonate solutions,” University of British Columbia, 2006.

[356] F. F. Eliyan, F. Mohammadi, and A. Alfantazi, “An electrochemical investigation on the effect of the chloride content on CO2 corrosion of API-X100 steel,” *Corros. Sci.*, vol. 64, pp. 37–43, 2012.

[357] F. F. Eliyan, E.-S. Mahdi, Z. Farhat, and A. Alfantazi, “Interpreting the passivation of HSLA steel from electrochemical corrosion investigations in bicarbonate-oil aqueous emulsions,” *Int. J. Electrochem. Sci.*, vol. 8, 2013.

[358] A. P. Moon, S. Sangal, S. Layek, S. Giribaskar, and K. Mondal, “Corrosion Behavior of High-Strength Bainitic Rail Steels,” *Metall. Mater. Trans. A*, vol. 46, no. 4, pp. 1500–1518, 2015.

[359] R. C. Newman, “The dissolution and passivation kinetics of stainless alloys containing molybdenum—1. Coulometric studies of Fe-Cr and Fe-Cr-Mo alloys,” *Corros. Sci.*, vol. 25, no. 5, pp. 331–339, Jan. 1985.

[360] D. A. Stout, J. B. Lumsden, and R. W. Staehle, “An Investigation of Pitting Behavior of Iron-Molybdenum Binary Alloys,” *Corrosion*, vol. 35, no. 4, pp. 141–147, Apr. 1979.

[361] K. Ogura and T. Ohama, “Pit formation in the cathodic polarization of passive iron IV. Repair mechanism by molybdate, chromate and tungstate,” *Corrosion*, vol. 40, no. 2, pp. 47–51, 1984.

[362] E. McCafferty, “Validation of corrosion rates measured by the Tafel extrapolation method,” *Corros. Sci.*, vol. 47, no. 12, pp. 3202–3215, Dec. 2005.

[363] M. Stern and A. L. Geary, "Electrochemical polarization I. A theoretical analysis of the shape of polarization curves," *J. Electrochem. Soc.*, vol. 104, no. 1, pp. 56–63, 1957.

[364] Y. H. Yau and M. A. Streicher, "The Effect of Chromium Content (0 to 35%) in Fe-Cr Alloys on Corrosion Rates and Mechanisms in 1.0 N Sulfuric Acid," *Corrosion*, vol. 47, no. 5, pp. 352–359, 1991.

[365] W. Li and D. Y. Li, "Influence of surface morphology on corrosion and electronic behavior," *Acta Mater.*, vol. 54, no. 2, pp. 445–452, Jan. 2006.

[366] T. Hong and M. Nagumo, "Effect of surface roughness on early stages of pitting corrosion of Type 301 stainless steel," *Corros. Sci.*, vol. 39, no. 9, pp. 1665–1672, Sep. 1997.

[367] J. Mora-Mendoza and S. Turgoose, "Fe3C influence on the corrosion rate of mild steel in aqueous CO2 systems under turbulent flow conditions," *Corros. Sci.*, vol. 44, no. 6, pp. 1223–1246, Jun. 2002.

[368] S. Al-Hassan, B. Mishra, D. L. Olson, and M. M. Salama, "Effect of Microstructure on Corrosion of Steels in Aqueous Solution Containing Carbon Dioxide," *Corros. Eng. Sect.*, vol. 54, no. 6, pp. 480–491, Jun. 1998.

[369] J. K. Heuer and J. F. Stubbins, "Microstructure Analysis of Coupons Exposed to Carbon Dioxide Corrosion in Multiphase Flow," *Corrosion*, vol. 54, no. 7, pp. 566–575, 1998.

[370] M. Nordsveen, S. Nešić, R. Nyborg, and A. Stangeland, "A Mechanistic Model for Carbon Dioxide Corrosion of Mild Steel in the Presence of Protective Iron Carbonate Films—Part 1: Theory and Verification," *Corrosion*, vol. 59, no. 5, pp. 443–456, May 2003.

[371] D. A. López, T. Pérez, and S. N. Simison, "The influence of microstructure and chemical composition of carbon and low alloy steels in CO2 corrosion. A state-of-the-art appraisal," *Mater. Des.*, vol. 24, no. 8, pp. 561–575, Dec. 2003.

[372] D. W. Shannon, "Role of chemical components in geothermal brine on corrosion," in *NACE Corrosion*, 1978.

[373] W. C. Baek, T. Kang, H. J. Sohn, and Y. T. Kho, "In situ surface enhanced Raman spectroscopic study on the effect of dissolved oxygen on the corrosion film on low carbon steel in 0.01 M NaCl solution," *Electrochim. Acta*, vol. 46, no. 15, pp. 2321–2325, Apr. 2001.

[374] D. A. López, W. H. Schreiner, S. R. de Sánchez, and S. . Simison, "The influence of carbon steel microstructure on corrosion layers," *Appl. Surf. Sci.*, vol. 207, no. 1–4, pp. 69–85, Feb. 2003.

[375] P. Li, J. Y. Lin, K. L. Tan, and J. Y. Lee, "Electrochemical impedance and X-ray photoelectron spectroscopic studies of the inhibition of mild steel corrosion in acids by cyclohexylamine," *Electrochim. Acta*, vol. 42, no. 4, pp. 605–615, Jan. 1997.

[376] A. Welle, J. D. Liao, K. Kaiser, M. Grunze, U. Mäder, and N. Blank, "Interactions of N,N′-dimethylaminoethanol with steel surfaces in alkaline and chlorine containing solutions," *Appl. Surf. Sci.*, vol. 119, no. 3–4, pp. 185–198, Oct. 1997.

[377] Y. Gonzalez, M. C. Lafont, N. Pebere, G. Chatainier, J. Roy, and T. Bouissou, "A corrosion inhibition study of a carbon steel in neutral chloride solutions by zinc salt/phosphonic acid association," *Corros. Sci.*, vol. 37, no. 11, pp. 1823–1837, Nov. 1995.

[378] K. Kurosawa, H. L. Li, Y. Ujihira, and K. Nomura, "Characterization of Carbonitrided and Oxidized Layers on Low-Carbon Steel by Conversion Electron Mössbauer Spectrometry," *Corrosion*, vol. 55, no. March, pp. 238–247, 1999.

[379] A. Dugstad, H. Hemmer, and M. Seiersten, "Effect of Steel Microstructure upon Corrosion Rate and Protective Iron Carbonates Film Formation," *Corros. Houston, TX, NACE*, vol. Paper. 24., no. 4, pp. 369–378, 2000.

[380] G. S. Frankel, "Pitting Corrosion of Metals," *J. Electrochem. Soc.*, vol. 145, no. 6, pp. 2186–2198, 1998.

[381] Z. Smialowska, "Pitting Corrosion of Metals," in *Corrosion*, 1986.

[382] J. Mankowski and Z. Szklarska-Smialowska, "Studies on accumulation of chloride ions in pits growing during anodic polarization," *Corros. Sci.*, vol. 15, no. 6–12, pp. 493–501, Jan. 1975.

[383] J. Xie, A. T. Alpas, and D. O. Northwood, "The Effect of Erosion on the Electrochemical Properties of AISI 1020 Steel," *J. Mater. Eng. Perform.*, vol. 12, no. February, pp. 77–86, 2003.

Appendix A

Materials Characterization

Table A-1 Inductively Coupled Plasma Mass Spectrometry (ICP) analysis for carbon and pipeline steels.

Elements	AISI 1018	AISI 1080	API X42	API X70	API X100
C	0.182	0.814	0.169	0.061	0.103
Si	0.095	0.120	0.067	0.150	0.151
Mn	0.754	0.598	0.372	1.223	1.221
Cr	0.181	0.122	0.027	0.018	0.070
P	0.040	0.040	0.040	0.010	0.010
Cu	0.186	0.230	0.008	0.008	0.009
Ti	0.008	0.001	0.002	0.015	0.018
V	0.001	0.021	0.001	0.028	0.036
S	0.021	0.014	0.004	0.002	0.001
Mg	0.001	0.002	0.002	0.001	0.002
Mo	0.052	0.012	0.001	0.001	0.009
Na	0.003	0.003	0.005	0.004	0.004
Ni	0.173	0.055	0.006	0.006	0.007
W	<0.005	<0.005	<0.005	<0.005	0.021
Nb	<0.001	<0.001	<0.001	0.057	0.058
Zn	<0.005	0.006	<0.005	0.001	0.001
Zr	<0.001	<0.001	<0.001	<0.001	<0.001
Ta	<0.010	<0.010	<0.010	<0.010	<0.010
Te	<0.010	<0.010	<0.010	<0.010	<0.010
Ge	<0.010	<0.010	<0.010	<0.010	<0.010
In	<0.010	<0.010	<0.010	<0.010	<0.010
K	<0.005	<0.005	<0.005	<0.005	<0.005
La	<0.001	<0.001	<0.001	<0.001	<0.001
Li	<0.001	<0.001	<0.001	<0.001	<0.001
Fe	balance	balance	balance	balance	balance

Appendix B

Erosion Data

Table B-1 Normalized erosion rate of different steels at different impact angle and particle velocity.

Sample	Erodent	Impact angle (°)	Normalized velocity	Normalized erosion rate	Erosion mode	Reference
AISI 304	SiC	30	65	4.62×10^{-4}	Severe	[56]
		45	65	3.87×10^{-4}	Severe	
		60	65	7.25×10^{-4}	Severe	
		90	65	5.17×10^{-4}	Severe	
AISI 316	SiC	30	65	3.75×10^{-4}	Severe	[56]
		45	65	4.68×10^{-4}	Severe	
		60	65	5.35×10^{-4}	Severe	
		90	65	4.93×10^{-4}	Severe	
AISI 420	SiC	30	65	6.74×10^{-5}	Moderate	[56]
		45	65	4.55×10^{-5}	Mild	
		60	65	5.97×10^{-5}	Moderate	
		90	65	4.95×10^{-5}	Moderate	
AISI 420	SiC	30	62	8.60×10^{-5}	Moderate	[62]
		45	62	7.80×10^{-5}	Moderate	
		60	62	6.50×10^{-5}	Moderate	
		90	62	3.50×10^{-5}	Mild	
AISI 420	SiC with steel round grit	30	62	3.60×10^{-5}	Mild	[62]
		45	62	2.60×10^{-5}	Mild	
		60	62	2.00×10^{-5}	Ultra- mild	
		90	62	1.30×10^{-5}	Ultra- mild	
2.25 Cr-1 Mo-Virgin	Dry Alumina powder	30	137	2.90×10^{-2}	Severe	[72]
		45	392	7.40×10^{-2}	Severe	
		60	950	3.00×10^{-2}	Severe	
		75	1700	3.20×10^{-2}	Severe	
		90	2667	1.10×10^{-2}	Severe	
2.25 Cr-1 Mo-33012	Dry Alumina powder	30	667	7.14×10^{-3}	Severe	[72]
		45	550	4.80×10^{-2}	Severe	
		60	1175	8.70×10^{-3}	Severe	
		75	1900	2.90×10^{-2}	Severe	
		90	283	2.00×10^{-2}	Severe	
2.25 Cr-1 Mo-35402	Dry Alumina powder	30	1133	1.10×10^{-2}	Severe	[72]
		45	2000	2.40×10^{-2}	Severe	
		60	1100	7.30×10^{-3}	Severe	
		75	196	1.49×10^{-2}	Severe	
		90	475	1.10×10^{-2}	Severe	

Table B-1 Normalized erosion rate of different steels at different impact angle and particle velocity.

Sample	Erodent	Impact angle (°)	Normalized velocity	Normalized erosion rate	Erosion mode	Reference
2.25 Cr-1 Mo-35402	Dry alumina powder	30	1425	8.26×10^{-2}	Severe	[72]
		45	2267	2.10×10^{-2}	Severe	
		60	333	4.39×10^{-3}	Severe	
		75	275	1.40×10^{-2}	Severe	
		90	783	3.70×10^{-3}	Severe	
2.25 Cr-1 Mo-38374	Dry alumina powder	30	1567	4.39×10^{-3}	Severe	[72]
		45	237	1.70×10^{-2}	Severe	
		60	567	3.65×10^{-3}	Severe	
		75	1333	7.30×10^{-3}	Severe	
		90	825	4.13×10^{-3}	Severe	
AISI 1078	Al_2O_3	15	175	6.00×10^{-5}	Severe	[70]
		15	342	3.60×10^{-4}	Severe	
		15	412	3.60×10^{-4}	Severe	
		30	342	2.10×10^{-4}	Severe	
		30	412	3.70×10^{-4}	Severe	
		45	342	2.40×10^{-4}	Severe	
		60	342	1.70×10^{-4}	Severe	
		90	342	1.30×10^{-4}	Severe	
		90	412	2.50×10^{-4}	Severe	
		90	175	5.00×10^{-5}	Severe	
AISI 10105	Al_2O_3	15	175	7.00×10^{-5}	Moderate	[70]
		15	175	6.00×10^{-5}	Moderate	
		15	175	5.00×10^{-5}	Moderate	
		15	342	1.50×10^{-4}	Severe	
		15	412	3.50×10^{-4}	Severe	
		30	342	1.80×10^{-4}	Severe	
		45	342	2.40×10^{-4}	Severe	
		45	412	3.70×10^{-4}	Severe	
		60	342	1.60×10^{-4}	Severe	
		90	342	1.40×10^{-4}	Severe	
		90	412	2.80×10^{-4}	Severe	
Ductile iron	SiO_2	10		9.00×10^{-5}	Moderate	[311]
		75		2.00×10^{-6}	Ultra-mild	

Table B-1 Normalized erosion rate of different steels at different impact angle and particle velocity.

Sample	Erodent	Impact angle (°)	Normalized velocity	Normalized erosion rate	Erosion mode	Reference
AISI 403, tempered at 390° C	SiC	30	94	3.00×10^{-3}	Severe	[348]
		60	94	2.80×10^{-3}	Severe	
		90	94	2.00×10^{-3}	Severe	
AISI 403, tempered at 520° C	SiC	30	94	4.30×10^{-3}	Severe	[348]
		60	94	3.80×10^{-3}	Severe	
		90	94	3.20×10^{-3}	Severe	
AISI 403, tempered at 520° C	SiC	30	94	4.60×10^{-3}	Severe	[348]
		60	94	4.40×10^{-3}	Severe	
		90	94	3.70×10^{-3}	Severe	
EN-24 steel	Crushed soda glass	12.5		5.57×10^{-5}	Moderate	[349]
		22.5		5.14×10^{-5}	Moderate	
		32.5		4.26×10^{-5}	Mild	
		47.5		3.65×10^{-5}	Mild	
		62.5		3.19×10^{-5}	Mild	
EN-24 steel	Soda glass beads	10		2.18×10^{-5}	Mild	[349]
		20		6.00×10^{-6}	Ultra-mild	
		30		6.80×10^{-6}	Ultra-mild	
		45		3.00×10^{-6}	Ultra-mild	
		60		2.00×10^{-6}	Ultra-mild	
Mild steel	Steel ball	30	141851	2.00×10^{-3}	Severe	[131]
		30	283703	1.30×10^{-2}	Severe	
		30	218856	6.70×10^{-3}	Severe	
		40	218856	2.00×10^{-4}	Severe	
AISI 1075-Fine pearlite	SiC	30	46	2.70×10^{-5}	Mild	[104]
		90	46	9.00×10^{-6}	Ultra-mild	
AISI 1075-Course pearlite	SiC	30	46	2.60×10^{-5}	Mild	[104]
		90	46	8.50×10^{-6}	Ultra-mild	
AISI 1075-Fine pearlite	SiC	30	46	2.20×10^{-5}	Mild	[104]
		90	46	7.00×10^{-6}	Ultra-mild	

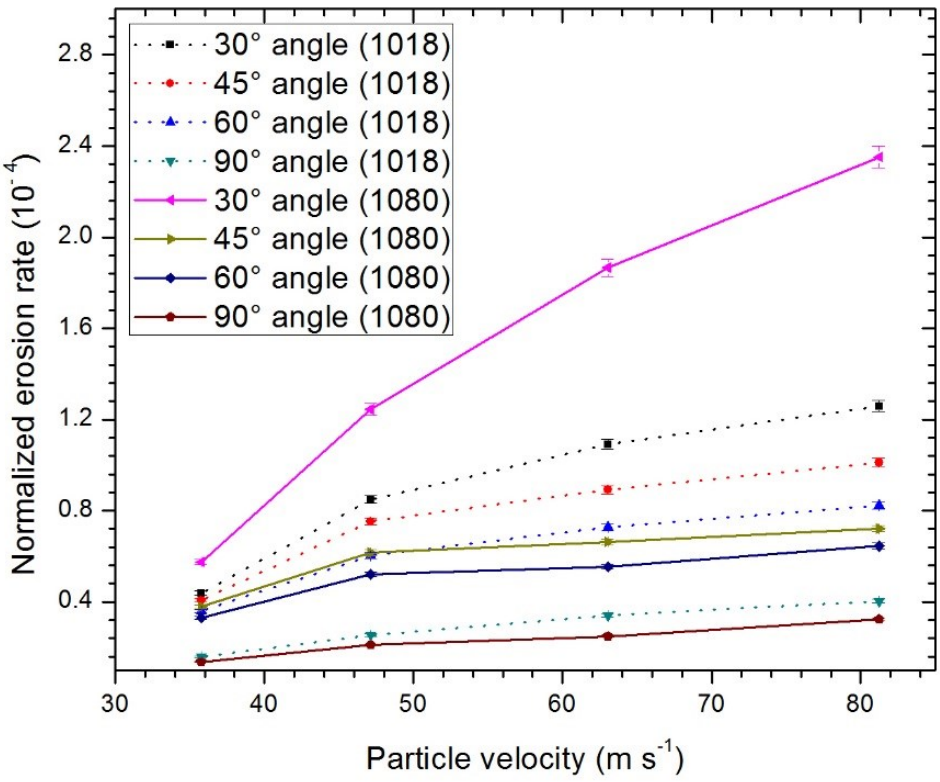

Figure B-1 Normalized erosion rate as a function of particle velocity for AISI 1018 and AISI 1080 steels.

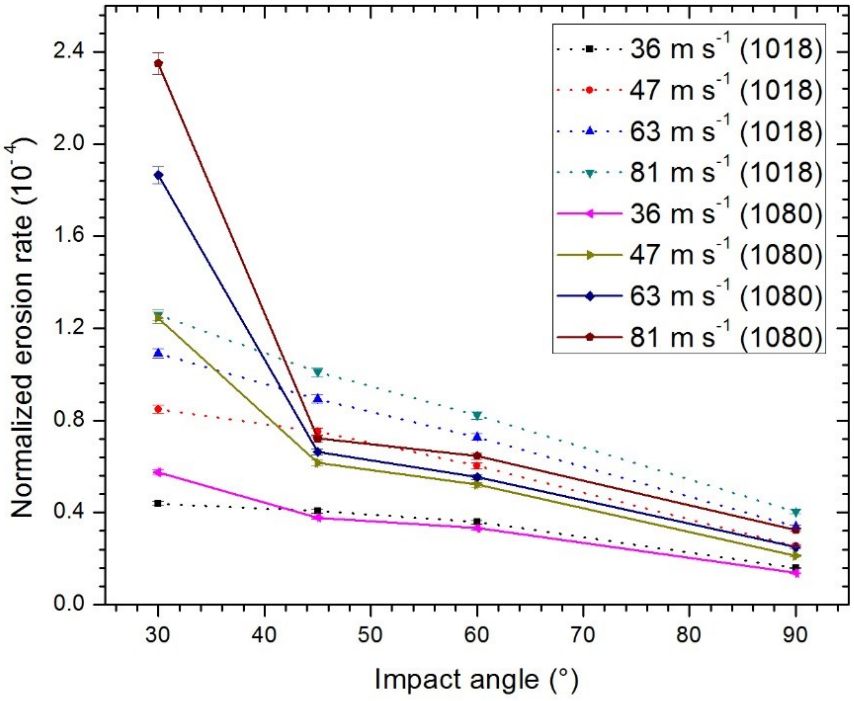

Figure B-2 Normalized erosion rate as a function of impact angle for AISI 1018 and AISI 1080 steels.

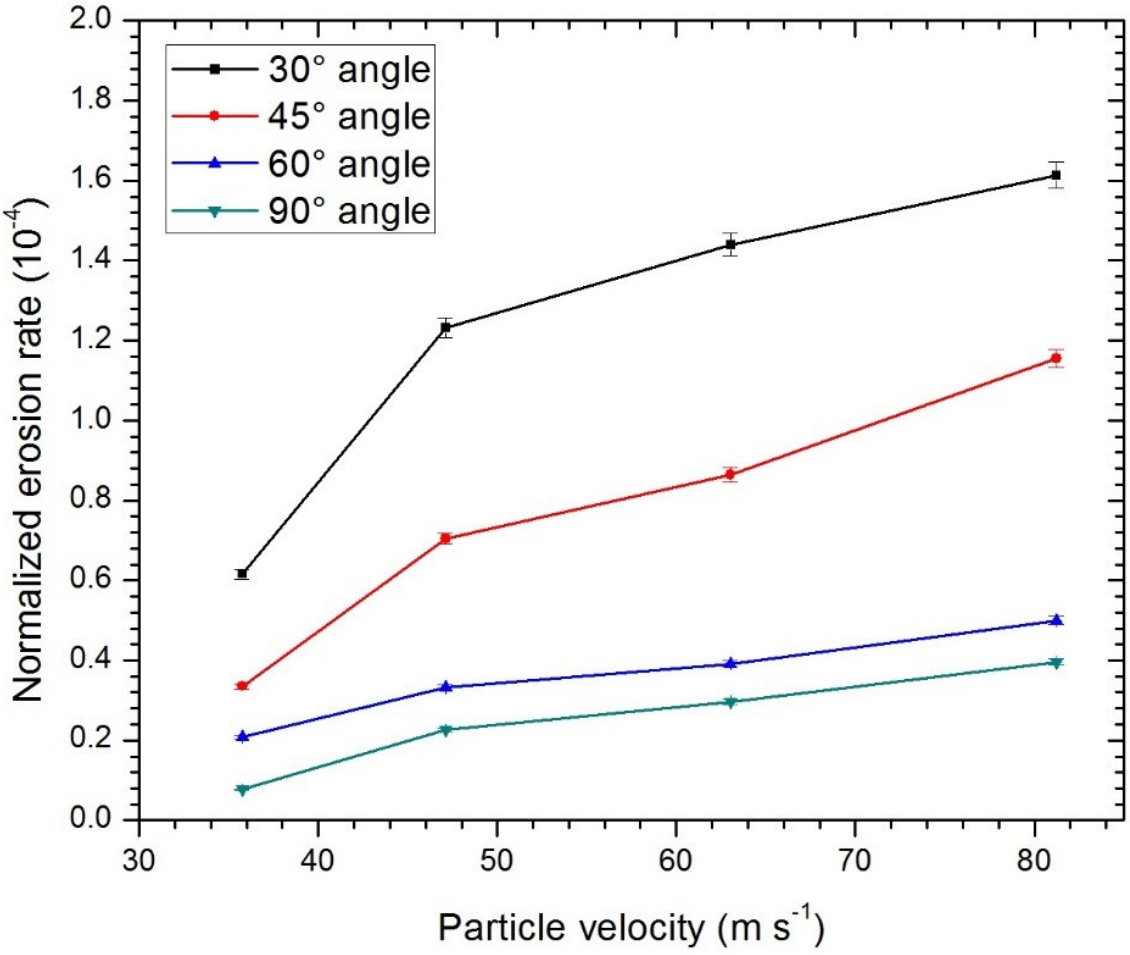

Figure B-3 Normalized erosion rate as a function of particle velocity for API X70 steel.

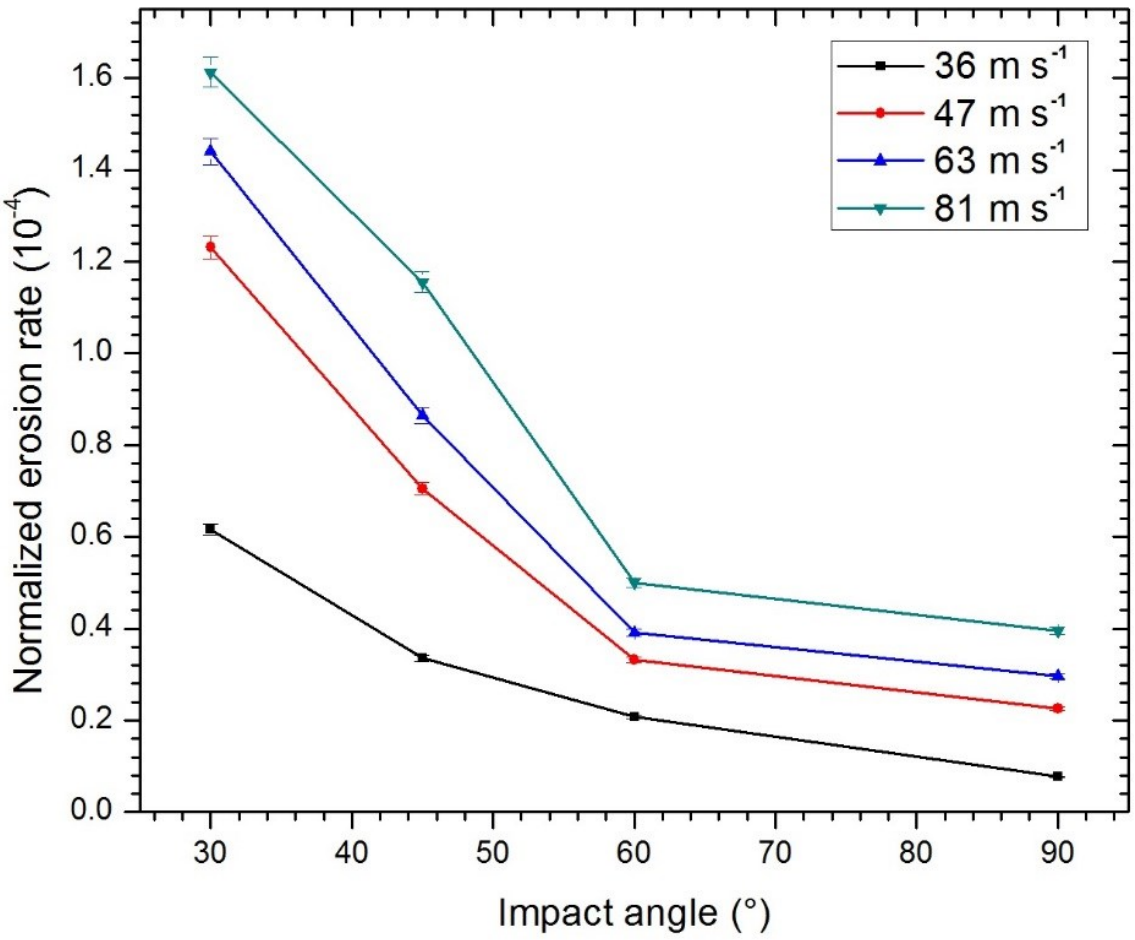

Figure B-4 Normalized erosion rate as a function of impact angle for API X70 steel.

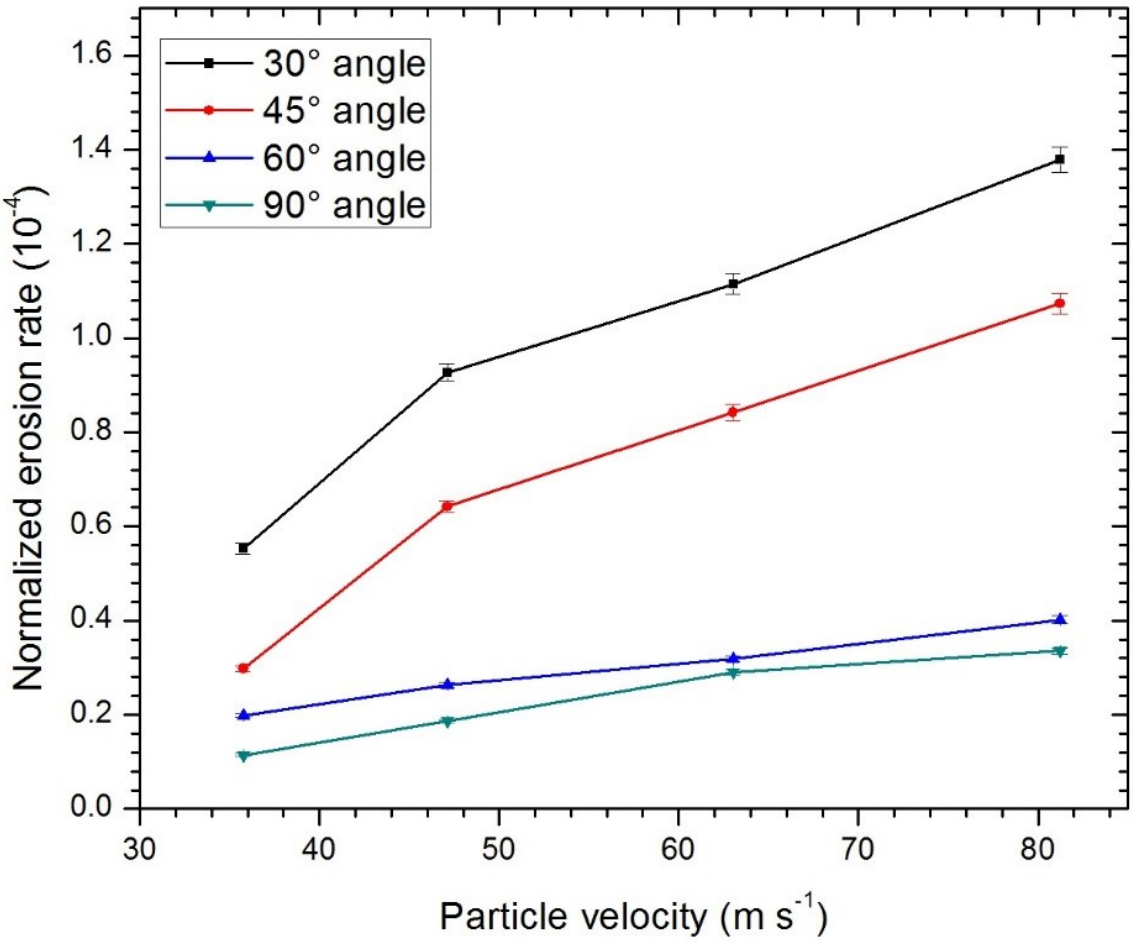

Figure B-5 Normalized erosion rate as a function of particle velocity for API X100 steel.

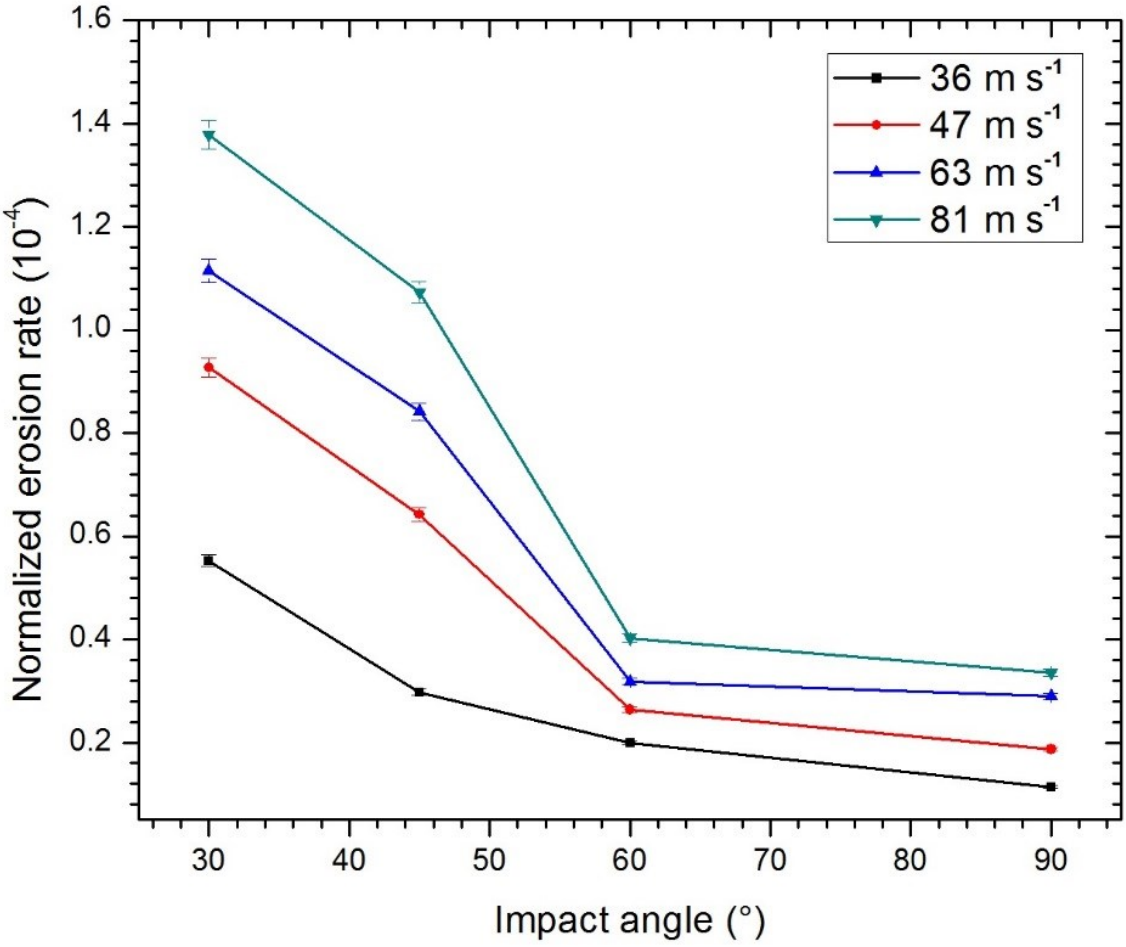

Figure B-6 Normalized erosion rate as a function of impact angle for API X100 steel.

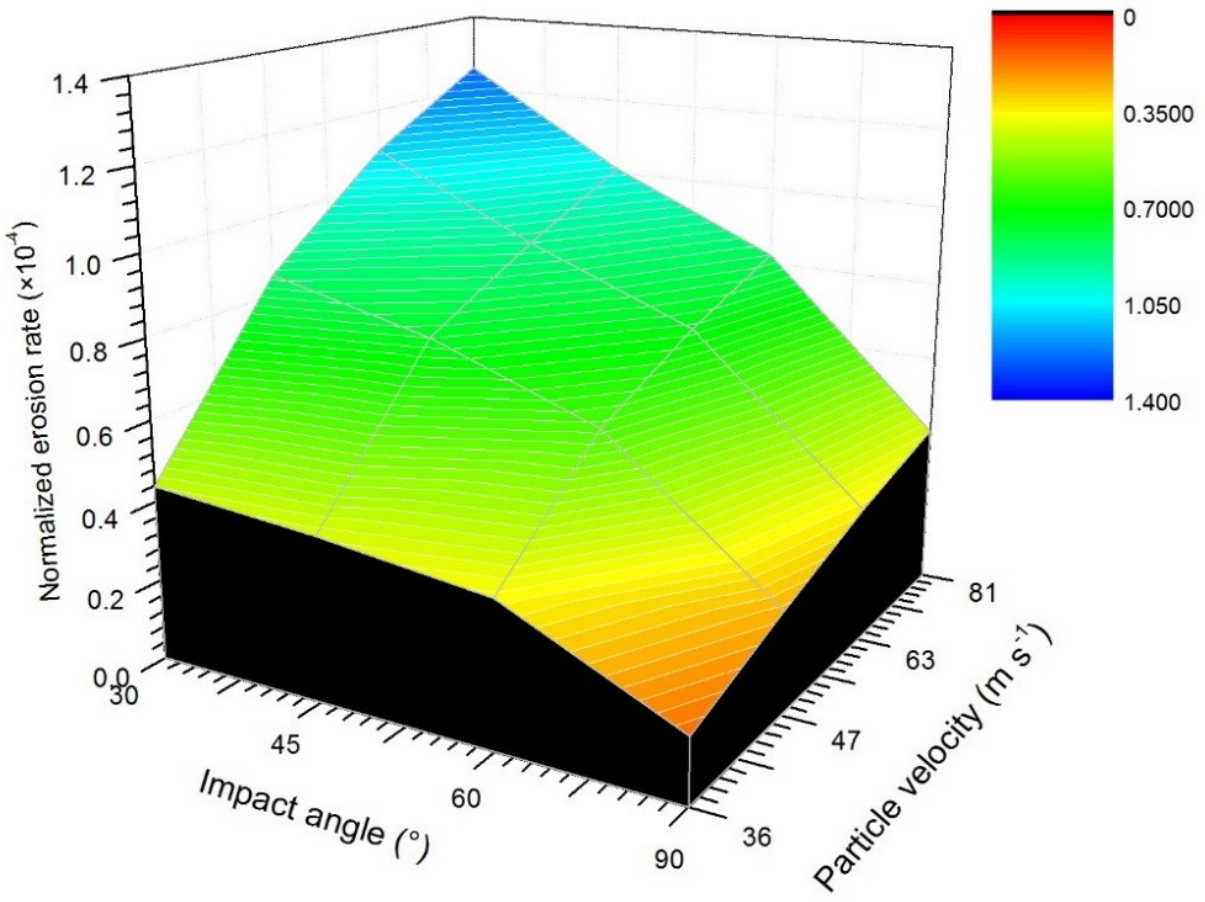

Figure B-7 Normalized erosion rate as a function of impact angle and particle velocity for AISI 1018 steel.

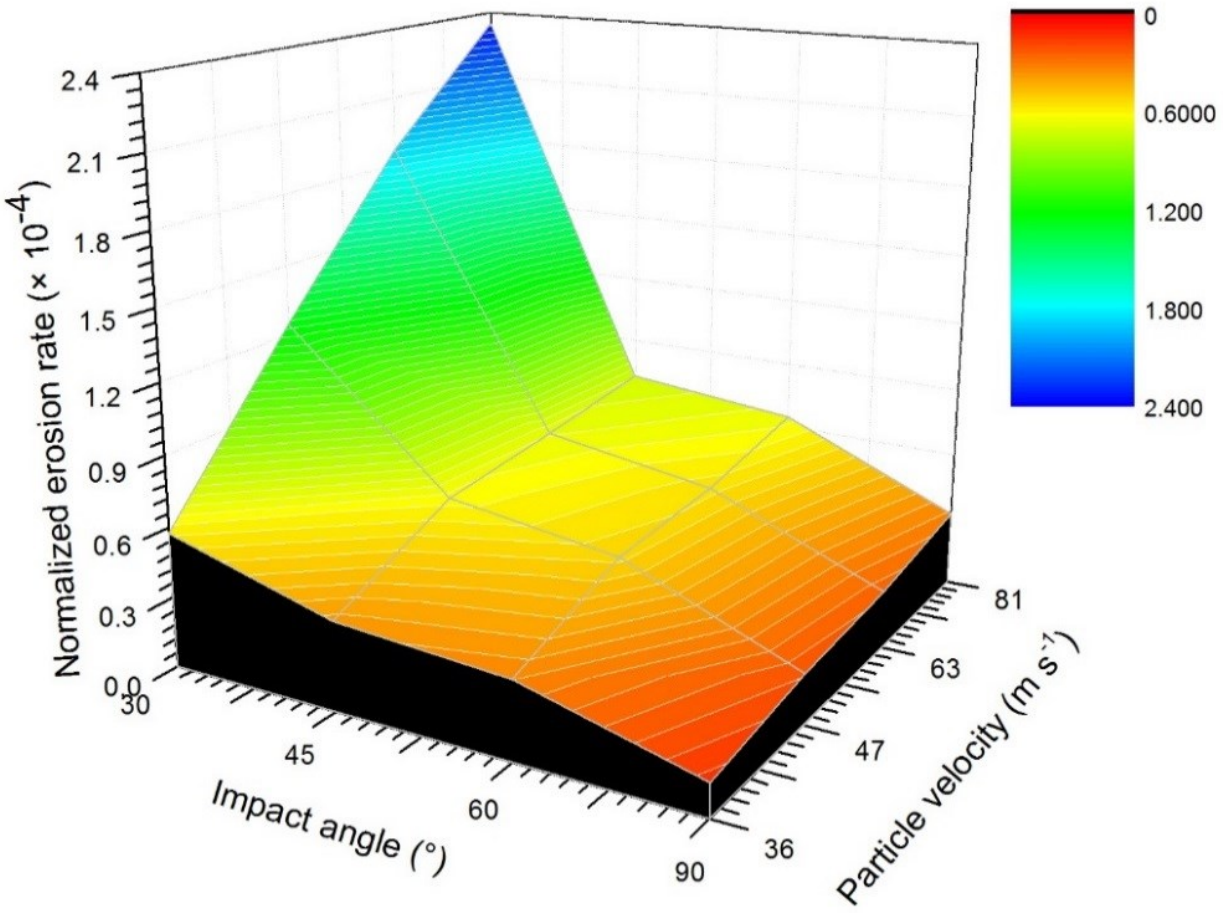

Figure B-8 Normalized erosion rate as a function of impact angle and particle velocity for AISI 1080 steel.

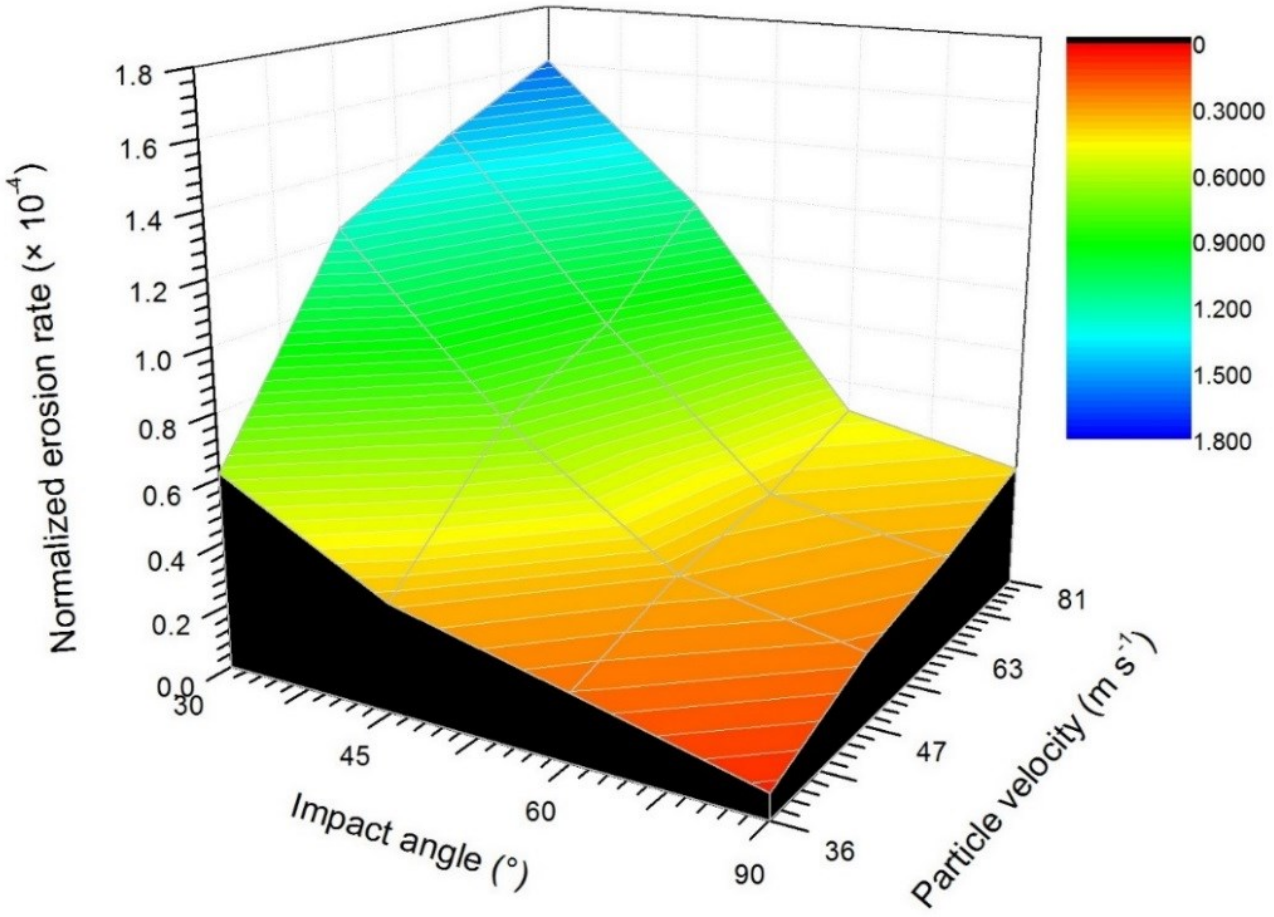

Figure B-9 Normalized erosion rate as a function of impact angle and particle velocity for API X70 steel.

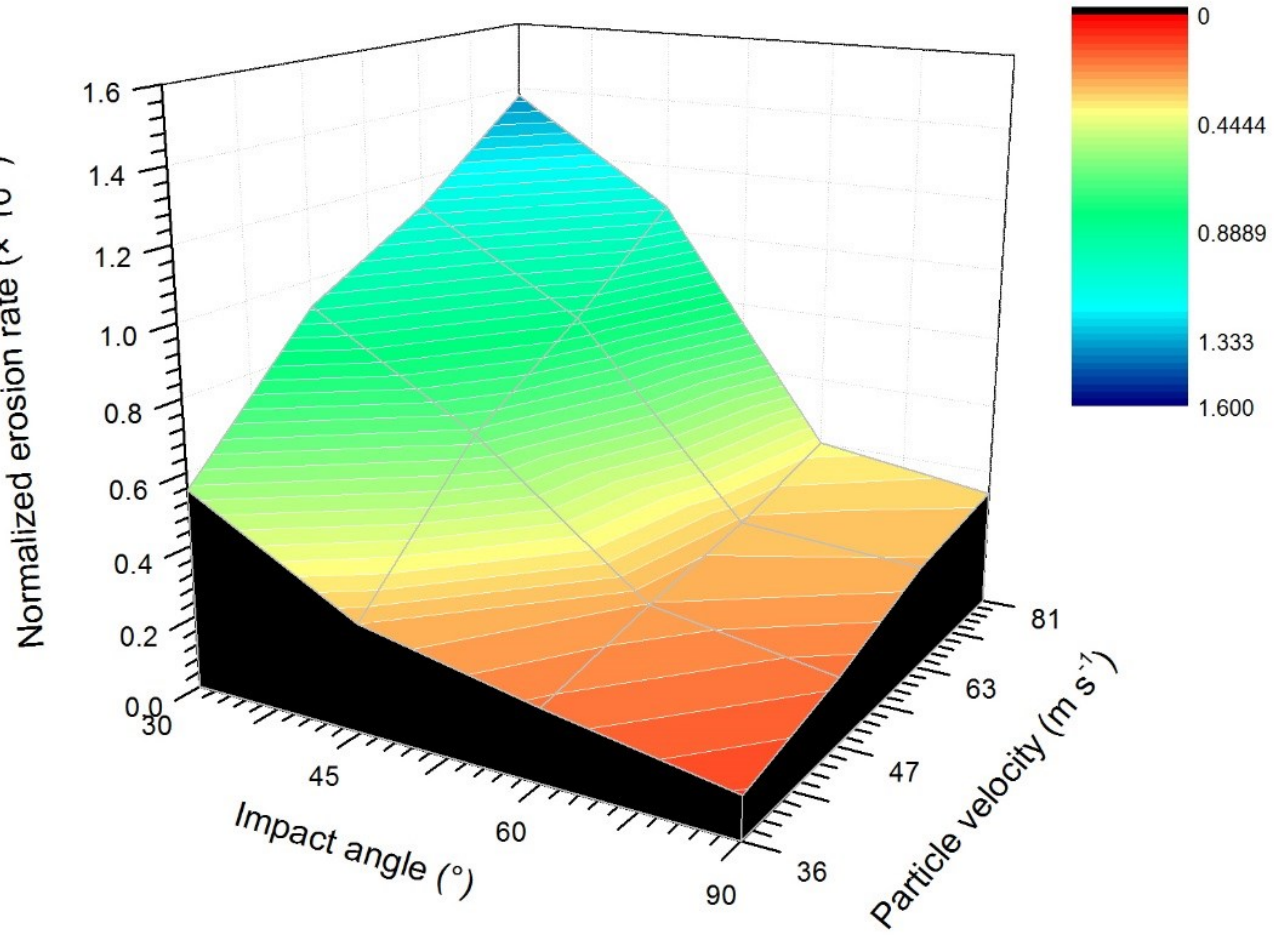

Figure B-10 Normalized erosion rate as a function of impact angle and particle velocity for API X100 steel.

Appendix C

Corrosion Data

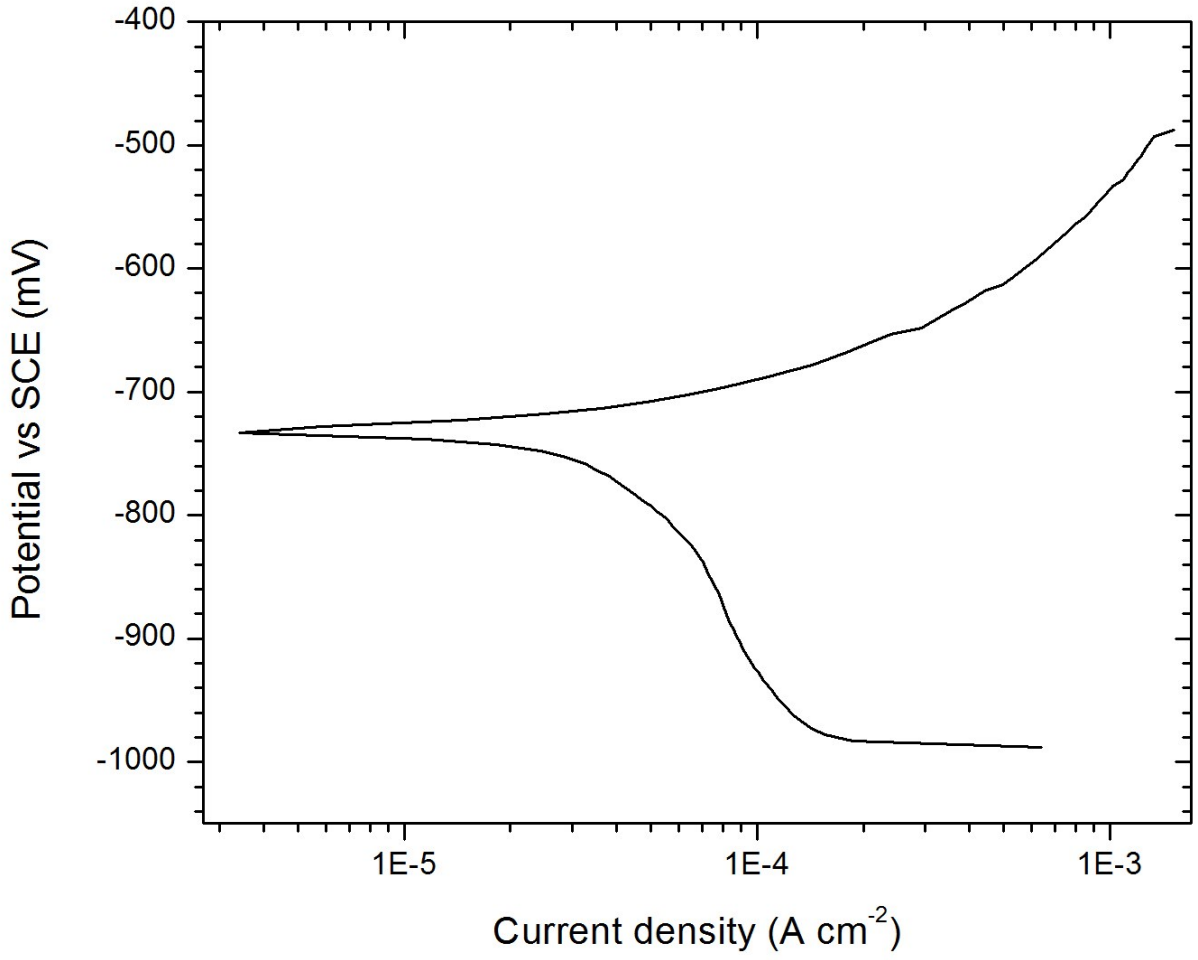

Figure C-1 Potentiodynamic polarization curve for API X70 steel in 2 g l^{-1} NaCl saturated with CO_2. Corrosion current density was measured from Tafel extrapolation.

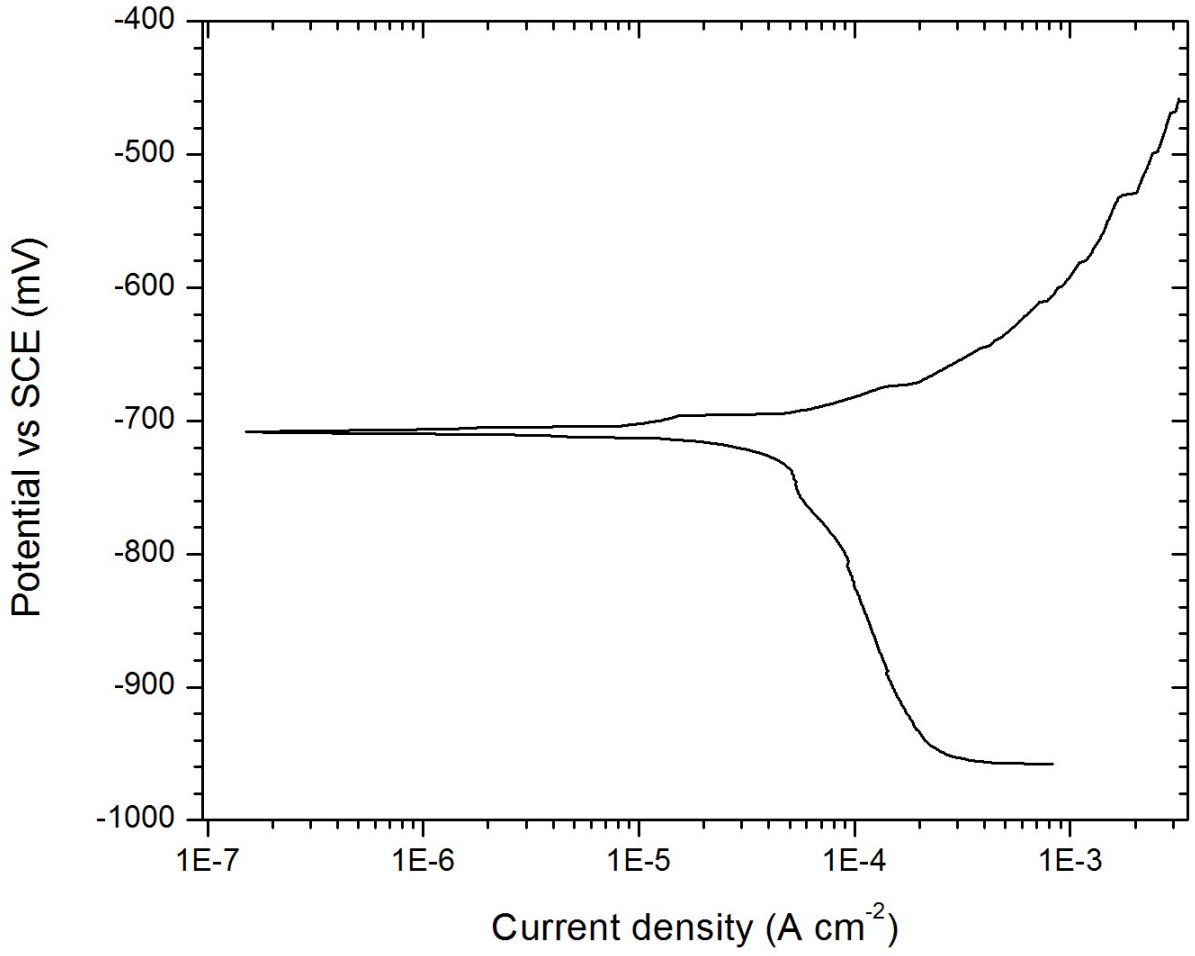

Figure C-2 Potentiodynamic polarization curve for API X100 steel in 2 g l^{-1} NaCl saturated with CO_2. Corrosion current density was measured from Tafel extrapolation.

Appendix D

Erosion-Corrosion Data

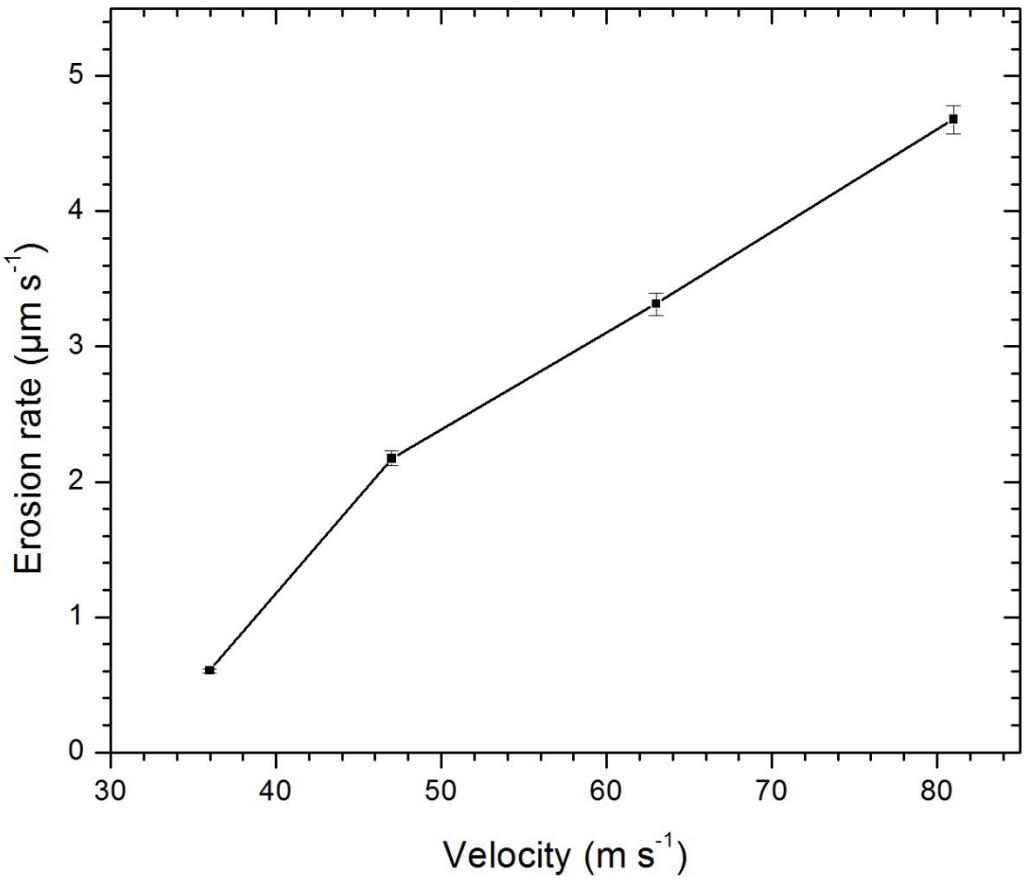

Figure D-1 Pure erosion rate (E_0) (based on 50 s of erosion) vs abrasive particle velocity for API X70 steel showing an increase in erosion rate with particle velocity.

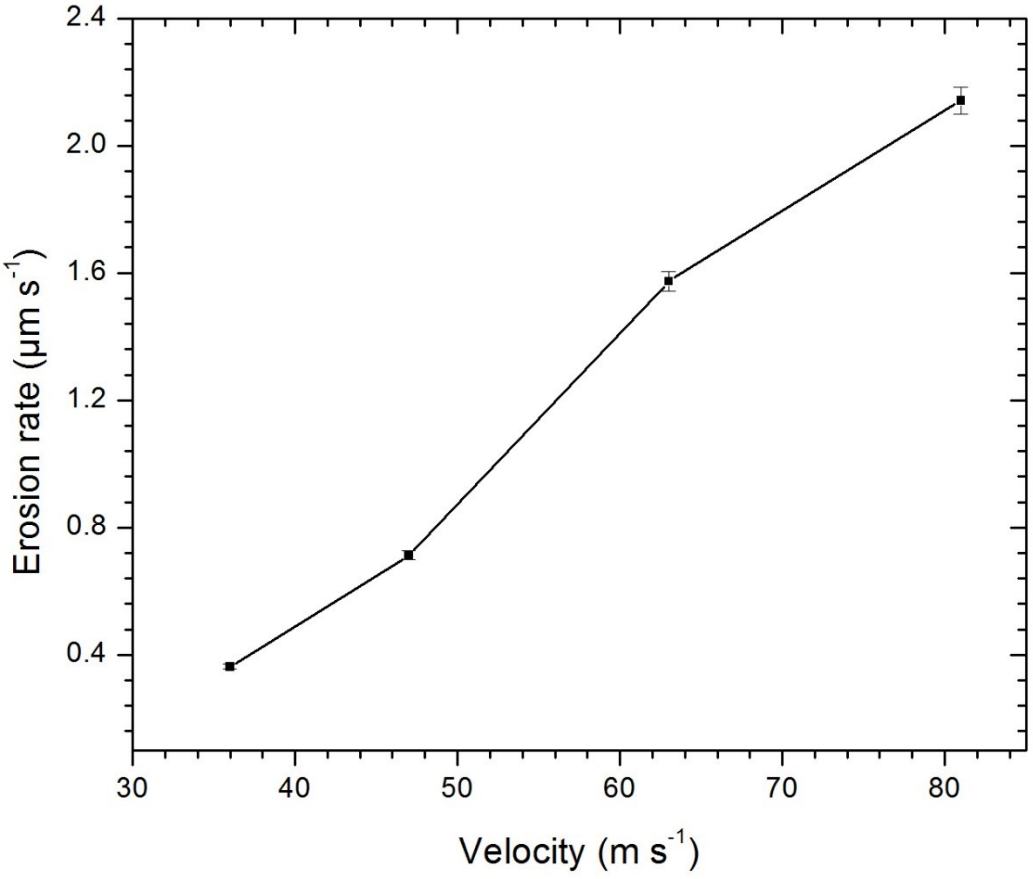

Figure D-2 Pure erosion rate (E_0) (based on 50 s of erosion) vs abrasive particle velocity for API X100 steel showing an increase in erosion rate with particle velocity.

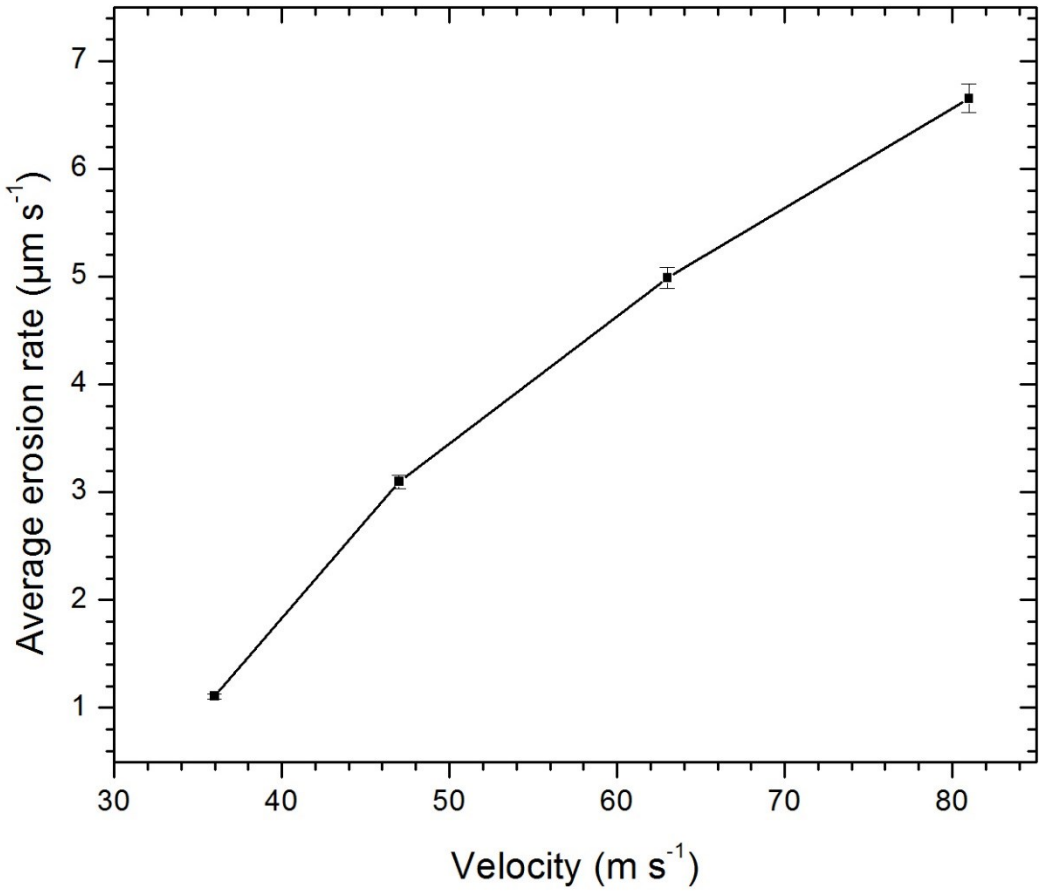

Figure D-3 Average erosion rate (E_c) vs particle velocity for API X70 steel during erosion-corrosion process. Each data point is an average of five erosion cycles.

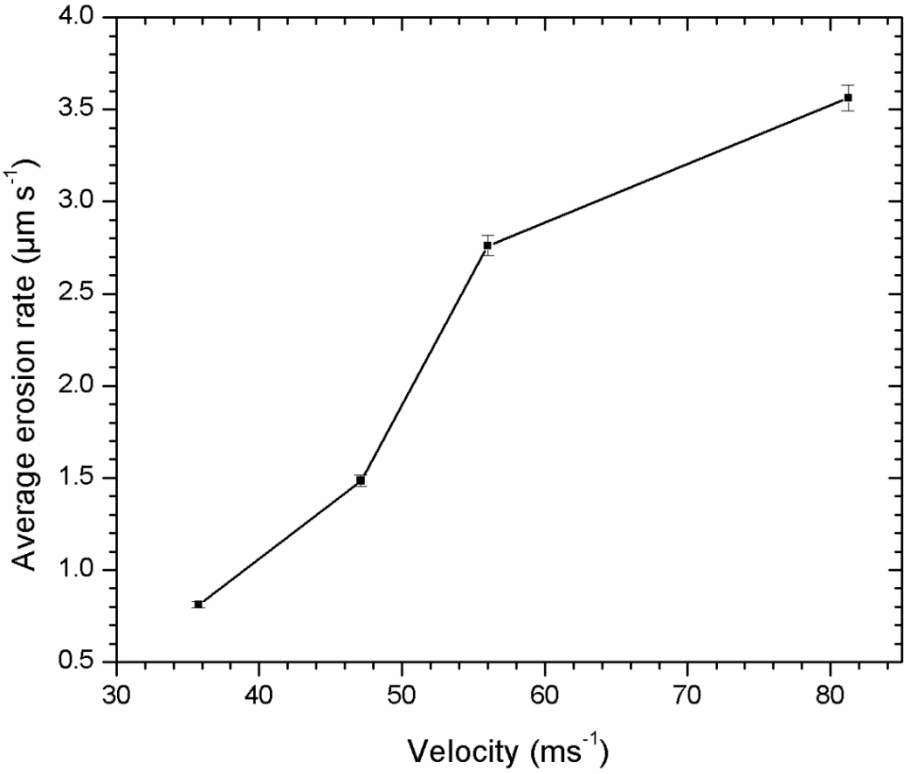

Figure D-4 Average erosion rate (E_c) vs particle velocity for API X100 steel during erosion-corrosion process. Each data point is an average of five erosion cycles.

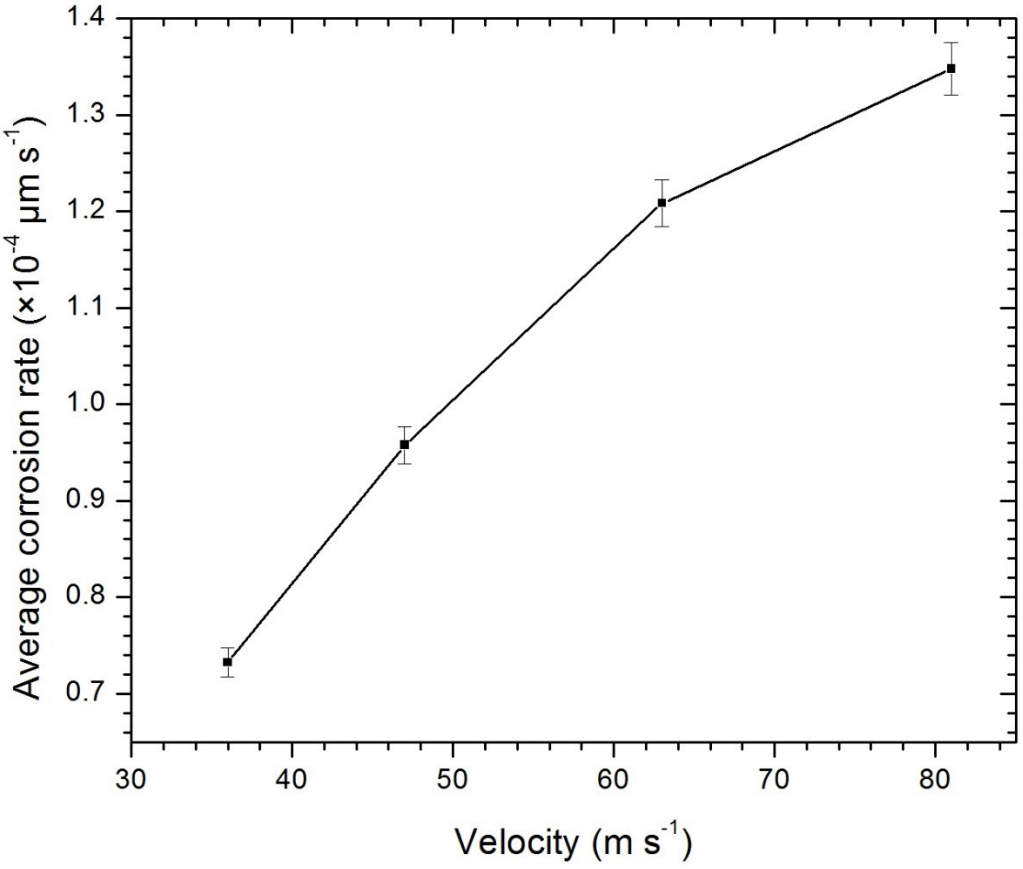

Figure D-5 Average corrosion rate (C_e) (based on weight loss) vs particle velocity for API X70 steel during erosion-corrosion test in which each data point is an average of five corrosion cycles.

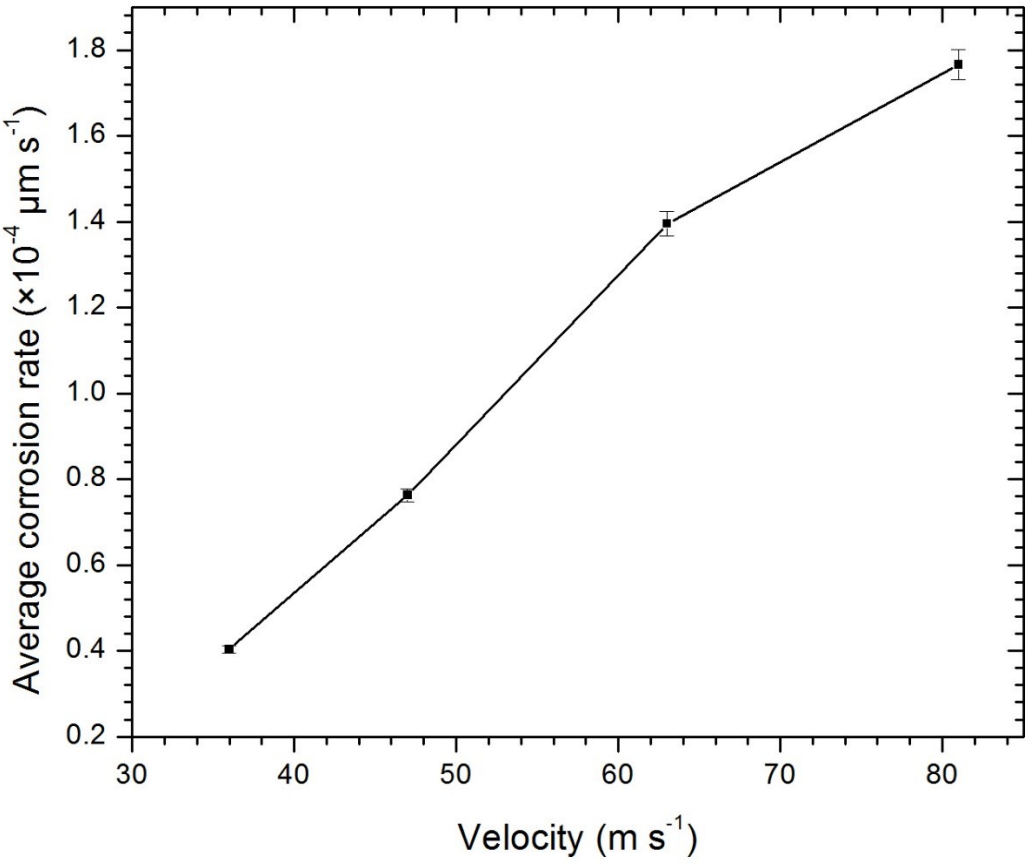

Figure D-6 Average corrosion rate (C_e) (based on weight loss) vs particle velocity for API X100 steel during erosion-corrosion test in which each data point is an average of five corrosion cycles.

Table D-1 Summary of erosion-corrosion data for API X42 steel based on weight loss.

Particle velocity ($m\ s^{-1}$)	Material loss rate ($\mu m\ s^{-1}$)							% increase in erosion due to corrosion ($\Delta E_c / E_0$)	% increase in corrosion due to erosion ($\Delta C_e / C_0$)
	Total material loss (T) ($\mu m\ s^{-1}$)	Total erosion component (E_c) ($\mu m\ s^{-1}$)	Erosion rate in absence of corrosion (E_0) ($\mu m\ s^{-1}$)	Total corrosion component (C_e) ($\mu m\ s^{-1}$)	Corrosion rate in absence of erosion (C_0) ($\mu m\ s^{-1}$)	Change in erosion rate due to corrosion (ΔE_c) ($\mu m\ s^{-1}$)	Change in corrosion rate due to erosion (ΔC_e) ($\mu m\ s^{-1}$)		
36	1.21	1.20	0.77	9.22×10^{-5}	3.80×10^{-6}	0.43	8.83×10^{-5}	55	2.3×10^{3}
47	3.13	3.12	2.72	13.24×10^{-5}	3.80×10^{-6}	0.39	12.86×10^{-5}	15	3.3×10^{3}
63	5.63	5.62	4.16	17.72×10^{-5}	3.80×10^{-6}	1.46	17.34×10^{-5}	35	4.5×10^{3}
81	7.02	7.012	5.24	19.33×10^{-5}	3.80×10^{-6}	1.77	18.95×10^{-5}	34	4.9×10^{3}

Table D -2 Summary of erosion-corrosion data for API X70 steel based on weight loss.

Particle velocity ($m\ s^{-1}$)	Material loss rate ($\mu m\ s^{-1}$)							% increase in erosion due to corrosion ($\Delta E_c / E_0$)	% increase in corrosion due to erosion ($\Delta C_e / C_0$)
	Total materia l loss (T) ($\mu m\ s^{-1}$)	Total erosion component (E_c) ($\mu m\ s^{-1}$)	Erosion rate in absence of corrosion (E_0) ($\mu m\ s^{-1}$)	Total corrosion component (C_e) ($\mu m\ s^{-1}$)	Corrosion rate in absence of erosion (C_0) ($\mu m\ s^{-1}$)	Change in erosion rate due to corrosion (ΔE_c) ($\mu m\ s^{-1}$)	Change in corrosion rate due to erosion (ΔC_e) ($\mu m\ s^{-1}$)		
36	1.11	1.10	0.60	7.32×10^{-5}	3.48×10^{-6}	0.50	6.97×10^{-5}	83	2.0×10^{3}
47	3.10	3.09	2.17	9.57×10^{-5}	3.48×10^{-6}	0.93	9.23×10^{-5}	43	2.6×10^{3}
63	4.99	4.98	3.31	12.10×10^{-5}	3.48×10^{-6}	1.67	11.75×10^{-5}	50	3.3×10^{3}
81	6.66	6.65	4.68	13.47×10^{-5}	3.48×10^{-6}	1.97	13.12×10^{-5}	42	3.7×10^{3}

Table D-3 Summary of erosion-corrosion data for API X100 steel based on weight loss.

Particle velocity ($m\ s^{-1}$)	Material loss rate ($\mu m\ s^{-1}$)							% increase in erosion due to corrosion ($\Delta E_c / E_0$)	% increase in corrosion due to erosion ($\Delta C_e / C_0$)
	Total material loss (T) ($\mu m\ s^{-1}$)	Total erosion component (E_c) ($\mu m\ s^{-1}$)	Erosion rate in absence of corrosion (E_0) ($\mu m\ s^{-1}$)	Total corrosion component (C_e) ($\mu m\ s^{-1}$)	Corrosion rate in absence of erosion (C_0) ($\mu m\ s^{-1}$)	Change in erosion rate due to corrosion (ΔE_c) ($\mu m\ s^{-1}$)	Change in corrosion rate due to erosion (ΔC_e) ($\mu m\ s^{-1}$)		
36	0.81	0.80	0.36	4.03×10^{-5}	2.37×10^{-6}	0.45	3.80×10^{-5}	123	1.6×10^{3}
47	1.49	1.48	0.71	7.63×10^{-5}	2.37×10^{-6}	0.77	7.40×10^{-5}	108	3.1×10^{3}
63	2.76	2.75	1.57	13.95×10^{-5}	2.37×10^{-6}	1.19	13.70×10^{-5}	75	5.7×10^{3}
81	3.56	3.55	2.14	17.66×10^{-5}	2.37×10^{-6}	1.42	17.42×10^{-5}	66	7.3×10^{3}

Appendix E

SEM Micrograph

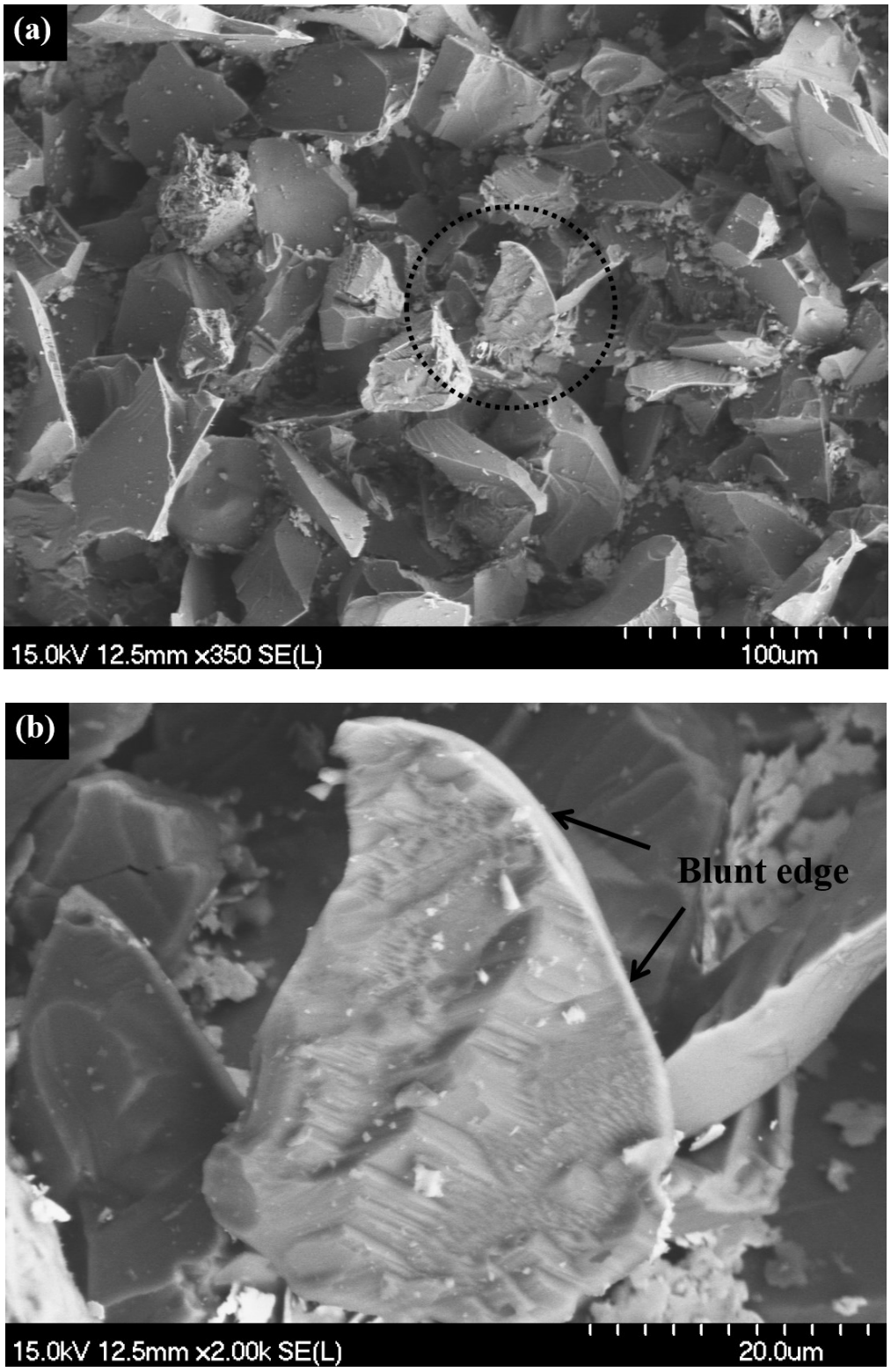

Figure E-1 SEM micrograph of the alumina abrasive after erosion.